



Hughes, Matt (2014) *Silica supported transition metal phosphides- Alternative materials for the water-gas shift reaction*. PhD thesis.

<https://theses.gla.ac.uk/5548/>

Copyright and moral rights for this work are retained by the author

A copy can be downloaded for personal non-commercial research or study, without prior permission or charge

This work cannot be reproduced or quoted extensively from without first obtaining permission in writing from the author

The content must not be changed in any way or sold commercially in any format or medium without the formal permission of the author

When referring to this work, full bibliographic details including the author, title, awarding institution and date of the thesis must be given

Enlighten: Theses

<https://theses.gla.ac.uk/>
research-enlighten@glasgow.ac.uk

**Silica supported transition metal phosphides-
Alternative materials for the water-gas shift
reaction**



**University
of Glasgow**

Matt Hughes

School of Chemistry

University of Glasgow

Thesis presented for fulfilment of the degree

Doctor of philosophy

June 2014

Abstract

Transition metal phosphides remain relatively unexplored as water-gas shift catalysts; however the little that has been done has produced promising results in terms of performance due to the presence of oxygen rich phases. They can be produced through a number of approaches, the most common being reduction of the phosphate precursor using hydrogen. Bimetallic phosphides have also generated interest recently, e.g. with the addition of cerium there are improvements to the phosphides' activity and with the addition of palladium a decrease in reduction temperature is evident in the precursor material.

Nickel phosphide and a range of bimetallic derivatives on a silica support were investigated for their activity in both high and low temperature water-gas shift reactions. All of the catalysts were tested using a continuous flow, fixed bed reactor. Characterization of the catalysts was carried out using XRD, EXAFS, XPS, FTIR, SEM and TEM. The comparison of supported nickel phosphide and an iron based industrial catalyst shows supported nickel phosphide to have good mass normalized activity in comparison to the industrial counterpart under high temperature water-gas shift conditions. The results complement previous studies with regards to potential of nickel phosphide as a water-gas shift catalyst. In view of the results obtained so far for other transition metal phosphides, Ni_2P appears to be superior for the water-gas shift reaction.

One of the most promising aspects of using nickel phosphide in the water-gas shift reaction is its potential resistance to sulfur. Catalyst poisoning caused by impurities such as sulfur are known to deactivate current commercial catalysts for both high and low temperature shift conditions, therefore a catalyst which is resistant to sulfur is an attractive prospect. The sulfur resistant properties of the nickel phosphide catalysts were highlighted by testing them under high temperature water-gas shift conditions in the presence of sulfur. Whilst the catalysts deactivated under the conditions, they showed some residual catalytic activity still remained after sulfur was removed from the feed. Compared with the industrial catalyst, nickel phosphide displayed greater resistance to deactivation.

Acknowledgements

I would like to take this opportunity to acknowledge the many people that help me throughout the duration of my PhD, without their help I would not have been able to get to this point. I would first like to thank both of my supervisors, Dr Justin Hargreaves and Prof. David Jackson for their support and guidance throughout. I would also like to thank my industrial supervisors, Dr Martin Fowles, and Dr Norman MacLeod for all of their support as well as taking the time to come to Glasgow and accommodate me down in Billingham.

I would like to say a big thank you to Andy Monaghan for all his help with technical aspects of day to day life in lab and for being there when things go wrong especially with the XRD. I would also like to say thanks to everyone in the Hargreaves and Jackson groups for their help in various aspects of the project over the last 4 years and for generally being a great bunch to spend the last few years working with.

Finally, thanks to my friends and family for always being there for me and helping me see light at the end of the tunnel, especially in the last few months. Finally I would like to say thanks to Catriona Smith my wonderful girlfriend who has been there through all the ups and downs of the PhD you truly have the patience of saint!

Declaration

The work contained in this thesis, submitted for the degree of Doctor of Philosophy, is my original work, except where due reference is made to other authors. No material within has been previously submitted for a degree at this or any other university.

.....

Matt Hughes

Contents

Chapter 1: Introduction	20
1.1 Background.....	20
1.2 The water-gas shift reaction	21
1.3 Thermodynamics of the water-gas shift reaction.....	23
1.4 Kinetics and proposed reaction mechanisms for the water-gas shift reaction	25
1.4.2 The regenerative mechanism	25
1.4.3 The associative mechanism	27
1.5 Water-gas shift process catalysts	30
1.6 Sulfur poisoning of water-gas shift catalysts	32
1.7 Transition metal phosphides	33
1.7.1 General properties of transition metal phosphides	34
1.7.2 Review of recent publications in the synthesis of transition metal phosphides.	37
1.7.4 Review of recent publications in the catalytic application of transition metal phosphides.....	43
1.8 References	50
Chapter 2: Experimental procedure	53
2.1 Catalyst Synthesis	53
2.1.1 Micro reactor for material synthesis	54
2.1.2 Bulk phase synthesis.....	54
2.1.3 Synthesis of supported materials	57
2.2 List of all nickel phosphide catalysts	58
2.3 Testing Material Stability	59
2.4 Summary of bulk phase synthesis of nickel phosphide	59
2.5 Water-Gas Shift Reaction.....	60
2.5.1 Reactor procedure	62

2.5.2 Gas chromatographic analysis of gases	63
2.5.3 Mass flow controllers (MFCs)	64
2.5.4 GC gas standards	65
2.5.5 Sulfur poisoning	66
2.7 Characterization of materials	66
2.7.1 Thermo-gravimetric analysis (TGA)	67
2.7.2 Scanning electron microscope	67
2.7.3 Powder X-ray diffraction	68
2.7.4 X-ray photoelectron spectroscopy	69
2.7.5 Diffuse Reflectance Infrared Spectroscopy (DRIFTS)	70
2.7.6 Transmission Electron Microscopy (TEM)	72
2.7.7 Extended X-ray absorption fine structure spectroscopy (EXAFS)	74
2.7.8 Raman Spectroscopy	76
2.8 Calculations	78
2.8.1 CO conversion	78
2.8.2 Carbon balance	78
2.8.3 Selectivity of carbon based products	78
2.8.4 Water-gas shift reaction equilibrium	79
Chapter 3: Nickel phosphide, a novel material for application in the water-gas shift reaction	80
3.1 Introduction	80
3.2 Catalytic activity of Nickel Phosphide	80
3.3 Development and characterisation of bulk phase nickel phosphide	83
3.4 Preparation and characterisation of silica supported nickel phosphide	101
3.5 Catalytic testing of silica supported nickel phosphide	117

3.6 Characterisation of post-reaction silica supported nickel phosphide	123
3.7 Conclusions	131
3.8 References	134
Chapter 4: Bimetallic nickel phosphide catalysts for application in the water-gas shift reaction.....	136
4.1 Introduction	136
4.2 Development and activity of bimetallic nickel phosphide catalysts.	136
4.3 The development and characterisation of cerium doped Ni ₂ P/SiO ₂ catalysts.	140
4.4 The catalytic testing of cerium doped Ni ₂ P/SiO ₂ catalysts.	156
4.5 The characterisation of post-reaction tested cerium doped Ni ₂ P/SiO ₂ catalysts.....	167
4.6 The development and characterisation of further bimetallic transition metal phosphide catalysts.	178
4.7 The catalytic testing of further bimetallic transition metal phosphide catalyst.	210
4.8 Conclusions	218
4.9 References	224
Chapter 5: The catalytic performance of silica supported nickel phosphide catalysts under high-temperature water-gas shift conditions in the presence of sulfur	226
5.1 Introduction	226
5.2 The catalytic testing of silica supported nickel phosphide under sulfur poisoning conditions.	229
5.3 Post-sulfur testing characterisation of materials.....	251
5.4 Conclusions	262
5.5 References	266

Chapter 6: Conclusions and future work	268
6.1 General conclusions	268
6.2 Future work.....	273
Chapter 7:Appendix	275

Figures

Figure 1-1: Flow chart detailing the role of syn-gas in a number of industrial processes ^[6]	22
Figure 1-2: An illustration of the relationship between free energy and temperature (a) and equilibrium constant and temperature (b). ^[8]	24
Figure 1-3: Schematic depicting the regenerative mechanism for the interaction between the reagents and catalyst surface for the water-gas shift.....	26
Figure 1-4: Illustration of the associative pathway by which the water-gas shift reaction proceeds	28
Figure 1-5 : Schematic diagram of the two mechanisms by which the water-gas shift is proposed to proceed through on the Cu (111) surface under low temperature conditions. ^[13]	29
Figure 1-6: The trigonal prism crystal structure seen in transition metal phosphides. ^[22]	36
Figure 1-7: Illustration of different crystal structures seen in transition metal phosphides. ^[22]	37
Figure 1-8: The catalytic activity of a range of transition metal phosphides and the commercially used nickel-molybdenum sulfide catalyst for hydrotreatment of sulfur and nitrogen containing compounds. ^[21]	44
Figure 1-9: The two different nickel environments present in Ni ₂ P. Ni (1) is tetrahedral whilst Ni (2) is square pyramidal. ^[23]	46
Figure 1-10: The catalytic activity as well as the presence and importance of the oxy-layers on the surface of nickel phosphide, doped nickel phosphide, elementary nickel and copper in the water-gas shift reaction. ^[5]	49
Figure 2-1: Schematic showing the silica glass fixed bed plug flow micro reactor where catalysts were developed.	54
Figure 2-2: Schematic of the reactor in which water gas shift reactions were conducted.	61
Figure 2-3: Column temperature profile for GC sample run.....	63

Figure 2-4: Plot showing relationship between recorded flow rate and the MFC set point on the control panel.	64
Figure 2-5: GC calibration standards for gases	65
Figure 2-6: Diagram depicting the working of an X-ray diffractometer	69
Figure 2-7: Schematic depicting the layout of the DRIFT spectrometer used for analysing samples.	72
Figure 2-8: Interactions between a sample material and the electrons from the primary source upon which TEM focuses.	73
Figure 2-9: Schematic of the interaction between source X-rays and the target atoms core electron shells and the different modes of interaction between the source and sample in X-ray absorption spectroscopy.	75
Figure 2-10: (above) Raman scattering energy diagrams for different modes of scattering. (below) Stokes, Rayleigh and anti-Stokes bands as they would appear in spectrum.	77
Figure 3-1: XRD patterns showing nickel phosphide produced using alternative precursors.	84
Figure 3-2: TGA reduction profile for nickel phosphate produced using nickel nitrate precursor.	86
Figure 3-3: TGA reduction profile for nickel phosphate produced using nickel nitrate precursor.	86
Figure 3-4: SEM micrographs showing the morphology of Ni ₂ P from both the nickel nitrate (a) and nickel oxide (b) precursor	87
Figure 3-5: Diffraction patterns for a single batch of Ni ₂ P characterised during a one year period.	88
Figure 3-6: X-ray diffraction patterns for different species of nickel phosphide produced.....	89
Figure 3-7: SEM micrographs for Ni ₅ P ₂ (a) and Ni ₃ P (b)	90
Figure 3-8: In-situ XRD patterns detailing the reduction of NiPS ₃ under flowing hydrogen from room temperature to 800°C.	91
Figure 3-9: SEM images showing surface morphology of NiPS ₃ (a) and Ni ₂ P produced from NiPS ₃ (b)	92
Figure 3-10: Raman spectrum for bulk phase nickel phosphide (Ni ₂ P)	93
Figure 3-11: Fresh and steam tested bulk Ni ₂ P sample tested at 400°C	94

Figure 3-12: Nickel 2p XPS spectra for fresh and steamed samples...	95
Figure 3-13: Phosphorus 2p XPS spectra for fresh and steamed samples.....	96
Figure 3-14: SEM micrographs for Ni ₂ P both fresh and steamed for the nickel oxide precursor (a) fresh and (b) steamed.....	98
Figure 3-15: DRIFTS profile for CO chemisorption on bulk phase Ni ₂ P.....	99
Figure 3-16: Ni ₂ P bulk reaction profile for low temperature water-gas shift reaction.....	101
Figure 3-17: Comparison of XRD patterns for Ni ₂ P/SiO ₂ , SiO ₂ and Ni ₂ P.....	103
Figure 3-18: TGA reduction profile for silica supported nickel phosphide from nitrate.....	104
Figure 3-19: SEM micrograph showing silica supported Ni and P.....	105
Figure 3-20: Raman spectrum for Ni ₂ P/SiO ₂ compared alongside bulk phase Ni ₂ P spectrum.....	107
Figure 3-21: XPS spectra for Ni 2p for Ni ₂ P/SiO ₂ and bulk Ni ₂ P.....	108
Figure 3-22: XPS spectra for P 2p for Ni ₂ P/SiO ₂ and bulk Ni ₂ P.....	109
Figure 3-23: k ³ weighted EXAFS spectra for Ni K edge of Ni ₂ P/SiO ₂ including theoretical fit.....	111
Figure 3-24: Fourier transformed Ni K edge EXAFS spectra for Ni ₂ P/SiO ₂ including theoretical fit.....	111
Figure 3-25: TEM micrograph of Ni ₂ P/SiO ₂ showing Ni ₂ P particle on support.....	114
Figure 3-26: DRIFTS spectra for CO chemisorption between RT and 400°C on Ni ₂ P/SiO ₂	116
Figure 3-27: Reaction profile for Ni ₂ P/SiO ₂ based on GC data under low temperature water-gas shift conditions.....	118
Figure 3-28: Comparison of H ₂ and CO ₂ produced during low temperature water-gas shift reaction testing of Ni ₂ P/SiO ₂ and Cu based industrial catalyst.....	119
Figure 3-29: Reaction profile for Ni ₂ P/SiO ₂ tested under high temperature water-gas shift reaction conditions.....	120

Figure 3-30: Reaction profiles showing formation of CO ₂ and H ₂ per weight of catalyst for Ni ₂ P/SiO ₂ and industrial catalyst for HT WGS conditions.	122
Figure 3-31: Formation rates of H ₂ and CO ₂ after 24 hours of running for Ni ₂ P/SiO ₂ and industrial catalyst for HT WGS conditions.	122
Figure 3-32: XRD patterns for Ni ₂ P/SiO ₂ pre and post HT water-gas shift testing.	124
Figure 3-33: SEM micrograph showing Ni ₂ P/SiO ₂ post HT water-gas shift reaction testing.	125
Figure 3-34: Ni ₂ P/SiO ₂ Ni 2p spectra for pre- and post-reaction samples.	127
Figure 3-35: Ni ₂ P/SiO ₂ P 2p spectra for pre- and post-reaction samples.	128
Figure 3-36: Reaction profile for Ni/SiO ₂ catalyst tested under high temperature water-gas shift reaction conditions.	129
Figure 3-37: Reaction profile for P/SiO ₂ tested under high temperature water-gas shift reaction conditions.	130
Figure 4-1: H ₂ formation rates for catalysts and O XPS signal for catalysts. Graphic reproduced from study by Rodriguez and co-workers. [3]	138
Figure 4-2: XRD patterns for Ce-Ni ₂ P/SiO ₂ catalysts with Ce loadings of 0.5%, 1%, 5% and 10%.	142
Figure 4-3: TGA reduction profile for Ce-Ni ₂ P/SiO ₂ catalyst with 1% Ce loading.	143
Figure 4-4: TGA reduction profile for Ce-Ni ₂ P/SiO ₂ catalyst with 10% Ce loading.	144
Figure 4-5: SEM micrograph for Ce-Ni ₂ P/SiO ₂ catalyst with 1% Ce loading.	145
Figure 4-6: SEM micrograph for Ce-Ni ₂ P/SiO ₂ catalyst with 10% Ce loading.	147
Figure 4-7: TEM micrographs showing Ce-Ni ₂ P/SiO ₂ with 10% Ce loading.	148
Figure 4-8: Raman spectra for Ce-Ni ₂ P/SiO ₂ (10% Ce loading), Ni ₂ P/SiO ₂ and bulk Ni ₂ P.	149

Figure 4-9: XPS Ni 2p and Ce 3d spectrum for Ce-Ni ₂ P/SiO ₂ using 10% Ce w.t loading.	151
Figure 4-10: XPS P 2p spectrum for Ce-Ni ₂ P/SiO ₂ using 10% Ce w.t. loading	152
Figure 4-11: k ³ weighted Ni K edge EXAFS spectrum for Ce-Ni ₂ P/SiO ₂ (10% w.t. Ce) catalyst along with theoretical curve fit.	153
Figure 4-12: Fourier transformed spectrum for Ce-Ni ₂ P/SiO ₂ (10% w.t. Ce) catalyst along with theoretical curve fit.	155
Figure 4-13: Reaction profile for Ce-Ni ₂ P/SiO ₂ (10% w.t. Ce loading) under high temperature water-gas shift conditions.....	157
Figure 4-14: Comparison of H ₂ and CO ₂ formation rates for industrial catalyst and Ce-Ni ₂ P/SiO ₂ (10% w.t. Ce loading) under high temperature water-gas shift conditions.	158
Figure 4-15: Reaction profile for Ce-Ni ₂ P/SiO ₂ (5% w.t. Ce loading) under high temperature water-gas shift conditions.....	159
Figure 4-16: Comparison of H ₂ and CO ₂ formation rates for industrial catalyst and Ce-Ni ₂ P/SiO ₂ (5% w.t. Ce loading) under high temperature water-gas shift conditions.	160
Figure 4-17: Reaction profile for Ce-Ni ₂ P/SiO ₂ (1% w.t. Ce loading) under high temperature water-gas shift conditions.....	161
Figure 4-18: Comparison of H ₂ and CO ₂ formation rates for industrial catalyst and Ce-Ni ₂ P/SiO ₂ (1% w.t. Ce loading) under high temperature water-gas shift conditions.	162
Figure 4-19: Reaction profile for Ce-Ni ₂ P/SiO ₂ (0.5% w.t. Ce loading) under high temperature water-gas shift conditions.....	163
Figure 4-20: Comparison of H ₂ and CO ₂ formation rates for industrial catalyst and Ce-Ni ₂ P/SiO ₂ (0.5% w.t. Ce loading) under high temperature water-gas shift conditions.	164
Figure 4-21: Mass normalised hydrogen formation rates after 24hrs of running for all Ce doped catalysts contrasted with Ni ₂ P/SiO ₂	165
Figure 4-22: Mass normalised methane formation rates after 24hrs of running for all Ce doped catalysts contrasted with Ni ₂ P/SiO ₂	166
Figure 4-23: XRD patterns for fresh and post-reaction sample of Ce-Ni ₂ P/SiO ₂ with 0.5% w.t. Ce loading.	167

Figure 4-24: XRD patterns for fresh and post-reaction sample of Ce-Ni ₂ P/SiO ₂ with 10% w.t. Ce loading.....	168
Figure 4-25: Ce-Ni ₂ P/SiO ₂ (10% w.t. Ce) Ni 2p and Ce 3d spectra for pre and post-reaction samples.....	169
Figure 4-26: Ce-Ni ₂ P/SiO ₂ (10 w.t. % Ce) P 2p spectra for pre- and post-reaction samples.....	171
Figure 4-27: Ni K-edge k ³ weighted EXAFS spectrum for post-reaction Ce-Ni ₂ P/SiO ₂ (10% w.t. Ce) along with the theoretical fit.	172
Figure 4-28: Ni K-edge EXAFS Fourier transforms spectrum for post-reaction Ce-Ni ₂ P/SiO ₂ (10 w.t. % Ce) along with theoretical fit.	174
Figure 4-29: SEM micrograph for post HT shift reaction testing Ce-Ni ₂ P/SiO ₂ catalyst with 10% Ce loading.....	176
Figure 4-30: SEM micrograph for post HT shift reaction testing Ce-Ni ₂ P/SiO ₂ catalyst with 1% Ce loading.....	177
Figure 4-31: XRD patterns for a number of silica supported bimetallic nickel phosphide catalysts.....	181
Figure 4-32: TGA reduction profile for the phosphate precursor to Cu-NiP/SiO ₂	182
Figure 4-33: TGA reduction profile for the phosphate precursor to Fe-NiP/SiO ₂	183
Figure 4-34: TGA reduction profile for the phosphate precursor to Cs-Ni ₂ P/SiO ₂	184
Figure 4-35: TGA reduction profile for the phosphate precursor to Pd-Ni ₂ P/SiO ₂	185
Figure 4-36: SEM micrograph for Fe-NiP/SiO ₂	187
Figure 4-37: SEM micrograph for Cu-NiP/SiO ₂	188
Figure 4-38: SEM micrograph for Cs-Ni ₂ P/SiO ₂	189
Figure 4-39: SEM micrograph for Pd-Ni ₂ P/SiO ₂	190
Figure 4-40: TEM micrographs at two magnifications for Cu-NiP/SiO ₂	192
Figure 4-41: TEM micrographs at two magnifications for Cs-Ni ₂ P/SiO ₂	194
Figure 4-42: TEM micrographs at two magnifications for Pd-Ni ₂ P/SiO ₂	195

Figure 4-43: XPS nickel 2p spectrum for Fe-NiP/SiO ₂	197
Figure 4-44: XPS phosphorus 2p spectrum for Fe-NiP/SiO ₂	198
Figure 4-45: Iron 2p spectrum for Fe-NiP/SiO ₂	199
Figure 4-46: XPS nickel 2p spectrum for Cs-Ni ₂ P/SiO ₂	201
Figure 4-47: XPS phosphorus 2p spectrum for Cs-Ni ₂ P/SiO ₂	201
Figure 4-48: The k ³ weighted EXAFS spectrum for Cu-NiP/SiO ₂ catalyst along with theoretical curve fit.	203
Figure 4-49: Fourier transforms spectrum for Cu-NiP/SiO ₂ catalyst along with theoretical curve fit	204
Figure 4-50: The k ³ weighted EXAFS spectrum for Pd-Ni ₂ P/SiO ₂ catalyst along with theoretical curve fit.....	205
Figure 4-51: Fourier transformed spectrum for Pd-Ni ₂ P/SiO ₂ catalyst along with theoretical curve fit.	206
Figure 4-52: EXAFS spectrum for Fe-NiP/SiO ₂ catalyst along with theoretical curve fit.....	207
Figure 4-53: Fourier transformed spectrum for Fe-NiP/SiO ₂ catalyst along with theoretical curve fit.	209
Figure 4-54: Reaction profile for Cu-NiP/SiO ₂ under high temperature water-gas shift conditions.	211
Figure 4-55: Reaction profile for Fe-NiP/SiO ₂ under high temperature water-gas shift conditions.	212
Figure 4-56: Reaction profile for Cs-Ni ₂ P/SiO ₂ under high temperature water-gas shift conditions.	214
Figure 4-57: Reaction profile for Cs-Ni ₂ P/SiO ₂ under high temperature water-gas shift conditions.	215
Figure 4-58: Mass normalised hydrogen formation rates after 24hrs of running for all bimetallic nickel phosphide catalysts.	216
Figure 4-59: Hydrogen formation rates after 24hrs of running for all bimetallic nickel phosphide catalysts per volume of catalyst.....	217
Figure 5-1: CO DRIFTS profile for Ni ₂ P/SiO ₂ treated with thiophene.	231
Figure 5-2: CO adsorption DRIFTS profile for Ni/SiO ₂ treated with thiophene.....	233
Figure 5-3: CO adsorption DRIFTS profile for Ni/SiO ₂	233

Figure 5-4: Reaction profile for sulfur testing of the HT industrial catalyst.....	235
Figure 5-5: CO conversion profile for sulfur testing of the HT industrial catalyst.....	236
Figure 5-6: Sulfur deactivation plot for the HT industrial catalyst.	237
Figure 5-7: Reaction profile sulfur testing of Ni ₂ P/SiO ₂ catalyst tested under HT water gas shift conditions.	239
Figure 5-8: CO conversion profile for sulfur testing of Ni ₂ P/SiO ₂ catalyst tested under HT water gas shift conditions.	240
Figure 5-9: Sulfur deactivation plot for Ni ₂ P/SiO ₂ catalyst	241
Figure 5-10: Reaction profile for then sulfur testing of Ce-Ni ₂ P/SiO ₂ (1%Ce loading) catalyst tested under HT water-gas shift conditions.	243
Figure 5-11: CO conversion profile for sulfur testing of Ce-Ni ₂ P/SiO ₂ (1% Ce loading) catalyst tested under HT water gas-shift conditions.	244
Figure 5-12: Sulfur deactivation plot for Ce-Ni ₂ P/SiO ₂ (1% Ce loading) catalyst.....	245
Figure 5-13: Reaction profile for sulfur testing of Ni/SiO ₂ catalyst tested under HT water-gas shift conditions.	246
Figure 5-14: CO conversion profile for sulfur testing of Ni/SiO ₂ catalyst tested under HT water gas-shift conditions.	247
Figure 5-15: Sulfur deactivation plot for Ni/SiO ₂ catalyst.....	248
Figure 5-16: Estimated S:Ni ratio of nickel based catalysts at which the initial CO conversion drops by 50%.....	250
Figure 5-17: XRD patterns for pre- and post-sulfur testing Ni ₂ P/SiO ₂	251
Figure 5-18: XRD patterns for pre- and post-sulfur testing Ce-Ni ₂ P/SiO ₂	252
Figure 5-19: XRD patterns for pre and post sulfur testing Ni/SiO ₂	253
Figure 5-20: Ni ₂ P/SiO ₂ Ni 2p spectra for pre- and post-sulfur testing reaction samples.	254
Figure 5-21: Ni ₂ P/SiO ₂ P 2p spectra for pre and post sulfur testing reaction samples.	256

Figure 5-22: Ce-Ni ₂ P/SiO ₂ Ni 2p spectrum for the post sulfur testing reaction sample.....	258
Figure 5-23: Ce-Ni ₂ P/SiO ₂ P 2p spectrum for the post sulfur testing reaction sample.....	259
Figure 5-24: Ni/SiO ₂ P 2p spectrum for the post sulfur testing reaction sample.	261
Figure 7-1 Nickel 2p spectra for pre- and post-steam treated bulk phase Ni ₅ P ₂	275
Figure 7-2: Phosphorus 2p spectra for pre- and post-steam treated bulk phase Ni ₅ P ₂	275
Figure 7-3: Nickel 2p spectra for pre- and post-steam treated bulk phase Ni ₃ P.....	276
Figure 7-4: Phosphorus 2p spectra for pre- and post-steam treated bulk phase Ni ₃ P.....	277

Tables

Table 2-1: Summary of the catalysts prepared and tested during the project.....	58
Table 2-2: Summary table of preparation routes for bulk phase nickel phosphide.....	59
Table 3-1: Summary of binding energy peaks shown in spectra for Ni ₂ P and those reported in previous studies.....	97
Table 3-2: Table of results for Ni ₂ P/SiO ₂ elemental analysis carried out by EDX.....	106
Table 3-3: Summary of binding energy peaks shown in spectra for bulk and silica supported Ni ₂ P.....	109
Table 3-4: Curve fitting results of the Ni K-edge EXAFS spectra for Ni ₂ P/SiO ₂	113
Table 3-5 Elemental analyses of post-reaction Ni ₂ P/SiO ₂	125
Table 3-6: Summary of binding energy peaks shown in spectra for silica supported Ni ₂ P pre- and post-catalytic testing.....	128
Table 4-1: Table summarising EDX analysis of target particles.....	146
Table 4-2: Summary of EDX analysis results for targeted crystallite structure.....	148
Table 4-3: Summary of binding energy peaks shown in spectra for Ni ₂ P/SiO ₂ and Ce-Ni ₂ P/SiO ₂	152
Table 4-4: Summary of curve fit results for Ce-Ni ₂ P/SiO ₂ (10% w.t. Ce) EXAFS spectrum.....	155
Table 4-5: Summary of binding energy peaks shown in spectra for Ni ₂ P/SiO ₂ and Ce-Ni ₂ P/SiO ₂ pre and post HT shift.....	171
Table 4-6: Curve fitting results of the Ni K-edge EXAFS spectra for post-reaction Ce-Ni ₂ P/SiO ₂ (10 w.t. % Ce).....	174
Table 4-7: Table summarising EDX analysis of target particles.....	176
Table 4-8: Table summarising EDX analysis of target particles.....	177
Table 4-9: Summary of EDX results from analysis of target area on the micrograph.....	187
Table 4-10: Summary of EDX results from analysis of target area on the micrograph.....	189

Table 4-11: Summary of EDX results from analysis of target area on the micrograph.....	191
Table 4-12 Summary of EDX results from analysis of the micrograph.	192
Table 4-13: Summary of EDX results from analysis of target area on the micrograph.....	194
Table 4-14: Summary of EDX results from analysis of target area on the micrograph.....	196
Table 4-15: Summary of binding energy peaks shown in the XPS spectra for Ni ₂ P/SiO ₂ and Fe-NiP/SiO ₂	199
Table 4-16: Summary of binding energy peaks shown in the XPS spectra for Ni ₂ P/SiO ₂ and Cs-Ni ₂ P/SiO ₂	202
Table 4-17: Summary of curve fit results for Cu-NiP/SiO ₂ EXAFS spectrum.....	204
Table 4-18: Summary of curve fit results for Pd-Ni ₂ P/SiO ₂ EXAFS spectrum.....	207
Table 4-19: Summary of curve fit results for Pd-Ni ₂ P/SiO ₂ EXAFS spectrum.....	209
Table 5-1: Summary of binding energy peaks shown in spectra for Ni ₂ P/SiO ₂ pre and post HT shift sulfur testing.	256
Table 5-2: Summary of binding energy peaks shown in spectra for Ni ₂ P/SiO ₂ with Ce-Ni ₂ P/SiO ₂ post HT shift sulfur testing.	259
Table 5-3: Summary of binding energy peaks shown in literature for Ni metal with Ni/SiO ₂ post HT shift sulfur testing.....	261
Table 7-1: Binding energies associated with given spectra for pre- and post-steam treated bulk phase Ni ₅ P ₂	276
Table 7-2: Binding energies associated with given spectra for pre- and post-steam treated bulk phase Ni ₅ P	277

Chapter 1 : Introduction

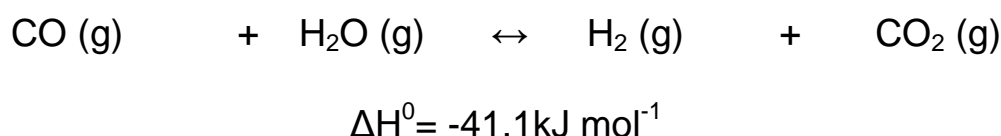
1.1 Background

The decline in the quality and abundance of fossil fuels has led to a great deal of research into optimization of current chemical processes and alternative fuels for use. Catalysis plays a vital role in many processes used today including the Fischer-Tropsch process; steam reforming and the water-gas shift reaction are heavily reliant upon the catalytic materials that are used. ^[3] It is therefore essential that current catalysts are improved and new novel materials developed for these processes. Catalysts must be developed that improve upon current materials particularly in conversion of energy, the production of chemicals, and the elimination of pollutants as well as attaining improvements in efficiency. ^[1] One of the major challenges to overcome in the development of new catalysts is poisoning of the potential catalysts due to the use of “dirty” feedstocks containing sulfur, chlorine, heavy metals and other such contaminants, which often cause a large drop in catalytic activity. ^[2] This aspect will become more important in coming years as the quality of feedstock sources decreases. It is therefore essential that any new materials for potential catalytic application are tolerant to these components. To achieve this goal, new and innovative materials must be studied as potential catalysts. ^[3] In recent years, a number of theoretical and experimental studies have been carried out to investigate new and innovative materials for application in the water-gas shift reaction to replace the catalysts used currently in the industrial production of hydrogen. ^[4-5] The main objective in these studies has been to maintain catalytic activity and efficiency of the process whilst improving upon current disadvantages such as susceptibility to poison through sulfur containing compounds found in feedstocks.

1.2 The water-gas shift reaction

Hydrogen has been billed as a fuel of the future, with minimal pollution and high enthalpy of combustion and is commonly seen by many as having a great deal of potential as an alternative fuel source. Such has been the potential of hydrogen as a fuel source that many efforts have been made to invest heavily in the development of hydrogen production to allow it to become a significant contributor to the energy market in the future. Hydrogen can be obtained from natural gas, liquid hydrocarbon fuels (including biomass fuels such as ethanol), landfill gases, water and electricity (via the process of electrolysis), biological processes including those involving algae, and from gasification of biomass, wastes and coal.^[8] Currently, hydrogen has many applications and sizeable demand already exists. Applications include hydrotreating crude oil, which is essential for removing contaminants within the oil such as sulfur, oxygen and nitrogen which can be harmful to the environment and cause a drop in catalytic activity for downstream catalysts sensitive to poisoning.^[9]

The water-gas shift reaction was first reported over 120 years ago. Steam was reacted with coke at temperatures of 1000⁰C to produce hydrogen gas and carbon dioxide. This process was optimized over the years by using carbon monoxide as the carbon based feed.^[3] The water-gas reaction has played a vital role in the production of ammonia for almost 100 years. The hydrogen produced from the water-gas shift is reacted with nitrogen gas to produce ammonia.^[3] The water-gas shift reaction is a stoichiometrically even reaction in which an equal number of moles of water and carbon monoxide react to produce the equivalent moles of hydrogen and carbon dioxide. Hydrogen-rich mixtures are achieved by altering the stoichiometric ratio between carbon monoxide and water in favour of water. The chemical equation for the reaction is given below:



In carbon-based hydrogen production, the water-gas shift reaction (abbreviated to WGS) is the intermediate step used for hydrogen enrichment and CO reduction in synthesis gas streams. Syn-gas is used in a number of processes such as the Fischer-Tropsch process to produce long chain hydrocarbons, many of which are vital in the production of wide range of chemical and products such as diesel and gasoline. ^[3-4] The importance of syn-gas in terms of industrial processes can be described more accurately as an intermediate between the primary sources (coal, oil and gas) and the conversion into energy. The schematic shown in Figure 1-1 indicates the conversion routes of synthesis gas to liquid fuels. ^[6]

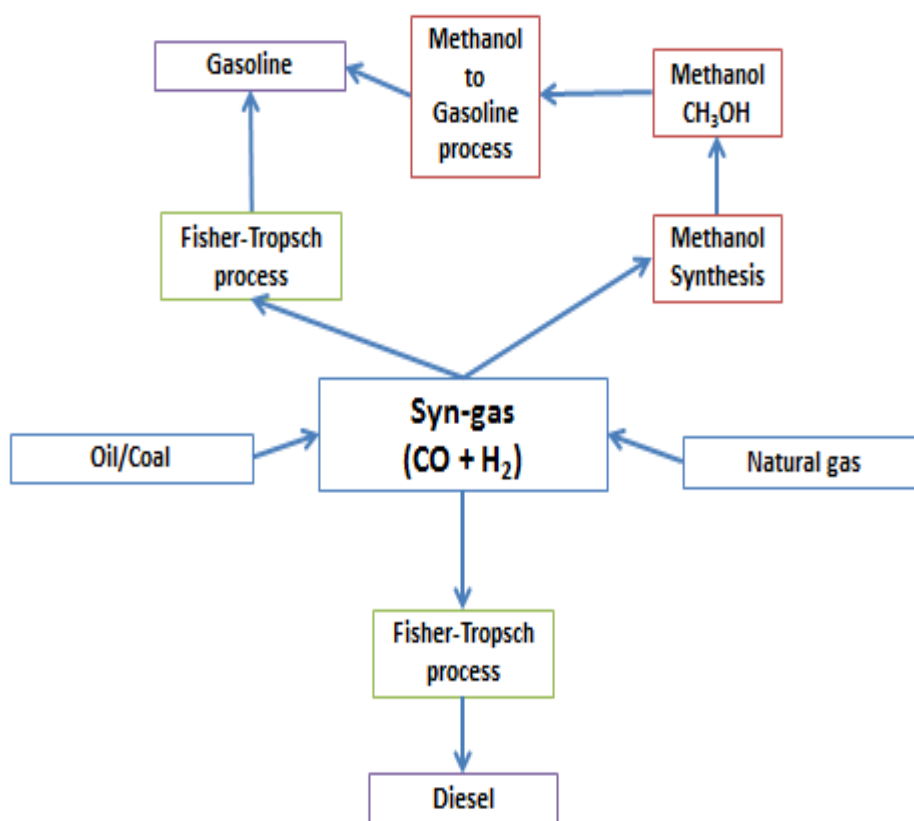


Figure 1-1: Flow chart detailing the role of syn-gas in a number of industrial processes ^[6]

Due to its moderately exothermic nature, the WGS reaction is thermodynamically unfavourable at elevated temperatures. ^[3] This is illustrated by the continuous decline and eventual sign change in the Gibbs free energy as a function of temperature, and the corresponding decreasing equilibrium constant as temperature increases. The kinetics of the catalytic reaction are more favourable at higher temperatures. In order to overcome this thermodynamic limitation while maintaining high reaction rates, WGS is normally conducted in multiple adiabatic stages with inter-stage cooling to obtain higher conversions overall. This can be seen in many industrial plants by using high temperature shift in the first stage where operation temperatures range 350°C to 500°C, whilst the low temperature shift occurs in the second stage with a temperature range of 150°C to 300°C. Inter-stage cooling ensures that little heat is lost. ^[1-3] Industrially, the water-gas shift reaction under both high and low temperature reactions are catalysed heterogeneously using a combination of transition metals and metal oxides.

1.3 Thermodynamics of the water-gas shift reaction

The water-gas shift reaction is reversible and hence the equilibrium position of the plays an important role in productivity of the reaction. Equilibrium considerations favour lower operating temperatures over higher temperatures. This is due to a decrease in equilibrium that coincides with increasing temperature. This is a consequence of the exothermic nature of the water-gas shift process. ^[10] This is further evident from the decline and eventual sign change in Gibbs free energy for the reaction as a result of an increase in reaction temperature. ^[3] Pressure does not play a role in the position of equilibrium due to the reactants and products being stoichiometrically equal. ^[3] Figure 1-2 highlights the relationship between the equilibrium constant which decreases with increasing temperature. Figure 1-2 also plots the free energy and temperature associated with the water-gas shift process and depicts increasing free energy with increasing temperature ^[3].

1.4 Kinetics and proposed reaction mechanisms for the water-gas shift reaction

There have been many studies of the reaction kinetics for the water-gas shift reaction over the years, with a number of kinetic expressions for both the high and low temperature processes being proposed. ^[11-13] The two which are generally accepted in literature are the regenerative and associative mechanisms. The regenerative mechanism can be described as a cyclic redox process in which the catalyst is oxidised then reduced upon interaction with CO and H₂O. The associative process proceeds via an intermediate transition phase usually identified as formate. There have been various studies published that highlight evidence supporting both the associative and regenerative reaction mechanisms. ^[11-13] The high temperature process has been the subject of most interest in terms of the kinetics of the reaction with a number of models and expressions being proposed. ^[3, 10, 16] The water-gas shift process has been shown to fit best the Langmuir-Hinshelwood model in terms of its rate law equation.^[3] The Langmuir-Hinshelwood model is best described as the reaction taking place in the absorbed phase on catalyst surface. The reaction mechanism by which the steam and carbon monoxide interact with the surface of the catalyst has been identified as regenerative for the iron/chromium oxide based high temperature shift catalyst. ^[1-3]

1.4.2 The regenerative mechanism

The regenerative mechanism proceeds in such a way that a cyclic change in oxidation state occurs in the catalyst upon interaction with the reactants. In terms of the water-gas shift reaction, it can be considered that carbon monoxide is oxidised to carbon dioxide whilst reducing an oxidised metal site. Then in a separate step, water is reduced to hydrogen on the surface of the catalyst. This process oxidises the surface, returning the site back to its original oxidation state. ^[5] This mechanism is also known as the redox mechanism due to the reduction/oxidation processes

occurring on the catalyst surface. ^[12] This process is summarised by the steps below and the schematic presented in Figure 1-3.

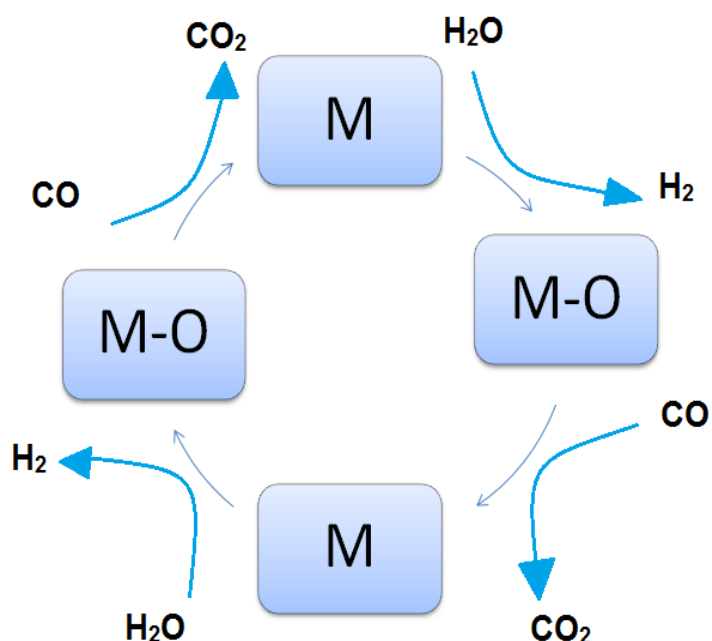
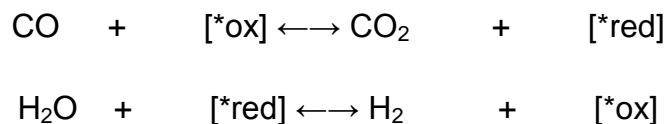


Figure 1-3: Schematic depicting the regenerative mechanism for the interaction between the reagents and catalyst surface for the water-gas shift.

The kinetic expression for the redox mechanism of the high temperature shift which is most widely presented in literature in the form of the equation presented below. [3]

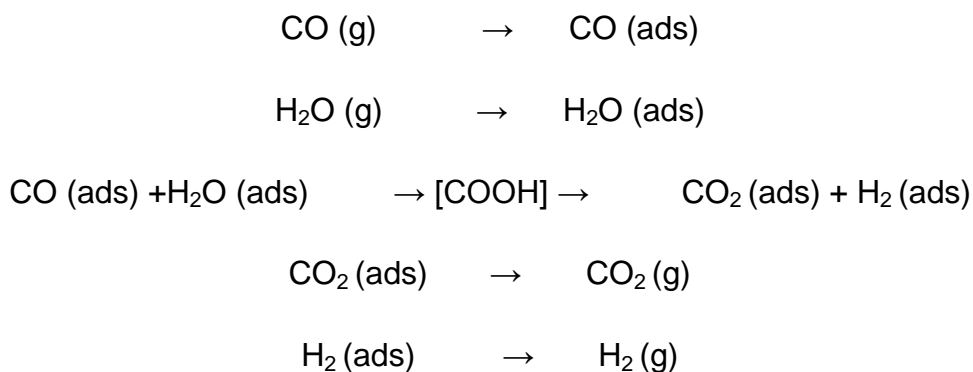
The rate equation for the high temperature shift is defined below. R is defined as the reaction rate, k as the rate constant and K is the equilibrium constant and (CO), (H₂O), (H₂) and (CO₂) are the partial pressures of gases present in the process.

$$R = \frac{kK_{H_2O}K_{CO} \left(\frac{(CO)(H_2O) - (CO_2)(H_2)}{K} \right)}{(1 + K_{CO}(CO) + K_{H_2O}(H_2O) + K_{CO_2}(CO_2) + K_{H_2}(H_2))^2}$$

1.4.3 The associative mechanism

There is more uncertainty about the mechanism by which the reaction proceeds under low temperature conditions using a copper/zinc oxide catalyst. The reaction kinetics of the low temperature shift reaction have been less well documented in comparison to the high temperature shift reaction but work done suggests that the reaction can be described well in terms of the Langmuir-Hinshelwood model, although the low temperature shift process exhibits a degree of pore diffusion limitation which modifies the rate law. [3] Due to the uncertainty of the kinetic pathway undertaken by the low temperature copper-based catalyst, there have been a number of different kinetic expressions derived. The Langmuir-Hinshelwood model is best described as the absorption of both reactants on the catalyst. It is in this adsorbed phase that reaction takes place through the formation of an intermediate, commonly suggested to be formate. [11] After the intermediate step, the product is formed then desorbed from the catalyst. This is summarised by the following mechanism proposed by Rhodes and colleagues: [11]

Chapter 1: Silica supported transition metal phosphides, novel materials for the water-gas shift reaction



A schematic of the associative mechanism proposed for the interaction between the reactants and the surface of the catalysts is displayed in Figure 1-4. This process can simply be described in the terms of a Langmuir-Hinshelwood process in which the carbon monoxide and water molecules adsorb onto the catalyst surface. In the adsorbed layer of the catalyst, an intermediate complex is formed. This complex is in the form of formate on the surface of the metal. The formate complex decomposes on the surface to give hydrogen and carbon dioxide gas which desorb from the catalyst. ^[11-13]

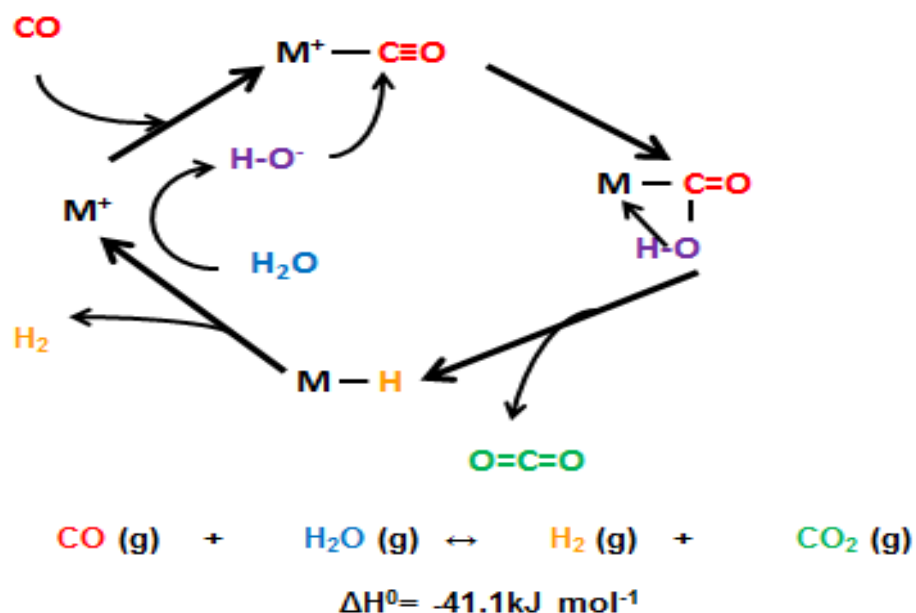


Figure 1-4: Illustration of the associative pathway by which the water-gas shift reaction proceeds

Using DFT calculations, Gokhale and colleagues investigated the kinetic pathways and reaction mechanisms for the low temperature water-gas shift reaction on a Cu (111) surface. From these studies, they were able to estimate activation energies for each proposed step in the mechanism. ^[13] Figure 1-5 summarises the redox and associative reaction mechanisms which through which the water-gas shift reaction is thought to proceed via under the low temperature regimes on a Cu (111) surface.

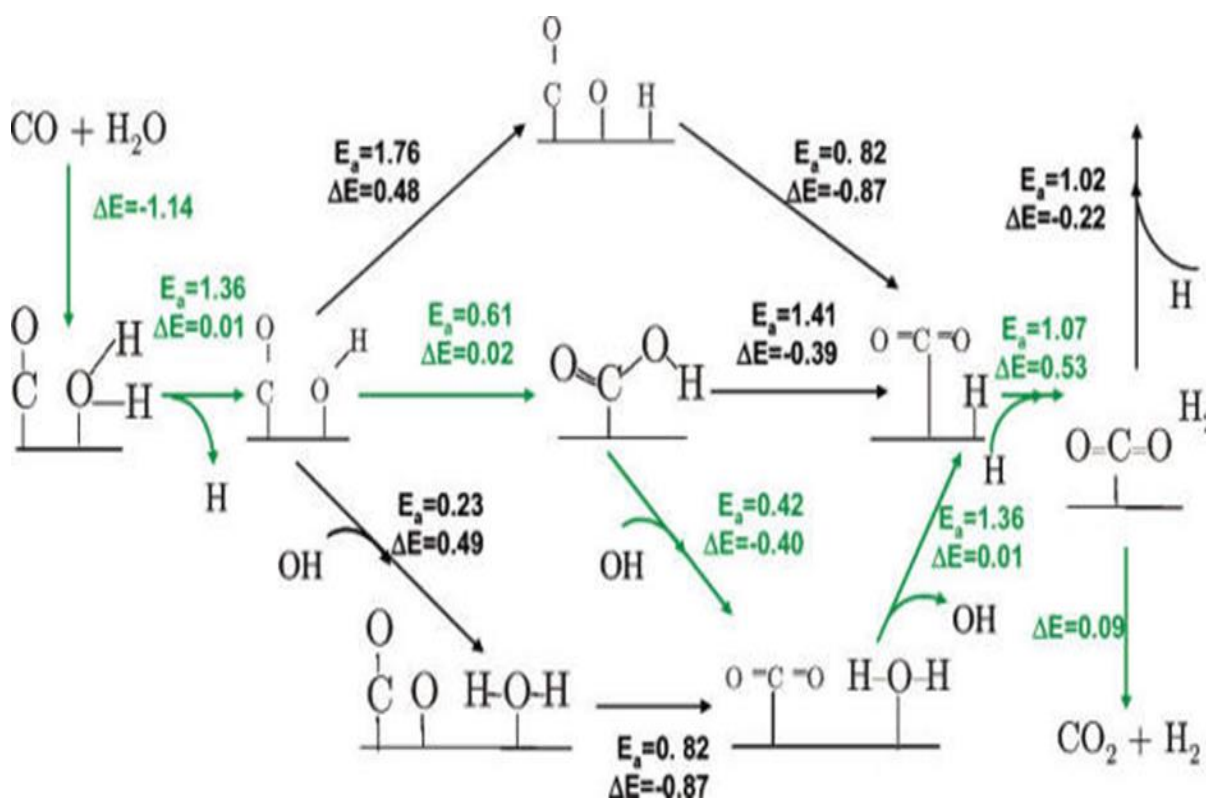


Figure 1-5 : Schematic diagram of the two mechanisms by which the water-gas shift is proposed to proceed through on the Cu (111) surface under low temperature conditions. ^[13]

1.5 Water-gas shift process catalysts

Due to the multiple stages at which the water-gas shift reaction is usually carried out industrially, different catalysts are used depending on the reaction conditions in order to maximise the process efficiency. Generally there are four types of water-gas shift catalysts that are used commercially. The exact composition of these catalysts may vary according to their specific applications and their accompanying supports. ^[8] Under high temperature water-gas shift reaction conditions, iron oxide based catalysts have been used commercially for the last 60 years. The high temperature shift process classically uses an iron/ chromium oxide catalyst ($\text{Fe}_3\text{O}_4/\text{Cr}_2\text{O}_3$), which is usually operated at 400-500°C. The addition of chromium to the iron catalyst helps stabilise the catalyst and prevent sintering of the catalyst, which is the largest contributor to catalyst deactivation. The high temperature shift catalyst, whilst being durable and robust, displays relatively poor selectivity toward hydrogen due to the unfavourable thermodynamic conditions as well as displaying poor activity when temperature is lowered to more thermodynamically favourable conditions. ^[9]

The low temperature water-gas shift uses a copper/zinc and aluminium oxide catalyst ($\text{CuO}/\text{ZnO}/\text{Cr}_2\text{O}_3/\text{Al}_2\text{O}_3$). The active phase in this catalyst is copper/zinc oxide. The active species is supported by ZnO and Cr_2O_3 which are added to help prevent poisoning by halogens or sintering respectively. ^[8] The Al_2O_3 is largely inactive and helps in the dispersion and minimizes pellet shrinkage. Copper is more susceptible to thermal sintering and hence should not be operated at higher temperature. The lower temperature of operation is restricted by the dew point of the mixture in industrial conditions. ^[3] The exit concentration of CO from the low temperature reactor is much lower than at high temperatures, which is desirable for use in further processes such as ammonia synthesis. ^[8] The advantages of the lower temperature catalyst are the high selectivity towards hydrogen due to the more thermodynamically favourable conditions under which the catalyst operates. Side reactions are minimized due to the lower operating temperatures used. The major drawback to the copper/zinc oxide commercial catalyst is the susceptibility to deactivation either by sintering or poisoning by feed impurities, especially sulfur. Due

to the susceptibility of the copper-based catalyst to deactivate via poisoning as well the decrease in the quality of feedstocks available, sulfur tolerant catalysts have been developed. These catalysts usually comprise of mixtures of cobalt and molybdenum sulfides as the active ingredients. Catalysts of this type are sulfur-tolerant and can be used in sulfur-containing “sour gas” streams and are therefore called “sour gas shift catalysts”.^[9] Whilst these catalysts remain active in the presence of sour feedstocks, their activity is much poorer than that displayed by the copper-based catalyst under the low temperature conditions. Medium temperature water-gas shift catalysts have also been developed to bridge the gap between the operating temperature of the high and low temperature shifts. The medium temperature catalysts are usually based on low temperature shift copper-zinc catalysts that are modified (usually with iron oxide) to operate at slightly higher temperatures (275–350°C) than the commercial low temperature water-gas shift catalyst. These catalysts are not overly active due to the inefficient thermodynamic operating conditions under which they are run.^[8]

The limitations of currently used commercial catalysts combined with the interest in hydrogen as an alternative fuel has prompted a great deal of interest over the last decade in the development of alternative catalysts. Precious metal catalysts such as Pd, Pt and Au on easily reducible supports have all been shown to display encouraging potential under both high and low temperature shift conditions.^[14] The catalytic activity of precious metal catalysts are reported to be higher than activity displayed by current commercial catalysts.^[8-9] The main draw back with these materials is expense of the catalysts as well as lack of robustness of the catalysts, which are more susceptible to poisoning or sintering than their industrial counterparts.^[14] This has led to the investigation of more inexpensive metals and alloys and lighter elements. These alternative materials are the focus of the project and will be discussed at length later.

1.6 Sulfur poisoning of water-gas shift catalysts

As mentioned previously, decreasing quality of feedstocks of natural gas has led to the presence of higher concentrations of sulfur containing compounds. The presence of sulfur can have a profound effect on the activity of the catalyst used in the process. The commercially used water-gas shift catalysts under high and low temperature shift conditions are both susceptible to deactivation due to sulfur poisoning of the active phase. The iron-based high temperature shift catalyst and copper-based low temperature shift catalyst both are affected differently by interaction with sulfur. The copper based low temperature catalysts are particularly vulnerable to sulfur poisoning due to the strong affinity between the copper active phase and the sulfur containing impurities. The copper catalyst is permanently deactivated by sulfur and cannot be regenerated meaning poisoned catalysts must be replaced. ^[15-16] The iron-based high temperature shift catalyst is more durable in comparison, forming iron sulfide phases. The sulfided catalyst remains water-gas shift active; however the activity is much lower than the original oxide phase. ^[18-19] An alternative in the presence of high sulfur content in feedstocks is the use of sulfided Mo/Co catalysts. These catalysts are not deactivated in the presence on sulfur. In their review of the water-gas shift process, Ratnasamy and Wagner suggest that the use of these sulfide catalysts usually require very large concentrations of sulfur in the feedstock to be effective (reported to require excess of 300 ppm) and maintain the catalytic activity. These concentrations of sulfur are much higher than that usually associated with a sour feedstock. However Ratnasamy and Wanger also suggest that if the catalyst is effectively pre-sulfided that it is possible to achieve good catalytic active at sulfur concentrations as low as 35 ppm. ^[8] There have been a number of novel catalysts developed for both high and low temperature water-gas shift reaction conditions with the aim of improving sulfur resistance whilst maintaining high activity and selectivity. Cobalt chromium oxide based catalysts have also been reported to display good catalytic activity under high temperature water-gas shift conditions. The materials display sulfur tolerance in the presence of large concentrations of sulfur (in excess of 200 ppm). Lanthanum oxy-sulfide catalysts have also shown promise with regards to sulfur tolerance under high temperature shift conditions. Whilst these catalysts, display better sulfur tolerance than the iron-

based commercial catalyst, activity is much lower in comparison, as much as six times lower in some cases.^[20] It is therefore apparent that sulfur tolerant catalysts must be developed which are able to bridge this gap in activity in comparison to the industrial catalyst.

1.7 Transition metal phosphides

Metal phosphides have been extensively investigated and have generated some interest as alternative hydrotreating catalysts, with particular attention centering upon nickel phosphide.^[21-25] The transition metal phosphides are an interesting class of compounds that combine the physical properties of ceramics, such as hardness and strength, with the transport properties of metals, such as high thermal and electrical conductivity.^[21] They can be prepared readily from inexpensive phosphate precursors by reduction in hydrogen. A large number of bulk and supported transition metal phosphides have been documented in the literature in monometallic and bimetallic form. In addition a very large number of stoichiometries, and hence structural variants, have been documented for transition metal phosphides.^[22] Transition metal phosphides have found use in a number of fields including magnetic and electronic applications. However, the greatest potential displayed by these materials have been as heterogeneous catalysts.^[25] Transition metal phosphides have been studied extensively over the last decade as alternative novel materials in a number of catalytic processes such as hydrogenation and hydrotreating reactions, removing unwanted elements from feedstocks and could be utilised as catalysts showing a greater resistance to poisoning.^[21-25] Nickel phosphide has been identified as the most catalytically active of the transition metal phosphides based on a larger number of studies on a number hydrotreating and hydrogenation reactions. The superior performance over commercial catalysts for hydrotreating reactions has been documented for Ni₂P catalysts in the removal of oxygen, nitrogen and sulfur from a number of compounds.^[21-25] However the potential of metal phosphides as catalysts for syn-gas related reactions has been relatively unexplored, although they may be of interest.^[9] The only published evidence of the catalytic potential of nickel phosphide for the water-gas shift reaction was a study by Rodriguez and colleagues.

^[9] The investigation used a combination of computational and experimental work to show the materials exhibited promising activity for the process. The experimental work used single crystals of Ni₂P and studied catalytic performance of the material for the water-gas shift reaction between 300 and 375°C. Ni₂P displayed much higher hydrogen formation rates than Ni and Cu catalysts tested under the same conditions. Ni₂P was then doped with small amounts of Caesium which improved the hydrogen formation rate. XPS analysis revealed that under the reaction conditions, most of the P sites of are covered with oxygen. Oyama suggests that residual oxygen plays a vital role in good catalytic activity displayed by nickel phosphide.^[9] This was further evident upon addition of caesium to the nickel phosphide surface. XPS analysis indicated that Caesium increases the saturation coverage of oxygen resulting in the enhanced catalytic activity displayed by the doped crystallite. The theoretical study carried out by the group helped explain the relationship between nickel phosphide and oxygen during the reaction. It was proposed that the oxygen atoms facilitate the WGS reaction in both direct and indirect ways. Oxygen is thought to lower the energy barrier for water dissociation, whilst deactivating the nickel site allowing for moderate bonding to the absorbate. The theoretical study also proposes the catalyst adopts the associative reaction pathway, forming a formate intermediate.^[9]

1.7.1 General properties of transition metal phosphides

Phosphorus reacts with many elements of the periodic table to form a wide range of phosphides. The bonding of phosphides can range from ionic bonding exhibited by alkali and alkaline earth metal phosphides, to metallic bonding observed for transition metal phosphides and covalent bonding seen in main group phosphides.^[22] Over the last 40 years, transition metal phosphides have been studied due to the novel chemical and physical properties they possess. Due to significant interest in these materials, a number of novel synthetic routes have been used to produce phosphides.^[24] The most simple method of synthesis and the most commonly used method is the reduction of inexpensive phosphate precursors to form the phosphide; these are usually reduced under hydrogen gas flow at high temperatures. A large number of transition metal phosphides have been documented in a number of

stoichiometries. There are currently 8 different species of nickel phosphide reported in the literature and the same number reported for a number of other transition metal phosphides. [22, 25] These stoichiometries range from metal rich forms such as MP and M_2P which possess chemical and physical properties akin to metals to phosphorus rich material such as MP_2 which are more covalent in nature and less stable. The wide range of compositions displayed by metal phosphides have led to the materials being used broad range of applications. Electronic applications include the use of phosphorus rich nickel phosphide (NiP_2) being used in lithium ion batteries as an alternative electrode, whilst phosphorus rich cobalt phosphide (CoP_3) and iron phosphide (FeP_4) have been investigated for use as thermoelectric materials. [29-30] The magnetic properties of metal phosphides are also well documented. Metal rich transition metal phosphides are known to exhibit a range of magnetic behaviours depending on their composition. Iron phosphide displays the greatest magnetic character and depending on stoichiometry displays ferromagnetic behaviour. [31] Due the magnetic character displayed by metal rich phosphides many studies have investigated their potential use in magnetic data-storage devices. A large number of bimetallic transition metal phosphides have also been documented and have been studied with regards to improving the physical and chemical properties of monometallic phosphides. These have been mostly with regards to applications in catalytic processes and have yielded mixed results which will be discussed at length later. [25]

The physical and chemical properties of these materials are similar to those of transition metal carbide, nitride, boride and silicides. [21] Thus, they are good conductors of heat and electricity, are hard and strong, and have high thermal and chemical stability. Whilst transition metal phosphides share similar chemical and physical properties with transition metal carbides and nitrides, the crystal structures of phosphides differ significantly. This is due to larger size of phosphorus atoms in comparison to carbon or nitrogen meaning that phosphides do not form the simple lattice structures displayed nitrides and carbides. Instead, the structures of metal-rich phosphides are based on trigonal prismatic units as displayed in Figure 1-7, which accommodate the relatively large phosphorus atoms very effectively.

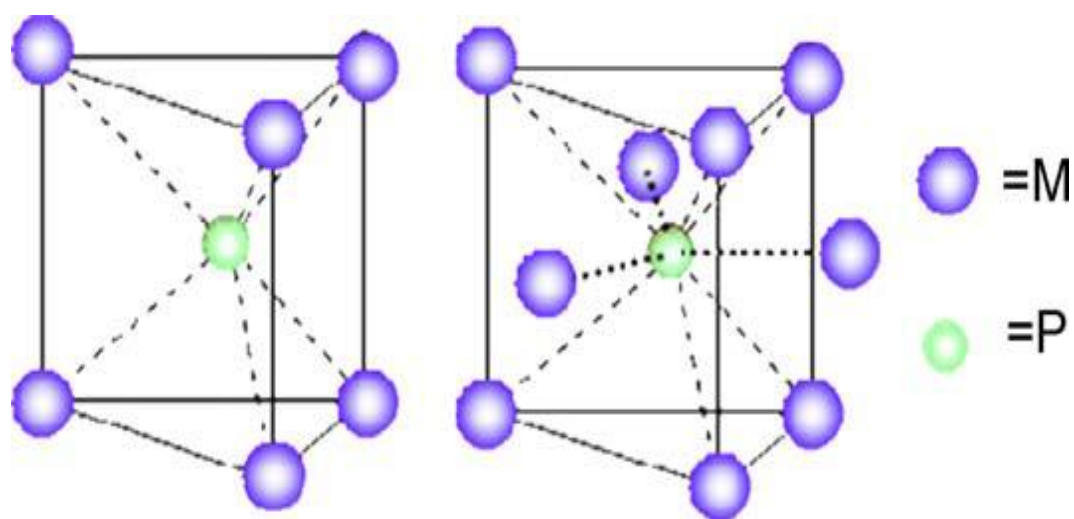


Figure 1-6: The trigonal prism crystal structure seen in transition metal phosphides.^[22]

The prisms are similar to those found in some transition metal sulfides such as MoS_2 ; however phosphides do not take on the layered structure of atoms seen in sulfides and are metallic conductors, not insulators or semiconductors. Due to the difference in the packing of atoms in comparison to the sulfides, transition metal phosphides display an isotropic crystal morphology. This means that there is better exposure of surface metal atoms to fluid phase reactants which means that phosphides should display good catalytic activity due to the uniform nature of the surface of the materials in comparison with the sulfides which are less isotropic in composition. Different arrangements of these trigonal prism units give rise to a number of different crystal structures depending on which transition metal is used to form the phosphide or the ratio of M:P used in the synthesis. As discussed previously, a large number of transition metal phosphides have been documented including MoP, VP, CrP and Ni_2P . Figure 1-8 details a range of documented crystal structures displayed by transition metal phosphides across a range of stoichiometries.

Crystal Structures of Transition Metal Phosphides

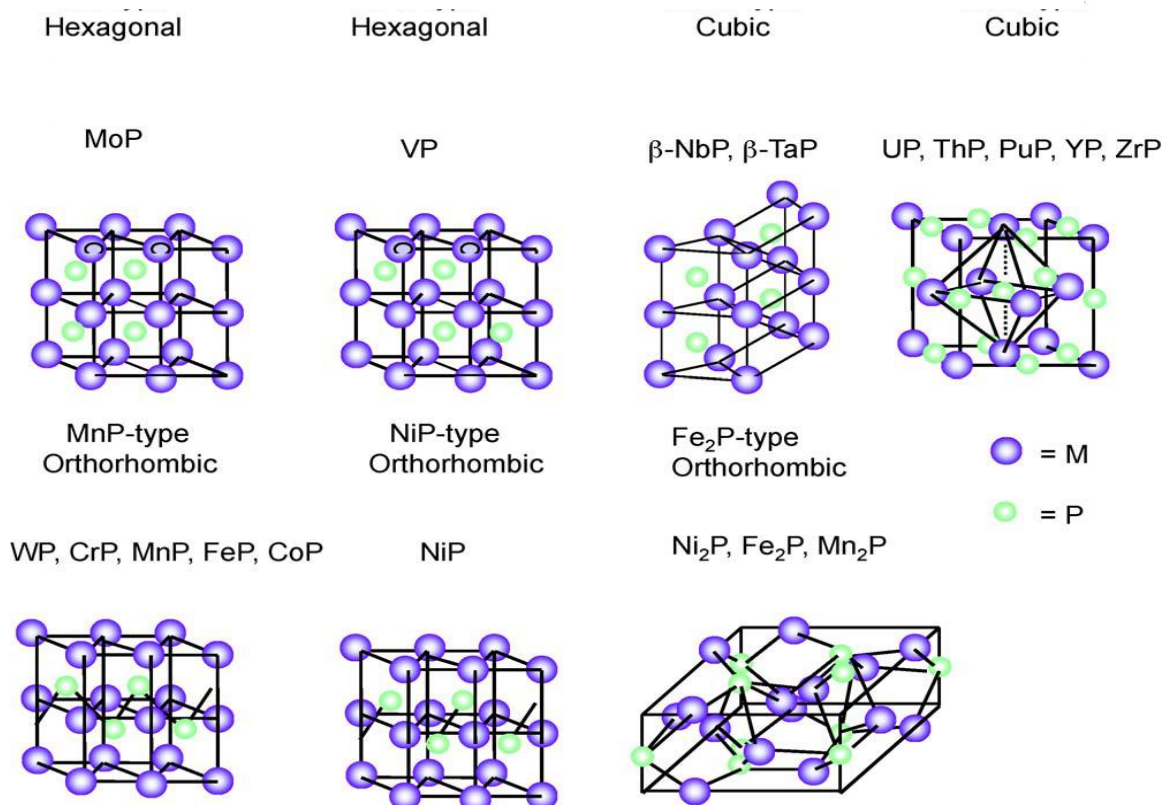


Figure 1-7: Illustration of different crystal structures seen in transition metal phosphides. ^[22]

1.7.2 Review of recent publications in the synthesis of transition metal phosphides.

1.7.2.1 Synthesis of bulk transition metal phosphides

The synthesis of transition metal phosphides have been reported for over a century. ^[24] However, It is only in last two decades that interest in these materials has grown. This has largely been due to favourable chemical and physical properties displayed by transition metal phosphides. ^[21-22] They have been shown to display favourable magnetic and catalytic activity. In light of this there have been a number of studies

published describing various approaches to synthesizing transition metal phosphides, both in bulk form as well as on supports. The approach mainly used for preparation of bulk materials is the reduction of metal phosphate-containing precursors at high temperatures (500–750°C) under hydrogen gas flow. The phosphate precursors are relatively inexpensive to produce through simple precipitation processes, using compounds such as transition metal nitrates as the metal source in the precipitation. Metal nitrates are generally highly toxic and harmful to the environment. Although this approach is simple for small scale production, the high temperature at which the materials are reduced mean that this method may be impractical on a large industrial scale which the materials would be produced if used in catalytic processes.^[24] Another disadvantage with this synthesis method is large particle size and low surface area phosphides are produced. This is as a result of the high reduction temperatures required to reduce the P=O bond, which are in excess of 500°C. For these reasons, other synthetic strategies for making metal phosphide materials have been developed which include solvothermal reactions,^[26, 28] thermal decomposition of nickel thiophosphate (NiPS₃),^[27] mixture of trioctylphosphine (TOP) with metal salts or metal hypophosphite precursors, co-reaction of metal or metal oxide with phosphines and thermal solid-reactions.^[32-33] Whilst these methods do produce transition metal phosphides displaying small particle sizes and larger surface areas, most are impractical and inefficient for large scale synthesis or for the placement of the active phase onto a support.

Popular alternative reduction methods include the use of alternative phosphorus donors. A number of transition metal phosphides have been produced using metal oxides and flowing phosphine-hydrogen mixtures (PH₃/H₂) using lower reduction temperatures due to the lower P-H bond energy in comparison to the P=O bonding found in the phosphate precursor.^[34] Cecilia and co-workers used a phosphite precursor (NiH₂PO₃) to produce bulk Ni₂P with high surface area.^[35] This was a result of the phosphite precursor reducing under lower temperature conditions (400°C) in comparison to a phosphate counterpart, due to the lower oxidation state of phosphite (+III) in comparison to the phosphate (+V). The use of hypophosphite (H₂PO₂⁻) as a precursor has also been well documented, resulting in lower reduction temperatures required to form the phosphide due to the lower oxidation state of the

hypophosphite precursor (+I).^[32] The higher surface area materials produced using alternative phosphorus precursors have yielded strong catalytic activity in a number of hydrotreating processes in comparison to the traditionally synthesized counterpart phosphides due to the improved surface areas and particle sizes displayed by the materials.^[32-33] While the catalytic results are encouraging, the synthesis approach is still impractical due to use of expensive precursors in comparison to the phosphate reduction method.

The solvothermal synthesis of bulk transition metal phosphides has been applied for many years with M_2P materials being the most commonly produced. However, a study carried out by Brock and colleagues demonstrated the formation of metal phosphide particles with alternative shapes, which may be beneficial to the catalytic activity of the materials for application in hydrotreating processes. Stable high surface area Ni_2P , Cu_3P and Co_2P were produced by reacting metal chlorides with yellow phosphorus in ethyldiamine/water at 100-140°C.^[25] A similar study using cobalt as the metal donor produced Co_2P nanorods from a reaction with $CoCl_2$ in aqueous ammonia at 220°C.^[26] Another solvothermal synthesis study was carried out by Liu and colleagues using red phosphorus (a less toxic form of phosphorus in comparison to yellow) and nickel chloride in water at 200°C for between 24-48 hours. Liu and colleagues showed that an increase in the Ni/P ratio resulted in better crystallization of Ni_2P , while increasing the reaction time went against obtaining pure Ni_2P , instead promoting the formation of $Ni_{12}P_5$.^[36] Other studies in this area include the synthesis of micron sized copper phosphide and cobalt phosphide particles.^[37] Despite the promise shown by using solvothermal synthesis techniques to form phosphide particles with novel structures, they have been found to be unsuitable for catalytic application. This is due to a number of drawbacks; namely the material produced lacks monodispersity and is aggregated, rather than disperse, making it difficult to study their size-dependent physical properties. These materials have not been tested under high temperature conditions. This suggests that there is uncertainty regarding the thermal stability under reaction conditions of the nanostructures formed.^[25-26]

Koranyi, as well as Berhault and co-workers, have explored nickel thiophosphate (NiPS_3) as an alternative to the phosphate precursor which, upon decomposition, generates unsupported nickel phosphides at lower temperatures, exploiting the more favourable cleavage of the P–S bond relative to the P–O bond which is known to be very strong ^[27]. Intriguingly, there are distinct differences between the behaviour of crystalline NiPS_3 and an amorphous precursor prepared at room temperature from reaction of nickel nitrate with Li_2PS_3 in water. Crystalline NiPS_3 transforms initially to Ni_5P_4 beginning at 400°C , Ni_2P starts to appear at 500°C and the product is single phase Ni_2P by 600°C . In contrast, amorphous NiPS_3 transforms at low temperature to Ni_2P (300°C), and produces single phase Ni_2P by 400°C . Continued heating leads to formation of Ni_5P_4 (450°C) and single-phase, highly crystalline Ni_2P is recovered at 600°C . ^[27] Judging from X-ray broadening, the amorphous precursor also permits recovery of a less crystalline Ni_2P product, which may be advantageous for catalytic applications. It has already been shown that by adding small amounts of sulfur to nickel phosphide the catalytic activity of the material is improved for hydrodesulfurization (HDS); metal phosphides have also been well documented as being resistant to sulfur poisoning ^[21-25]. This is a highly attractive property especially for use in processes such as the water-gas shift reaction where feedstock quality into the processes has decreased due to diminishing stocks of high purity oil and gas, leading to a greater risk of catalyst poisoning from sulfur. ^[9]

One of the major stumbling blocks in the preparation of transition metal phosphides is the low surface areas of materials, which may present problems depending on which catalytic process the metal phosphide is being used for. ^[33] Materials that are produced using some of the more conventional approaches mentioned previously have been shown to display low surface areas due to high reduction temperatures causing poor dispersion and activity. Yang and colleagues reported the synthesis of high surface area nickel phosphide (Ni_2P) with use of a polymer surfactant during the reduction process. ^[33] Ni_2P which was shown to possess a high surface area ($130\text{m}^2/\text{g}$) and strong catalytic HDS activity. These materials were prepared in a similar fashion to the reduction of metal phosphate precursors, the only major difference being the presence of the polymer surfactant and ethylene glycol when dissolving the nickel nitrate used as the nickel source for the phosphate precursor.

This mixture is added to a dissolved solution of diammonium hydrogen phosphate. The amount of time which the solvated solutions are left to mix is also increased to allow better dispersion of the reagents. The reduction of nickel phosphate under hydrogen is carried out at 500°C which is a lower reduction temperature than what has been used regularly for the reduction of nickel phosphide. This lower temperature reduction was shown to be beneficial to the catalytic activity of the materials in comparison to high reduction temperatures used on the same materials. [33]

1.7.2.2 Synthesis of supported transition metal phosphides

The synthesis of supported transition metal phosphides is well documented in the literature due to the physical limitations of the bulk phase materials with regards to their application in catalytic processes. Transition metals on supports such as SiO₂, Al₂O₃ and carbon have shown a great deal of catalytic potential with a more uniform dispersion of metal phosphide phases resulting in materials that are robust and catalytically active. In general, supported metal phosphides are produced in a similar method to that generally used to produce the bulk phase materials. The incipient wetness technique is used to impregnate the support. Metal and phosphate ions are dissolved from appropriate precursors to give an aqueous solution of the desired metal phosphide. The solution is then added to the support using the incipient wetness technique to impregnate the support which is then calcined producing the metal phosphate precursor on the support. The phosphate precursor is then reduced at high temperature under flowing hydrogen to give the appropriate supported metal phosphide. [21-23]

The synthesis of a range of transition metal phosphides on alumina and silica supports have been shown in research by Guan and Li via the reduction of hypophosphite precursors. [32] In this study, the supported phosphides were produced by impregnation of the support with a metal salt. A specific amount of support was added to a solution of the desired metal nitrate. The sample was dried, and

supported metal oxide was obtained by the calcination of sample. The supported metal oxide was then impregnated using the incipient wetness technique with solvated sodium hypophosphite. The study reports that the metal oxide is reduced by PH_3 resulting from the decomposition of the sodium hypophosphite. The sample was dried and then heated under static argon to an appropriate reduction temperature. Guan and Li used this method to produce supported nickel, copper, molybdenum and indium phosphides.^[32] The study suggests that the morphology of the metal phosphides can be successfully inherited from the metal oxide precursors, which indicates that it is possible to synthesize metal phosphides with selected morphology with the potential to alter catalytic activity of the materials. The study also indicated that the materials displayed strong HDS activity in comparison with an industrial sulfide catalyst.

1.7.3.3 Synthesis of Bimetallic transition metal phosphides.

The synthesis of bulk phase and supported bimetallic transition metal phosphides is similar to that of the monometallic phosphides described previously. The most commonly used in the literature is that of the temperature programmed reduction of easily produced phosphate precursors under hydrogen. It is in the production of the phosphate precursor that the second metallic element is added. A large number of bimetallic systems reported have focused on the use of nickel phosphide either supported or in the bulk phase with addition of a secondary metallic element. This is due to nickel phosphides well documented status as the most catalytically active member of the transition metal phosphides. The addition of a secondary metallic element has been attempted by a number of groups to improve the catalytic, chemical and physical properties of the material. The secondary metallic elements added to nickel phosphide include iron, cobalt and molybdenum. One such example is a study by Gaudette and colleagues in which iron/nickel phosphide ($\text{Fe}_x\text{Ni}_{2-x}\text{P}/\text{SiO}_2$) systems were prepared using metal compositions corresponding to x values in the range 0.01 and 2.00, where x is the stoichiometric quantity of each of the elements within the bimetallic system. Calculated stoichiometric quantities of iron and nickel nitrate were dissolved in deionized water and added to a solution of

dissolved diammonium hydrogen phosphate and the resulting precipitate was dried and calcined. It was then reduced under hydrogen at high temperature to the desired mixed metal phosphide.^[40]

1.7.4 Review of recent publications in the catalytic application of transition metal phosphides.

The main focus in recent studies of bulk phase and supported transition metal phosphides in the literature has been in the application of the materials to catalytic processes. Due to the low surface areas and large particle sizes of the bulk phase phosphide the majority of catalytic studies have been based on supported phosphide catalysts, which improve dispersion and surface area. Research has shown transition metal phosphides to have good catalytic activity for many processes.^[21-25] In general the phosphides catalyse the hydrogenation of alkenes, alkynes, dienes, and nitro-compounds. Studies carried out by a number of groups have led to the conclusion that Ni₂P displays the greatest catalytic potential. The hydrogenation activity for a number of first row silica supported transition metal phosphides was found in general to be of the order Ni₂P > Co₂P > FeP.^[21] A number of studies have supported the previously discussed good catalytic potential displayed by these materials both for hydrodesulfurization (HDS), hydrodenitrogenation (HDN) and more recently hydrodeoxygenation (HDO) processes.^[21-25] Transition metal phosphides have shown to be particularly promising hydrotreating catalysts with many of the studies reporting catalytic activity and selectivity superior to the industrially used sulfided catalysts. Ni₂P/SiO₂ was shown to display a greater activity in comparison to the commercially used sulfided Ni–Mo/Al₂O₃ and Co–Mo/Al₂O₃ catalysts in the HDN of quinoline.^[23] The superior HDN and HDS activity displayed by Ni₂P/SiO₂ over the sulfided catalysts has been attributed to nickel phosphide adopting a more efficient kinetic pathway as a result of the materials synergistic relationship with hydrogen in comparison to the commercially used catalysts.^[23] Transition metal phosphides have also shown strong stability under the reaction conditions, quickly reaching steady state and maintaining high catalytic conversion over extended periods of time.^[22]

The catalytic activity of a series of phosphides for HDN and HDS (displayed in Figure 1-8) were tested and compared in a trickle bed reactor operated under industrial conditions ^[21]. The activity of the catalysts was shown in the order of increasing activity as follows $\text{Fe}_2\text{P} < \text{CoP} < \text{MoP} < \text{WP} < \text{Ni}_2\text{P}$. Both nickel and tungsten phosphides performed better than the conventionally used sulfided catalysts. The figure below shows tungsten to outperform the conventional catalyst in HDN whilst nickel greatly outperforms the conventional catalyst in both HDN and HDS processes. Oyama also suggests that nickel phosphide shows an overall superior catalytic activity in comparison to the sulfide catalyst on the basis of both turnover rate and surface area. ^[21] It must also be noted that the activity recorded was higher when compared with the best mixed metal systems for both carbides and nitrides this is unusual as mixed systems can outperform monometallic compounds in most cases. The metal phosphides also showed a lower hydrogenation activity than the commercial sulfide catalyst indicating a more effective use of hydrogen and less chance of cracking of hydrocarbons. ^[12]

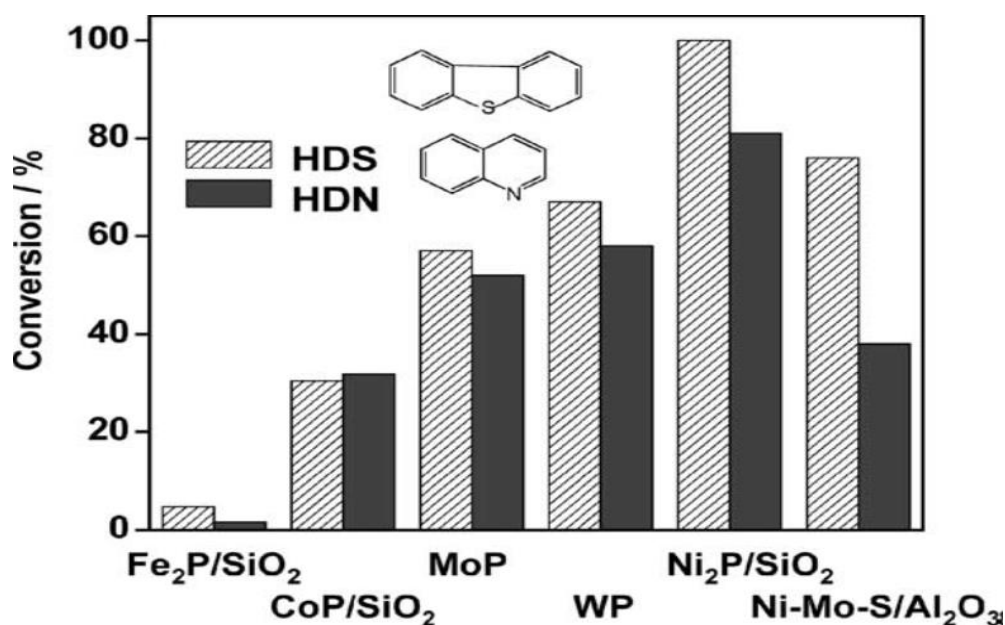


Figure 1-8: The catalytic activity of a range of transition metal phosphides and the commercially used nickel-molybdenum sulfide catalyst for hydrotreatment of sulfur and nitrogen containing compounds. ^[21]

The role of nickel phosphide as the most active of the transition metal phosphides has led to studies which attempt to better understand its physical and chemical properties. Oyama and Lee showed that Ni_2P on a silica support displayed high HDS activity in comparison to the commercially used $\text{Ni-Mo-S/Al}_2\text{O}_3$ catalyst. They decreased the crystallite size of the Ni_2P phase to determine if particle size played a role in improving the catalytic activity of the material. ^[23] It was proposed that HDS proceeded via by the direct desulfurization pathway for the large particle size catalyst and as particle size decreased the hydrogenation pathway became the preferable mechanism. The selectivity and performance was shown to be higher on the more dispersed catalysts. This was attributed to the increase in the number and quality of active sites. Ni_2P particles were shown to display two different nickel environments. Figure 1-9 presents an illustration of the Ni_2P structure illustrating the two different nickel co-ordination environments which occur in the material: 1) tetrahedral and 2) square pyramidal. ^[23] The study suggested that the two nickel sites had differing catalytic activity for hydrotreating processes. Using EXAFS line shape analysis Oyama and Lee were able to conclude that both types of nickel environments are present on large crystallites but that the square pyramidal type nickel sites are more numerous on the more active and more highly dispersed samples which displayed smaller particles of the active phase. These results indicated that in the nickel phosphide the two different nickel sites operate via different mechanisms. It was suggested that the two nickel sites in the nickel phosphide particles would likely also possess differing activity for other catalytic processes nickel phosphide may be applied to.

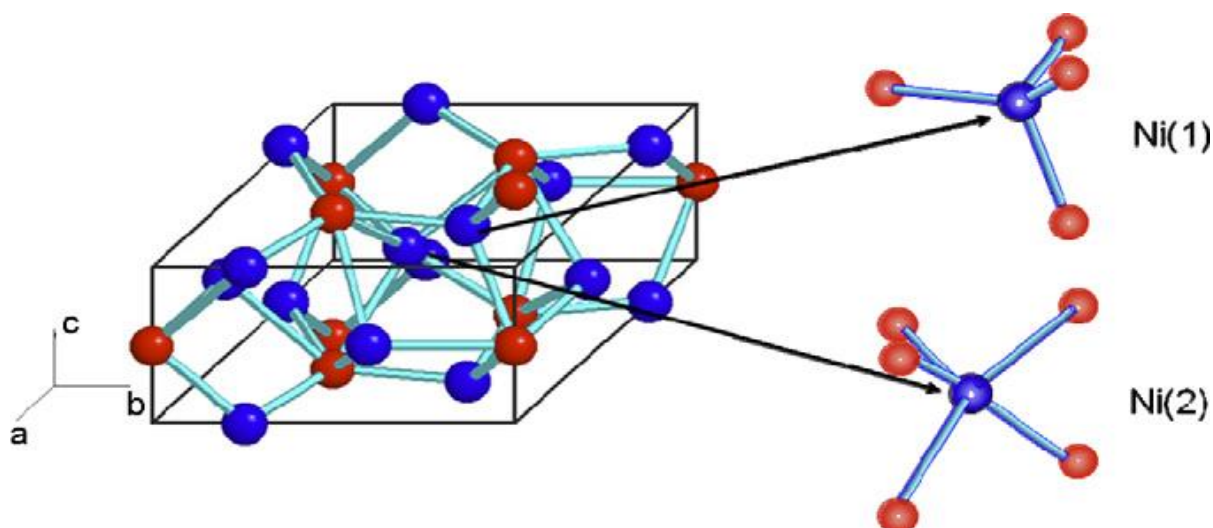


Figure 1-9: The two different nickel environments present in Ni₂P. Ni (1) is tetrahedral whilst Ni (2) is square pyramidal.^[23]

The catalytic activity of monometallic phosphides can be improved by the addition of a second metal to form bimetallic phosphides.^[38-40] Whilst bimetallic phosphides have not been explored in as much detail, there have been sufficient studies produced in recent years to suggest that these mixed systems could be very useful materials for catalytic processes. The addition of cobalt to bulk Ni₂P to give Co_{0.08}Ni₂P was reported by Abu and Smith. This material was tested as an HDS catalyst and was shown to display a much greater activity in comparison to Ni₂P which is already known as a highly active HDS catalyst.^[38] A similar improvement in catalytic activity was also observed by Burns and co-workers when using a supported mixed phosphide system Co_{0.08}Ni_{1.92}P₂/SiO₂.^[39]

Bimetallic phosphide systems have not always yielded beneficial results in terms of the catalytic activity. The well-known synergism of cobalt and nickel with molybdenum in sulfide catalysts has led to some researchers investigating mixed metal phosphides like NiMoP and CoMoP.^[39-40] The surprising finding is that these compositions are poorly active as hydrotreating catalysts. However, little explanation has been offered, aside from suggestions of alteration of the chemical nature, or interactions with the support.^[23] In a review of phosphides as hydrotreating catalysts, Oyama suggests this is caused by alteration of the active sites present on the

corresponding monometallic phosphide, citing Ni_2P as an example in which it has two different nickel environments (as described earlier) with differing activities and stating that the molybdenum replaces the square pyramidal type nickel site causing a drop in the catalytic activity of bimetallic system. ^[22]

A recent study by Gaudette and Burns supports the idea that has been shown in the previous studies of bimetallic phosphides that nickel rich mixed systems yield the greatest catalytic activity. ^[40] In their study, they added various amounts of iron into nickel phosphide and found that materials with a stoichiometric quantity of iron less than 0.6 displayed much high activity in HDS reactions. It was concluded that iron in small quantities replaced nickel in the tetrahedral environment leaving the highly active square pyramidal nickel site intact, when iron was content was more than 0.6 the iron favoured displacing the square pyramidal site causing catalytic activity to be poor. The optimum stoichiometry for good catalytic activity was shown to be $\text{Fe}_{0.03}\text{Ni}_{1.97}\text{P}_2/\text{SiO}_2$ and this was shown to display a catalytic activity 40% higher than that of the optimized $\text{Ni}_2\text{P}/\text{SiO}_2$ material for hydrotreating reactions. ^[40]

The exciting potential displayed by transition metal phosphides in hydrotreating processes, combined with the strong performance of the materials as hydrogenation catalysts, has led to the application of phosphides to other processes. One such process is the water-gas shift reaction. It has been suggested that transition metal phosphides should show good activity in the reaction as well as Fischer-Tropsch and ammonia synthesis. However, there has been little research published in this area. ^[21] As stated earlier, Rodriguez and co-workers however have published a study in which they have tested single crystals of Ni_2P in the water-gas shift reaction. ^[6] The results from their work showed that nickel phosphide performed better than standard nickel and copper metal catalysts, with copper especially known as being highly active water-gas shift catalyst. It was suggested that the high activity displayed by Ni_2P as a water-gas shift catalyst is due to the formation of oxy-phosphides on the surface of the material, which are formed due to the strong interaction between oxygen and phosphorus. Under reaction conditions, most of the phosphorus in the nickel phosphide was shown to be covered with oxygen but not the nickel sites. This

was determined using XPS analysis of the material looking at the binding energies of oxygen, phosphorus and nickel on the surface and near surface region of the material. In this study they also doped the nickel phosphide with caesium which was shown to greatly improve the catalytic activity of the material in the water-gas shift reaction. It was postulated that the addition of caesium led to an increase in the saturation coverage of oxygen on the surface hence the increase in activity. Previously it was shown that caesium doping has a similarly positive effect on copper water-gas shift reaction catalysts. [6] The presence of oxygen atoms on the surface of nickel phosphide was shown in the study to facilitate the water-gas shift reaction both directly (by promoting the dissociation of the water) and indirectly (by deactivating nickel sites on the surface to provide moderate bonding to the adsorbates lowering the barriers for each elementary step in the WGS process become lower). The catalytic activity of the materials compared in the study are summarised in Figure 1-10 along with presence of oxygen of the materials surface, highlighting the significant role which oxygen binding to the surface of these catalysts plays. This study by Rodriguez and colleagues shows that nickel phosphide materials have significant potential to be designed for use in the water-gas shift process as highly active catalysts.

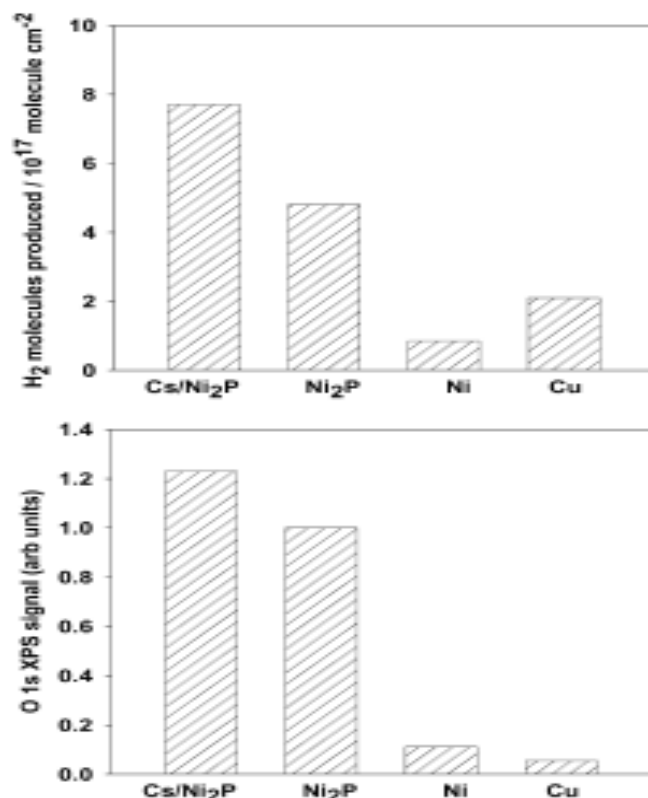


Figure 1-10: The catalytic activity as well as the presence and importance of the oxy-layers on the surface of nickel phosphide, doped nickel phosphide, elementary nickel and copper in the water-gas shift reaction.^[5]

The catalytic application of nickel phosphide in water-gas shift has been shown to display excellent potential. However, there is a lot that remains unknown and untested with regards to the use of nickel phosphide in the water-gas shift reaction. This thesis will explore these unknown areas. The thesis will detail the development and characterisation of bulk and supported nickel phosphide materials as well as a range of supported bimetallic nickel phosphide. These materials have not yet been investigated for application in the water-gas shift reaction in the literature. The catalytic application of the materials under high temperature water-gas shift conditions will be explored along with their durability and activity under sulfur containing conditions.

1.8 References

- 1) Satterfield CN. Heterogeneous catalysis in industrial practice. 2nd ed. Malabar: McGraw-Hill; 1991.
- 2) A. König , G. Herding, B. Hupfeld, Th. Richter, K. Weidmann, Top. Catal; 23 (2001) pg 16-17
- 3) M. V. Twigg; ICI Catalyst Handbook 2nd Ed.; Wolfe Publishing; pg 283-338.
- 4) S. Suzuki, K. Kapoor, M. P. Ohashi, F. Osaki, T. Appl. Catal; 213; (2001) pg 47-56.
- 5) P. Liu, J. A. Rodriguez, Y. Takahashi, K. Nakamura; J. Catal; 262; (2009) pg 294–303
- 6) L. Basini, Catal. Today; 106; (2005) pg 34-40.
- 7) M.A. Pena, J.P.Gomez, J.L.G. Fierro, App. Catal. A: Gen; 144; (1996)
- 8) C. Ratnasamy, J.P. Wagner; Catal. Rev; 51; (2009); pg 325-440.
- 9) C. Hulteberg, Intl. J. Hydrogen Energy; 37; (2012) pg 3978-3992
- 10) J. R. Ladebeck, J. P. Wagner; Fuel Tech. Appl; 3; (2003) pg 190-201
- 11) C. Rhodes, G.J. Hutchings, A.M. Ward; Catal. Today; 23; (1995) pg 43-58
- 12) R.J. Smith, Intl. J. Chem. Eng, 8 (2010) pg 1-29
- 13) A. A. Gokhale, J. A. Dumesic, M. Mavrikakis, J. Am. Chem. Soc. 9; 130; (2008) pg 1402-1414
- 14) R. Farrauto, S. Hwang, L. Shore, W. Ruettinger, J. Lampert, T Giroux; A. Rev. Mater. Res. 33 (2003) pg1-27
- 15) I. Kirm, J. Brandin, M. Sanati; Top. Catal; 45, (2007), pg 7-31
- 16) S.S Hla, D. Park, G.J. Duffy, J.H. Edwards, D.G. Roberts; Chem. Eng. J; 146, (2009) pg 154-148

- 17) Y. Choi, H. G Stenger; *Appl. Catal.*; 38; (2002) pg 259-265.
- 18) S.S. Hla, G.J. Duffy, L.D. Morpeth, A. Cousins, D.G. Roberts, J.H. Edwards; *Catal. Communications*; 10; (2009), pg 967-70.
- 19) L. Zhang, J. Millet, U.S. Ozkan; *J. Mol. Catal. A. Chem*; 309, (2009); pg 63-70
- 20) I. Valsamakis, M. Stephanopoulos; *Appl. Catal. B. Environmental*; 106; (2011) pg 255-263
- 21) S.T. Oyama , *J. Catal*; 216; (2003) pg 343–352
- 22) S.T. Oyama, *Catal. Today*; 143; (2009) pg 94–107
- 23) S.T. Oyama, Y.K. Lee; *J. Catal*; 258; (2008) pg 393–400
- 24) S.L. Brock, K. Senevirathne; *J. Solid State Chem*; 181; (2008) pg 1552–1559
- 25) M. Bussell, R. Prins; *Catal. Lett*; 142; (2012); pg 1413–1436
- 26) H. Hou, Q. Yang, C. Tan, G. Ji, B. Gu, Y. Xie; *Chem. Lett*; 33; (2004), pg 1272–1273.
- 27) H. Loboue, C. Guillot-Deudon, A. Popa, A. Lafond, B. Rebours, C. Pichon, T. Cseri, G. Berhault, C. Geantet; *Catal. Today*; 130; (2008) pg 63–68
- 28) S. Liu, X. Liu, L. Xu, Y. Qian, X. Ma; *J. Crystal Growth*; 304; (2007), pg 430–434.
- 29) F. Gillot, S. Boyanov, L. Dupont, M. Doublet, M. Morcrette, L. Monconduit, J. M. Tarascon; *Chem. Materials*; 17; (2005), pg 6327–6337
- 30) Ø. Prytz, R. Sæterli, O.M. Løvvik, J. Taftø; *Micron*; 39; (2008), pg 685–689
- 31) O. Tegus, E. Bruck, K. Buschow, F. R. de Boer; *Natur*;, 415; (2002) pg 150–152
- 32) Q. Guan, W. Li; *J. Catal*; 263; (2009) pg 1–3
- 33) S. Yang, C. Liang, R. Prins; *J. Catal*; 237; (2006) pg 118.
- 34) E.L. Muetterties, J.C. Sauer; *J. Am. Chem. Soc*; 96 (1974) pg 3410–3415
- 35) J.A. Cecilia, A. Infantes-Molina, E. Rodríguez-Castellon, A. Jimenez-Lopez; *J. Catal*, 263, (2009) pg 4–15

- 36) Z. Liu, X. Huang, Z. Zhu, J. Dai; *Cer. Int*; 36; (2010) pg 1155–1158
- 37) Y. Xie, H.L. Su, X.F. Qian, X.M. Liu, Y.T. Qian; *J. Solid State Chem*; 149; (2000) pg 88-98.
- 38) I.I. Abu, K.J. Smith; *Ap. Catal. A: Gen*; 328; (2007) pg 58–67
- 39) A.W. Burns, A. F. Gaudette, M. E. Bussell; *J. Catal*; 260; (2008) pg 262–269
- 40) A. F. Gaudette, A. W. Burns, J. R. Hayes, M. C. Smith, R. H. Bowker, T. Seda, M. E. Bussell; *J. Catal*; 272 ; (2010) pg18–27

Chapter 2 : Experimental procedure

This chapter discusses the experimental procedures for developing, analysing and testing the catalysts and materials used in this project. There is also a brief description of the analysis techniques used.

2.1 Catalyst Synthesis

Nickel phosphide and silica supported nickel phosphide were synthesised over a range of stoichiometries. Bimetallic transition metal phosphides and doped catalysts were also produced with the addition of further metals. Relatively simple to synthesize precursors were used to make the materials, such as nickel phosphate and thiophosphate. The precursors were then reduced under flowing hydrogen at elevated temperatures to produce nickel phosphide. This standard approach to the synthesis of transition metal phosphides, which has been extensively documented in literature, is a simple approach in comparison to some novel methods which have been explored for the preparation of transition metal phosphides discussed previously.

2.1.1 Micro reactor for material synthesis

All of the materials and catalysts developed for this project were produced using a silica glass fixed bed plug flow reactor. The figure below presents a schematic of the reactor used.

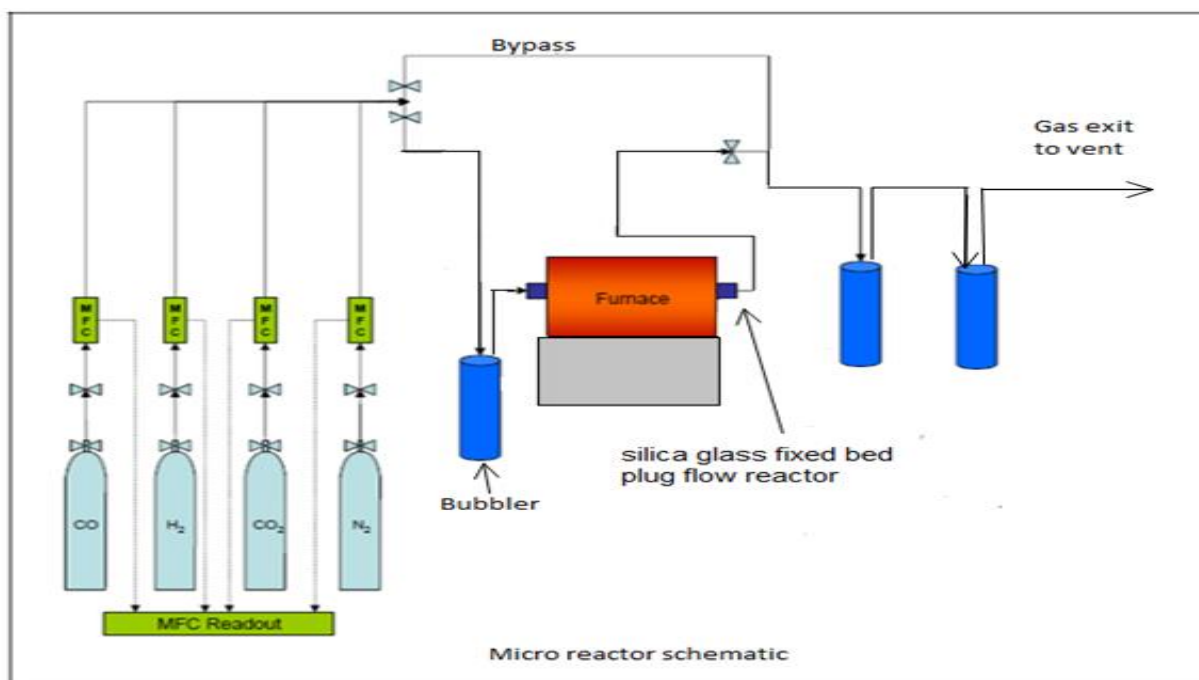


Figure 2-1: Schematic showing the silica glass fixed bed plug flow micro reactor where catalysts were developed.

2.1.2 Bulk phase synthesis

The preparation of the phosphate precursor was achieved from two different routes. Firstly, stoichiometric quantities of diammonium hydrogen phosphate ($(\text{NH}_4)_2\text{HPO}_4$) (Sigma Aldrich >98%) and nickel nitrate ($\text{Ni}(\text{NO}_3)_2 \cdot 6\text{H}_2\text{O}$) (Sigma Aldrich >98%) were dissolved in 100ml of deionised water separately. The dissolved nickel nitrate solution was deep green and the diammonium hydrogen phosphate solution clear. The diammonium hydrogen phosphate solution was then added to the nickel nitrate solution and stirred continuously for one hour. After stirring, a pale green precipitate

was formed. The solution was then dehydrated at 100°C for 12 hours to remove excess water. The precipitate was then collected and calcined in static air for 6 hours at 500°C to decompose any excess nitrates and ammonia still present. By altering the Ni:P molar ratio in the precursors used to synthesize nickel phosphate, it was possible to achieve number of different stoichiometeries of nickel phosphide using this procedure. The standard reaction used a Ni:P ratio of 2:1 giving Ni₂P, ratios of 1:1, 3:1, 4:1 and 5:1 in terms of the nickel to phosphorus ratio were also used. The second route used to produce nickel phosphate was the impregnation of nickel (II) oxide (Alfa Aesar >97%) with phosphate ions using the incipient wetness technique. Nickel (II) oxide powder was placed in a beaker. The amount of material used was double the calculated molar value of diammonium hydrogen phosphate (Sigma Aldrich >98%) to ensure the molar ratio between Ni and P remained at 2:1. However, it must also be noted that like the previous approach the phosphorus was kept in excess of this ratio due to loss of some of the phosphorus in calcination and reduction. The diammonium hydrogen phosphate was dissolved in a volume of deionised water which was equivalent to the point of incipient wetness with regards to the quantity of the nickel oxide used. Once the diammonium hydrogen phosphate was dissolved, the solution was then added drop-wise to the nickel (II) oxide powder and stirred. Once the point of incipient wetness was reached and all the solution was added to the powder. It was then dried in an oven at 100°C for 24 hours. The dried material was then collected, ground and calcined in an open air furnace for 6 hours at 600°C removing any moisture and excess salts from material.

The reduction of nickel phosphate to nickel phosphide was carried out in a silica glass fixed bed plug flow reactor. The reaction took place under a hydrogen/argon gas mixture (BOC 75% hydrogen; 25% argon) with a flow rate of 60ml/min at temperatures of either 700°C (for the nickel nitrate precursor to the phosphate) or 750°C (for the nickel oxide precursor) for differing lengths of time (2.5, 3.5 or 5 hours) and at ambient pressure. The sample was cooled to ambient temperature under H₂/Ar mixture gas flow then passivated overnight by back diffusion of air into the reactor.

The alternative to using phosphates as a precursor to nickel phosphide is using a thiophosphate precursor, which is similarly reduced to the phosphide. With the presence of sulfur in the precursor this allows for novel applications in the future as well as a decrease in reduction temperature. There are two different methods that have been used for producing nickel thiophosphate. The first was high temperature annealing of nickel, phosphorus and sulfur powders mixed together in a ratio of 1:1:3 (corresponding to the stoichiometry of NiPS_3). The mixed powder was then sealed in nitrogen atmosphere and heated at 700°C for 48 hours. The sulfur content was subsequently reduced in later experiments to produce lower sulfur content in the materials produced by altering the stoichiometric ratio between the nickel, phosphorus and sulfur mixture used. The second method used was via a room temperature precipitation reaction using sodium thiophosphate (NaPO_3S) (Alfa Aesar >97%) and displacing the sodium ion with nickel from a nickel donating salt (i.e. nickel nitrate). The sodium is readily displaced under ambient conditions and the precipitate is then filtered, dried and calcined in a similar method to that used for the phosphate precursors described previously. Reduction of the thiophosphate precursor to nickel phosphide was carried out in a similar manner to the aforementioned procedure for the phosphate precursor with the only difference being the reduction temperature. The P-S bond is much easier to reduce to the phosphide than the P=O bond under these conditions hence reduction begins at 400°C . This produces a catalytically inactive species Ni_5P_4 , described by Berhault and colleagues. As the reduction temperature increases towards 600°C the structure of the nickel phosphide is further reduced to Ni_2P .^[1] A summary of all of the bulk phase synthesis procedures undertaken throughout this investigation is presented in Table 2-2 in the following section.

2.1.3 Synthesis of supported materials

The transition metal phosphides produced in bulk phases in the project have also been placed on a silica Q10 support to allow the materials to be tested in the high pressure steam reactor. Some of the approaches to synthesis for bulk phase materials such as the high temperature annealing of precursor were not suitable for applying to supported systems. Placing the active phase on a support is necessary due to the high pressure conditions the reactor operates under, which are unable to accommodate fine powders such as those produced via precipitation. Another reason is due to the extremely low surface area which bulk phase transition metals exhibit due to high reduction temperatures. Supporting nickel phosphide results in a much better dispersion of particles, potentially resulting in improved catalytic activity.

The supported catalysts produced were of 20% wt loading with respect to nickel content. The catalysts were prepared firstly by adding the stoichiometric equivalent of nickel nitrate (or the other transition metal nitrate) required for the desired loading on the support. This is then dissolved in the appropriate volume of water needed to saturate the support to the point of incipient wetness and then added to the support. This was then dried and the same approach was again taken when adding the diammonium hydrogen phosphate or sodium thiophosphate to the support. The supported materials were then dried, calcined and reduced under similar conditions the bulk phase systems described previously. For supported catalysts containing more than one metallic element such as Ce-Ni₂P/SiO₂ the donor salt for the 2nd metal was added along with the nickel nitrate salt. The weight percentage of the 2nd metal varies and is displayed in the list on the following page.

2.2 List of all nickel phosphide catalysts

Table 2-1 on the following page is a list of all of the catalysts developed and tested in this project

Catalyst	Description	Testing conditions		
		HT shift	LT shift	Sulfur tested
$\text{Ni}_2\text{P}/\text{SiO}_2$	Prepared using nickel nitrate and diammonium hydrogen phosphate precursors with Ni loadings of 20%, 40% and 60% on the support.	✓	✓	✓
$\text{Ni}_2\text{P}/\text{SiO}_2$	Prepared via citric acid precursor 20%wt Ni on support.	✓	✓	
$\text{Ni}_2\text{P}/\text{SiO}_2$	thiophosphate precursor using in preparation of catalyst 20%wt Ni on support.	✓	✓	
$\text{CeO-Ni}_2\text{P}/\text{SiO}_2$	10%, 5%, 1% and 0.5% wt Ce with 20%wt Ni on support.	✓	✓	
$\text{Fe-Ni}_2\text{P}/\text{SiO}_2$	10%wt Fe and 20%wt Ni on support.	✓	✓	
$\text{Fe-NiP}/\text{SiO}_2$	20%wt Fe and 20%wt Ni on support.	✓	✓	✓
$\text{Pd-Ni}_2\text{P}/\text{SiO}_2$	1%wt Pd and 20%wt Ni on support.	✓	✓	
$\text{Cu-Ni}_2\text{P}/\text{SiO}_2$	10%wt Cu and 20%wt Ni on support.	✓		
$\text{K-Ni}_2\text{P}/\text{SiO}_2$	1%wt K and 20%wt Ni on support.	✓	✓	
$\text{Cs-Ni}_2\text{P}/\text{SiO}_2$	1%wt Cs and 20%wt Ni on support.	✓	✓	
CoP/SiO_2	20%wt Co on support.	✓		
CeP/SiO_2	20%wt Ce on support.	✓		
Ni/SiO_2	20% wt Ni on support. Used as a bench mark to compare Ni_2P catalysts.	✓		✓
P/SiO_2	20% wt P on support. Used as a bench mark to compare Ni_2P catalysts.	✓		

Table 2-1: Summary of the catalysts prepared and tested during the project.

2.3 Testing Material Stability

The nickel phosphide that was produced was tested in terms of its stability under conditions designed to mimic those of the water-gas shift reaction as well as nickel phosphides tolerance to sulfur containing compounds. These tests were carried out in the same silica fixed bed plug flow reactor used in the reduction, using a similar operating procedure with the addition of bubbler to allow carrier gas to pass through liquid before reaching the microreactor. The bubbler was filled with either steam or thiophene and introduced into feed by using a hydrogen / argon gas mixture (BOC hydrogen 75% argon 25%) at a flow rate of 60 ml/min^{-1} as a carrier gas. Nickel phosphide samples were “steamed” for a range of times between 2 hours and 5 hours at temperatures of 300, 400 and 500°C . The materials were then gradually cooled to ambient temperature in the reactor. The resultant materials were then characterised.

2.4 Summary of bulk phase synthesis of nickel phosphide

Precursors	Method of preparation	Calcination	Reduction	Precursor phase	Stoichiometries of phosphide achieved and Ni:P ratio of precursors	Steam tested	Sulfur treated
-Nickel nitrate $\text{Ni}(\text{NO}_3)_2$ -Diammonium hydrogen phosphate $(\text{NH}_4)_2\text{HPO}_4$	precipitation	Air 500°C 5 Hours	700°C 3 hours Under H_2/Ar mixture.	Amorphous $\text{Ni}(\text{PO}_3)_2$	Ni_2P (1:1, 2:1 and 3:1) Ni_5P_2 (4:1) Ni_3P (5:1)	Yes stable	Yes Stable
-Nickel oxide NiO -Diammonium hydrogen phosphate $(\text{NH}_4)_2\text{HPO}_4$	Impregnation	Air 500°C 5 Hours	750°C 3 hours Under H_2/Ar mixture.	$\text{Ni}(\text{PO}_3)_2$	Ni_2P from all ratios of Ni:P attempted (1:1, 2:1, 3:1 and 4:1)	Yes stable	Yes Stable
-Sodium thiophosphate NaPO_3S -Nickel nitrate $\text{Ni}(\text{NO}_3)_2$	Precipitation	Air 500°C 5 Hours	700°C 3 hours Under H_2/Ar mixture.	NiPO_3S	Ni_2P	Yes stable	Yes stable
-Nickel Powder -Phosphorus powder -Sulfur powder	High temperature annealing	N/A	Between 400-600 depending on species formed	NiPS_3	Ni_2P and Ni_5P_4	Yes stable	Yes Stable

Table 2-2: Summary table of preparation routes for bulk phase nickel phosphide.

2.5 Water-Gas Shift Reaction

The catalysts were tested in water-gas shift reaction under both high and low temperature conditions. The testing was carried out in a reactor similar to that shown in Figure 2-2. This is a continuous flow, high pressure, fixed bed reactor using a 3/16 inch internal diameter and 18.5 inch long glass-lined stainless steel reactor tube in which the catalyst bed was packed with boiling chips on either side of the bed. An external thermocouple was aligned with the reactor bed to maintain the operating temperature at a continuous level. Both the thermocouple and the heater unit were controlled using a temperature controller. The temperature controller was used to run temperature programmes to allow extended runs with changes in temperature for different stages if required, such as pre-reaction reduction of the catalyst. The pressure in the reactor was maintained by a variable pressure valve which was run at 20 barg. Gases used in the reactor were controlled using digital mass flow controllers which allow flow rates of between 5 and 250 ml/min⁻¹. Steam was fed into the reactor in the form of water using an HPLC pump from a reservoir of deionised water. The water was pumped into the vaporiser which converted the water to steam operating at 400°C for the duration of the run. The upper line between the vaporiser and the reactor tube was heated and maintained at 250°C to avoid condensation. Excess steam from the reactor was condensed and separated from the product gas in a knockout pot which was maintained by a refrigeration unit which flowed coolant around the knockout vessel and operated at 6°C. The gaseous products remaining were analysed using an on-line GC (Varian 3400).

The reactor is summarised in the schematic below:

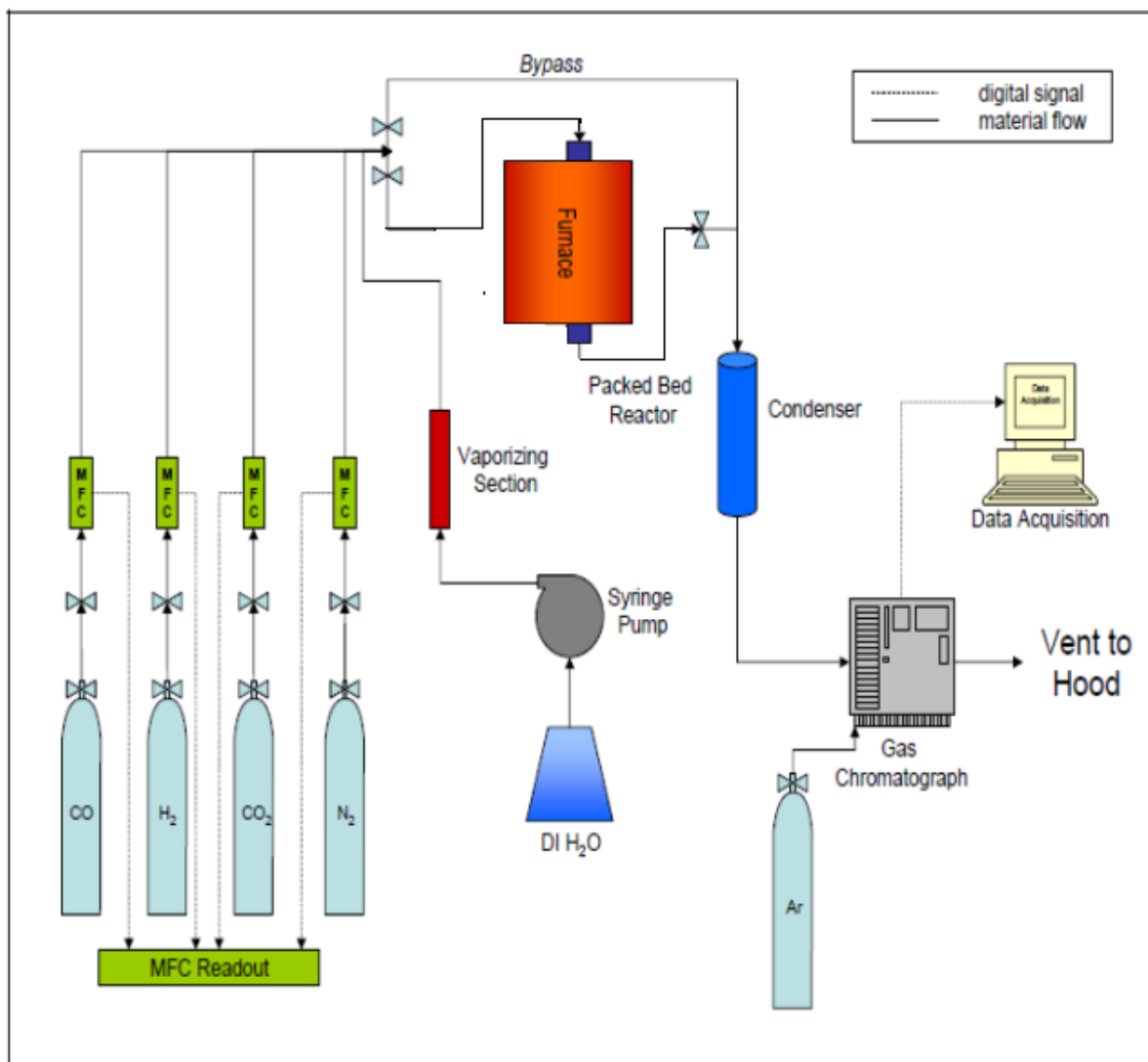


Figure 2-2: Schematic of the reactor in which water gas shift reactions were conducted.

2.5.1 Reactor procedure

The catalysts were tested using the following conditions in the high pressure steam reactor;

A feedstock of H₂O and CO was used in a molar ratio of 1:1 using a gas hourly space velocity of 15,000 h⁻¹ for the duration of reaction run. To achieve the desired space velocity the necessary flow rates for the reactants were calculated. The carbon monoxide flow rate set at 125 ml/min⁻¹ and the water flow rate set 1.48 ml/min⁻¹ for every reaction run. The volume of catalyst used throughout testing was 1cm³. The weight of each catalyst was also noted prior to testing. The average catalyst particle size used was between 250 and 425 microns. Before the reactor was brought online the catalyst was pre-treated with flowing H₂ (60ml/min⁻¹) for 3 hours at 350°C in the reactor to ensure the active phase of the material was reduced. The operating temperatures used were, 210°C for the low temperature water gas shift reaction and 410°C for the high temperature water gas shift reaction. The reactor used an operating pressure of 20 barg which was maintained for the duration of the catalyst testing. The reaction time for all reactions was 105 hours, samples were analysed every 30 minutes for the duration of the reaction by auto-sampling GC.

2.5.2 Gas chromatographic analysis of gases

The exit feed from the steam reactor was analysed using an online Varian Gas Chromatograph 3400, fitted with a 30 m CarboxenTm1010 plot column using a TCD detector. Ar was used as the carrier gas which had a flow rate of $25\text{ml}/\text{min}^{-1}$. The CarboxenTm1010 plot column was used for the separation of H_2 , CO , CO_2 , CH_4 and C_2H_6 where the sample loop volume in this GC was $250\ \mu\text{l}$. An initial sample was taken immediately once the reactant gases are switched on and then at 30 minute intervals for the duration of the reaction. This time allowed for all the products to pass through the capillary column as well as an additional 2 minutes for GC equilibration. The computer software used for this analysis was Star Chromatography workstation version 5.5.1.

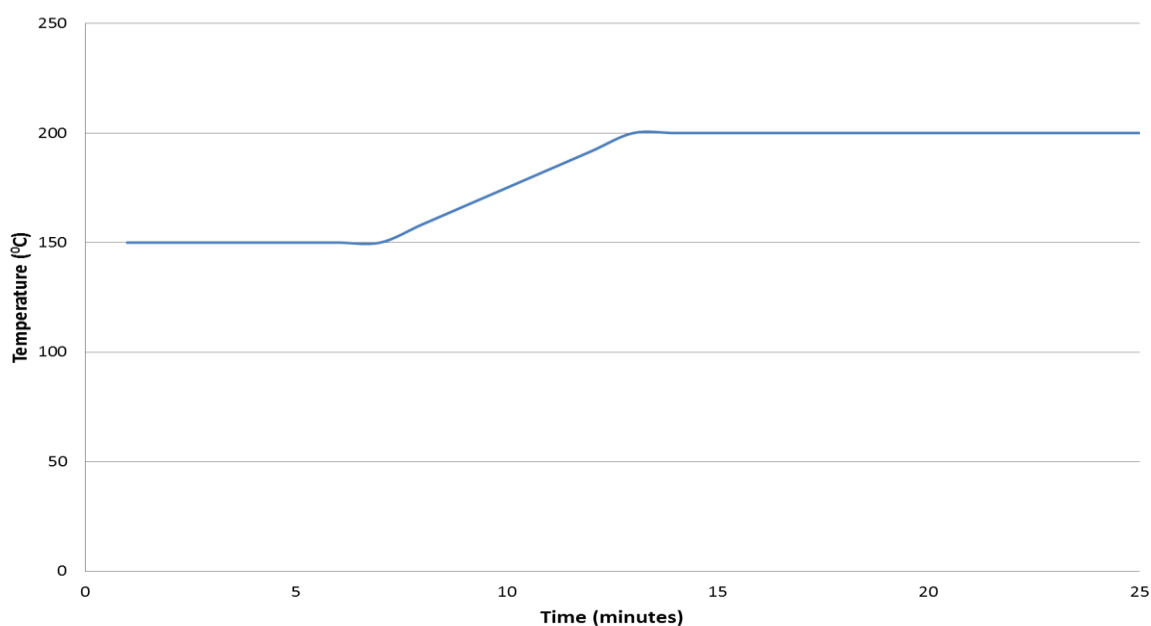


Figure 2-3: Column temperature profile for GC sample run.

2.5.3 Mass flow controllers (MFCs)

The MFCs, which controlled the flow of gases to the reactor, were calibrated using a digital flow meter connected to the vent of the high-pressure reactor. For each gas, the MFC was fixed at a particular flow rate and allowed to stabilise before a reading was taken. The MFC set points and actual readings from the digital flow meter are plotted in Figure 2-4. The actual flow rate calculated from the plot and was used to determine the MFC set point for the reaction.

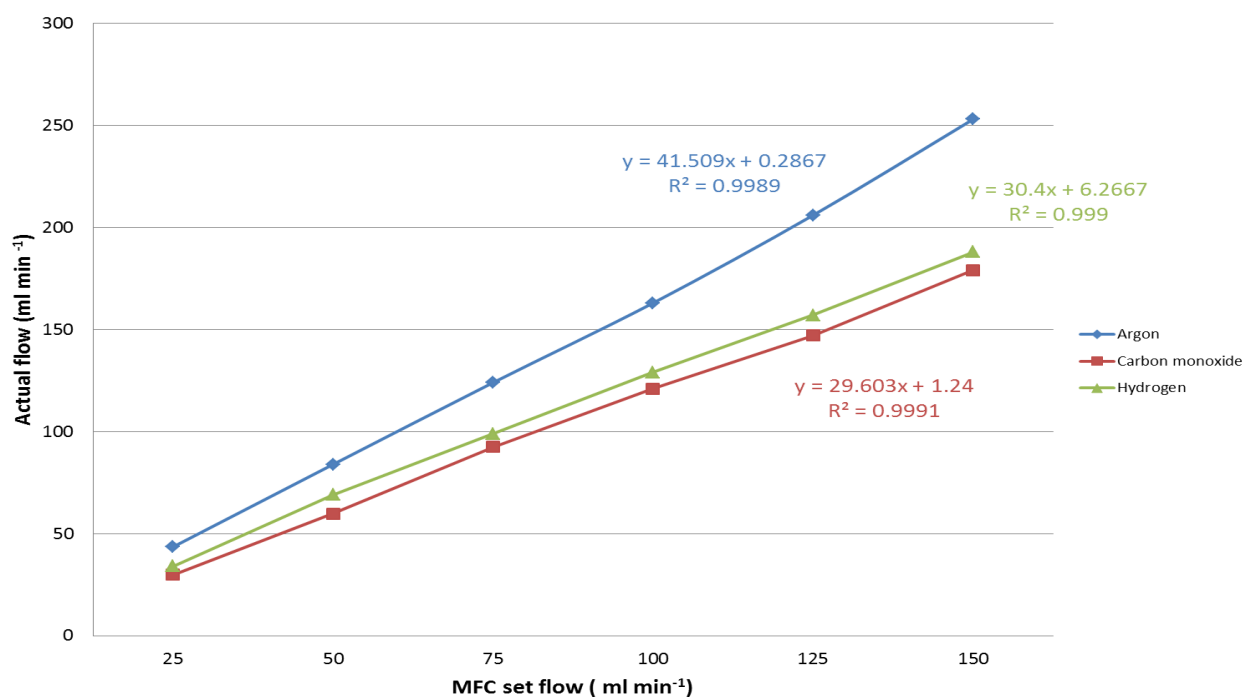


Figure 2-4: Plot showing relationship between recorded flow rate and the MFC set point on the control panel.

2.5.4 GC gas standards

Calibration standards for reactants and products (with the exception of water which is condensed and separated before it reaches the GC) were prepared by analysing varied, known concentrations of each of the gases along with the carrier gas (argon), whilst ensuring the total flow rate of the gas mixture was kept constant. From the analysis of the data, a linear plot was created with the gradient of the plot for each gas used to establish the relationship between the concentrations of gases and peak areas from the GC data analysis. The number of moles of gas being injected into the GC was calculated using the following relationship:

$$\text{Number of moles} = (PV/RT) * \% \text{ of gas in mixture}$$

Where

P = pressure (1atm),

V = total volume of gas

R = gas constant ($0.0821 \text{ L atm K}^{-1} \text{ mol}^{-1}$)

T = temperature of laboratory

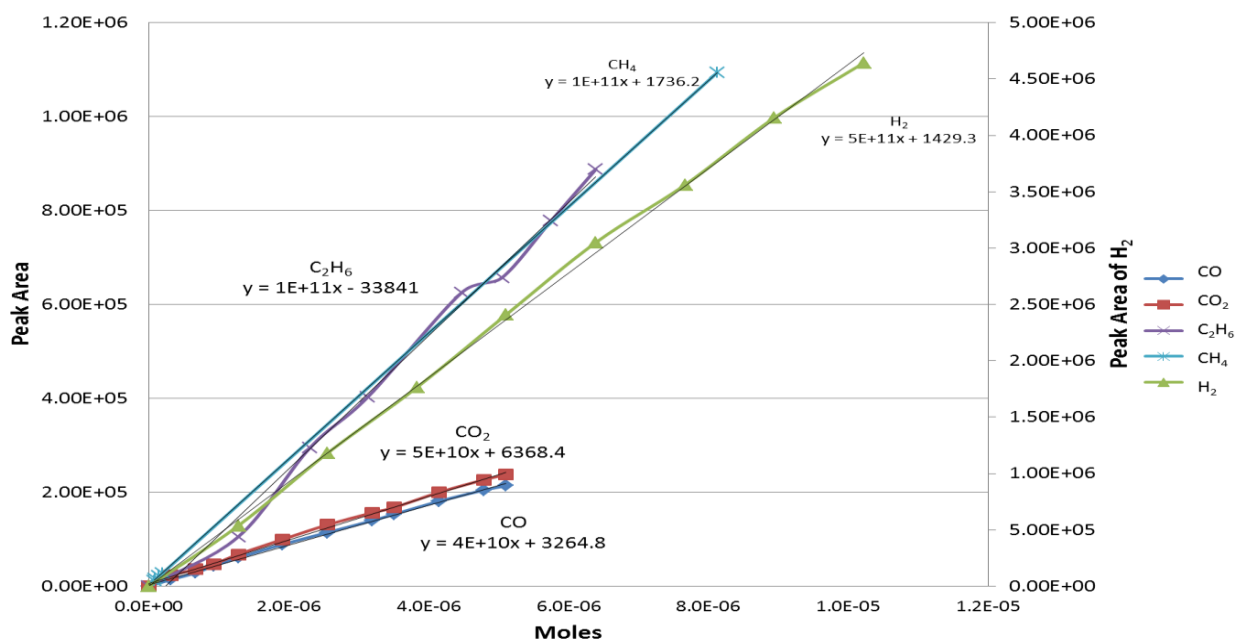


Figure 2-5: GC calibration standards for gases

2.5.5 Sulfur poisoning

The transition metal phosphide catalysts were tested under water-gas shift reaction conditions in the presence of sulfur. The materials were tested for the tolerance to sulfur and compared to industrial catalysts tested under similar conditions. The steam reactor was run as previously described for reaction runs without the presence of sulfur. The feed of water was switched over from a clean feed to a sulfur-containing feed after a period of running for 48 hours to enable the reaction to reach a steady state. The feed was switched to a feed of water which had been pre-treated with H₂S gas to volume of 10 parts per million of sulfur. The sulfur containing feed was then run until the activity of the catalyst dropped down to a steady state according to GC analysis of the exit feed from the reactor. The feed was then once more switched to the water feed which did not contain any sulfur and run until activity returned to a steady state.

2.7 Characterization of materials

All materials synthesized including precursors have have been characterised using a range of techniques. XRD, SEM, TEM, TGA, XAS, Raman spectroscopy, DRIFTS and XPS characterisation techniques were used to define the chemical and physical properties of the materials. Catalysts were also characterized using this range of techniques after use in reactions/ processes. A brief description of these techniques and their application in the field of heterogeneous catalysis and material development will be discussed.

2.7.1 Thermo-gravimetric analysis (TGA)

Thermo-gravimetric analysis was carried out in samples using the TGA/DCS SDT Q600 thermal analyser which was used in conjunction with an ESS mass spectrometer. For all temperature programmed reductions, the samples were heated from room temperature (25°C) to 800°C with a temperature ramp rate of 10°C per minute using an 5 % H₂/N₂ gas mixture with a flow rate set at 100 ml/min⁻¹. Mass-spectroscopic data along with the thermographic analysis of the sample was obtained via online analysis.

2.7.2 Scanning electron microscope

Scanning electron microscopy (SEM) is a technique which uses a source beam of electrons to produce highly magnified images of samples, giving a valuable insight into the morphology. If used in conjunction with EDX elemental analysis composition of the material can also be determined. The signal results from interactions of the electron beam with atoms at or near the surface of the sample. The most common mode of detection is by secondary electrons emitted by atoms excited by the electron beam. The number of secondary electrons is a function of the tilt of the surface. On a flat surface, the transmission of secondary electrons is mostly contained by the sample, but on a tilted surface, the secondary electron transmission is partially exposed meaning more electrons are emitted. By scanning the sample and detecting the secondary electrons, an image displaying the tilt of the surface is obtained. SEM Microscope (Model Philips XL30 SEM) was used to analyse the material surfaces at a number of highly magnified ranges. The microscope operated using a beam power of 20 kV with a working distance of 10mm under high vacuum conditions. Sample materials were placed onto an electrically conductive carbon disc which is mounted on an aluminum pin. The carbon disc has adhesive surface causing the sample to stick to the disc. All samples were gold coated to reduce the effects of sample charging. The SEM microscope was also equipped with EDX

analysis meaning that the samples were also quantified in terms of the elemental composition with regards to the area of interest.

2.7.3 Powder X-ray diffraction

Powder X-ray diffraction (XRD) is a very useful characterization technique able to define bulk phase properties of powdered materials such as structural properties of materials. This is achieved by exposing the sample to X-rays. These X-rays are the elastically scattered by the electrons in atoms within a periodic lattice. In order for a sample to scatter, the sample must be ordered (i.e. have a crystalline structure) meaning that diffracted waves are synchronised. This is known as constructive interference. The theta–theta X-ray diffractometer experiment can be described simply as the sample being placed in a horizontal plane and remaining in a fixed position, while the X-ray monochromator source and detector move counter to one and other. This is done symmetrically to the incident energy resulting in monochromatic X-rays. The sample is then rotated so that the angle increase in steps therefore scattering is detected throughout a range of angles, enabling the dimensions of the crystal structure to be determined through subsequent fitting of the powder diffraction data. The crystal structure is identified by the Bragg equation which is able to determine the lattice spacings of the material. The equation is applicable for any given compound therefore diffraction patterns can be used as fingerprint technique to identify phases within materials. The Bragg equation is expressed as follows:

$$n\lambda = 2 d \sin \theta$$

n= integer

λ = wavelength of incident radiation

θ = angle of scattering

d= d-spacing

Materials were analysed using an X-ray Diffractometer (Model Siemens D5000) which used a Cu K α (1.5418 Å) radiation source. The materials were analysed between angles 5-85° 2θ , using a 0.02° step size and a counting time of 1 sec/step. A number of the catalysts were reduced *in situ* under flowing hydrogen using the diffractometer “hot stage” facility. The materials were analysed at set temperatures (in steps of 100°C). This was gradually increased to allow for the a diffraction patterns to be collected at a range of temperatures as the system is heated to reduction temperature and then cooled to room temperature.

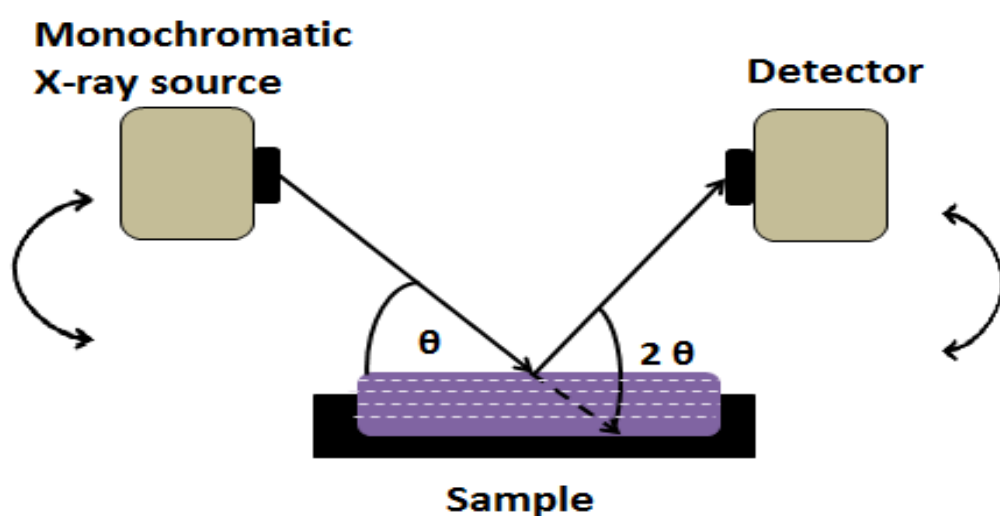


Figure 2-6: Diagram depicting the working of an X-ray diffractometer

2.7.4 X-ray photoelectron spectroscopy

X-ray photoelectron spectroscopy (XPS) analyses of samples was carried out using a Kratos AXIS ULTRA using a monochromatic X-ray source. This was carried out at the EPSRC access facility at Cardiff University. XPS analysis is a quantitative technique which is able to show the electronic state of the elements present at or near the surface of the material being analysed. It may also be used to give valuable information regarding the elemental composition and empirical formula of the material. It is also possible to determine the surface chemistry of the material by

bombarding the surface with heavy atoms in order to remove some of the surface layers of the material, known as sputtering. This allows comparison between the surface and the bulk of the material.

The XPS spectra are obtained by exposing a material to high energy X-rays which cause the emission of electrons in the material due to the photoelectric effect. The XPS spectrum is derived from the number of detected photoelectronically emitted electrons per energy interval versus their kinetic energy. The kinetic energies of the electrons are determined by the spectrometer comparing the energy difference between the initial and final states after the photoelectrons have been emitted. The photons from the X-ray source have limited surface penetration on the sample (usually only 10 micrometers); therefore X-ray photoelectron spectroscopy is classed as a surface or near surface technique.

Usually the XPS spectrum consists of a plot of the number of electrons detected (sometimes per unit time) versus the binding energy of the electrons detected. There is a characteristic set of peaks for each of the elements, which have binding energies corresponding to the electron shells associated with the element (such as 4s, 3d, 4p etc.), thus identifying the species present upon the surface of the material. The number of detected electrons in each of the characteristic peaks is directly related to the amount of element within the area which has been exposed to the x-rays.

2.7.5 Diffuse Reflectance Infrared Spectroscopy (DRIFTS)

DRIFTS is a form of infrared spectroscopy which uses diffuse reflectance for measurement of fine particles and powders and can be used to determine the interactions between a material surface and reactants, such as the adsorption of molecules on a materials surface. Diffuse reflectance arises from the scattering of light from powdered sample which has absorbed incident radiation in the form of infrared light. The light is scattered by reflection, refraction and diffraction which is focused into the detector using a series of elliptical mirrors (see Figure 2-7). The

majority of light which collected is reflected light which has had little or no interaction with the material because the beam of light which has been reflected has the angle between it and the sample material equal to that of the incident beam and sample. This is known as a specular reflection. The diffusely reflected light has transferred energy to the sample and has scattered light in all directions. Therefore it is important with this technique that the light which is diffusely reflected is amplified with respect to light which has been specularly reflected, because the diffusely reflected light is relatively low in comparison to the specularly reflected light. Due to the low ratio of diffusely reflected light to specularly reflected light, the technique requires a very sensitive spectrometer such as a spectrometer using Fourier transform calculations. There are a number of benefits to using DRIFTS compared to other IR techniques. One of the main advantages is that the samples need little or no preparation when being analysed. The use of powdered samples allows the materials to be tested in *in situ* environments such as having gas flowing over the sample allowing the gas to interact with the surface of the materials. Analysis can also be done using different temperatures allowing for temperature profiles for adsorption and desorption of gases under different temperature conditions. DRIFTS studies for this project were carried out at the Johnson Matthey Technology Centre and where carried out under flowing CO and syn-gas (60% CO 40% H₂) at a range of temperatures, from room temperature up to 400°C. This was carried out in order to better understand the adsorption and desorption CO on a range of catalysts under temperature conditions similar to those under which the water-gas shift reaction operates.

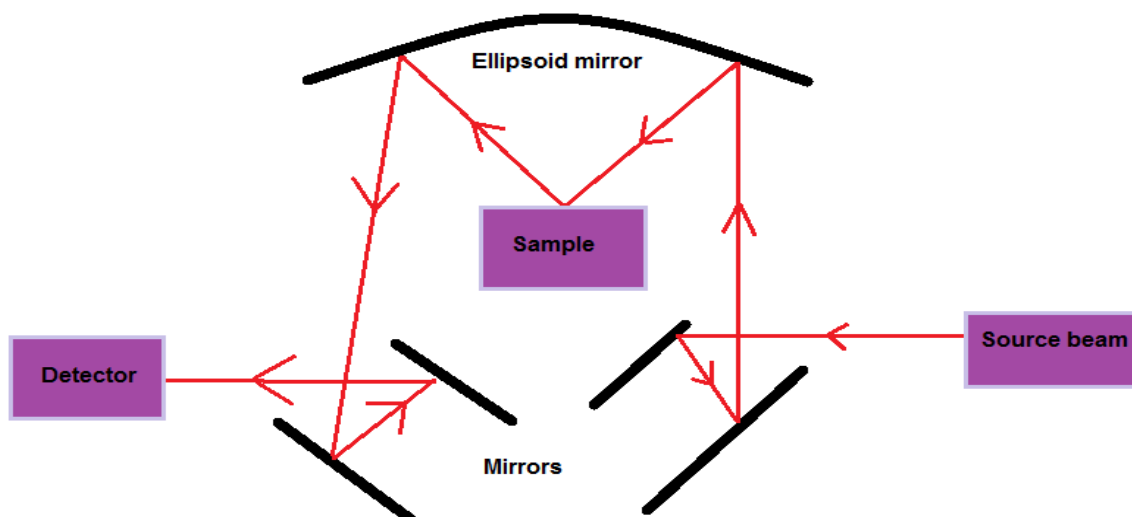


Figure 2-7: Schematic depicting the layout of the DRIFT spectrometer used for analysing samples.

2.7.6 Transmission Electron Microscopy (TEM)

Transmission Electron Microscopy (TEM) is a technique where a high powered electron beam interacts and passes through a specimen. Electrons are scattered from both electrons and nuclei in the material. Upon interaction with the beam, a sample can affect the electrons in a number of ways. TEM utilises electrons that are transmitted and diffracted by the sample to produce high-resolution images. TEM provides topographical, morphological, compositional and crystalline information about a material. This is due to the small de Broglie wavelengths of the electron in comparison to visible light. Electrons from the primary electron source will interact with sample surface either by transmission (passing through the sample unaffected) or by scattering of the electrons (diffracted). The transmission of unscattered electrons is inversely proportional to the specimen thickness. This means that areas of the sample that are thicker will have fewer transmitted unscattered electrons and so will appear darker. Conversely, the thinner areas will have more transmitted and thus will appear lighter, whilst diffracted electrons give dark field images. All electrons from the primary source have the same energy; these interact with the

material normal to its surface. Electrons that are diffracted by the same species present in the material are diffracted by the same angle.

These diffracted electrons are detected using magnetic lenses, which are then collated together to give a pattern of spots which reveal information about a materials crystal structure including the determination of lattice parameters, atomic arrangements and orientation. Figure 2-8 illustrates the interactions between electrons from a primary source a material surface. X-rays are a side-effect of electron bombardment of a material. The fluorescence of a material caused by electrons from the material vacating and entering different shells and the energy associated with those transitions are specific to each element. Therefore with TEM fluorescence is measured within the material and an elemental map is collated.

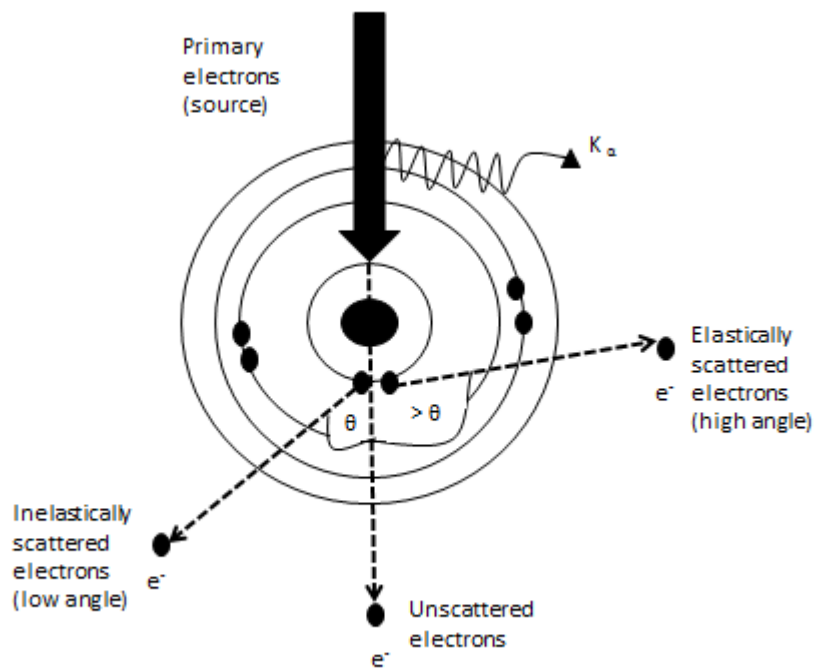


Figure 2-8: Interactions between a sample material and the electrons from the primary source upon which TEM focuses.

2.7.7 Extended X-ray absorption fine structure spectroscopy (EXAFS)

EXAFS analysis of materials was carried out at the Diamond Synchrotron Research Facility in Oxfordshire through the catalysis research Hub at Harwell Research Facility. Materials were ball milled to decrease particle size and added to cellulose, then pressed into discs to allow for dilution of metal content in the sample to be analysed to allow for better spectra to be achieved. All materials were analysed in the nickel region of the absorption spectra, looking at the K-edge energy transitions for the materials.

EXAFS utilises high energy X-rays in order to cause the target element atoms in a material to transition into an excited state. This is achieved by x-rays being absorbed at an energy level which is equal to that of the binding energy for core electrons. This is different and specific for each element. EXAFS theory correlates the absorption coefficients of the target atom with the ground, excited and decaying states which the atom transitions through. Upon interaction with X-rays of energy equal to or greater than the binding energy of electrons in a specific shell of the element of interest, the material reaches an excited state. Once in the excited state, a core level electron is ejected from the atom leaving a vacancy in the electron shell. This phenomenon is a result of the photoelectric effect, characterised by what is known as an “edge” which is viewed as climb in absorption on the spectrum. The vacancy in the core level electron shell is then filled by an electron from a higher energy shell, causing an X-ray to be emitted in the process. This is known as fluorescence, which can be described as the decay of the excited state back to the ground state. The photoelectron which has been ejected from the central atom is scattered by surrounding neighbouring atoms back towards the central atom. This is characterised by oscillations shortly after the edge gap. These oscillations can give information regarding the environment and neighbouring atoms that surround the target atom. Figure 2-9 illustrates the photoelectric effect and the different modes of

interaction between the source X-rays and the sample ultimately showing the alternative methods of analysing samples using X-ray absorption spectroscopy.

The technique is especially sensitive to the formal oxidation state, coordination chemistry, and the distances, coordination number and species of the atoms immediately surrounding the selected element. It is possible to analyse almost any element present within a sample even down to trace amounts. This is especially useful when dealing with catalysts which have been doped with small amounts of metals or if trace amounts of sulfur are present on the surface after testing in the presence of sulfur. The ability of EXAFS to provide information about a specific atom's local environment has widespread application, because the technique does not require materials to be crystalline. Therefore, analysis of amorphous materials can be readily studied. This is especially useful in catalysis when many of the supports used when making catalysts are very amorphous in nature, making it very difficult to obtain quantifiable data for active phases on the support by conventional methods such as X-ray diffraction.

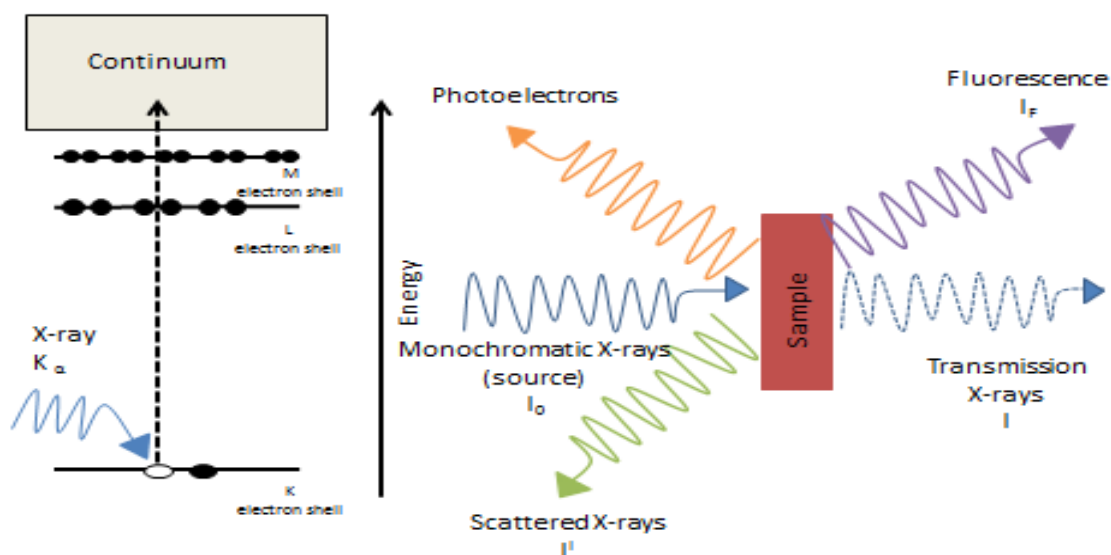


Figure 2-9: Schematic of the interaction between source X-rays and the target atoms core electron shells and the different modes of interaction between the source and sample in X-ray absorption spectroscopy.

2.7.8 Raman Spectroscopy

Raman spectra of the catalysts were obtained using a Horiba LabRAM High Resolution spectrometer. The excitation source for the laser was a Kimmon IK series He-Cd using a wavelength of 532.17 nm. Laser light was focused for 10 seconds using a 50x objective lens. This was repeated for 4 points to improve the resolution of the peak. The scattered light was collected in a backscattering configuration and was detected using a nitrogen cooled charge-coupled detector. A scanning range of between 200 and 1600 cm^{-1} was applied.

Raman spectroscopy involves the study of molecular vibrations from molecules exposed to a monochromatic light source. It differs from Infra-red spectroscopy, which looks at molecular vibrations of molecules that elastically scatter photons, because it focuses on quantifying the molecular rotations and vibrations caused by the inelastic scattering of photons. Figure 2-10 illustrates the possible interactions between photons and the sample. Light that is scattered elastically (i.e. no loss of energy in the scattered photon) is known as Rayleigh scattering and is inactive in the Raman spectrum. Most of the monochromatic light which interacts with the sample will be scattered in this manner. Light from the source that does not interact with molecules by Rayleigh scattering are Raman active and this gives rise to Stokes and anti-Stokes bands.

When a molecule excited by the light source upon relaxation returns to the first vibrational level it is said to inelastically scatter because the photon now has less energy than it had initially. This gives a peak in the Raman spectrum known as a Stokes band. Anti-Stokes bands occur when a molecule upon relaxation scatters a photon with more energy than the initial incident photon; these types of bands are much smaller in intensity in comparison to Stokes bands in the Raman spectrum. Figure 2-10 also illustrates the appearance of different bands in a Raman spectrum. In Raman spectroscopy, like infrared spectroscopy, not all molecular vibrations are observable in the spectrum. According to Raman spectroscopy selection rules, only

vibrations which result in a change in the polarisability of the molecule are Raman active. Many molecules and molecular vibrations are active for Raman spectroscopy but inactive for infrared. Due to this, both techniques often complement one another. The benefits of Raman over infrared spectroscopy include the ability to analyse black samples, low frequencies (i.e. below 1000cm^{-1}) are observable in Raman spectroscopy, finally the use of a laser as the light source means that much smaller volumes of material can be analysed.

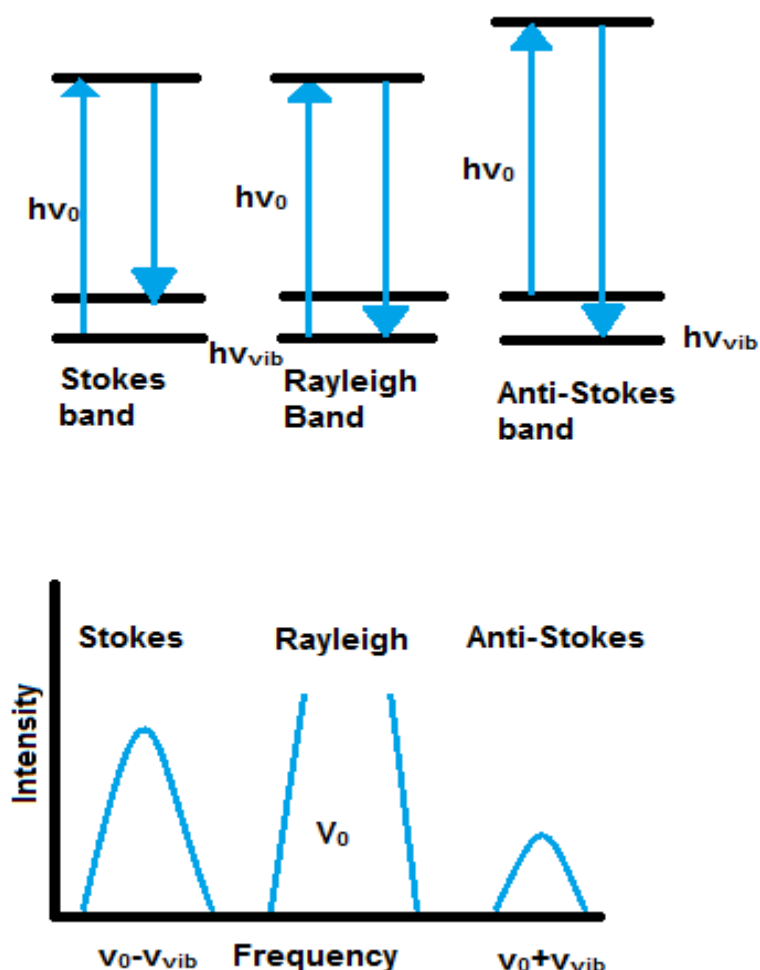


Figure 2-10: (above) Raman scattering energy diagrams for different modes of scattering. (below) Stokes, Rayleigh and anti-Stokes bands as they would appear in spectrum.

2.8 Calculations

The calculations presented in this section were used in the interpretation of data from the catalytic testing of the materials for the water-gas shift reaction. These are present in following results chapters.

2.8.1 CO conversion

The percentage conversion of CO was calculated as;

$$CO\ Conv\ \% = \left[\frac{(moles\ in - (moles\ out \times (\frac{gas\ flow\ rate\ in}{gas\ flow\ rate\ out}))}{(moles\ in)} \right] \times 100$$

2.8.2 Carbon balance

Carbon balance percentage was calculated using the equation below;

$$Carbon\ balance\ \% = \left[\frac{\left((moles\ of\ carbon\ out) \times (\frac{gas\ flow\ rate\ in}{gas\ flow\ rate\ out}) \right)}{(moles\ of\ carbon\ in)} \right] \times 100$$

2.8.3 Selectivity of carbon based products

The percentage selectivity of each product was calculated using the follow equation;

$$Selectivity\ of\ products\ \% = \left[\frac{(moles\ of\ product)}{(moles\ of\ products\ produced)} \right] \times 100$$

2.8.4 Water-gas shift reaction equilibrium

The water-gas shift reaction as discussed previously is an equilibrium reaction therefore in order to compare and contrast catalysts based on activity it is essential that point of equilibrium be identified and be avoided. The equilibrium constant and Gibbs free energy were calculated for the reaction under the reaction conditions using the following equations;

$$K = \frac{P_{CO_2}P_{H_2}}{P_{CO}P_{H_2O}} = \frac{x_{CO_2}x_{H_2}}{x_{CO}x_{H_2O}} = \exp\left(-\frac{\Delta G^\theta}{R_{gas}T}\right)$$

$$\Delta G^\theta = \Delta H^\theta - T \cdot \Delta S^\theta$$

K= equilibrium constant

P=partial pressure of gas

x= moles

ΔG^θ = Gibbs standard free energy change

R= gas constant

T= temperature

ΔH^θ = standard enthalpy change

ΔS^θ = standard entropy change

Chapter 3 : Nickel phosphide, a novel material for application in the water-gas shift reaction

3.1 Introduction

This chapter covers the preparation, characterisation and catalytic testing of nickel phosphide. It was initially prepared as a bulk material which was characterised and tested using the techniques previously described in the experimental chapter. Nickel phosphide was supported on high surface area silica to yield a highly dispersed and mechanically robust active catalyst. The preparation of nickel phosphide catalysts was modified by changing the precursors used to produce the final catalyst, which enabled a greater understanding of the synthesis and active phases of the materials, as well as showing which synthesis route provided the most active catalyst. The nickel phosphide materials were tested for application in water-gas shift reaction under both high and low temperature regimes. The materials were characterised using a range of techniques pre- and post-reaction.

3.2 Catalytic activity of Nickel Phosphide

Transition metal phosphides are an interesting and diverse group of materials; they have been studied with considerable interest for application in a number of different fields due to their useful chemical and physical properties.^[1-4] The combination of physical properties such as hardness and strength, with good thermal and electrical conductivity have meant that they have found use in a number of areas such as electronic and magnetic applications, it is however their application as high performance process catalysts which has drawn the greatest amount of attention in recent years.^[1]

Metal phosphides have been extensively investigated and have generated interest as alternative catalysts, with particular attention centring upon nickel phosphide. Most of the research with regards to the catalytic activity of nickel phosphide has focused on the materials potential as hydrotreating and hydrogenation catalysts. The Oyama group have published a great deal of research on transition metal phosphides and their application over the last ten years. [1, 4, 6, 8, 9]

Transition metal phosphides remain relatively unexplored as water-gas shift catalysts; however the little that has been done has produced promising results. Rodriguez and colleagues published a study in which they tested bulk Ni_2P in the water-gas shift reaction. [5] The results from their work showed that nickel phosphide performed better than standard nickel and copper metal catalysts. The superior performance of nickel phosphide over the copper catalysts is significant, the commercial use of copper catalysts as highly active water-gas shift catalyst. Rodriguez suggests that the high activity displayed by Ni_2P as a water-gas shift catalyst is due to the formation of oxy-phosphides on the surface of the material, these are formed due to the strong interactions between oxygen and phosphorus. Under reaction conditions most of the phosphorus in the nickel phosphide was shown to be covered with oxygen but not the nickel sites. [5] The presence of oxygen atoms on the surface of nickel phosphide was shown in the study to facilitate the water-gas shift reaction both directly; by promoting the dissociation of the water and indirectly; by deactivating nickel sites on the surface to provide moderate bonding to the adsorbates causing the barriers for each elementary step in the WGS process become lower. [5]

This study by Rodriguez and colleagues shows that nickel phosphide materials have significant potential to be designed for use in the water-gas shift process as highly active catalysts. This is currently the only published study based on Ni_2P and its application in the water-gas shift reaction therefore it is essential that more be done in discovering and understanding the effectiveness and suitability of the materials for this process.

Metal phosphides can be produced through a number of relatively simple approaches using inexpensive precursors, the most common being reduction of the phosphate precursor under hydrogen gas. One of the major stumbling blocks in the preparation of transition metal phosphides is the low surface area materials due to a high reduction temperatures used to break the P=O bond present in phosphate precursors.^[2-3] Low surface area materials may present problems depending on which catalytic process the metal phosphide is being used. The materials may be ineffective catalytically due to different mechanisms by which the reactants interact with the surface and optimum activity may depend on high surface area materials.^[11] Another problem that is faced, with the material's application in catalytic processes in mind, is the form in which bulk phase transition metal phosphides are produced. In most cases transition metal phosphides are prepared in the form of fine powders with particle sizes lower than 250 microns unless binders are used. The small particle size of the materials means that materials are not suitable for use high pressure reactors such as the steam reforming reactors which water-gas shift processes are carried out.

Poor dispersion and mechanical strength have been overcome in recent studies involving transition metal phosphides by placing active phases onto high surface area supports. The transition metal phosphides are placed on to supports such as SiO₂, Al₂O₃ and carbon to give uniform dispersion of particles and improve mechanical strength. The majority of studies that have developed supported transition metal phosphides have focused on application of the materials for hydrotreating processes.^[11-14] The production of supported transition metal phosphides is relatively straight forward with little difference in the preparation from the bulk phase materials.^[6, 11-14] There have been numerous studies published investigating novel and alternative synthesis routes to producing transition metal phosphides using lower temperatures and alternative precursors.^[3,15-16] The studies published in this area have indicated that the morphology of the transition metal phosphides can be altered in comparison to the conventional synthesis route. This suggests that it is possible to synthesize transition metal phosphides with unusual morphologies using alternative synthesis routes with potential to alter catalytic activity of the materials.^[3] As described in the experimental chapter, the supported

metal phosphides for this project have been produced using incipient wetness technique to impregnate the support. Metal and phosphate ions are dissolved from appropriate precursors to give an aqueous solution of its phosphate. The solution was then added to the support using the incipient wetness technique to impregnate the support which is then calcined and reduced at high temperature to give the appropriate supported metal phosphide.

3.3 Development and characterisation of bulk phase nickel phosphide

Bulk phase nickel phosphide was produced using the synthesis routes described in the experimental chapter. Initially two synthesis routes were investigated to determine which was best suited for catalytic application. A detailed description of the synthesis route for bulk nickel phosphide has been discussed previously in experimental chapter. Nickel phosphate, the precursor to nickel phosphide, was produced using different nickel precursors, these were nickel oxide and nickel nitrate. The XRD patterns for nickel phosphide produced from both the nickel nitrate and nickel oxide precursors are compared in Figure 3-1 along with commercial nickel phosphate (Alfa Aesar 99%) which was reduced to nickel phosphide. The PXRD analysis of the nickel phosphide and nickel phosphate material detailed the composition of the materials. The diffraction patterns for the materials indicate that the materials produced are highly crystalline in nature as is evident from the well-defined diffraction peaks and low base line seen in Figure 3-1.

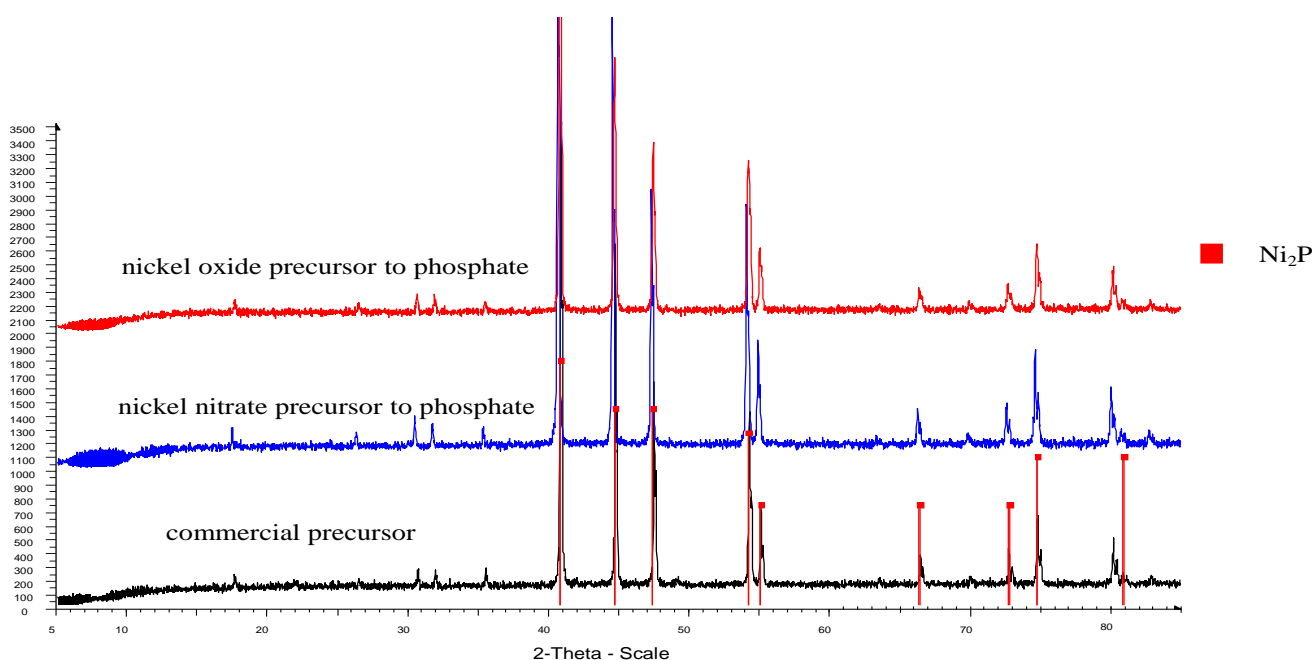


Figure 3-1: XRD patterns showing nickel phosphide produced using alternative precursors.

The diffraction patterns show diffraction peaks associated with the Ni_2P phase. The peaks at $2\theta=40.72^\circ$, 44.61° , 47.36° , and 54.20° are associated with the (111), (201), (210), and (300) planes of the Ni_2P crystal phase. These were cross-referenced with the XRD material database. These diffraction peaks are highlighted in Figure 3-3 with a red line. The diffraction patterns for the materials are also consistent with patterns presented literature.^[1,2] The material is highly crystalline as is evident from the well-defined diffraction peaks exhibited by the materials. Comparison of the diffraction patterns for the alternative precursors suggests that either synthesis approach produced highly crystalline nickel phosphide in the Ni_2P phase. The diffraction pattern for the commercial nickel phosphate precursor also produced highly crystalline Ni_2P .

The temperature programmed reduction was carried out under flowing H_2/N_2 (5% H_2) up to a temperature of $800^\circ C$ with a ramp rate of $10^\circ C/min^{-1}$. The two phosphate precursors produced using the two different precursors showed that both materials displayed similar reduction temperatures, which were similar to those reported in the literature for nickel phosphate reduction. Figures 3-2 and 3-3 show TGA reduction profiles for both the nickel nitrate and nickel oxide precursors under H_2 . Both phosphate precursors exhibit similar reduction profiles with both materials showing weight loss associated with reduction of nickel phosphate to nickel phosphide between $740-780^\circ C$. This temperature range is consistent with the reduction temperatures presented in literature. Prins and Bussell in their review of the transition metal phosphide state nickel phosphate displays a reduction temperature of approximately $750^\circ C$.^[2] The reduction profiles show the nickel oxide precursor has a slightly higher reduction temperature of $770^\circ C$ in comparison to the nickel nitrate precursor. The nickel oxide precursor phosphate also has a small feature at $450^\circ C$; this is consistent with the reduction of nickel oxide, suggesting that some nickel oxide is still present in the phosphate precursor. The presence of nickel metal is not evident in the XRD patterns (shown previously in Figure 3-1) of the reduced nickel phosphide. The TGA profile for the nickel nitrate precursor displays a feature at $100^\circ C$ associated with water loss. This feature is not present in the nickel oxide precursor profile, suggesting the phosphate precursor which was produced using nickel nitrate retains more water than nickel oxide precursor. The theoretical mass loss after reduction of the phosphate to phosphide is estimated to be 74%. The TGA profiles both show weight percentage changes of 86% approximately suggesting that a number of phases may be present in the precursor. This may indicate that the material has not been fully reduced. Further evidence of incomplete reduction is evident in both reduction profiles from the derivative weight plot; this does not drop to zero in either profile suggesting reduction is not complete. The complete reduction at $750^\circ C$ therefore requires an extended duration.

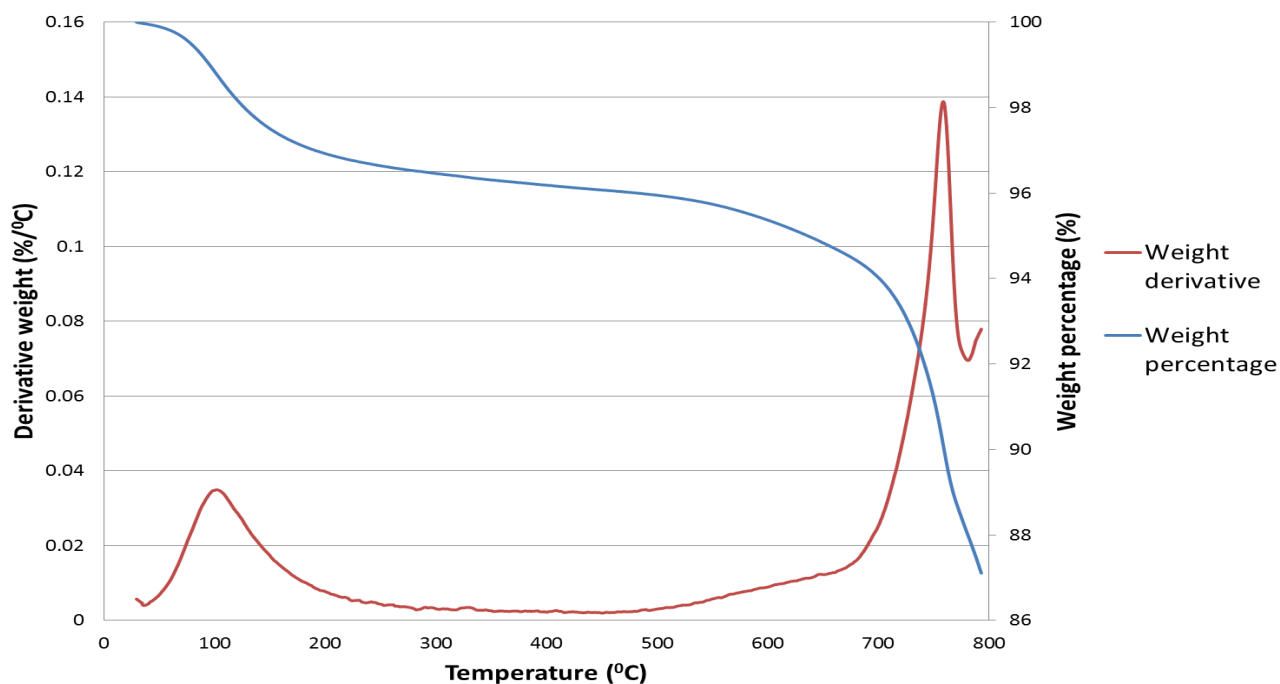


Figure 3-2: TGA reduction profile for nickel phosphate produced using nickel nitrate precursor.

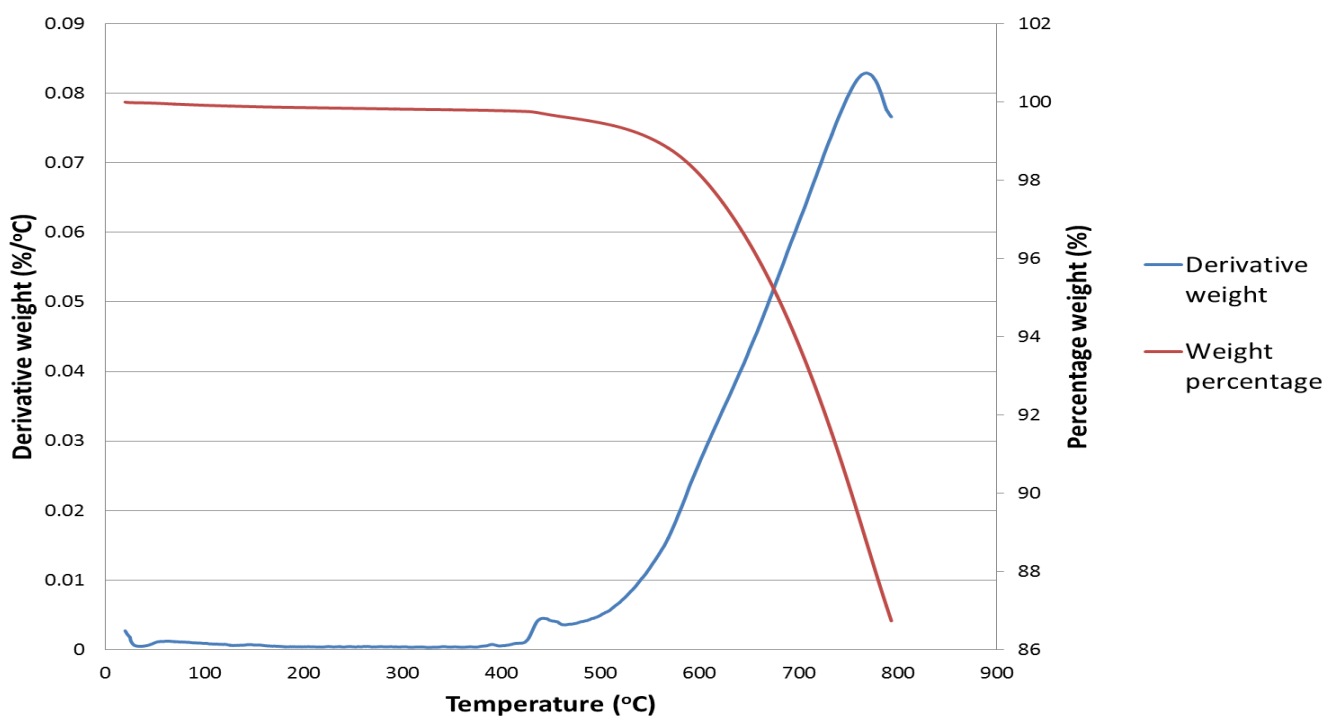


Figure 3-3: TGA reduction profile for nickel phosphate produced using nickel nitrate precursor.

SEM micrographs for bulk phase nickel phosphides are consistent with the similarities between the materials observed in their XRD and TGA profiles, showing the morphology of the Ni_2P produced using alternative precursors to be very similar. SEM micrographs, which show the surface morphology of the materials, also show similarities between nickel phosphide produced using both precursors. Figure 3-4 below compares the micrographs of both materials. One feature evident in both materials is what can be described as different morphologies present in the materials. These are seen as much lighter clusters on the surface of the darker bulk phase and this feature appears to be more prevalent in the nickel phosphide produced using a nickel nitrate precursor. Lighter morphologies seen in the micrograph could possibly be associated with larger electron densities in materials. This may be due more metallic content in these lighter areas. This suggests that there may be a degree of aggregation of metallic particles in the material which is not evident in their XRD patterns.

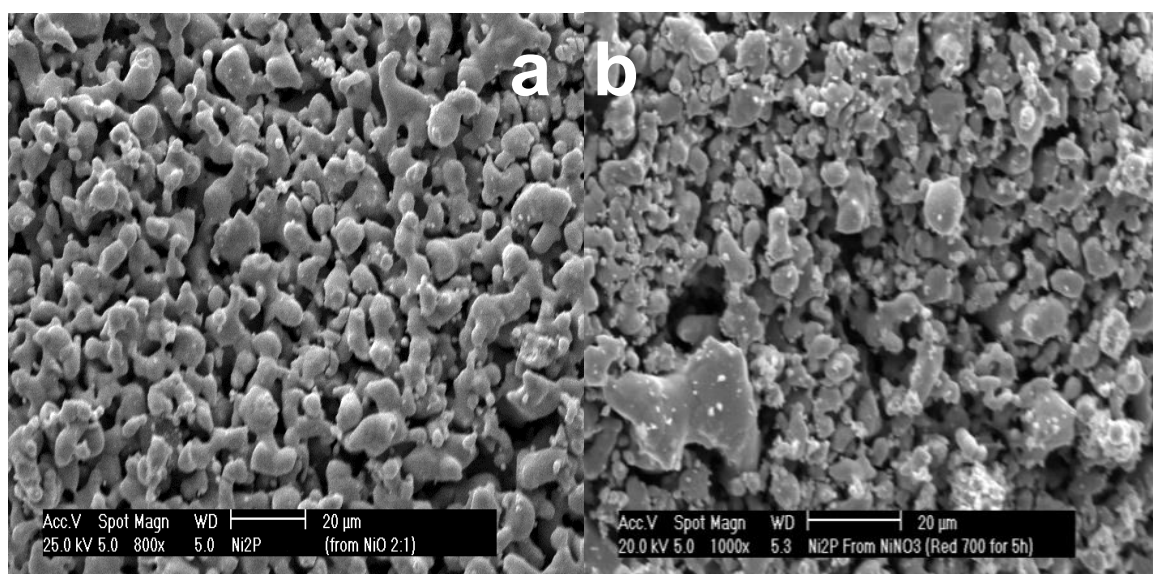


Figure 3-4: SEM micrographs showing the morphology of Ni_2P from both the nickel nitrate (a) and nickel oxide (b) precursor

Nickel phosphide was also shown to remain stable upon prolonged storage under ambient temperature and pressure with no decomposition of the materials or oxidation occurring over extended periods of time. Figure 3-5 shows a single nickel

phosphide batch periodically characterised using XRD analysis over a year after exposure to an ambient environment. Little change is evident in the diffraction patterns shown suggesting that the bulk phase remains stable upon prolonged storage. The nickel phosphide sample was produced using nickel nitrate as precursor to nickel phosphate, the nickel oxide precursor was not tested periodically. It is however assumed that due to the similarity of the materials produced using both approaches that the oxide precursor will also remain stable under prolonged exposure to ambient temperature and pressure.

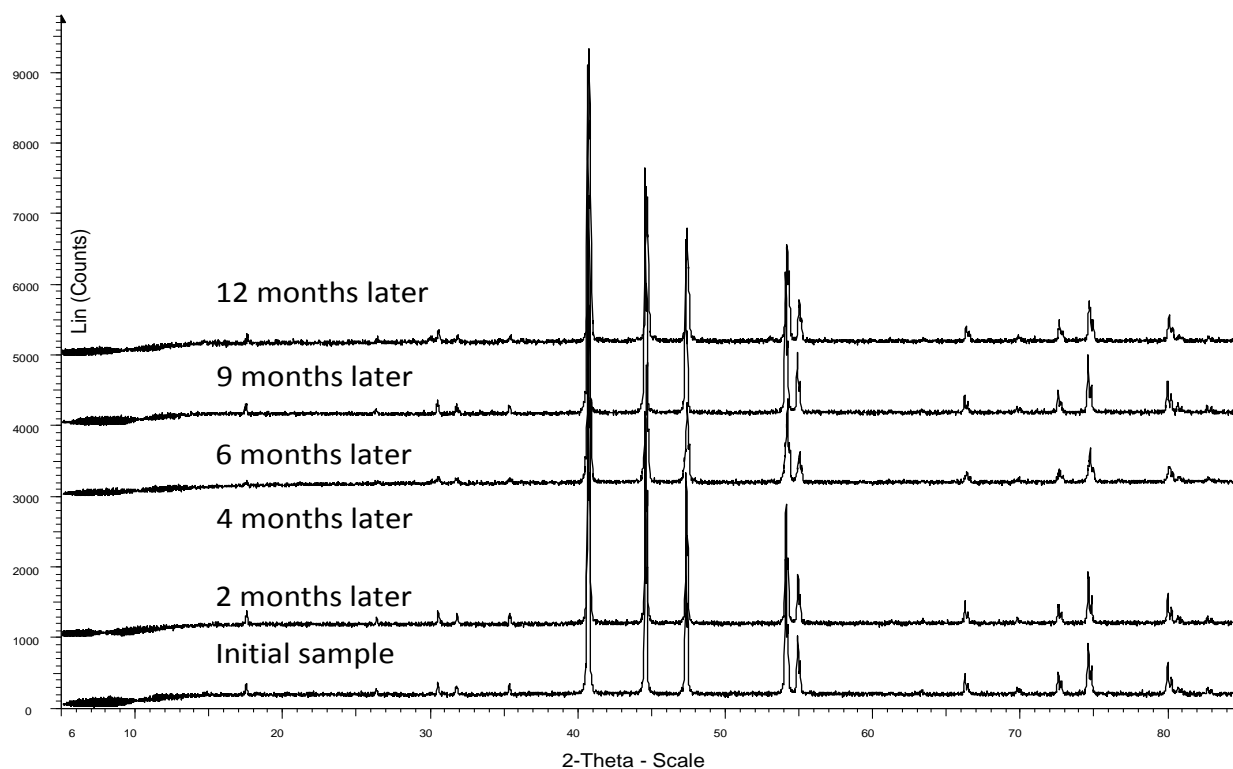


Figure 3-5: Diffraction patterns for a single batch of Ni_2P characterised during a one year period.

A number of nickel phosphide phases have been well documented in literature. Oyama's review of transition metal phosphides describes a whole range of stoichiometries being produced. Many phases of nickel phosphide were produced by altering the stoichiometric ratio of nickel to phosphorus in the reagents used to

produce the phosphate precursor. Figure 3-6 presents the XRD patterns for a number of phases of nickel phosphide that were produced during the project. The diffraction patterns for a number of phases of nickel phosphide differ significantly from one and other. The diffraction patterns for Ni_5P_4 and Ni_5P_2 display some small phase impurities most likely due to the formation of other phases of nickel phosphide within the material.

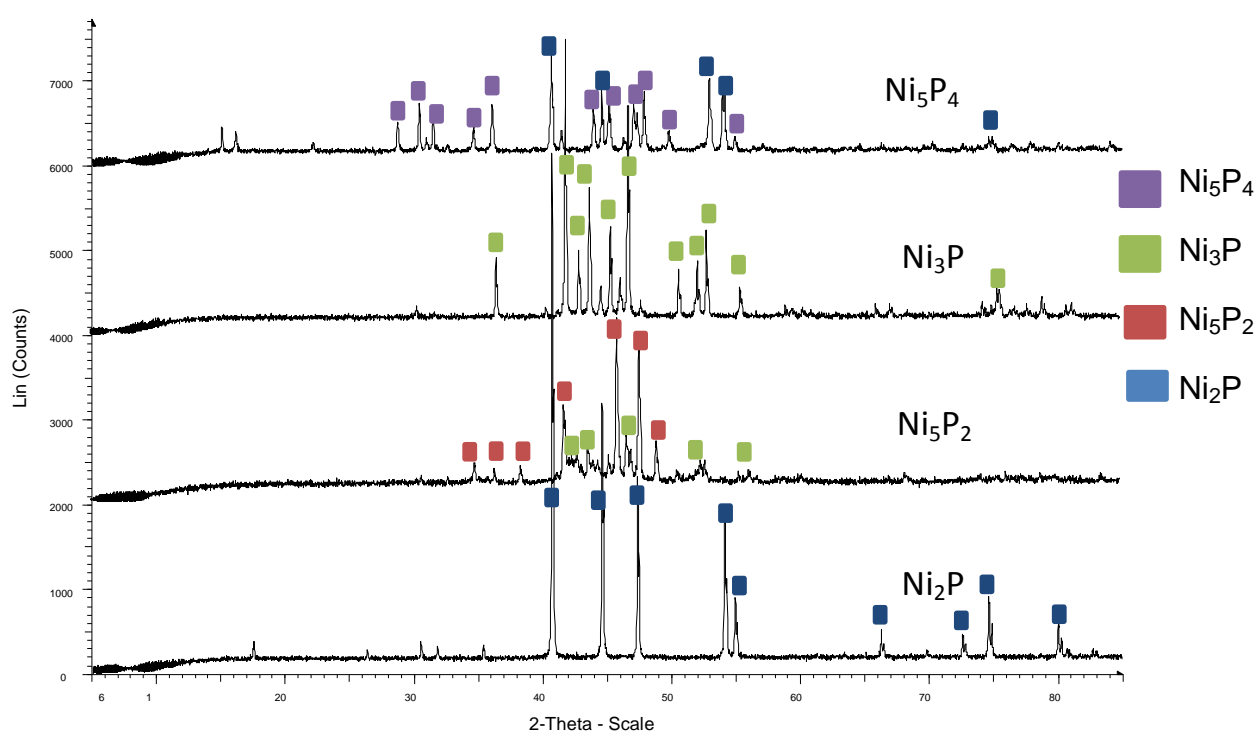


Figure 3-6: X-ray diffraction patterns for different species of nickel phosphide produced.

The diffraction patterns for different species of nickel phosphide have been shown to differ. SEM was used to study surface morphology of the Ni_3P and Ni_5P_4 phases as presented in Figure 3-7. The micrographs for Ni_3P and Ni_5P_4 show that the morphologies of the different species of nickel phosphide are similar to one and other and also to that of Ni_2P (Figure 3-4). The micrographs of nickel phosphide

species also show strong similarity to those of other studies which have been published by Prins and Pfeiffer. In both studies, nickel phosphide was reduced under flowing hydrogen gas at high temperatures, similar to the route undertaken in this project.^[11, 17]

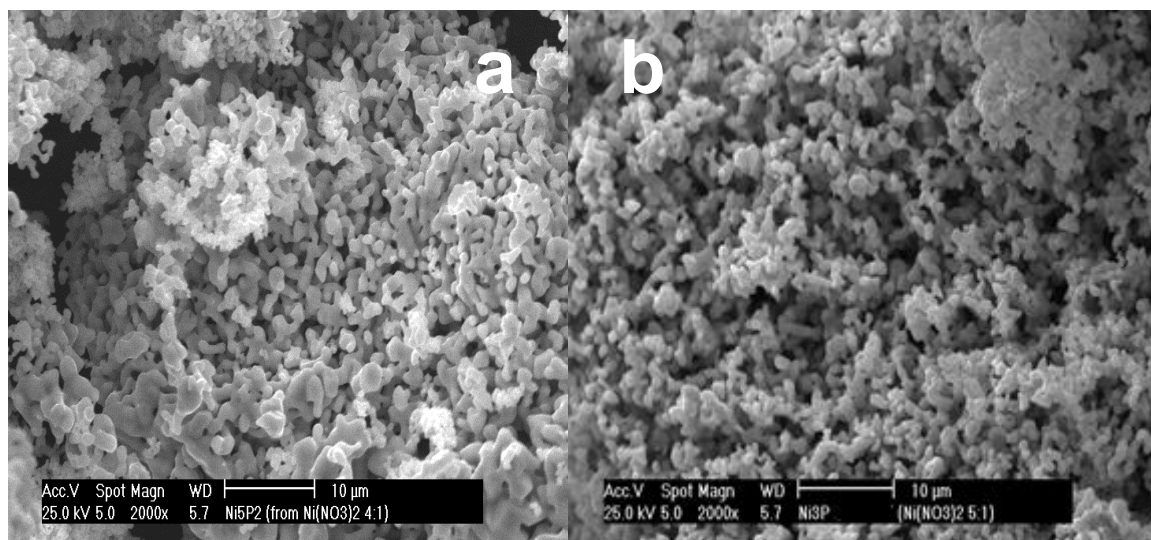


Figure 3-7: SEM micrographs for Ni_5P_2 (a) and Ni_3P (b)

There have been a number of novel approaches to producing transition metal phosphides explored in the last decade due to the promising catalytic activity displayed by the materials.^[16-19] Nickel thiophosphate was investigated as an alternative precursor to nickel phosphate in this project. The presence of sulfur in the precursor may have the potential to have a beneficial effect on the sulfur resistance of the ultimate nickel phosphide produced. Another potential benefit is the lower reduction temperature exhibited by the materials due to the lower reduction temperatures required with $NiPS_3$ in comparison to $Ni_3(PO_4)_2$. The high temperature synthesis of nickel thiophosphate described by Berhault and colleagues was used to produce nickel thiophosphate.^[16] Sulfur content was altered by decreasing the amount of sulfur powder added to the mixture which was annealed. $NiPS_3$ is the preferentially formed phase of nickel thiophosphate formed under the reaction conditions. Nickel thiophosphate was reduced under flowing hydrogen whilst being analysed by *in-situ* XRD at intervals of 100°C between room temperature and 800°C

the results are shown in Figure 3-8. The NiPS_3 species began to reduce at 400°C forming an intermediate phosphide identified as Ni_5P_4 , illustrated by disappearance of the peaks associated with sulfur. Ni_2P was then formed as the temperature of reduction increased to 600°C . A further increase in temperature did not have any further effect on the nickel phosphide with Ni_2P proving to be the final species formed.

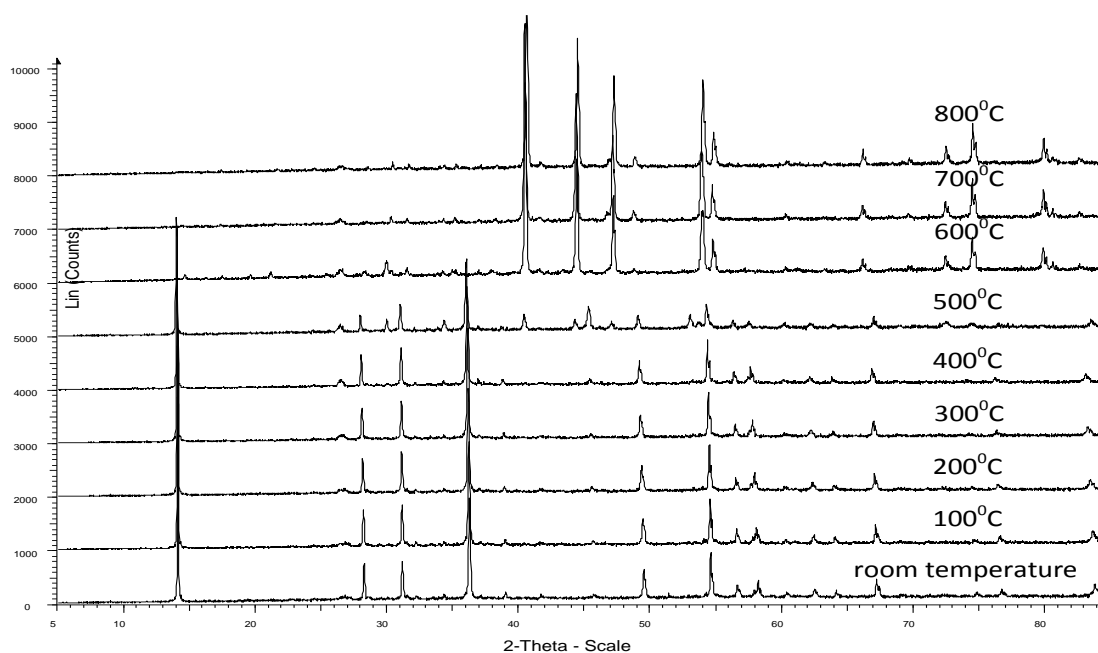


Figure 3-8: In-situ XRD patterns detailing the reduction of NiPS_3 under flowing hydrogen from room temperature to 800°C .

Nickel thiophosphate (NiPS_3) was further characterised using SEM to investigate the morphology of the material. The micrograph for nickel thiophosphate shows that the materials surface differs to the morphology exhibited by Ni_2P , Ni_3P and Ni_5P_2 presented previously as well as the nickel phosphide produced from the thiophosphate precursor. The difference between nickel thiophosphate and nickel phosphide is due to the conditions used in the synthesis of the material. Nickel thiophosphate was produced using high temperature annealing of elemental powders under vacuum for a period of 48 hours. This method of preparation

facilitated the growth of fine crystallites. Once nickel thiophosphate has been reduced to nickel phosphide, the morphology of nickel phosphide resembles that of the nickel phosphide samples produced using alternative precursors. The SEM images of nickel thiophosphate also indicate material is highly crystalline, as was also evident from the XRD patterns for the material. One of the most prominent features present in material are features with different morphologies present in the materials; these are seen as much lighter clusters on the surface of the darker bulk phase, this was also seen in the nickel phosphide materials. Lighter morphologies seen in the micrograph are associated with larger electron densities in materials. This may be due more metallic content in these lighter areas, suggesting that there may be a degree of aggregation of metallic particles in the material.

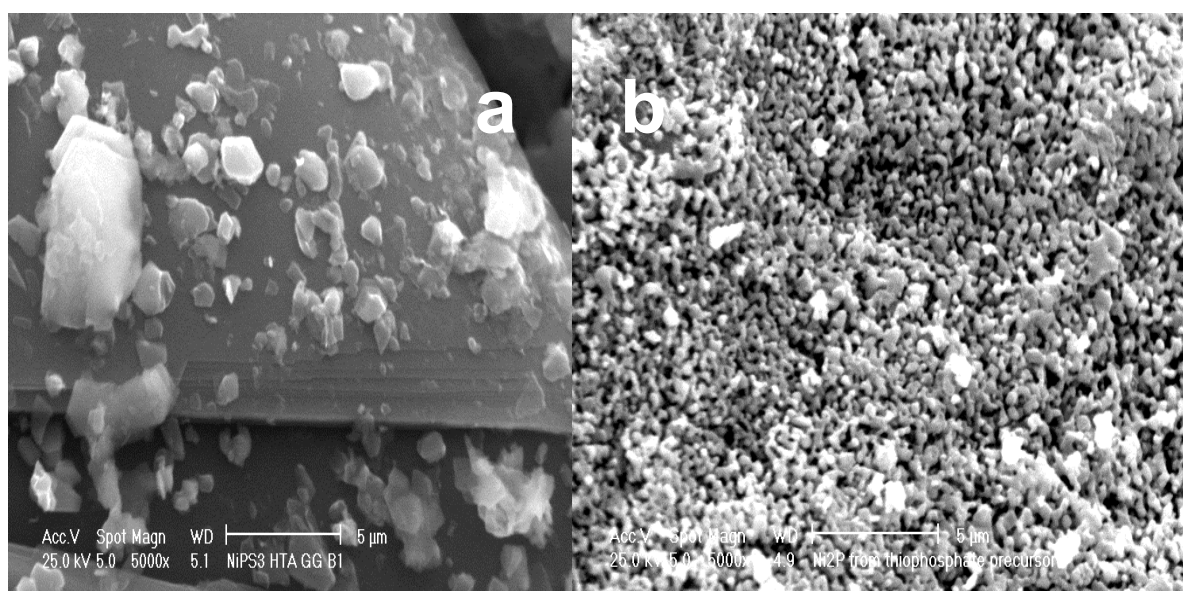


Figure 3-9: SEM images showing surface morphology of NiPS₃ (a) and Ni₂P produced from NiPS₃ (b)

Raman spectroscopic studies were performed on bulk phase nickel phosphide and are presented below in Figure 3-10. The figure shows distinguishable peaks which are associated with stretching modes within the material that are Raman active. The broad peak at 425 cm⁻¹ has been assigned as a nickel-phosphorus bond stretch. The smaller peaks at either side of broad peak at 580 cm⁻¹ and 260 cm⁻¹ are thought to be further nickel-phosphorus bond stretching modes, the spectrum displays peaks

which are similar to those reported in the literature for Ni-P and P=O stretching modes.^[20] The peaks at 820 cm^{-1} , 860 cm^{-1} and 950 cm^{-1} are known to be modes of phosphorus-oxygen bond stretches. There has been very little Raman spectroscopy applied to transition metal phosphides, therefore the assignment of peaks relies only upon a study by Zheng and co-workers and the use of a number of inorganic Raman spectroscopy databases.^[20]

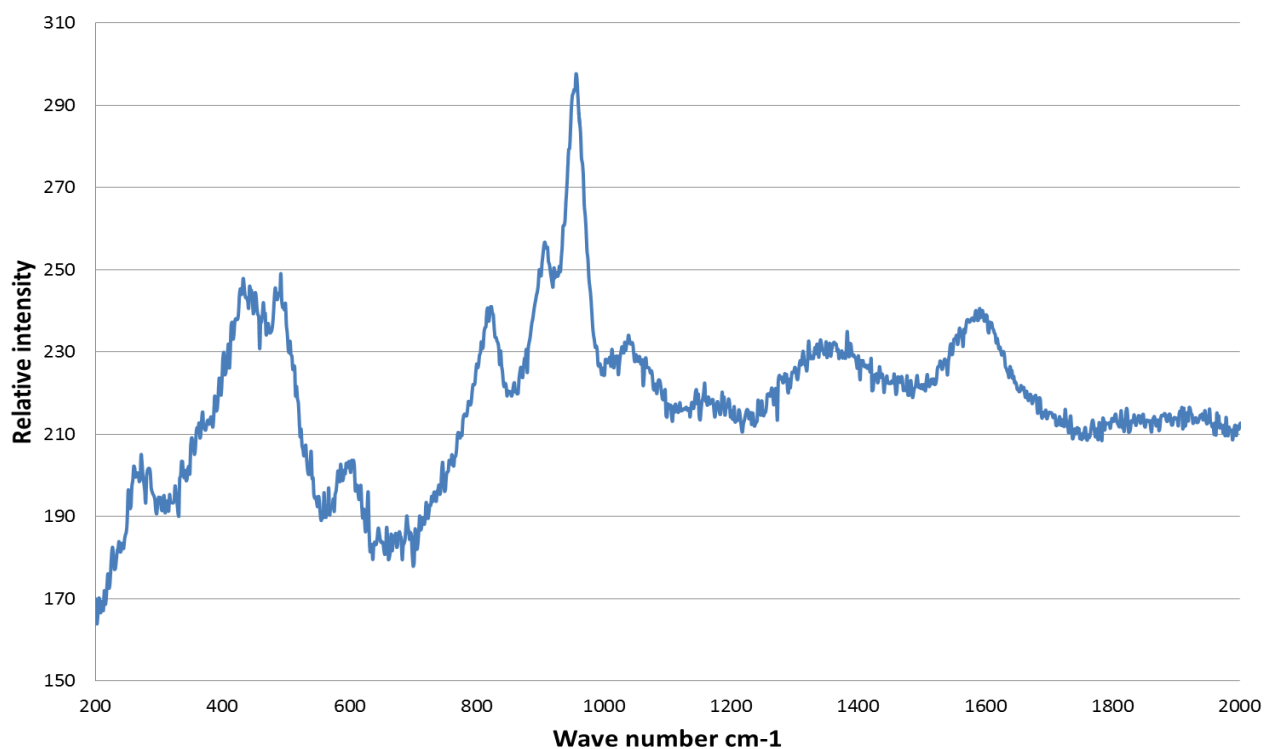


Figure 3-10: Raman spectrum for bulk phase nickel phosphide (Ni₂P)

The stability of nickel phosphide was also tested under temperatures similar to those used in the water-gas shift reaction for both high temperature (400°C) and low temperature (200°C) shift conditions. This was achieved by passing steam over the materials using Ar as a carrier gas in a fixed bed micro-reactor at the aforementioned temperatures. The detailed description of this procedure can be found in the experimental section. The XRD patterns for Ni₂P fresh and steamed samples are shown below in Figure 3-11. The diffraction patterns for steamed and fresh materials

exhibit little if any difference, suggesting bulk Ni_2P to be stable under water-gas shift conditions.

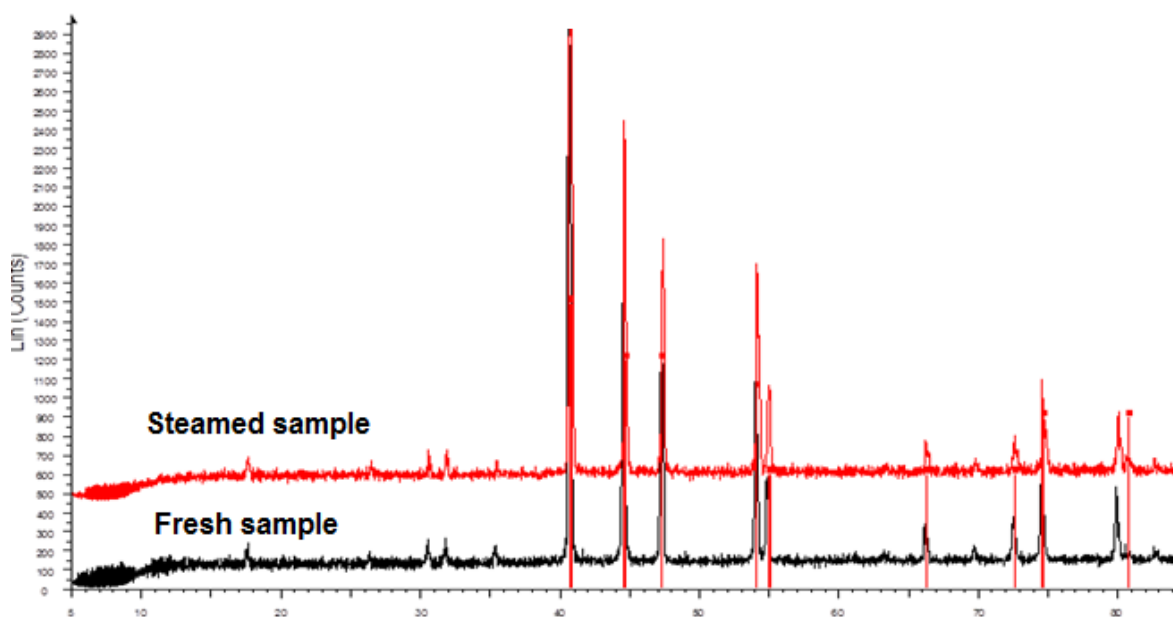


Figure 3-11: Fresh and steam tested bulk Ni_2P sample tested at 400°C

The XPS spectra for Ni_2P (Figures 3-12 and 3-13) also suggest that nickel phosphide shows stability in the near surface region of the material under water-gas shift temperature conditions. Table 3-1 summarises the binding energies displayed for standard and steamed materials along with those values given in the literature. The Nickel 2p spectrum (Figure 3-14) is consistent with previous studies using XPS to characterise Ni_2P . The Oyama group characterised Ni_2P using XPS and described the Ni 2p spectrum as showing peaks at 852.3 eV and 855.1 eV. These features were also visible in the Ni 2p spectrum presented in Figure 3-12. The peak at 852.3 eV has assigned to $\text{Ni}^{\delta+}$ which has a slightly positive charge that is estimated to be $0 < \delta < +2$ oxidation state this is associated with nickel in the phosphide species. ^[21-22] The peak at 855.1 eV has been identified as $\text{Ni}^{\text{II}+}$ species and is associated with nickel phosphate phases due to the passivation of the material after reduction. The

further peaks in the spectra are identified as features of the $2p_{1/2}$ spectrum associated with the $Ni^{\delta+}$ and Ni^{II+} species. [21-22] The greater intensity of the Ni^{II+} indicates a larger portion of the near surface of the material is in the passivated phosphate phase. The spectrum for the steamed sample shows an upward shift in binding energy associated with an increase in oxygen content on the material surface. This is characterised by an increase in binding energy in the $Ni^{\delta+}$ species from 852.3 eV to 853.1 eV and in the Ni^{II+} species 855.1 eV to 856.5 eV. [21-22]

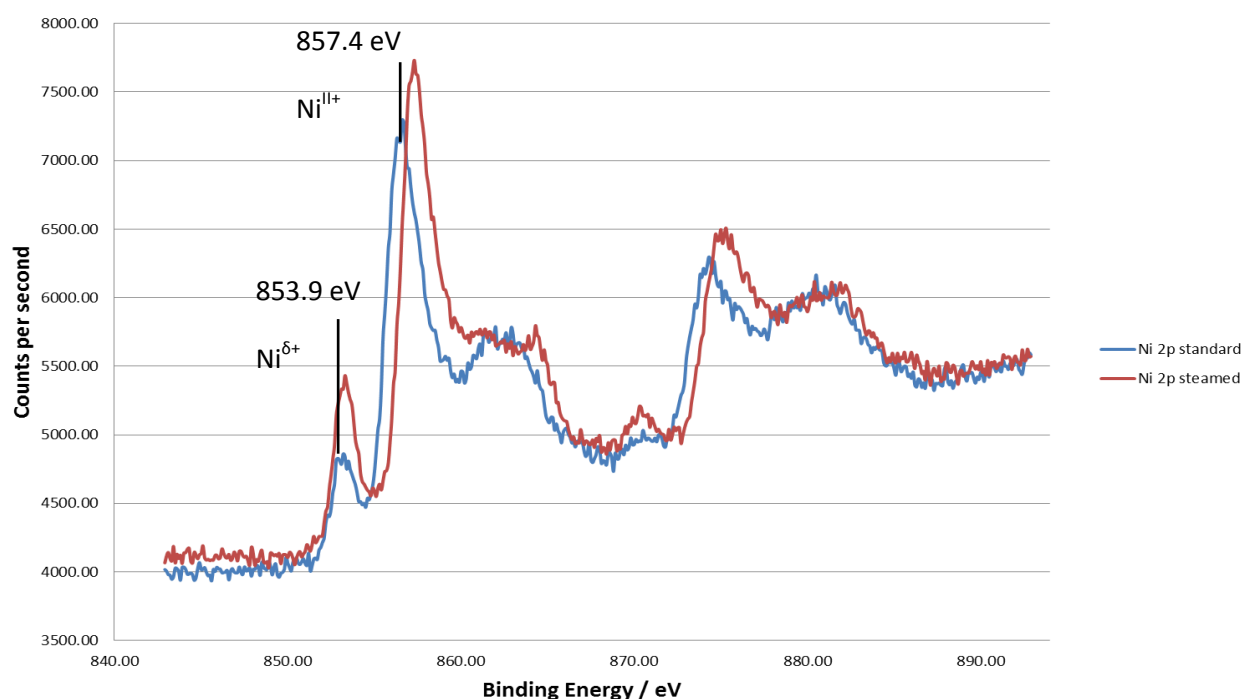


Figure 3-12: Nickel 2p XPS spectra for fresh and steamed samples.

The phosphorus 2p spectrum (Figure 3-13) shows a small peak at 130.6 eV which corresponds to $P^{\delta-}$ having a slightly negative charge counter balancing the nickel in the system where $0 < \delta < -1$ in nickel phosphide phase within the material. The phosphate (P^{V-}) species in literature has been identified at 133.7–134.8 eV. [21-22] Therefore the larger peak seen in the spectrum at 134.1 eV has attributed to an oxygenated species of phosphorus. This possibly corresponds to a passivated phosphate phase at the surface of the material. As was seen in the nickel spectrum,

the greater intensity of the P^{V-} species indicates that a larger amount of the near surface material is the passivated phosphate rather than phosphide which has much lower peak intensity. [21-22] Both the nickel and phosphorus 2p XPS spectra for the post-steamed materials exhibit a slight upward shift in binding energy in comparison to the fresh Ni_2P suggesting that the surface has become oxygenated. The phosphorus spectrum shows P^{V-} species shifts upward to 135.8 eV. The peak intensity is also larger indicating a greater presence of oxygen on the surface of the material. The $P^{\delta-}$ does not shift upward or increase intensity indicating that the phosphate species is associated with increase in surface oxidation.

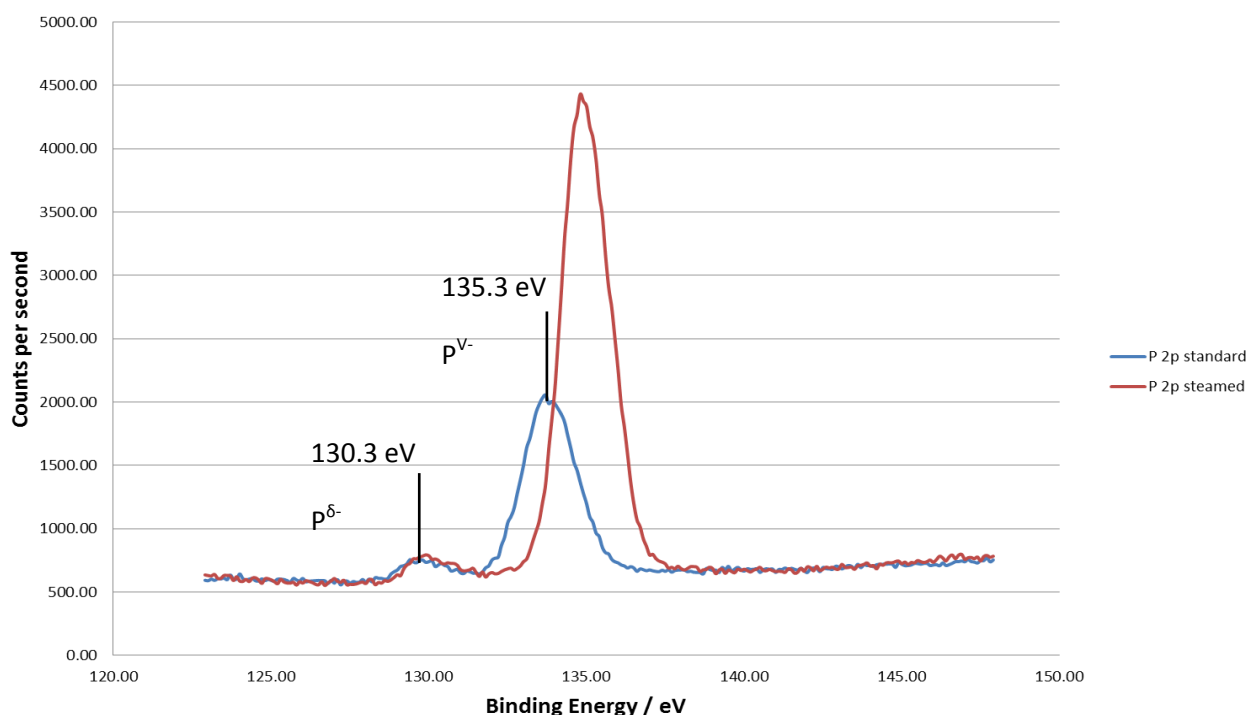


Figure 3-13: Phosphorus 2p XPS spectra for fresh and steamed samples.

The oxidation of the surface of the Ni_2P is to be expected, due to the oxidising nature of steam as well as nickel phosphides strong affinity for oxygen. Oxidation of the material is thought to be limited to the surface as the XRD diffraction patterns of the pre- and post-reaction materials reveal that the Ni_2P phase is consistent and stable over prolonged periods. The increase in binding energy is more pronounced in the

phosphorus 2p spectra. This is due to the affinity of phosphorus for oxygen giving rise to oxy-phosphide surfaces. These oxy-phosphide phases present in Ni₂P have been described by Rodriguez and colleagues.^[5] It was suggested in this study that oxy-phosphide surfaces were due to the conditions which the water-gas reaction operated under. The study by Rodriguez also suggests that the oxy-phosphide surfaces promote the catalytic activity of the nickel phosphide material.^[5] The change in peak intensity observed between the fresh and steamed materials suggest that the surface of the post steaming material displays greater oxygen content. The increase in peak intensity is significant in the phosphorus spectra; this suggests a greater presence of phosphorus at the surface, possibly due to the strong interaction between phosphorus and oxygen.^[5] Bulk phase nickel phosphide in the form Ni₃P and Ni₅P₂ have also been studied using XPS the spectra for these materials can be found in Chapter 7: Appendix. The spectra for Ni₃P and Ni₅P₂ displayed lower binding energies for both Ni 2p and P 2p suggesting that Ni₂P displays a greater degree of surface oxidation. This may be a result of the larger nickel content in Ni₅P₂ and Ni₃P in comparison to Ni₂P.

Sample	Ni ₂ P	Ni ₂ P post steaming	Ni ₂ P (values from literature) ^[21-22]
Element	Binding energy (eV)	Binding energy (eV)	Binding energy (eV)
Ni 2p	853.9 (Ni ^{δ+})	854.3 (Ni ^{δ+})	852.5-853.6(Ni ^{δ+})
	857.4 (Ni ^{II+})	858.5 (Ni ^{II+})	855.5-856.4 (Ni ^{II+})
P 2p	130.2 (P ^{δ-})	130.3 (P ^{δ-})	130.1-131.2(P ^{δ-})
	134.1 (P ^{v-})	135.3 (P ^{v-})	134.5-135.4 (P ^{v-})
O 1s	533.2	533.6	n/a
C 1s	285.0	285.0	285.0

Table 3-1: Summary of binding energy peaks shown in spectra for Ni₂P and those reported in previous studies

SEM analysis of the fresh and steamed nickel phosphide are presented in Figure 3-14. The comparison of the fresh and steamed materials indicates that the material morphology remains stable under high and low temperature water-gas shift reaction temperatures of 200°C and 400°C in the presence of steam. The materials were steamed for 8 hours in the micro-reactor. There are no apparent difference between the fresh nickel phosphide and post-steamed sample with regards to surface morphology of the materials.

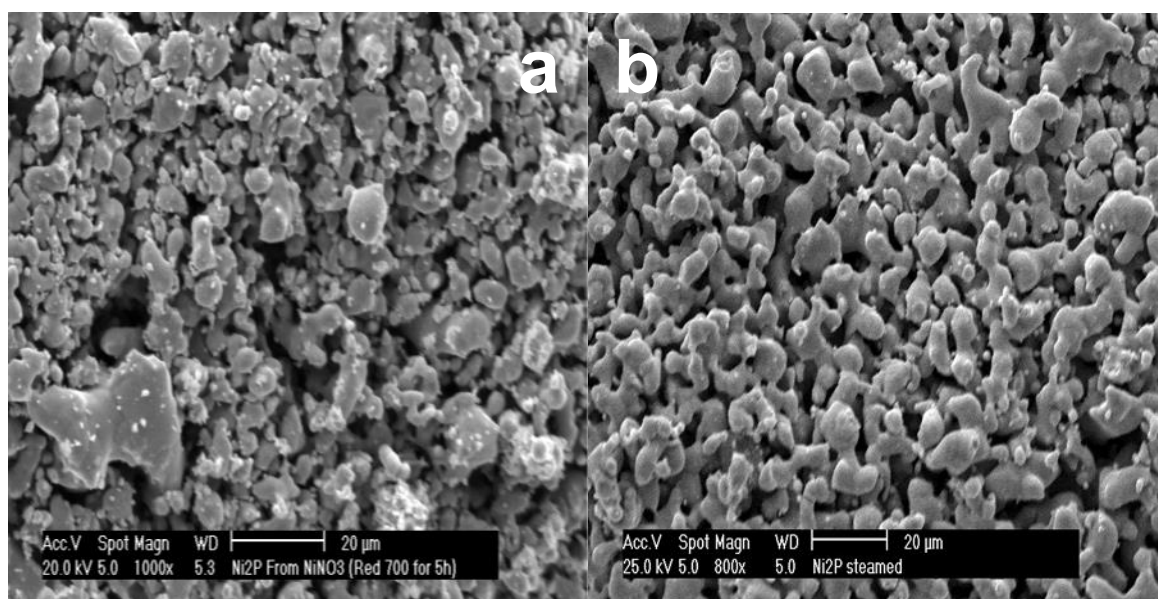


Figure 3-14: SEM micrographs for Ni_2P both fresh and steamed for the nickel oxide precursor (a) fresh and (b) steamed

BET analysis was used to probe the surface area of the nickel phosphide materials. The analysis of the materials showed that nickel phosphide, regardless of stoichiometry, exhibits low surface areas under $1\text{m}^2\text{g}^{-1}$. This is most likely a result of the high reduction temperatures that are used in the reduction of the phosphate. The low surface area displayed in bulk phase nickel phosphide was emphasised when the material was analysed using *in-situ* DRIFTS of carbon monoxide chemisorption on the surface of nickel phosphide (shown in Figure 3-17). Flowing carbon monoxide gas $5\text{ ml}/\text{min}^{-1}$ was passed over the sample in reactor vessel at a range of temperatures between ambient temperature and 400°C. The reactor vessel was immersed within a diffuse reflectance infrared spectrometer. Terminal CO bonding to

the metal site usually occurs at a range of 2070-2090 cm^{-1} and is distinguishable as single defined peak, whilst bridge bonding of CO to the metal site occurs in the range 1800-1950 cm^{-1} . [23] The DRIFTS profile for the bulk phase nickel phosphide indicates that unbound CO is present, characterised by two broad peaks at 2120 cm^{-1} and 2165 cm^{-1} , at every temperature. [23] The lack of any identifiable CO absorption peaks in the profile show that the materials exhibit little if any interaction with the CO which can be attributed to the poor surface area of nickel phosphide produced. There may be some weak terminal bonding of the CO molecules on the surface of nickel phosphide, which may be masked by the presence of unbound CO which is present in the reactor. Flushing the system with argon to remove any unbound CO was carried out whilst at each temperature, however no bound surface bound CO was detected, suggesting only weak, if any, CO-surface interactions occur.

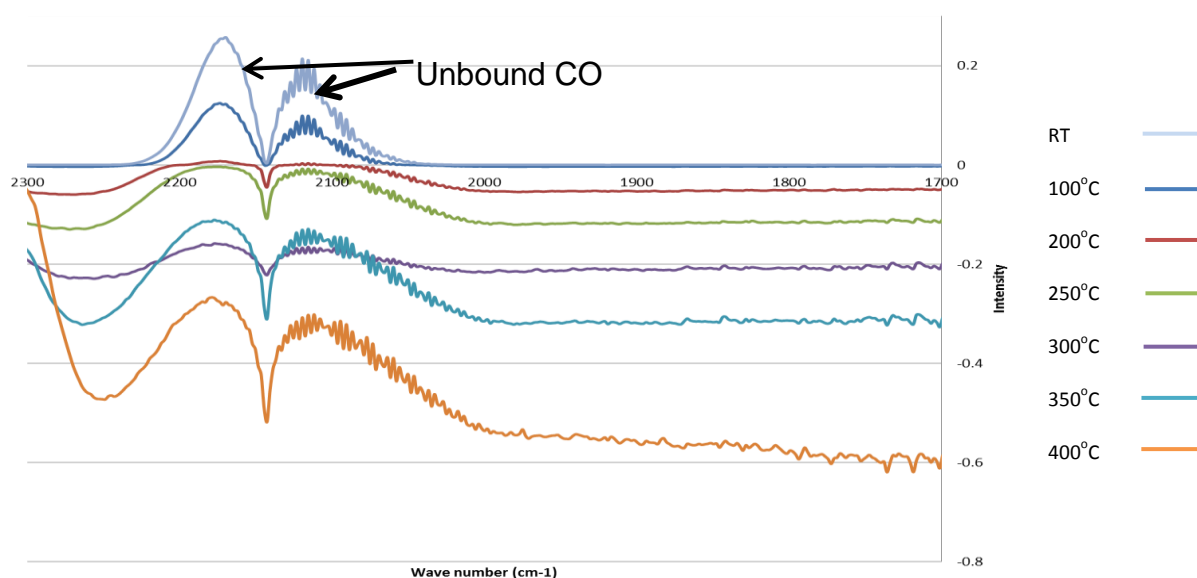


Figure 3-15: DRIFTS profile for CO chemisorption on bulk phase Ni_2P

The low surface area exhibited by nickel phosphide due to the large particle size suggests that the bulk phase nickel phosphide produced may not be suitable for application as a catalyst. Another problem with the use of bulk phase materials was the powdered form they are produced in. These have little mechanical strength and are problematic in high pressure flow reactors. Potential poor activity of bulk phase

nickel phosphide has already been potentially indicated previously in the project. This was highlighted in Figure 3-15; the DRIFTS studies carried out on the material indicated that CO-surface interactions were minimal. The inability of CO to effectively interact with the surface of the material suggests that catalytic activity of the material should be poor, especially if CO is a reactant, as is the case in the water-gas shift reaction. This trend of inactivity was evident when bulk phase nickel phosphide was used in the high pressure steam reactor. Figure 3-16 shows the reaction profile for bulk phase nickel phosphide under low temperature water-gas shift conditions. The reaction profile shows Ni₂P displays no catalytic activity under the reaction conditions and system blockage occurred due to the lack of mechanical strength in the powdered bulk nickel phosphide meaning the material was tightly packed blocking flow of the reactants. The result was the reactor shut down after 60 hours. The carbon balance for the reaction was calculated to be 91%. The reaction profile displays a drop in CO concentration after 45 hours of time on stream; this is due to the knockout pot for water being emptied and causing reactor pressure to drop. The result of the low temperature water-gas shift reaction testing contradicts the study by Rodriguez and colleagues who reported single crystals of nickel phosphide displayed good catalytic activity under low temperature water-gas shift reaction conditions. The Rodriguez study used reaction temperatures in between 250°C and 300°C. These operating conditions were significantly higher than was used for the low temperature water-gas shift reaction in this study and therefore may be the reason the activity of the materials differ. ^[5] It is also possible that preparation of nickel phosphide differed between the two studies. The reduction temperature can have a profound effect on both surface area and phosphorus content in transition metal phosphide. The alteration of these properties can significantly affect the catalytic activity of the material. This however, was not a problem with supported transition metal phosphides as is shown later in this chapter.

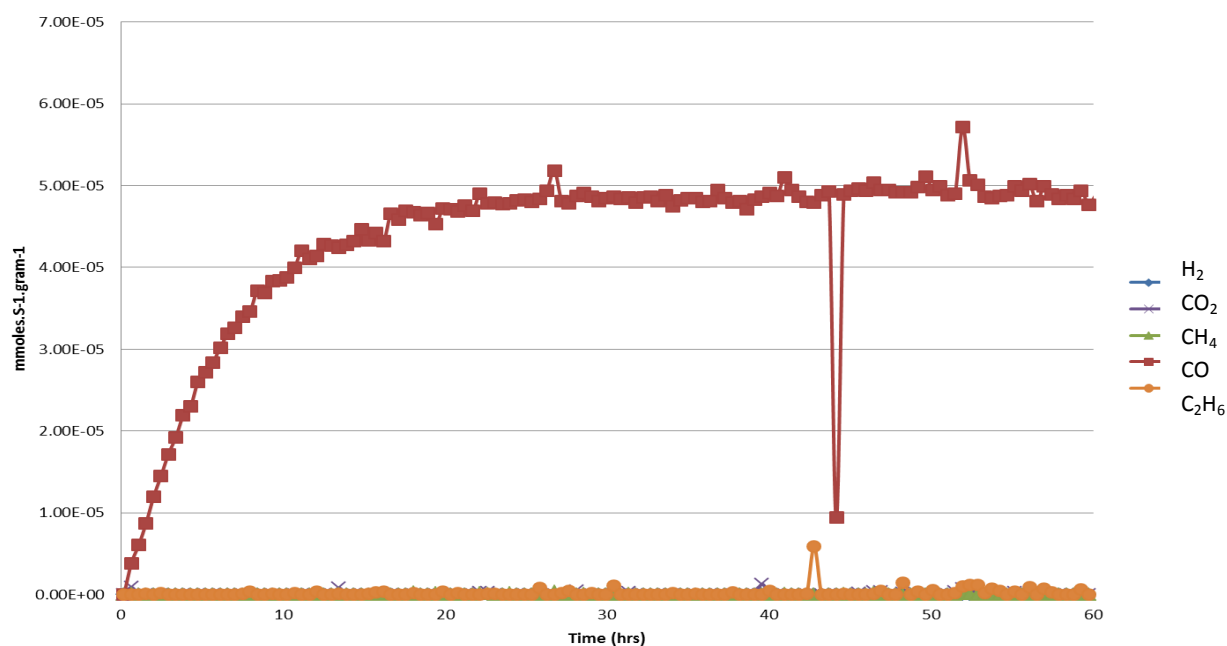


Figure 3-16: Ni_2P bulk reaction profile for low temperature water-gas shift reaction.

3.4 Preparation and characterisation of silica supported nickel phosphide

Bulk phase nickel phosphide has been shown to be unsuitable for application in water-gas shift reaction. This was due to a number of reasons, specifically poor mechanical strength and poor catalytic activity displayed by the materials which is thought to be a result large particle size and low surface areas exhibited by the materials. A large number of studies have identified Ni_2P as the most catalytically active nickel phosphide species. Therefore Ni_2P was the target phase of phosphide to be impregnated onto a high surface area support. Supporting the active phase gave better dispersion of the particles and also gave mechanical strength and robustness to the catalyst to improve the catalyst's performance in the water-gas shift reactions to which it is applied. Silica was selected as the support over alumina in order to avoid strong interactions between the alumina and phosphorus, and thus resulting in aluminium phosphate. The formation of this phase would alter the active phase which could cause the catalytic activity of the catalyst to be adversely

affected, and is something which has been highlighted a number of times in recent studies.^[6-9]

The experimental procedure for this preparation was similar to that applied for bulk phase nickel phosphide. Nickel nitrate hexahydrate and diammonium hydrogen phosphate were the salts used to form the nickel phosphate precursor when producing nickel phosphide. These were impregnated onto the silica using the incipient wetness technique. The resultant nickel phosphate on the silica support was reduced under flowing hydrogen at high temperatures to produce silica supported nickel phosphide.

The resultant silica supported nickel phosphide catalyst was analysed using powder X-ray diffraction. The diffraction pattern for the catalyst is presented below in Figure 3-19 along with bulk nickel phosphide (Ni_2P) and silica. Characterisation of bulk phase nickel phosphide has shown the material is highly crystalline in nature which is evident from sharp well defined diffraction peaks and light base line. The peaks at $2\theta=40.72^\circ$, 44.61° , 47.36° , and 54.20° associated with (111), (201), (210), and (300) planes.^[1] Silica is amorphous which is evident from the diffraction pattern seen in Figure 3-17. There are no distinguishable diffraction reflections, this being is synonymous with materials with X-ray amorphous nature. Nickel phosphide on silica support shows similar diffraction peaks to those seen in bulk phase nickel phosphide. These reflections match those associated with the crystal structure of Ni_2P .

The diffraction pattern for $\text{Ni}_2\text{P}/\text{SiO}_2$ appears broad and less intense due to the smaller amounts of nickel phosphide being present on the support and better dispersion of this particles; this means that many of smaller reflections that can be seen in bulk phase nickel phosphide associated with Ni_2P crystal phase are not visible in the silica supported material. The diffraction pattern for silica supported nickel phosphide suggests that Ni_2P has been successfully impregnated onto the silica support. The broadened peaks associated with Ni_2P for the diffraction pattern

for on the silica supported materials suggests a decrease in the size of the Ni_2P particles. The average particle size of nickel phosphide on the support was calculated using the Scherrer equation assuming that reflections have solely arisen from coherent diffraction domain size effects, and accordingly was estimated to be 25.2 nm. This indicates that the catalyst displays good dispersion of active phase, which was one of the main reasons for the use of a support.

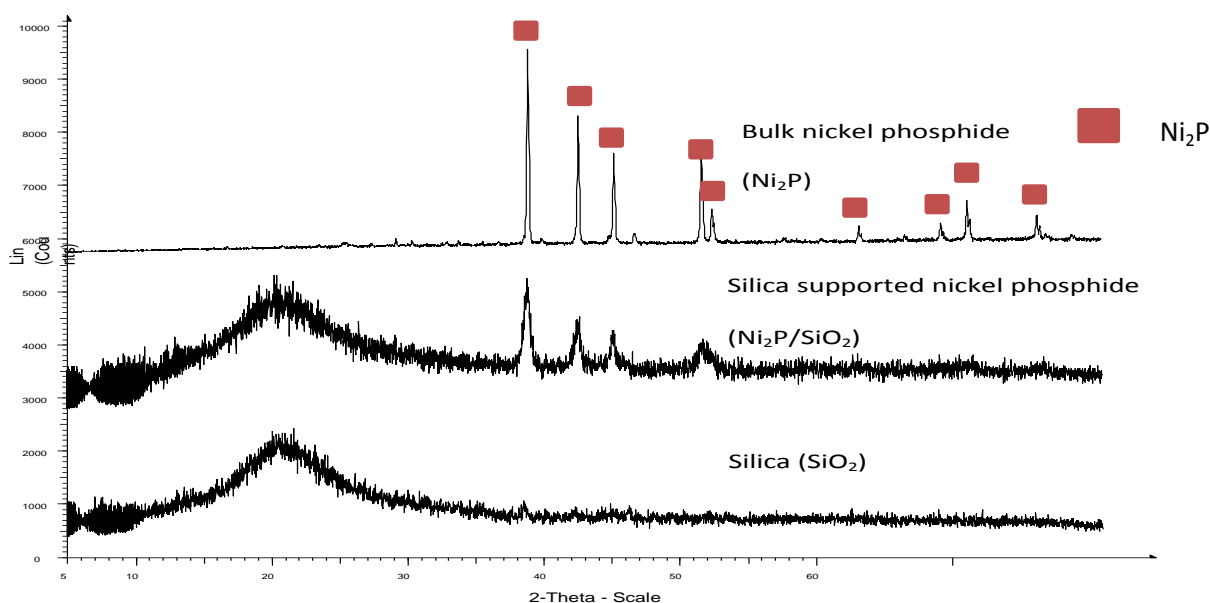


Figure 3-17: Comparison of XRD patterns for $\text{Ni}_2\text{P}/\text{SiO}_2$, SiO_2 and Ni_2P .

Figure 3-18 shows the thermogravimetric reduction profile for nickel phosphate on a Q10 silica support. The ramp rate was $10^\circ\text{C}/\text{min}^{-1}$ and the reduction was carried out under flowing H_2/N_2 (5% H_2). Nickel phosphate was reduced to nickel phosphide at 750°C , as was evident from peak in weight derivative combined with the loss of weight in the sample at this temperature. These phenomena are attributed to the loss of oxygen from material as it is reduced to nickel phosphide. The TGA profile for the supported nickel phosphide reduction indicates that silica supported nickel phosphate displays a reduction temperature that is consistent with the bulk phase nickel phosphate TGA reduction profile presented previously in Figures 3-2 and 3-3. The reduction temperature of 750°C for silica supported nickel phosphide has also

been widely documented in previous studies by other groups. [1-4, 6, 21-22] The reduction profile in Figure 3-18 also shows a broad weight derivative peak at 450°C which is associated with NiO reduction suggesting that the precursor has mixed phases of nickel species present in the material with another feature visible at 700°C. The presence of these mixed phases in the precursor may indicate a nickel metal phase present in the catalyst. The weight loss associated with reduction is seen to be 89 % in the profile; this is greater than the theoretical loss which was calculated to be 88% based on a 20% Ni loading. The difference may be attributed to the mixed phases of nickel oxide and nickel phosphate present on the support, or simply due to experimental error. This is however not evident from XPS and EXAFS analysis of the material presented later in the Chapter as well as the diffraction pattern for the material (Figure 3-17) where only diffraction peaks associated with Ni₂P and none that are associated with nickel metal are evident. Another possibility is that upon reduction, nickel oxide is converted to nickel phosphide due to the presence of excess phosphate on the support. This has been proposed by Oyama as the main route of formation of nickel phosphide on supports when the support is impregnated using the method applied in this project.

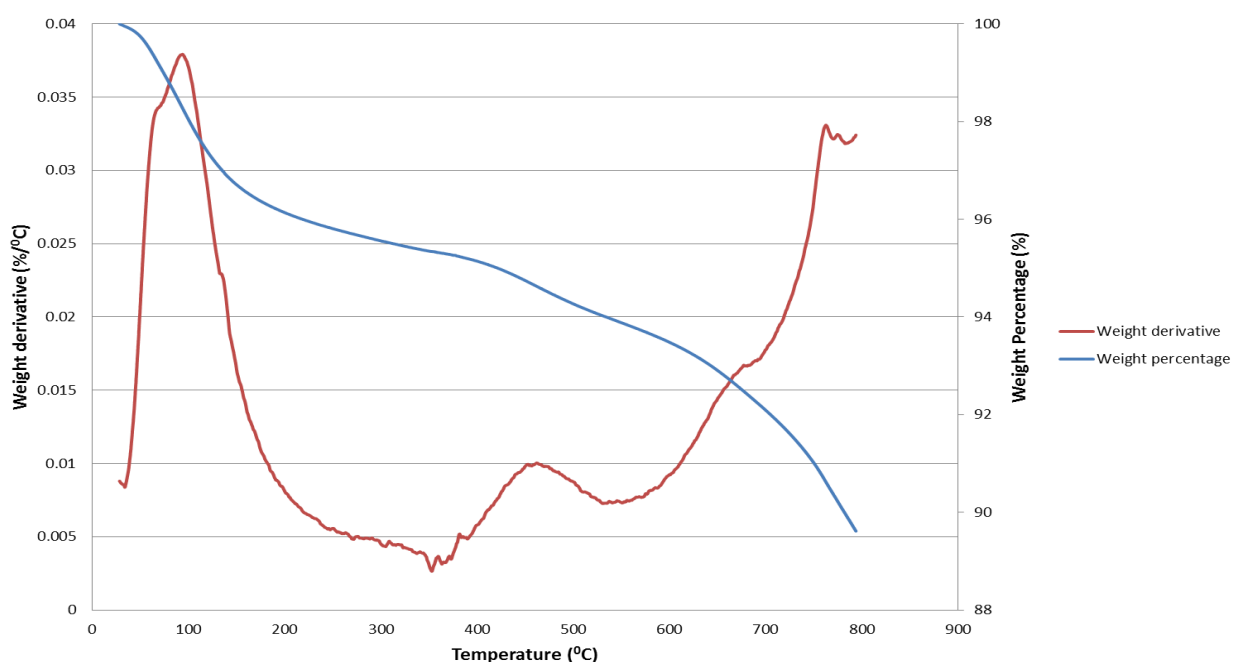


Figure 3-18: TGA reduction profile for silica supported nickel phosphide from nitrate

SEM analysis of $\text{Ni}_2\text{P}/\text{SiO}_2$ is presented in Figure 3-19 and Table 3-2. SEM and EDX analysis was carried out at a number of points on the sample to help confirm consistency of the sample. Figure 3-19, The SEM image shows small particles that are light in appearance these were assumed to be $\text{Ni}_2\text{P}/\text{SiO}_2$. EDX analysis of the particles confirms that the particles have nickel and phosphorus present in them indicating that Ni and P are present on the silica support. EDX analysis was carried out at seven different sites to determine consistency. The average atomic percentages for both nickel and phosphorus were calculated along with statistical range. The results of the EDX analysis of the particle labelled “spectrum 4” in Figure 3-19 and are summarised in Table 3-2. The results confirm the presence of both nickel and phosphorus in the particle in an atomic Ni:P ratio that is approximately 2:1. This supports further supports the XRD and TGA results presented previously in confirming that the catalyst produced is $\text{Ni}_2\text{P}/\text{SiO}_2$.

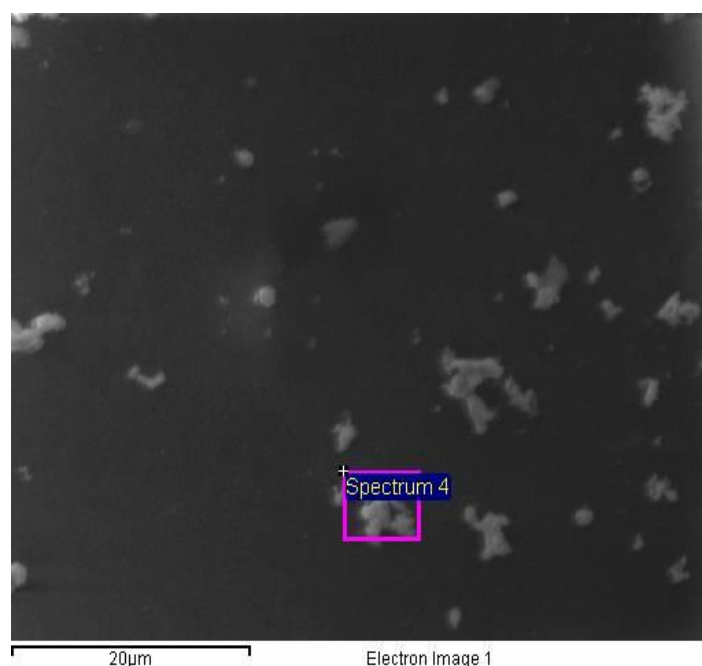


Figure 3-19: SEM micrograph showing silica supported Ni and P

Element (edge)	Weight%	Atomic%	Average atomic %
P (K)	23.63	36.97	39.16 (± 3)
Ni (K)	76.37	63.03	60.66 (± 7)
Total	100.00	100	

Table 3-2: Table of results for $\text{Ni}_2\text{P}/\text{SiO}_2$ elemental analysis carried out by EDX

Silica supported nickel phosphide was analysed using Raman spectroscopy. Figure 3-20 displays the resultant Raman spectrum for $\text{Ni}_2\text{P}/\text{SiO}_2$. This is compared alongside the bulk phase Ni_2P counterpart spectrum. The spectrum shows a number of broad peaks, with the largest of these centred at 950 cm^{-1} . These peaks are identified as a P=O stretch modes indicating the presence of oxygen in the nickel phosphide particles. This most likely attributed to the passivation of the material.^[20] The presence of the P=O peak was synonymous with the bulk phase Ni_2P sample that was run previously. There is also weak peak at 450 cm^{-1} , in the bulk phase material this is also present and was identified as Ni-P bond stretching. The supported nickel phosphide spectrum is weaker in comparison to the bulk phase material; this is highlighted by broadening of peaks and weaker intensity of peaks. The weaker Raman spectrum exhibited by $\text{Ni}_2\text{P}/\text{SiO}_2$ is a result of lower content of nickel phosphide being present in the sample, which is expected when comparing bulk phase materials to supported materials. The Raman spectrum for the supported nickel phosphide catalyst closely resembles that of the bulk phase material. This further supports previous characterisation of the nickel phosphide catalyst in suggesting that nickel phosphide is present on the silica support. The Q10 silica support without any active phase present was not studied using Raman spectroscopy. There are a number of Si-O stretching modes which occur between 400 and 500 cm^{-1} according to literature with many more modes occurring at higher frequencies above 1000 cm^{-1} . These stretching modes are not visible in the $\text{Ni}_2\text{P}/\text{SiO}_2$ spectrum.^[23]

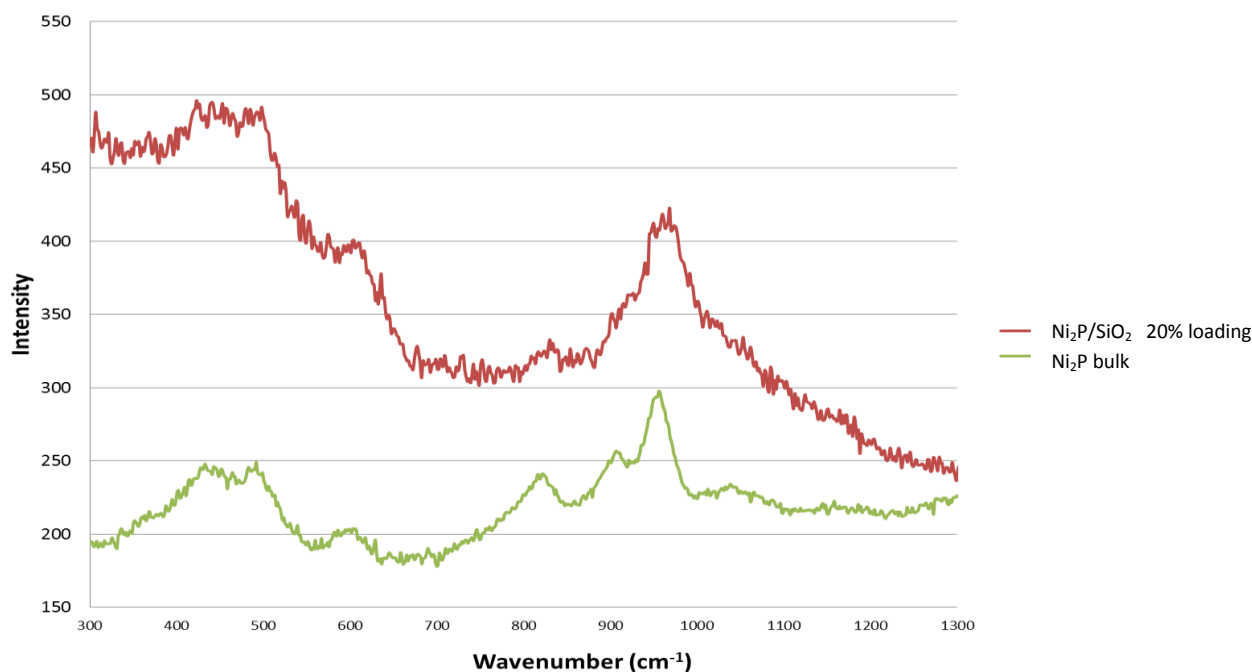


Figure 3-20: Raman spectrum for $\text{Ni}_2\text{P}/\text{SiO}_2$ compared alongside bulk phase Ni_2P spectrum

The XPS spectra for $\text{Ni}_2\text{P}/\text{SiO}_2$ were compared and contrasted to those of bulk phase Ni_2P . The resultant spectra for nickel 2p and phosphorus 2p are presented in Figures 3-21 and 3-22 respectively, along with a summary of the binding energies associated with the materials shown in Table 3-3. The nickel 2p spectrum, shown in Figure 3-21, reveals that in comparison to bulk phase Ni_2P , the silica supported nickel phosphide catalyst displays a lower binding energy and the spectra appears less intense. Bulk phase Ni_2P exhibits binding energy peaks at 853.9 and 857.4 eV associated with $\text{Ni}^{\delta+}$ and Ni^{2+} respectively, whereas the spectrum for $\text{Ni}_2\text{P}/\text{SiO}_2$ displays a broad peak at 853.5 eV and weak peak at 856.8 eV. Features of the $2p_{1/2}$ spectrum associated with $\text{Ni}^{\delta+}$ are also evident at 872.1 eV. These are weak due to lower Ni content in the supported material. The results for the supported material in terms of bonding energy peaks are similar to those reported by Bussell and colleagues in their study published in 2005 which used XPS to characterise silica supported nickel phosphide catalysts for application in HDS processes. ^[21-22] The peak at 853.5 eV in the Ni 2p spectrum for $\text{Ni}_2\text{P}/\text{SiO}_2$ has been identified as $\text{Ni}^{\delta+}$ where $0 < \delta < 2$ and is associated with nickel being bonded with phosphorus in the Ni_2P species. ^[21-23] This peak is higher than the corresponding peak in the bulk

phase material. The bulk material displays a binding energy peak at 857.4 eV associated with nickel phosphate (Ni^{2+}), which is shifted lower in the supported material, to 856.8 eV. It suggests that Ni^{2+} species in the supported material are less oxidised in comparison to the bulk material. The ratio of the binding energy peaks associated with the nickel species have changed indicating the $\text{Ni}^{\delta+}$ species associated with Ni_2P is more prevalent in the supported material. The spectra for $\text{Ni}_2\text{P}/\text{SiO}_2$ are weak in terms of intensity in comparison to bulk phase nickel phosphide spectra; this is especially prevalent in the spectrum for phosphorus 2p seen in Figure 3-22. This is likely due to the much lower nickel phosphide content in the supported material. The lower amount of active phase being sampled also indicates higher dispersion in comparison the bulk phase materials.

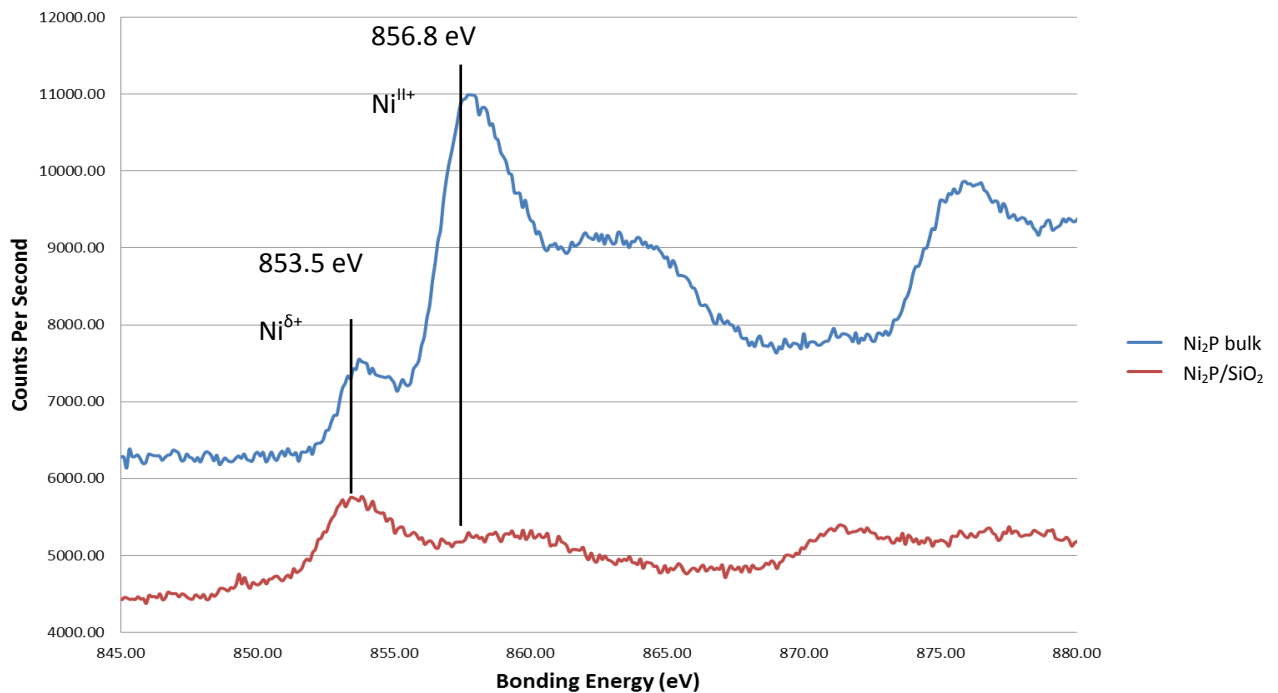


Figure 3-21: XPS spectra for Ni 2p for $\text{Ni}_2\text{P}/\text{SiO}_2$ and bulk Ni_2P

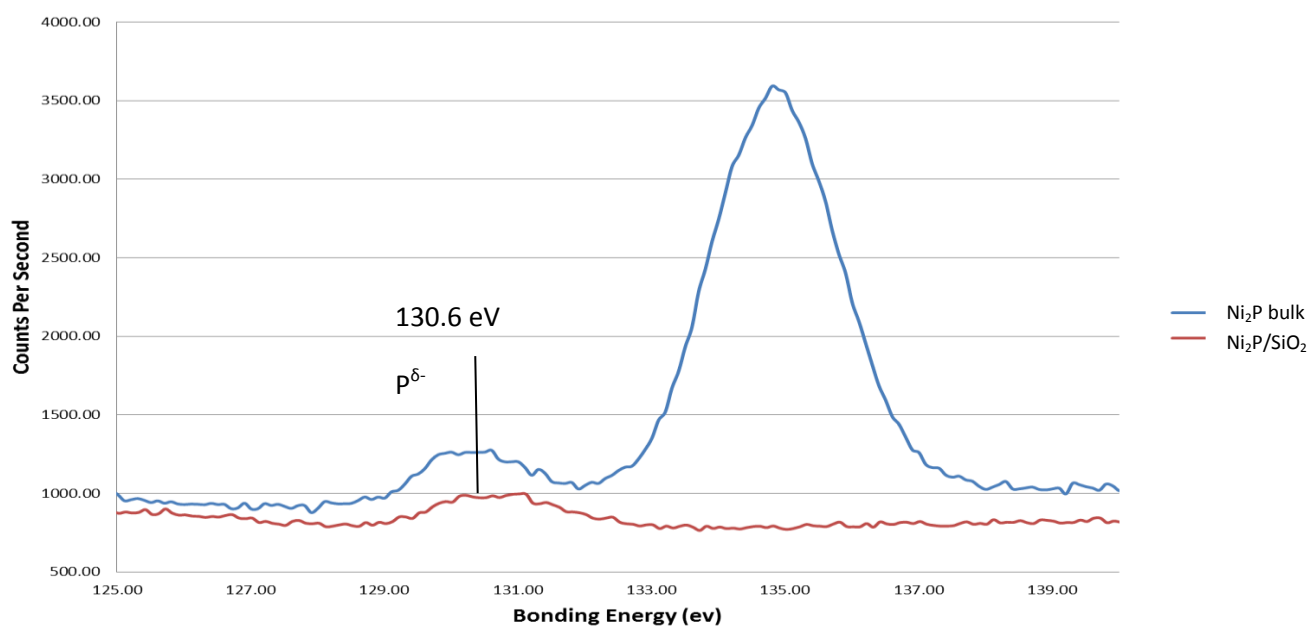


Figure 3-22: XPS spectra for P 2p for $\text{Ni}_2\text{P}/\text{SiO}_2$ and bulk Ni_2P

Sample	Ni_2P bulk phase	$\text{Ni}_2\text{P}/\text{SiO}_2$	Ni_2P (values from literature) ^[21-22]
Element	Binding energy (eV)	Binding energy (eV)	Binding energy (eV)
Ni 2p	853.9 ($\text{Ni}^{\delta+}$)	853.5 ($\text{Ni}^{\delta+}$)	852.5-853.6 ($\text{Ni}^{\delta+}$)
	857.4 (Ni^{II+})	856.8 (Ni^{II+})	855.5-856.4 (Ni^{II+})
P 2p	130.3 ($\text{P}^{\delta-}$)	130.6 ($\text{P}^{\delta-}$)	130.1-131.2 ($\text{P}^{\delta-}$)
	134.1 ($\text{P}^{\nu-}$)		134.5-135.4 ($\text{P}^{\nu-}$)
O 1s	533.2	532.8	n/a
C 1s	285.0	285.0	285.0

Table 3-3: Summary of binding energy peaks shown in spectra for bulk and silica supported Ni_2P .

A similar trend was seen in the phosphorus XPS spectrum for $\text{Ni}_2\text{P}/\text{SiO}_2$ as was noted with nickel, with a noticeably lower bonding energy in comparison to bulk phase Ni_2P . The peak for $\text{Ni}_2\text{P}/\text{SiO}_2$ has been identified at 130.6 eV in comparison to the bulk phase which was recorded as 130.3 eV for bonding energy in 2p spectrum. The upward shift in binding energy seen in the P^{5-} peak for the supported material is small and still remains within the reported values for nickel phosphide. [21-22] The upward shift is a likely consequence of final state effects due to a decrease in particle size associated with improved dispersion of the active phase on the support in comparison to the bulk phase material. The higher binding energy peak at 134.1 eV seen in the bulk phase Ni_2P is attributed to the presence of phosphate phases (P^{V}) of the material; this is not present in supported material indicating that passivated phases are not as prevalent. The lack of phosphate phases may indicate higher catalytic activity than the bulk phase material which was shown to catalytically inactive.

To greater understand the characteristics of the material and the physical state in which the active phase resides in, nickel phosphide was studied using X-ray absorption spectroscopy. This was focused primarily on the extended X-ray absorption fine structure (EXAFS) spectrum of the material. Figure 3-23 displays the k^3 weighted EXAFS spectrum for $\text{Ni}_2\text{P}/\text{SiO}_2$ and Figure 3-24 illustrates the Fourier transform spectrum for the material. Both spectra have been refined and a theoretical curve has been applied through collaboration with Prof G. Sankar from University College London.

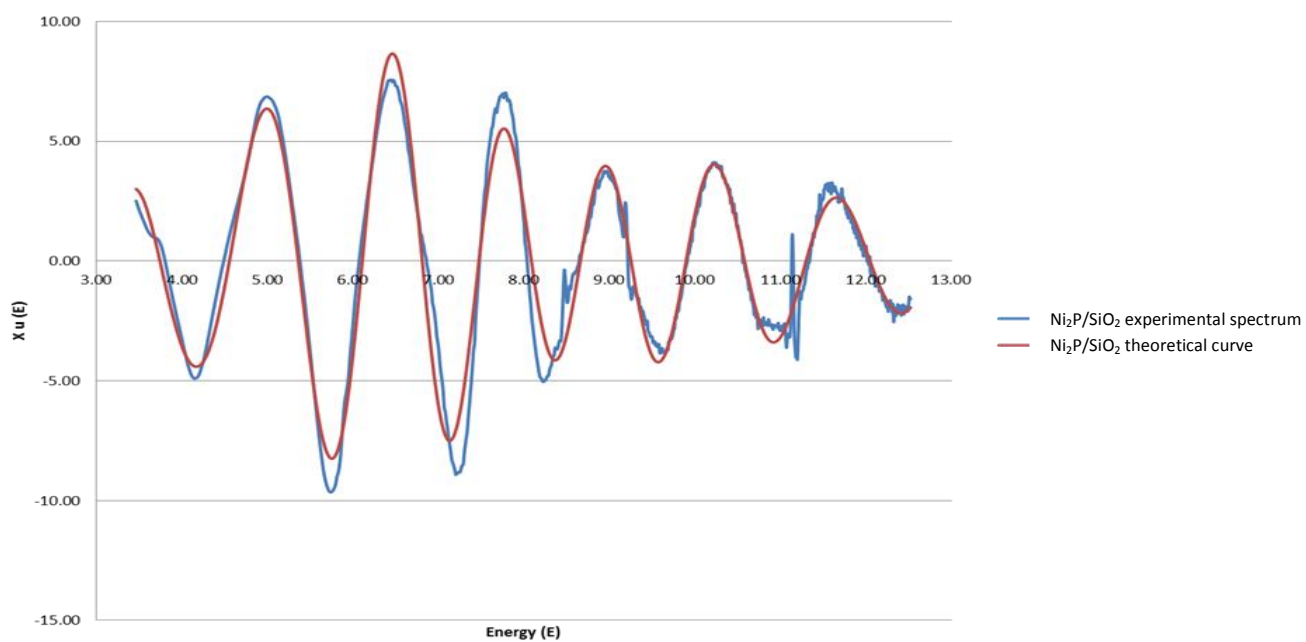


Figure 3-23: k^3 weighted EXAFS spectra for Ni K edge of $\text{Ni}_2\text{P}/\text{SiO}_2$ including theoretical fit.

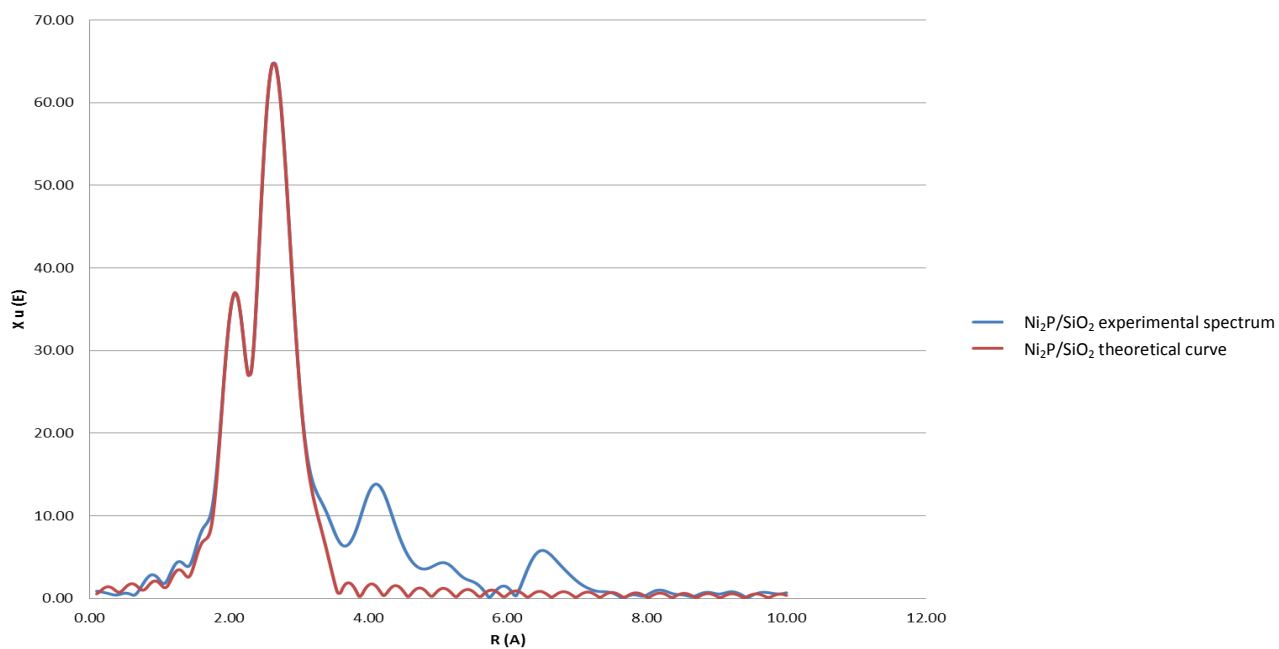


Figure 3-24: Fourier transformed Ni K edge EXAFS spectra for $\text{Ni}_2\text{P}/\text{SiO}_2$ including theoretical fit.

The curve fitting results for the Ni₂P/SiO₂ EXAFS spectrum are presented in Table 3-4. The nickel K edge FT spectrum for Ni₂P/SiO₂ displays two dominant peaks associated with the first two shells which were the basis for the theoretical fitting. The smaller of the two centres is at 0.221 nm and is centred within the region of the Ni-P bond which has been reported in range 0.218-0.231 nm.^[1,3,6] The curve fit indicated that there was an approximate co-ordination number of 4 for Ni-P suggesting that 4 P neighbours are present around the nickel atom. Nickel phosphide in the Ni₂P species has been identified as forming a hexagonal structure with lattice parameters $a = b = 0.5859$ nm and $c = 0.3382$ nm, in which the Ni atoms form two types of nine-fold arrangements around each P atom according to Oyama.^[6] The expected crystal structure of Ni₂P would therefore suggest that Ni sites should possess 6 co-ordination for full saturation of the site. The fit for the spectrum suggests that the nickel phosphide site is 4 co-ordinated; therefore suggesting the nickel phosphide particles are highly dispersed on the support. The second and larger peak is centred at 0.258 nm and has been identified as Ni-Ni bonding with a co-ordination number of 4, indicating 4 neighbouring Ni neighbours. These results closely resemble those reported by Lee and Oyama for silica supported nickel phosphide catalysts.^[6] As was discussed previously, Lee and Oyama reported the presence of two different nickel sites within nickel phosphide using FT EXAFS data to a fit curve which took into consideration close proximity of the Ni-Ni and Ni-P peaks. The two types of Ni and P sites (identified as tetrahedral and square pyramidal) form two different trigonal prisms in the Ni₂P unit cell. Such nine-fold arrangements are very common in metal-rich phosphides.^[6] These however were not visible in the spectrum for the Ni₂P/SiO₂ developed in this study. There are some difference between the results from this investigation and those reported by the Oyama group with regards to co-ordination numbers and oxidation states. This may be a result of more some differences in the experimental technique. Another reason for differences may be the better theoretical curve fit in the Oyama study in comparison this investigation, this is evident from the much higher reliability factor of the fit for data presented in this project meaning there may be some error in the fitting results.

The results suggested that there were further scatterings associated with Ni-P which were not visible in the spectra due to the close proximity of scattering between Ni-P and Ni-Ni meaning some oscillations could be masked. This was therefore accounted for in the curve fitting to allow for a more accurate fit. ^[1,3,6] The reported Ni-P distance of 0.2225 nm and Ni-Ni bond distance of 0.2625 nm are close enough to be regarded with the error of margin as closely matched results. The co-ordination numbers also support one and other with the combined number of Ni-P bonds given as 3.96 and Ni-Ni bonds given as 4.11, in comparison with results from this project with Ni-P co-ordination calculated to 4.05 and Ni-Ni being 4.21. The comparison of the EXAFS curve fit results for Ni₂P/SiO₂ to bulk phase standard sample Ni₂P indicate some differences between the standard material and the catalyst, specifically the bond distances for the supported phosphide are shorter and the co-ordination numbers for the nickel sites are also larger in the supported nickel phosphide. The bond distance for Ni-P bonds in bulk phase Ni₂P was calculated to be 0.228 nm whilst the Ni₂P/SiO₂ Ni-P distance was found to be 0.222 nm. A decrease in bond distance has been reported previously for supported transition metal phosphides and has been correlated to greater dispersion of the particles on the surface support. ^[6] The average co-ordination numbers would also be expected to decrease with bond distance however Oyama has attributed an increase in co-ordination number to an increased presence of phosphorus. ^[6] With the results of the theoretical fit for the spectrum close to those reported along with the XPS characterisation of the material, it is with some confidence that we can say the material that has been produced is Ni₂P/SiO₂. Table 3-4 displays the results of the curve fit for the EXAFS spectrum. The fitting of the spectrum is complex and requires a number of consideration or factors when calculating the fit. These are as follows; AFAC is the amplitude reduction factor, R-Factor is the reliability of curve fit factor, ΔE is the energy shift factor and the A term is the back scattering amplitude factor.

Shell	Scatterer	Bond distance (R)	co-ordination No	A	AFAC	ΔE	R-Factor
1	Ni-P	2.21871	4.05	0.01418	0.7735	3.2127	21.7229
2	Ni-Ni	2.58171	4.21	0.01438	0.7735		
3	Ni-Ni	2.97795	1.67	0.01438	0.7735		

Table 3-4: Curve fitting results of the Ni K-edge EXAFS spectra for Ni₂P/SiO₂

The transmission electron images showing silica supported nickel phosphide are presented in Figure 3-27. The micrographs show uniform particles with sizes between 15 and 20nm. The observed crystallites are slightly smaller than the values calculated from the XRD patterns using the Scherrer equation, which estimated crystallite size to 25nm. The presence of small particles is consistent with previous characterisation of materials with XRD, SEM and EXAFS all indicating good dispersion of nickel phosphide on the silica support. The TEM micrograph also indicates the presence of lattice planes corresponding to crystalline phases on the support which are believed to be nickel phosphide. The TEM image displayed in Figure 3-25 displays crystal fringes with lattice parameters of 1.94 Å and 2.14 Å indicating that there are two crystallographic planes present. The lattice parameter at 1.94 Å corresponds to the reflection at 47.3° 2theta in the XRD pattern for the material. This is consistent with the (2 1 0) crystallographic plane of Ni_2P . The second lattice parameter at 2.14 Å is consistent with the (2 0 1) plane of Ni_2P which corresponds to the reflection at 44.5° 2theta in the XRD pattern. The globular morphology of the nickel phosphide particle seen in Figure 3-25 is typical of supported transition metal phosphides. Globular morphologies have been reported in a number of transition metal phosphide catalysts these are associated with formation of nickel phosphide on the silica support. ^[21]

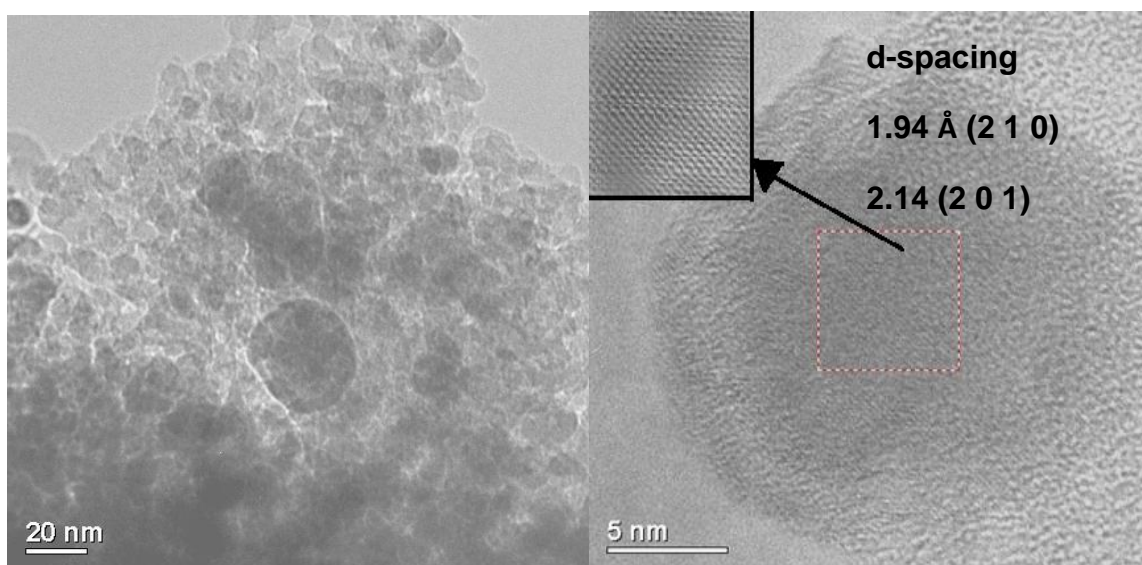


Figure 3-25: TEM micrograph of $\text{Ni}_2\text{P}/\text{SiO}_2$ showing Ni_2P particle on support.

Chemisorption of CO onto the catalyst surface was carried out and monitored in an *in-situ* DRIFTS microreactor at a range of temperatures between room temperature and 400°C. This has enabled an insight into the interaction between CO with the catalyst surface. CO is a good probe molecule for surface interactions, as well as being an integral part of the water-gas shift reaction. As was the case with the bulk materials, purging of unbound CO was undertaken using argon to purge the cell. This however resulted in the removal of both the bound and unbound CO. As a result, peaks associated with both forms of CO were not present after purging the system. DRIFTS studies of absorption of CO onto Ni metal sites have been extensively reported in literature. From the literature, alternative modes of CO bonding onto the Ni site have described as follows; CO bridge bonding occurring at 1800-2000 cm^{-1} and terminal CO bonding occurring at 2045-2145 cm^{-1} .^[21] The results of the DRIFTS studies carried out on $\text{Ni}_2\text{P}/\text{SiO}_2$ are presented in Figures 3-26 and 3-27. The DRIFT spectra for CO chemisorption onto $\text{Ni}_2\text{P}/\text{SiO}_2$ is given in Figure 3-26 displays a broad peak 1860 cm^{-1} . This feature is present at each temperature which the cell is operated at and has been identified as the CO bridging bond to the Ni sites.^[21] The presence of this peak at elevated temperatures indicates strong interaction between CO and the Ni site of the material. There is a further mode of bridging bond evident at 1950 cm^{-1} . This peak is weak in comparison to the previous bridge bonding mode and is only present between ambient temperature and 200°C. The disappearance of this mode of CO bridging peak above 200°C points toward a weaker interaction between CO and surface of the material in comparison to the lower mode of CO bridging bond.

The DRIFTS spectra display the distinctive broad double peaks associated with free unbound CO in the cell at 2115 and 2170 cm^{-1} , these peaks are seen at each set temperature range. This is to be expected with CO flowing through the microreactor. Another peak that is evident in this range is that which appears at 2076 cm^{-1} , this peak is most pronounced above 250°C. This peak has been identified as the terminal bonding of CO onto the $\text{Ni}^{\delta+}$. This figure is consistent with previous studies of CO adsorption onto Ni_2P catalyst with both Bussell and Li reporting CO terminal bonding occurring 2075 cm^{-1} .^[21,15] The presence of unbound CO and its appearance in the spectra could mean that CO terminal bonding modes are being masked at

lower temperatures by the unbound CO, below 250°C where it is not visible in the spectra. The strength of the terminal bonding of CO increases with temperature, signifying that terminal bonding is the mode of CO adsorption onto the Ni sites favoured under water-gas shift reaction temperature conditions. Bussell and co-workers also identified CO adsorption via a surface P site at 2200 cm^{-1} . This is not present in the spectra presented in Figure 3-26. [21] The absence of this peak could indicate that the catalyst displays surfaces that are predominantly nickel rich. Nickel phosphide particles exhibiting nickel rich surfaces are associated with higher reduction temperatures used to produce the catalysts, with Oyama reporting some loss of phosphorus via PH_3 under reduction temperatures greater than 400°C. [1] The reduction temperature for $\text{Ni}_2\text{P}/\text{SiO}_2$ used in the project was 750°C based on the TGA profile for the precursor shown previously in Figure 3-18.

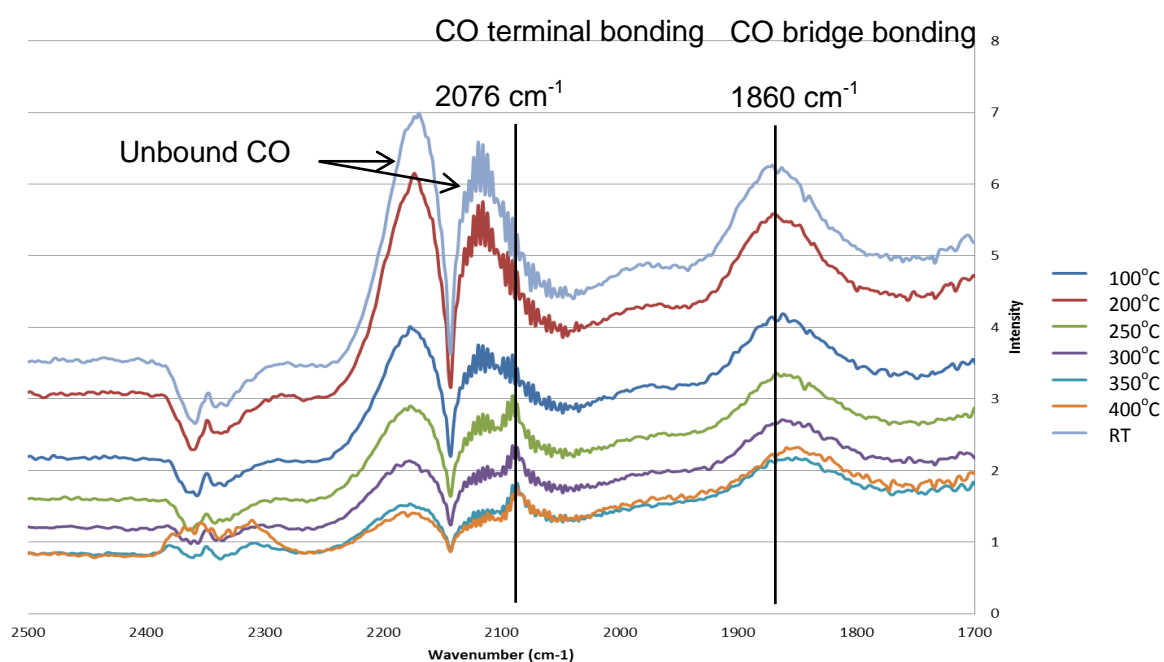


Figure 3-26: DRIFTS spectra for CO chemisorption between RT and 400°C on $\text{Ni}_2\text{P}/\text{SiO}_2$

The DRIFTS spectra for silica supported nickel phosphide differ greatly from the counterpart bulk phase nickel phosphide spectra presented in Figure 3-15. The spectra for the bulk phase materials showed little CO adsorption onto the material and no peaks associated with CO surface adsorption identified. The supported nickel

phosphide DRIFTS spectra indicate CO adsorption onto the catalyst. Both terminal and bridging bonding of CO are displayed in the spectra, suggesting the dispersion of nickel phosphide particles onto the silica support has greatly improved its affinity for CO. These results suggest silica supported nickel phosphide should display good potential as a water-gas shift catalyst especially under high temperature water-gas shift condition where strong adsorption of CO on the Ni sites is evident.

3.5 Catalytic testing of silica supported nickel phosphide

The materials were tested for application in the low temperature water-gas shift reaction using a high pressure fixed bed steam reactor. Gas-chromatography was used to analyse the composition of the exit feed from the reactor. The results of the testing using GC data are presented in Figure 3-27. The reaction profile for Ni₂P/SiO₂ tested under low temperature water-gas shift conditions shows CO as the predominant component of the exit feed, with very little CO₂ or H₂ evident. Small amounts of H₂ and CO₂ are present; suggesting a very small amount of water-gas activity present. The carbon balance for the reaction was estimated as 94 % based on an average for the duration of the run. The thermodynamic equilibrium limit with regards to CO conversion was calculated as 99.4 % conversion under the low temperature water-gas shift reaction conditions. Using the CO conversion limit based on equilibrium it was possible to estimate the limiting formation rate of products (i.e. the mass normalised rate which would be achieved if the material was catalysing the reaction to thermodynamic equilibrium) was calculated as 1.79×10^{-5} moles.s⁻¹.g⁻¹. The reaction profile indicates that the reaction is not at the thermodynamic equilibrium, operating under conditions away from equilibrium allow for a more accurate comparison of catalysts based on activity.

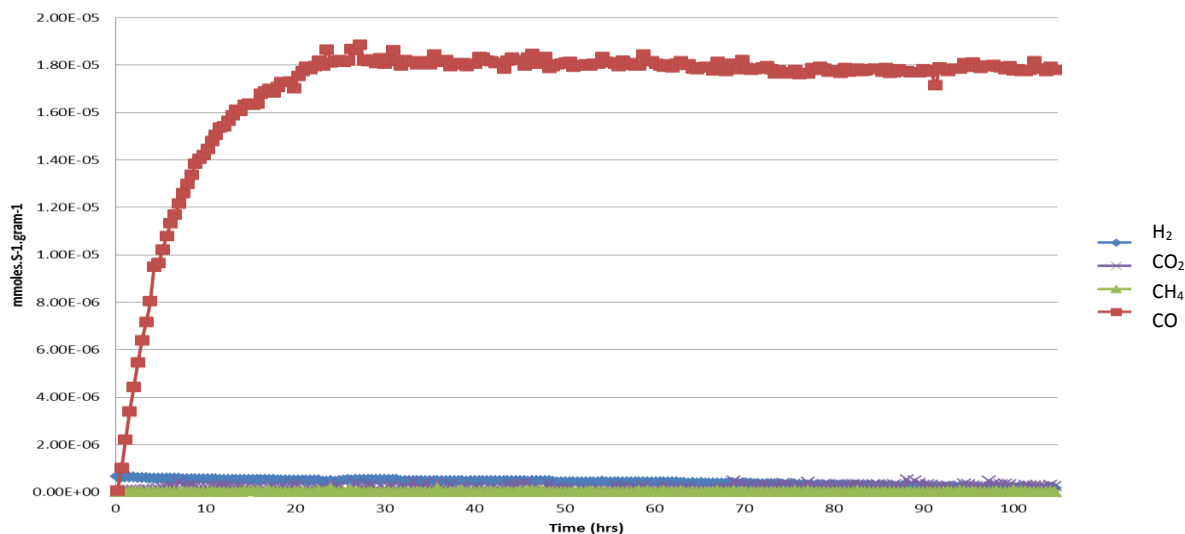


Figure 3-27: Reaction profile for Ni_2P/SiO_2 based on GC data under low temperature water-gas shift conditions.

The reaction profile suggests that the catalyst displays poor catalytic activity for the water-gas shift reaction under low temperature conditions. This result contradicts the study by Rodriguez and colleagues who reported bulk phase nickel phosphide displayed good catalytic activity under low temperature water-gas shift reaction conditions.^[3] The low temperature water-gas shift reaction test result for the silica supported nickel phosphide catalyst showed similarly poor catalytic activity with bulk nickel phosphide under the low temperature conditions presented in Figure 3-16.

The catalytic activity of Ni_2P/SiO_2 was compared with that of an industrial standard Cu catalyst provided by Johnson Matthey. The industrial catalyst was run under the same conditions at the nickel phosphide catalyst and has been used throughout catalytic testing of nickel phosphide catalysts as a bench mark in terms of catalytic activity displayed. Figure 3-28 compares the Cu industrial catalyst and the Ni_2P/SiO_2 catalysts with regards to the reaction profiles for CO_2 and H_2 produced per weight of catalyst. The comparison of the industrial catalyst to the supported nickel phosphide catalyst highlights the poor activity displayed by the latter material as is evident from much lower quantities of CO_2 and H_2 being produced in comparison to the industrial catalyst

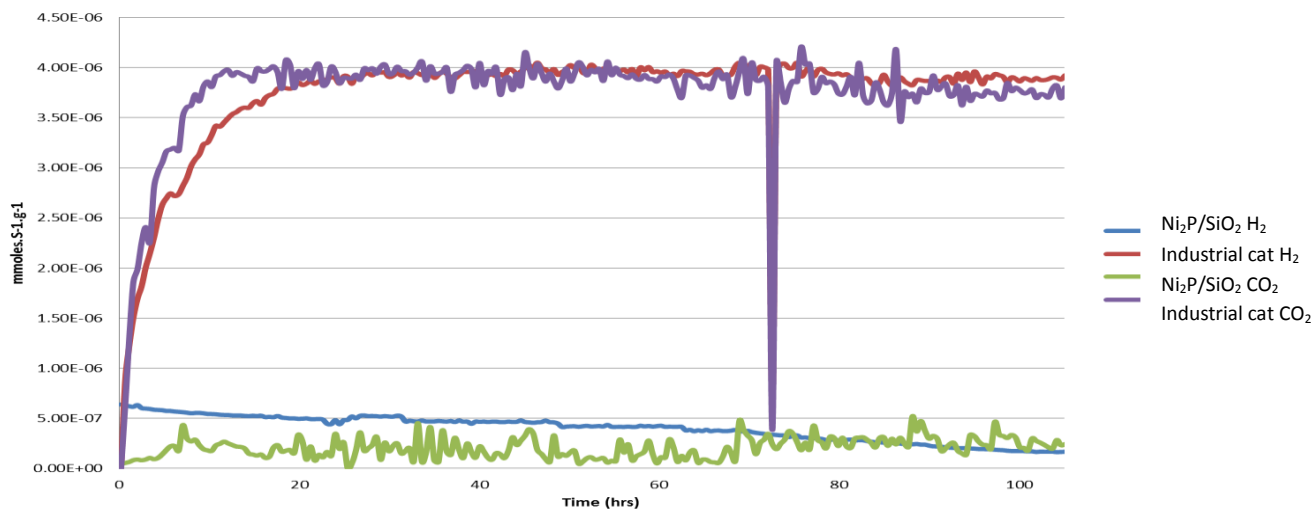


Figure 3-28: Comparison of H_2 and CO_2 produced during low temperature water-gas shift reaction testing of Ni_2P/SiO_2 and Cu based industrial catalyst.

The poor activity of Ni_2P/SiO_2 shown in catalytic testing of the catalyst under low temperature water-gas shift reaction conditions indicates that a higher temperature regime may be required to improve activity for the reaction. The study by Rodriguez and colleagues reported bulk Ni_2P as displaying good catalytic activity for the water-gas shift reaction at temperatures between 300 and 375°C. The study established a positive correlation between temperature and catalytic activity within the aforementioned temperature range. The operating temperature for the low temperature water-gas shift reaction for testing in this project was 210°C which is much lower than that used in the Rodriguez study. The DRIFTS studies carried out on the Ni_2P/SiO_2 catalyst presented in Figure 3-26 also support the suggestion that higher reaction temperatures are required. The adsorption of CO in the terminal bonding mode was evident at temperatures greater than 250°C. The terminal bonding pathway is thought to be the favoured pathway for the water-gas shift reaction mechanism according to DFT calculations carried out in the Rodriguez study.

The poor catalytic activity of $\text{Ni}_2\text{P}/\text{SiO}_2$ under low temperature water-gas shift conditions has led to the catalyst being run under high temperature water-gas shift reaction conditions, using an operating temperature of 410°C . The resultant reaction profile from the reaction testing is presented in Figure 3-29. The reaction profile under high temperature water-gas shift conditions shows significant quantities of hydrogen and carbon monoxide being produced, suggesting that the catalyst shows some catalytic activity at the higher temperature conditions for the reaction. The thermodynamic equilibrium limit with regards to CO conversion was calculated as 91.3 % conversion under the low temperature water-gas shift reaction conditions. Using the CO conversion limit based on equilibrium it was possible to estimate the limiting formation rate of products. The equilibrium limited formation rate of products was calculated as $1.55 \times 10^{-5} \text{ moles} \cdot \text{s}^{-1} \cdot \text{g}^{-1}$ for the reaction conditions used; the reaction profile indicates that the reaction is far from equilibrium. The carbon balance for the reaction was calculated as an average over the duration of the run and was found to be 92 %.

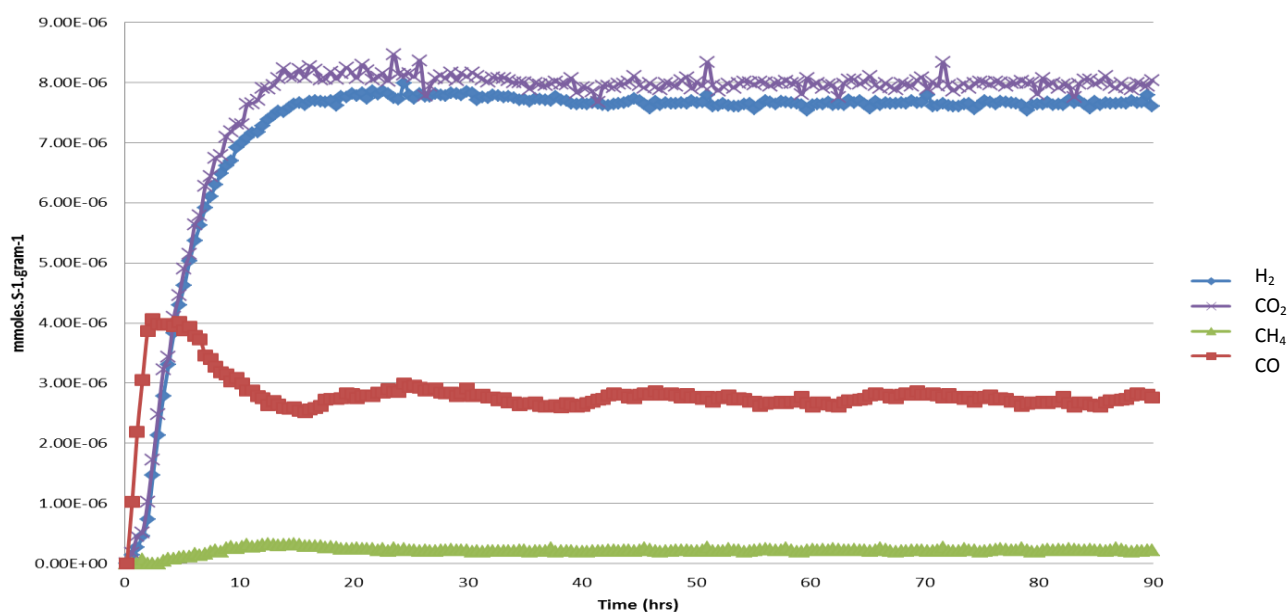


Figure 3-29: Reaction profile for $\text{Ni}_2\text{P}/\text{SiO}_2$ tested under high temperature water-gas shift reaction conditions

The reaction profile for the high temperature water-gas shift reaction testing of $\text{Ni}_2\text{P}/\text{SiO}_2$ (Figure 3-29) indicates that the reaction reaches steady state after 10 hours of running and remains steady for the duration of the run. The delay in the catalyst reaching steady state formation rates was evident in all catalysts tested. The reaction profile shows a slight discrepancy between H_2 and CO_2 , which is unusual for process that is stoichiometrically even. The difference in H_2 and CO_2 being produced in the reaction this can be attributed to limited formation of small amounts of methane being produced, as can be seen in the reaction profile. The formation of methane suggests the possible presence of a nickel metal phase fraction within the catalyst; nickel under the reaction conditions is an effective methanation catalyst. The nickel metal phase would be a minor component due to the small amount of methane being produced as well as characterisation of the catalyst indicating that nickel phosphide is the active phase prominently present on the support. The good activity shown by the catalyst at increased temperatures further supports the theory that CO adsorption via a terminal mode is the preferred kinetic pathway for the reaction, and the fact that CO terminal bonding is prominent at higher temperatures according to DRIFTS CO adsorption of the catalyst.

The catalytic activity of the $\text{Ni}_2\text{P}/\text{SiO}_2$ catalyst was compared with that of an iron based industrial catalyst supplied by Johnson Matthey and tested under same reaction conditions. The reaction profile showing the production of H_2 and CO_2 in both reaction runs is presented in Figure 3-30. The catalysts are compared on the formation rates of CO_2 and H_2 per weight of catalyst. $\text{Ni}_2\text{P}/\text{SiO}_2$ is shown to significantly outperform the industrial catalyst, with the nickel phosphide catalyst producing almost twice as much hydrogen and carbon dioxide per weight of catalyst. The industrial catalyst performs slightly better than the $\text{Ni}_2\text{P}/\text{SiO}_2$ catalyst on the basis of moles of products formed per unit of time. Figure 3-31 shows the formation rates for products after 24hrs of running. The industrial catalyst has a much higher loading of active phase in comparison to the 20% loading of the $\text{Ni}_2\text{P}/\text{SiO}_2$; it is therefore justifiable to compare catalysts activity on the basis of mass normalisation of the materials.

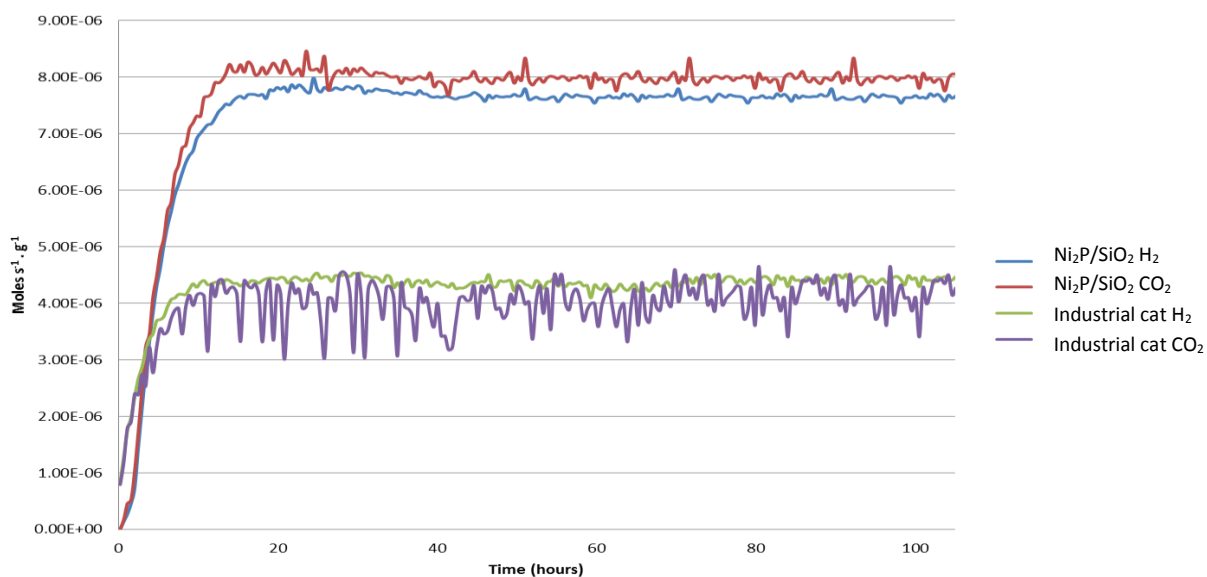


Figure 3-30: Reaction profiles showing formation of CO₂ and H₂ per weight of catalyst for Ni₂P/SiO₂ and industrial catalyst for HT WGS conditions.

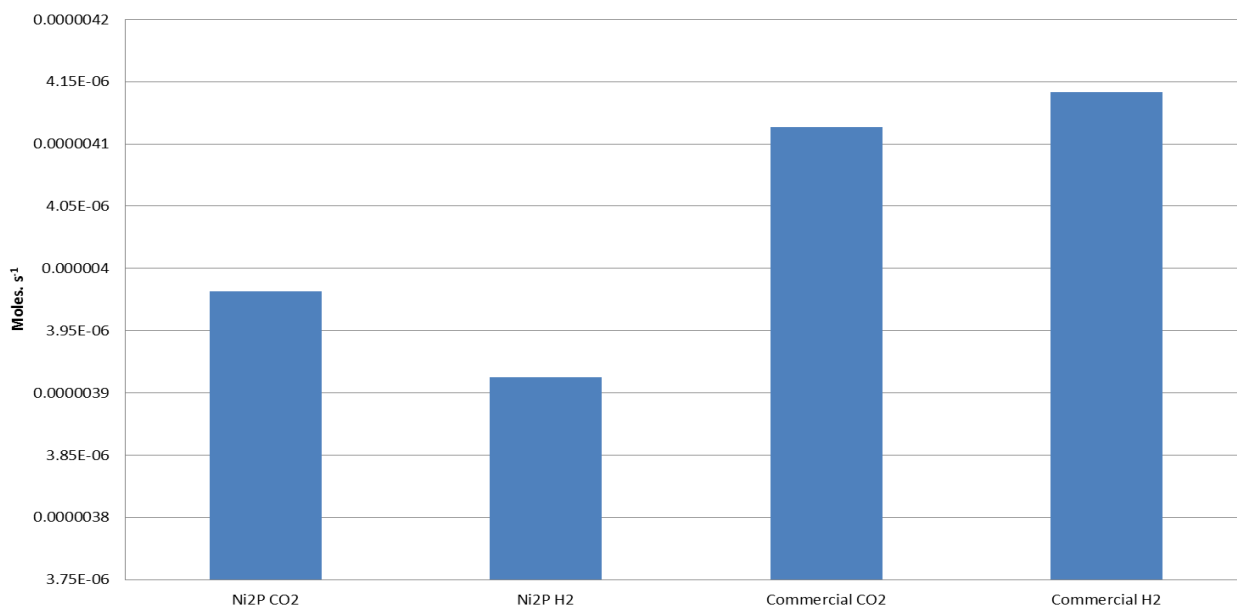


Figure 3-31: Formation rates of H₂ and CO₂ after 24 hours of running for Ni₂P/SiO₂ and industrial catalyst for HT WGS conditions.

3.6 Characterisation of post-reaction silica supported nickel phosphide

The nickel phosphide catalyst was characterised post high temperature water-gas shift reaction in order to establish if, firstly the catalyst remained stable after long running times under the conditions and secondly if there are any morphological, electronic or compositional changes in the catalyst. Ni₂P/SiO₂ catalyst was studied using XRD characterisation post high temperature water-gas shift reaction testing. The resultant diffraction pattern is presented in Figure 3-32 along with that of the fresh catalyst. The diffraction pattern for the post-reaction sample indicates the catalyst remains stable after running under high temperature water-gas shift reaction conditions over the duration of testing (105 hours). The diffraction pattern for the post-reaction sample shows no discernable difference in comparison to the diffraction pattern for the fresh sample. The average crystallite size was determined using the Scherrer equation, this was found to be 28.7 nm which is very slightly larger than that of the fresh material which was 25.2 nm suggesting that while the catalyst remains stable under the reaction conditions there may possibly be a small degree of particle aggregation occurring during the reaction.

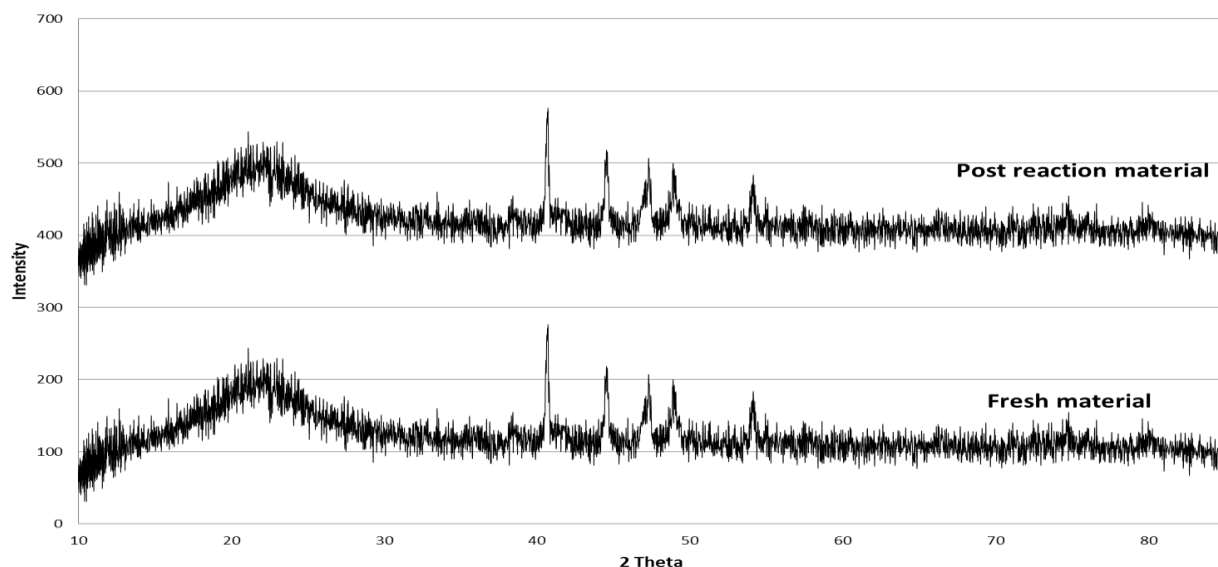


Figure 3-32: XRD patterns for $\text{Ni}_2\text{P}/\text{SiO}_2$ pre and post HT water-gas shift testing.

SEM and EDX analysis of the post-reaction catalyst are presented in Figure 3-33 and Table 3-5 respectively. The SEM micrograph for post-reaction catalyst shows nickel phosphide particles on the silica support. The $\text{Ni}_2\text{P}/\text{SiO}_2$ particles can be distinguished from the carbon pad as small light particles that are dispersed on the surface of the carbon support which is darker in colour. EDX elemental analysis of the surface particles was carried out at a number of points in the micrograph to ensure consistency. The micrograph highlights the area that was used to confirm elemental composition of the particle (labelled as “spectrum 3”). The results of EDX analyses are displayed in Table 3-5 show both atomic and weight percentages of the elements present. The atomic weight percentages for nickel and phosphorus are roughly in the ratio 2:1, consistent with the stoichiometry of Ni_2P . The EDX analysis of the fresh catalyst displayed in Table 3-1 also showed similar atomic and weight percentages. The consistency of elemental ratios between the pre and post-reaction catalyst support the stability of the catalyst with no significant phosphorus being lost from the active phase during the reaction testing.

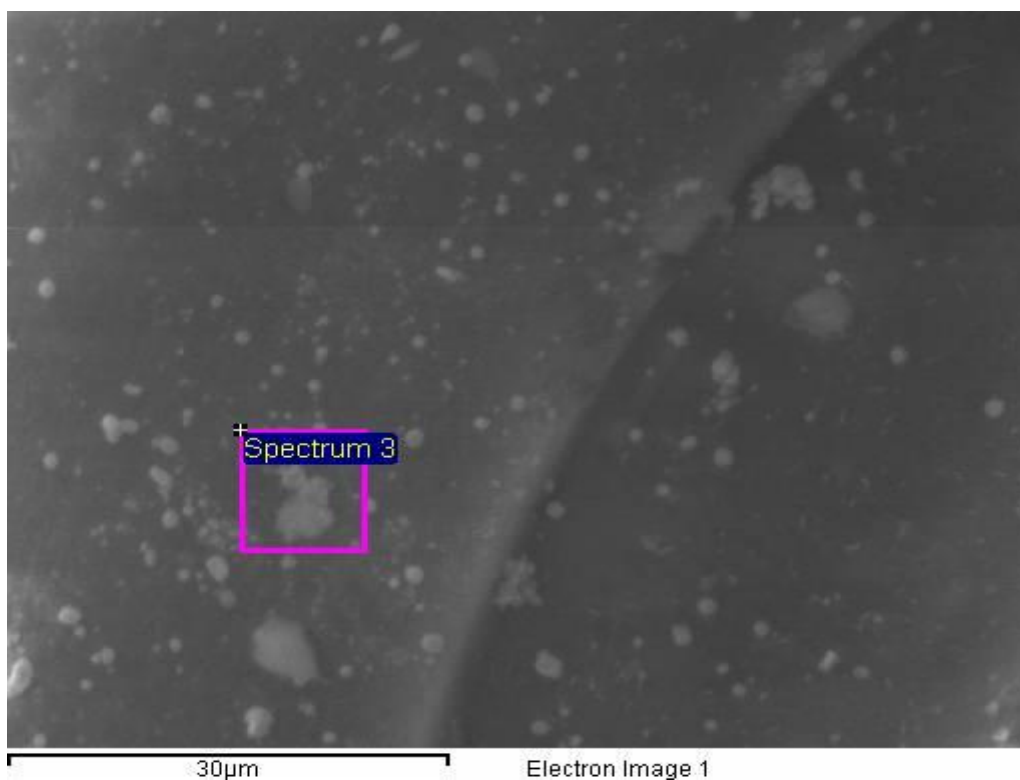


Figure 3-33: SEM micrograph showing $\text{Ni}_2\text{P}/\text{SiO}_2$ post HT water-gas shift reaction testing

Element (edge)	Weight%	Atomic%	Av Atomic % (deviation)
P (K)	27.26	41.54	32.00 (± 9)
Ni (K)	72.74	58.46	68.16 (± 9)
Total	100.00	100.00	

Table 3-5 Elemental analyses of post-reaction $\text{Ni}_2\text{P}/\text{SiO}_2$

X-ray photoelectron spectroscopy was also carried out on post-reaction $\text{Ni}_2\text{P}/\text{SiO}_2$ tested under high temperature water-gas shift conditions. The characterisation of catalyst using XPS was carried out to gain an insight to the electronic state of the active phase of the catalyst after test running. The XPS spectra depicting nickel 2p and phosphorus 2p binding energies for pre- and post-reacted $\text{Ni}_2\text{P}/\text{SiO}_2$ are presented in Figures 3-34 and 3-35 respectively.

The Ni 2p spectra for the post-reaction catalyst sample shows two peaks, a major peak at 853.9 eV and minor peak at 858.1 eV. The peak at 853.9eV has been identified as $\text{Ni}^{\delta+}$ which is consistent with it being bonded to phosphorus in Ni_2P as reported in previous studies in the literature.^[21-22] The minor peak in the spectra at 858.1 eV has been assigned to $\text{Ni}^{\text{II}+}$ species associated with nickel pyrophosphate. This is thought to be a result of oxy-phosphide surfaces that promote the catalytic activity of the material, although it is not clearly established from the spectra.^[5] There are two further peaks in spectra at 871.1 eV and 878.3 eV and are known to be features associated with $\text{Ni}^{\delta+}$ and $\text{Ni}^{\text{II}+}$ species in the $2p_{1/2}$ spectrum. The comparison of the pre- and post-reaction spectra for nickel indicate that the nickel electronic state is constant. This is evident from binding energy peaks associated with the both species of nickel present in the catalyst remaining the same. One noticeable difference between the pre- and post-testing nickel spectra is the increased intensity of the post-reaction spectra in comparison to fresh material. Increase in peak intensity can be attributed to an increased presence of nickel at the surface which suggests that particle mobility during the water-gas shift reaction. However XRD patterns confirm no peak broadening between the pre- and post-reaction samples suggesting particles remain dispersed without aggregating.

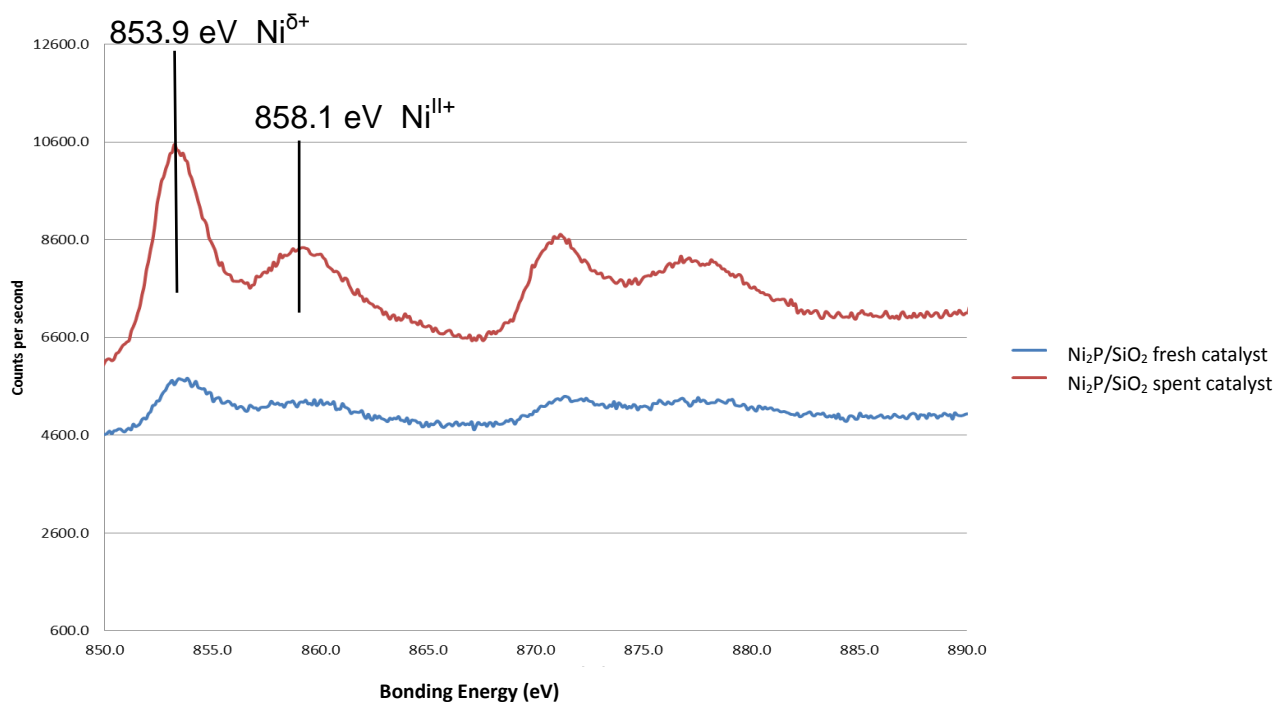


Figure 3-34: Ni₂P/SiO₂ Ni 2p spectra for pre- and post-reaction samples.

The post-reaction P 2p spectrum for Ni₂P/SiO₂ (Figure 3-35) shows a single peak suggesting a single species of near surface phosphorus present in the catalyst. The peak is centred at 130.8 eV and has been identified as P^{δ-}; the phosphorus peak is slightly higher than previously reported studies, with the peak centring at 129.0-131.0 eV. [21-22] The small difference can be attributed to the presence of oxy-phosphide phases as suggested in the Ni 2p spectrum for the catalyst. It is safe to assume that the phosphorus species present is P^{δ-} rather than a P^{V-} phosphate counterpart which has an approximate binding energy of 134-135 eV, which is much higher than the binding energy seen in the catalyst. Comparison of the pre- and post-reaction samples shows that the phosphorus 2p spectra indicate that the phosphorus electronic state remains unchanged after high temperature water-gas shift reaction testing. The reaction materials exhibit slight shifts in binding energy which have been attributed to an increase in surface oxygen on the catalyst. The post-reaction phosphorus spectrum has a greater intensity in comparison to the fresh catalyst. This was also seen in the nickel spectra and indicates an increase in the presence of phosphorus at the surface of the catalyst.

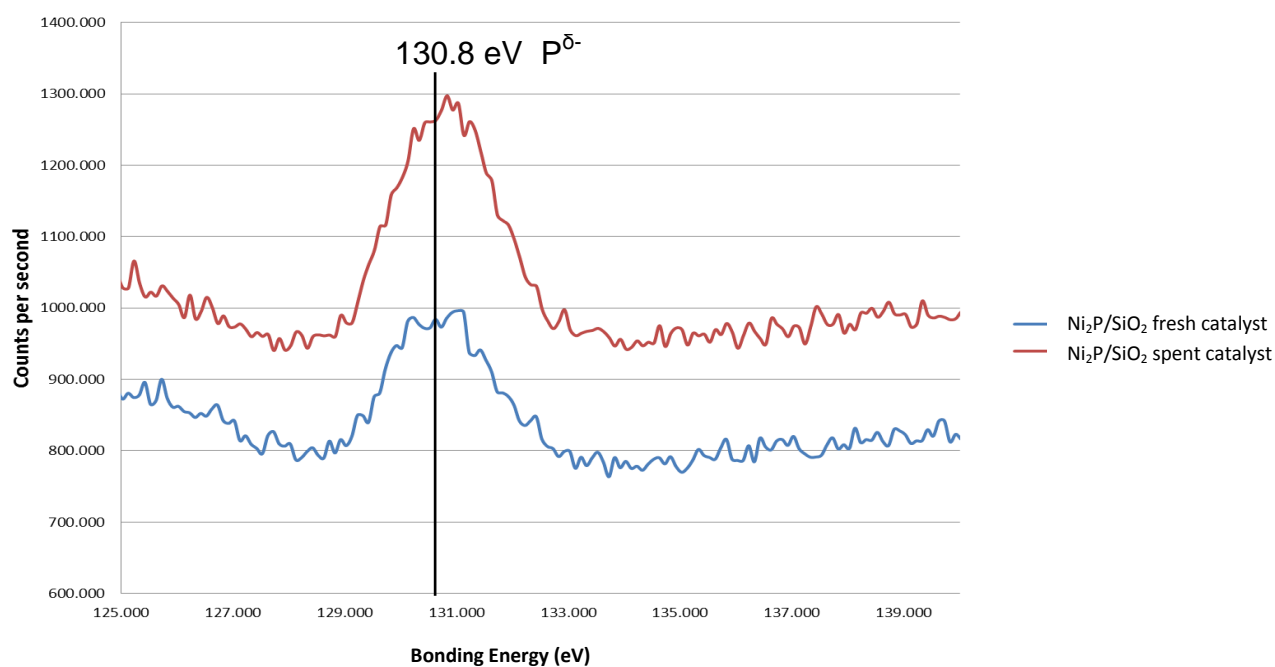


Figure 3-35: Ni₂P/SiO₂ P 2p spectra for pre- and post-reaction samples

Sample	Ni ₂ P/SiO ₂ post-reaction	Ni ₂ P/SiO ₂	Ni ₂ P (values from literature) ^[21-22]
Element	Binding energy (eV)	Binding energy (eV)	Binding energy (eV)
Ni 2p	853.9 (Ni ^{δ+})	853.5 (Ni ^{δ+})	852.5-853.6(Ni ^{δ+})
	858.1 (Ni ²⁺)	856.8 (Ni ²⁺)	855.5-856.4 (Ni ²⁺)
P 2p	130.8 (P ^{δ-})	130.6 (P ^{δ-})	130.1-131.2(P ^{δ-})
			134.5-135.4 (P ⁵⁺)
O 1s	533.4	532.8	n/a
C 1s	285.0	285.0	285.0

Table 3-6: Summary of binding energy peaks shown in spectra for silica supported Ni₂P pre- and post-catalytic testing.

The testing of separate components of the catalyst under the same reaction conditions were carried out to help identify if any nickel or phosphorus alone were responsible for the activity displayed by the nickel phosphide catalyst. A silica supported nickel catalyst of 20% loading with respect to nickel was tested under the same high temperature water-gas shift reaction conditions at the nickel phosphide catalyst. The resultant reaction profile is displayed in Figure 3-36. The reaction profile for the nickel catalyst shows the reaction reached steady state after 10 hours of running and the carbon balance was calculated as 87%. The nickel catalyst produces a significant amount of methane in comparison to the nickel phosphide catalyst. Nickel is a highly effective methanation catalyst under high temperature water-gas shift reaction conditions, so high methane formation rates are to be expected. The nickel catalyst also produced less hydrogen than the nickel phosphide catalyst, with almost 75% less hydrogen being produced by the nickel catalyst. The differences between reaction profiles for Ni/SiO₂ and Ni₂P/SiO₂ show inherent difference in the activity and selectivity of the two catalysts suggesting the two catalysts possess entirely different species of nickel in the active phases of the catalyst.

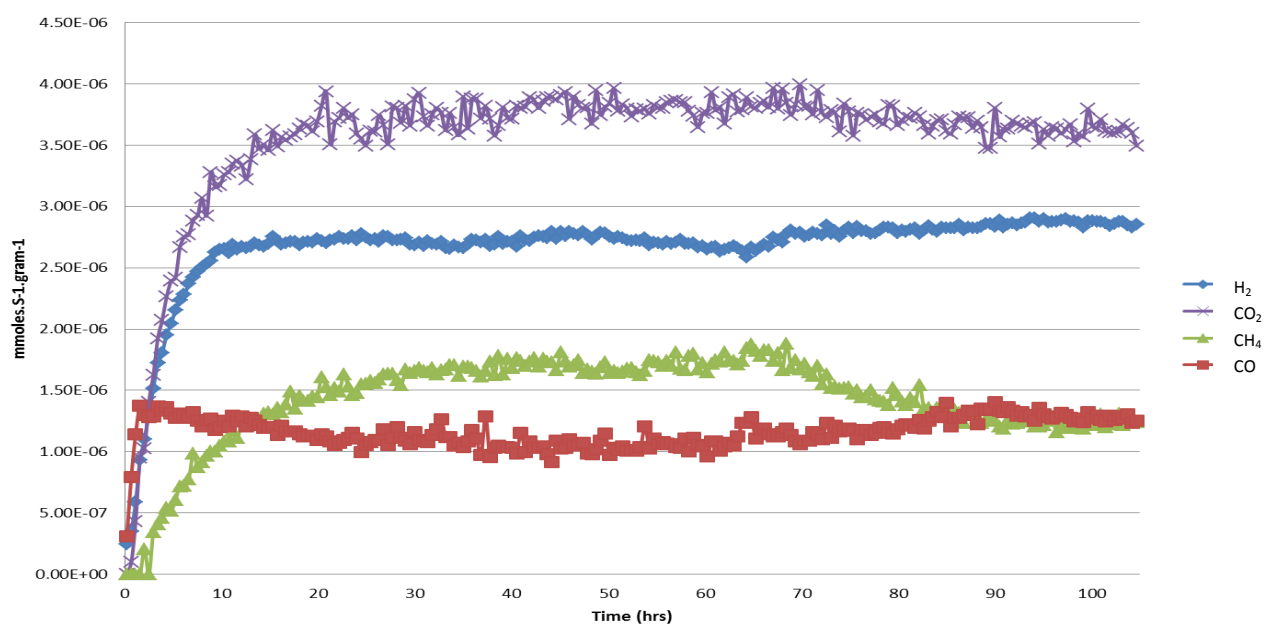


Figure 3-36: Reaction profile for Ni/SiO₂ catalyst tested under high temperature water-gas shift reaction conditions.

Figure 3-37 presented below shows the reaction profile for a P/SiO_2 material prepared using a 20% loading of phosphorus. The reaction profile for this material shows no formation of hydrogen or carbon dioxide, only the presence of the unreacted carbon monoxide feed is detected in the GC data. The lack of hydrogen and carbon monoxide being produced indicates that P/SiO_2 displays no catalytic activity for the water-gas shift reaction under high temperature shift conditions.

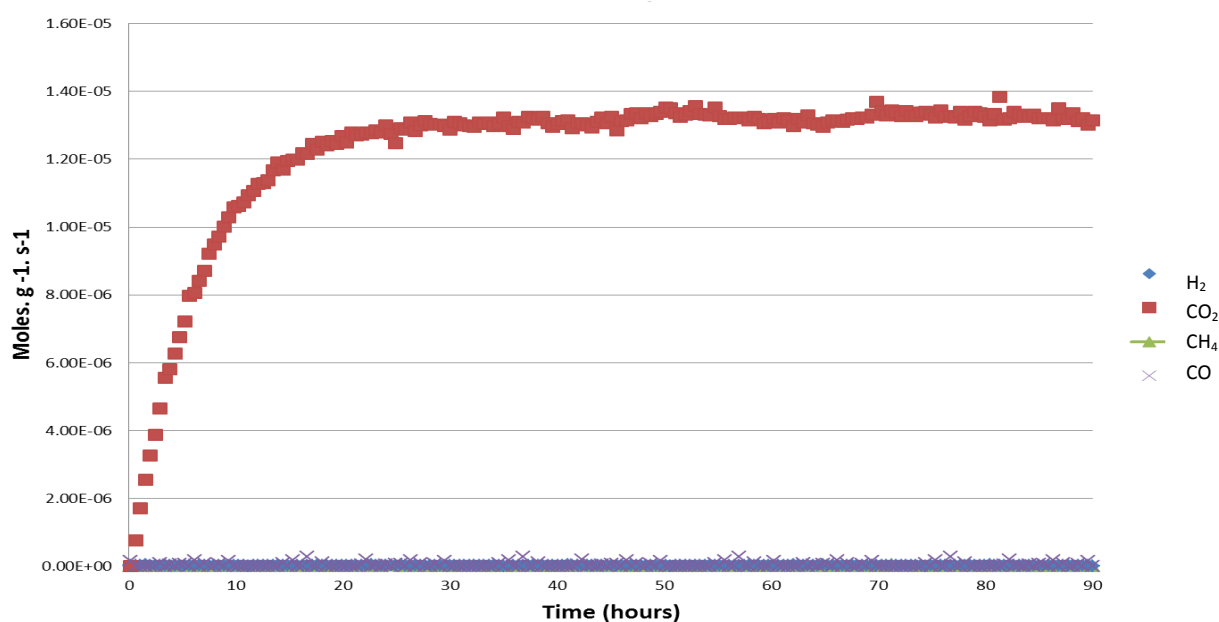


Figure 3-37: Reaction profile for P/SiO_2 tested under high temperature water-gas shift reaction conditions.

The testing of the separate components of the catalyst enables us to conclude that the catalytic activity of the Ni_2P/SiO_2 displayed under high temperature water-gas shift reaction conditions is related to the presence of both Ni and P components on the support. This is confirmed by the significantly different reaction profiles given by both the Ni/SiO_2 and P/SiO_2 catalysts under the same reaction conditions.

3.7 Conclusions

Characterisation through a number of techniques as well as catalytic testing presented throughout this chapter has confirmed that nickel phosphide was successfully produced and remained stable under water-gas shift reaction conditions. Silica supported nickel phosphide was also confirmed via characterisation of the material. The catalytic activity of the silica supported nickel phosphide catalyst was also shown to be good under high temperature water-gas shift reaction conditions.

The X-ray diffraction patterns (Figure 3-1) confirmed Ni_2P was produced. However nickel phosphide in a number of stoichiometries were produced by altering the Ni:P ratio in the precursors. Diffraction patterns shown in Figure 3-1 also confirmed this stoichiometry of nickel phosphide was made using a number of alternative precursors to nickel phosphate, specifically nickel nitrate and nickel oxide. The high reduction temperature used in the reduction of nickel phosphate resulted in low surface area materials being produced as was confirmed by BET analysis. The similarity of the Ni_2P samples produced using alternative precursors was further supported by SEM micrographs (Figure 3-4) indicating similar morphologies in the two materials. TGA profiles (Figures 3-2 & 3-3) for reduction for nickel phosphate to nickel phosphide showed the precursors displayed similar reduction temperatures.

Bulk phase nickel phosphide was tested with regards to the stability of the material under interaction with steam at temperatures under which both high and low temperature water-gas shift reactions are carried out. XRD and SEM analysis indicated the materials remain stable in terms of morphology and bulk phase composition. However XPS analysis indicated partial surface oxidation of the materials especially phosphorous which was attributed to the oxy-phases which commonly occur in transition metal phosphides under oxygen rich conditions. Carbon monoxide chemisorption onto bulk phase nickel phosphide (Ni_2P) was carried out at a range of temperatures from 25°C to 400°C to establish the behaviour

of the material in the presence of CO under reaction like temperature conditions. The DRIFTS study indicated that CO was not adsorbed onto the nickel phosphide under any of the temperature regimes. Poor CO adsorption was attributed to the low surface area exhibited by the material and hinted towards the materials being ineffective for application in the water-gas shift reaction. The poor catalytic activity of bulk phase Ni_2P was confirmed by testing the catalyst. The resultant reaction profile showed no catalytic activity under either high or low temperature water gas shift conditions.

The low catalytic activity of bulk phase nickel phosphide led to the decision to produce supported nickel phosphide catalyst to give better dispersion of particles and stronger mechanical strength to the catalyst to facilitate application under greater operating conditions. Nickel phosphate was impregnated onto a silica Q10 support which was then reduced under hydrogen to give the supported nickel phosphide catalyst ($\text{Ni}_2\text{P}/\text{SiO}_2$). TGA analysis of reduction of the catalyst precursor showed a similar reduction temperature to the bulk phase Ni_2P TGA profile. Characterisation of the catalyst using TEM, XRD, Raman spectroscopy, SEM and EDX further established the presence of nickel phosphide on the silica support. However, due to the amorphous nature of the support, XRD patterns were not fully conclusive. The qualitative nature of SEM and EDX led to the use of XPS and EXAFS to better quantify the catalyst. XPS analysis of the catalyst confirmed the presence of nickel phosphide on the silica support through the conformation electronic states of the elements. The XPS spectrum for nickel 2p for the catalyst revealed the oxidation state of nickel to be $\text{Ni}^{\delta+}$ where $0 < \delta < 2$, with the phosphorus oxidation state revealed as $\text{P}^{\delta-}$ where $0 < \delta < 1$. The results for the supported nickel phosphide catalyst were compared and showed consistency with bulk phase Ni_2P along with previous studies that used XPS to quantify silica supported nickel phosphide catalysts, indicating that the catalyst was $\text{Ni}_2\text{P}/\text{SiO}_2$. The EXAFS study carried out on the silica supported nickel phosphide catalyst further confirmed the presence of the nickel phosphide particles in the Ni_2P species through the identification of the Ni environment within the particles. The theoretical curve fitting confirmed the presence of multiple P and Ni neighbours to the target Ni atom.

The DRIFTS study of the chemisorption of CO onto the catalyst surface revealed strong interaction between CO and the catalyst surface. Temperature profiles for CO chemisorption indicated that CO was adsorbed on the catalyst surface via two different routes, the bridging bond occurred from ambient temperature up to 400°C were as terminal bonding occurred at temperatures in excess of 250°C. Terminal bonding has been identified in previous studies the reactive pathway for the catalyst, indicating that reaction temperature for this catalyst must exceed 250°C.

Catalytic testing of Ni₂P/SiO₂ under low temperature water-gas shift temperature regimes confirmed this, with poor catalytic activity shown by the material under low temperature water-gas shift conditions (210°C). The catalyst performed poorly in comparison to the copper based industrial catalyst under low temperature water-gas shift conditions. The reaction profile for high temperature water-gas shift testing of the catalyst showed the catalyst to exhibit good activity for the reaction under the conditions. The promising catalytic activity of Ni₂P/SiO₂ under high temperature shift conditions was confirmed upon comparison with the industrial iron based catalyst under the same conditions. Ni₂P/SiO₂ performed better than the iron based catalyst per weight of catalyst. Post-reaction characterisation of the catalyst revealed that material remained generally unchanged highlighting the catalysts robust and stable nature. XRD analysis revealed no peak broadening, suggesting particle size did not greatly increase under reaction. This was confirmed by SEM analysis showing Ni₂P particles with no significant aggregation of particles. EDX also showed Ni:P ratio in particles remained relatively constant between fresh and spent samples, showing no loss of phosphorus from the catalyst. The XPS spectra for the post-reaction catalyst indicated both the nickel and phosphorus oxidation states remained consistent. However, there was a slight upward shift binding energy in comparison to fresh samples. This was thought to be a result of an increase in oxygen content in the near surface regions of the catalyst, this increase is thought to be small due to the small shift in binding energy. There was also a noticeable increase in peak intensity in the post-reaction materials in the phosphorus spectra indicating the surface was enriched with phosphorus. This was attributed to relationship between phosphorus and oxygen which has been identified previously as a major factor in the catalytic activity of the material.

3.8 References

- 1) S.T. Oyama; J. Catal; 216 (2003) pg 343–352
- 2) M. Bussell, R. Prins; Catal. Lett; 142 (2012) pg 1413–1436
- 3) S.L. Brock, K. Senevirathne; J. Solid State Chem; 181 (2008) pg 1552–1559
- 4) S.T. Oyama, T. Gott, H. K. Lee, H. Zhao; Catal. Today; 143 (2009) pg 94–107
- 5) P. Liu, J. A. Rodriguez, Y. Takahashi, K. Nakamura; J. Catal; 262; (2009) pg 294–303
- 6) S.T. Oyama, Y.K. Lee; J. Catal; 258; (2008) pg 393–400
- 7) A. F. Gaudette, A. W. Burns, J. R. Hayes, M. C. Smith, R. H. Bowker, T. Seda, M. E. Bussell; J. Catal; 272 ; (2010) pg18–27
- 8) A. Iino , A.Cho, A.Takagaki, R. Kikuchi , S. T. Oyama ; J. Catal; 311 (2014) pg.17–27
- 9) S.T. Oyama, X. Wang, Y.K. Lee, W.J. Chun; J. Catal; 221 (2004) pg.263–273
- 10) E.L. Muetterties, J.C. Sauer, J. Am. Chem. Soc. 96 (1974) pg 3410
- 11) S. Yang, C. Liang, R. Prins; J. Catal; 237; (2006) pg 118.
- 12) S. Sawhill, D. Phillips, M. Bussell; J. Catal; 215, (2003) pg 208–219
- 13) T. Korányi, Z. Vít, D. Poduval, R. Ryood, H.Seung-Kim, E. Hensen; J. Catal; 253, (2008) pg 119–131
- 14)A. Wang, , L. Ruan, Y. Teng, X. Li, M. Lu, J. Ren, Y. Wang, Y.Hu; J. Catal; 229, (2005) Pg 314–321)

- 15) Q. Guan, W. Li; *J. Catal*; 271; (2010) pg 413–415
- 16) H. Loboue, C. Guillot-Deudon, A. Popa, A. Lafond, B. Rebours, C. Pichon, T. Cseri, G. Berhault, C. Geantet; *Catal. Today*; 130; (2008) pg 63–68
- 17) H. Pfeiffer, F. Tancret, T. Brousse; *M. Chem. and Phys*; 92, (2005), pg 534–539
- 18) Y. Xie, H. Su , X. Qian, X. Liu, Y. Qian; *J. Solid State Chem*; 149,(2000) pg 88–91
- 19) A. Henkes, Y. Vasquez, R. Schaak; *J. Am. Chem. Soc*; 129 ,(2007) pg 1896–1897
- 20) X. Liu, L. Xu, B. Zhang; *J. Solid State Chem*; 212 (2014) pg13–22
- 21) S. Sawhill, K. Layman, D. van Wyk, M. Engelhard, C. Wang, M. Bussell; *J. Catal*; 231 (2005) pg 300–313
- 22) H. Song, M.Dai, X.Wan, X. Xu, C. Zhang, H. Wang; *Catal. Comm*; 43 (2014) pg.151–154
- 23) K. Kingma, R. Hemley ; *A. Mineralogist*; 79,(1994), pg 269-273

Chapter 4 : Bimetallic nickel phosphide catalysts for application in the water-gas shift reaction.

4.1 Introduction

The success of Ni₂P/SiO₂ as a high temperature water-gas shift catalyst as reported in the previous chapter, led to the exploration of improving this catalyst with the addition of further metallic components. The addition of these metallic components has the potential to modify physical and catalytic properties of the silica supported nickel phosphide catalyst. This chapter details the development and characterisation of silica supported transition metal phosphide catalysts using XRD, Raman spectroscopy, SEM, TGA, TEM, EXAFS and XPS techniques. The bimetallic catalysts were also tested in terms of the catalytic activity for the high temperature water-gas shift reaction and the results were compared and contrasted with the standard nickel phosphide catalyst and the industrial catalyst tested under comparable conditions.

4.2 Development and activity of bimetallic nickel phosphide catalysts.

The promising catalytic activity displayed by nickel phosphide has prompted the development of nickel phosphide catalysts with the addition of further metal components to produce bimetallic nickel phosphide catalyst. ^[1,2] The reason for this is to explore the potential for further improvement of catalytic performance and physical properties. ^[4,5]

The synthesis of silica supported bimetallic nickel phosphide catalysts is similar to that of silica supported nickel phosphide described previously. The most commonly used procedure in the literature is that of the temperature programmed reduction of phosphate precursors under hydrogen. ^[2] It is in the production of the phosphate precursor that second metallic element is added. In the study by Gaudette and co-workers, silica supported iron/nickel phosphide systems were prepared using metal compositions corresponding to 0.01 and 2.00 with regards to the stoichiometric ratio between the Ni and Fe content within the materials, forming materials with $\text{Fe}_x\text{Ni}_{2-x}\text{P}/\text{SiO}_2$ composition which varied depending on Fe and Ni loading. Calculated stoichiometric quantities of iron and nickel nitrate were dissolved in deionized water and impregnated onto the silica support. ^[6] Once dried solvated diammonium hydrogen phosphate was added to the support; this was then dried and calcined. It was then reduced under hydrogen at high temperature to the desired silica supported mixed metal phosphide.

Mixed transition metal phosphide systems are a group of materials that in comparison to bulk and supported monometallic phosphides have been less well documented with regards to catalytic activity. However studies produced in recent years to suggest that these mixed systems could be very useful materials for catalytic processes if the correct combination of metals can be identified. The majority of interest in bimetallic transition metal phosphides has focused on their application in hydrotreating processes. ^[2,6,7,8] Recent work has suggested that the catalytic activity of bulk phase monometallic phosphides was improved by the addition of cobalt or molybdenum as the secondary metal to form bimetallic phosphides. ^[6,7,10] Studies by Burns, Bussell and Smith developed and tested nickel rich systems containing small amounts of Co, Fe or Mo. ^[6-9] The materials were tested in comparison to the monometallic Ni_2P with regards to their catalytic performance in a number of hydrotreating reactions. The results of these studies showed nickel rich systems to all perform better than monometallic phosphide catalysts under similar conditions. ^[6-9]

A study on the application on bulk phase Ni_2P catalysts for the water-gas shift reaction was published by Rodriguez and co-workers. It was reported that addition of small amounts of caesium dramatically improved the catalytic activity of bulk phase nickel phosphide for the water-gas shift reaction. An increase in activity displayed by the catalyst was attributed to the increase in surface oxygen present on the catalyst as result of caesium doping. Figure 4-1 is taken from the study and shows the correlation between H_2 formation rates shown by catalysts and oxygen content displayed by each catalyst. The oxy-phosphide phases present in nickel phosphide have previously been identified as playing an important part in the catalytic activity of nickel phosphide.^[3]

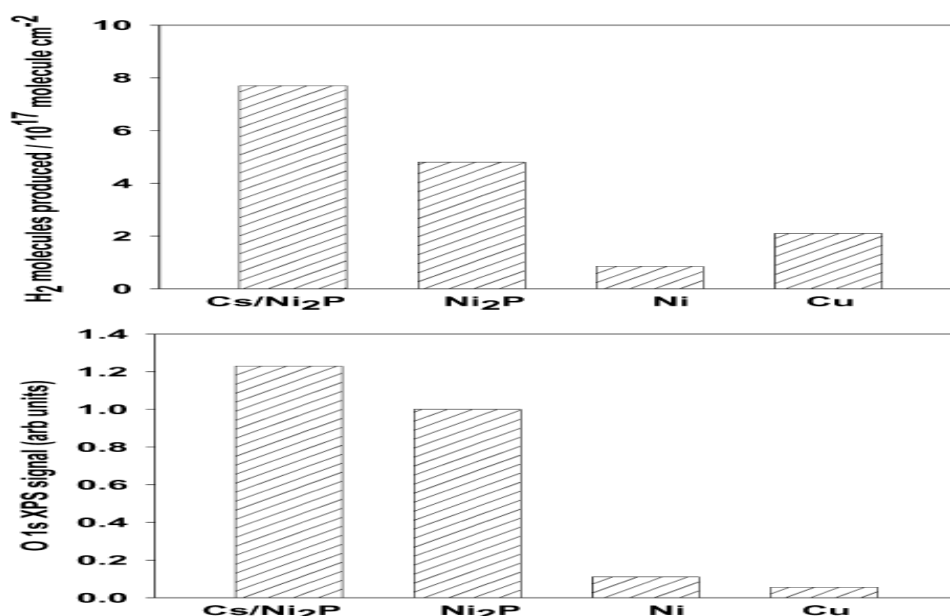


Figure 4-1: H_2 formation rates for catalysts and O XPS signal for catalysts. Graphic reproduced from study by Rodriguez and co-workers.^[3]

Not all studies of bimetallic phosphides have yielded positive results. A number of bimetallic systems which are less nickel rich have been developed by a number of groups. These have generally shown poor catalytic activity in comparison to the monometallic phosphides.^[23-24] However, little explanation has been offered, aside from suggestions of alteration of the chemical nature, or interactions with the support.^[23] In his review of phosphides as hydrotreating catalysts, Oyama suggests

this is caused by alteration of the active sites present on the corresponding monometallic phosphide, citing MoNiP in comparison to monometallic Ni₂P as an example, which has two different nickel environments of differing activities. In the bimetallic system the molybdenum replaces the square pyramidal type nickel site which is known to be highly active, with the molybdenum replacing this active nickel site this causes drop in catalytic activity.^[10] Previous studies on bimetallic transition metal phosphides have yielded mixed results with regards to improving catalytic performance of the catalyst in comparison to monometallic nickel phosphide catalysts. The previous studies indicated that nickel rich bimetallic nickel phosphide systems exhibited the best catalytic activity due to a greater presence on active Ni sites. The study by Rodriguez and co-workers established a direct correlation between the catalytic activity of bulk nickel phosphide in the water-gas shift reaction and the increase in surface oxygen present on the catalyst. This was result of doping nickel phosphide with small quantities of caesium. The use of ceria supports and cerium doping of nickel phosphide catalysts were reported by Wang and Liu respectively.^[13, 28] They were able to establish that the cerium positively affected oxygen presence on the catalyst surface which in turn boosted the hydrotreating activity of the catalyst in comparison to nickel phosphide catalyst that did not have any cerium present. An increase in catalytic activity for the water-gas shift reaction of silica supported nickel phosphide catalysts may also be possible with the addition of a second metallic component. The addition of secondary metal to nickel phosphide, such as caesium or cerium which have been previously reported, may improve catalyst activity due to an increase oxy-phosphide phases in the catalyst. However the quantity of secondary metal may also affect the activity negatively if it lowers the number of catalyst Ni sites present in the catalyst, therefore a balance in composition of the catalyst must be established to enable maximum catalytic potential.

4.3 The development and characterisation of cerium doped Ni₂P/SiO₂ catalysts.

The addition of cerium to the silica supported nickel phosphide catalyst was undertaken with a view to improving the catalytic activity of the catalyst for the water-gas shift reaction. The synergistic relationship between cerium and nickel phosphide has previously been reported, with the addition of cerium increasing surface oxygen. These oxygen rich phases have been identified as being beneficial to the activity of the catalyst. As well as potentially improving the activity of nickel phosphide, cerium has also been well documented as being an active water-gas shift catalyst in its own right and exhibits sulfur tolerance under the reaction conditions.^[21] The use of ceria as a support for water-gas shift catalysts has also been investigated, with Pd, Fe, Ni and Cu active phases all being placed upon ceria supports. The catalytic activity of these materials has been shown to be promising due to cerium promoting the activity of the metal site by improving the oxygen capacity displayed by the cerium support over silica.^[22] Cerium was added to Ni₂P/SiO₂ catalysts at loadings of 0.5%, 1%, 5% and 10 w.t % with regards to the metal loading. The cerium doped nickel phosphide catalysts were produced using a similar method to monometallic nickel phosphide catalysts supported on silica described previously in the experimental chapter. The only difference between preparation of bimetallic and monometallic nickel phosphide catalysts was the addition of the secondary metal nitride which was impregnated onto the silica support. The loading of nickel was consistent with the Ni₂P/SiO₂ catalyst described previously; this was 20% Ni with respect to the total weight of the catalyst. The impregnation of the support with the second metal solution was undertaken after the initial impregnation of the silica with the nickel nitrate solution.

The XRD patterns for Ce-Ni₂P/SiO₂ catalysts with weight loadings of 0.5%, 1%, 5%, and 10% of cerium are presented in Figure 4-2. The 10% Ce loaded nickel phosphide catalyst displays two diffraction peaks at 44° and 51° 2theta, which are associated with the (1 1 1) and (2 0 0) planes of Ni metal phase. This indicates a mixed phase of nickel metal and nickel phosphide are present. Diffraction peaks

associated with the Ni_2P crystal phase are not evident in the 10% Ce loaded catalyst. This is possibly a result of the particles being more highly dispersed on the support or the limited formation of the Ni_2P phase, as a consequence of the addition of Ce to the material. A decrease in particle size of Ni_2P on the support with the addition of Ce to the catalysts was reported by Li and co-workers.^[11] Formation of nickel metal clusters within the material is to be expected with addition of cerium influencing the species of nickel formed as has previously been reported by Li.^[14] The 0.5%, 1% and 5% Ce loading catalysts also display small peaks associated with Ni_2P which are weak due to the high dispersion of nickel phosphide particles on the amorphous silica support. The addition of Ce to the nickel phosphide materials also produced a mixed phase of nickel phosphide stoichiometries. Diffraction peaks attributed to Ni_{12}P_5 are present in all materials containing Ce; these peaks at 38° and 48° 2theta are not apparent in the diffraction pattern for bulk phase Ni_2P . The diffraction patterns for the Ce- $\text{Ni}_2\text{P}/\text{SiO}_2$ catalyst confirm a relationship between Ce loading of the catalysts and number of Ni metal sites present in the catalyst, as well as the formation of mixed phases of nickel phosphide within the material. This is characterised by reflections associated with Ni_2P becoming more prominent with decreasing Ce loading the catalysts. This is characterised by increasing prominence of peaks at 41° and 47° . These peaks are much clearer in the diffraction patterns for catalysts with 0.5% and 1% loadings of Ce. This may also indicate that these are more poorly dispersed due to the lower loading of Ce in the material. The catalysts with lower loadings of Ce also show less intense Ni metal diffraction peaks at 44° and 51° 2theta in comparison to the catalyst with 10% Ce loading, which suggests that there are less Ni metal sites present in these catalysts. Diffraction peaks associated with nickel cerium phosphides were not observed in the XRD patterns of the Ce- $\text{Ni}_2\text{P}(x)$ samples. There is however some evidence of lattice distortion in the cerium doped phosphides characterised by the small shift in reflections associated the Ni_2P and Ni_{12}P_5 crystal phases. The lattice distortion exhibited by the doped materials may affect the overall activity of the materials in comparison the mono metallic catalyst. The largest diffraction peaks for cerium are found at 28° , 47° and 56° 2theta and are associated with the (1 1 1), (2 2 0) and (3 1 1) planes respectively. These features are not evident in the diffraction patterns for any of the materials. Therefore, it remains unclear which state Ce exists within the materials from the XRD patterns. The average crystallite size within each catalyst was

estimated using the Scherrer equation based on each materials diffraction pattern. The average crystallite size for each material was estimated as follows; 10% Ce- 37.9 nm, 5% Ce- 41.5 nm, 1% Ce- 36.3 nm and 0.5% Ce- 37.1 nm. The average crystallite size for the Ce doped catalysts was generally much larger than the mono metallic Ni_2P catalyst which was estimated to have an average crystallite size of 25.2 nm. The addition of Ce to the nickel phosphide system appears to directly influence crystallite size.

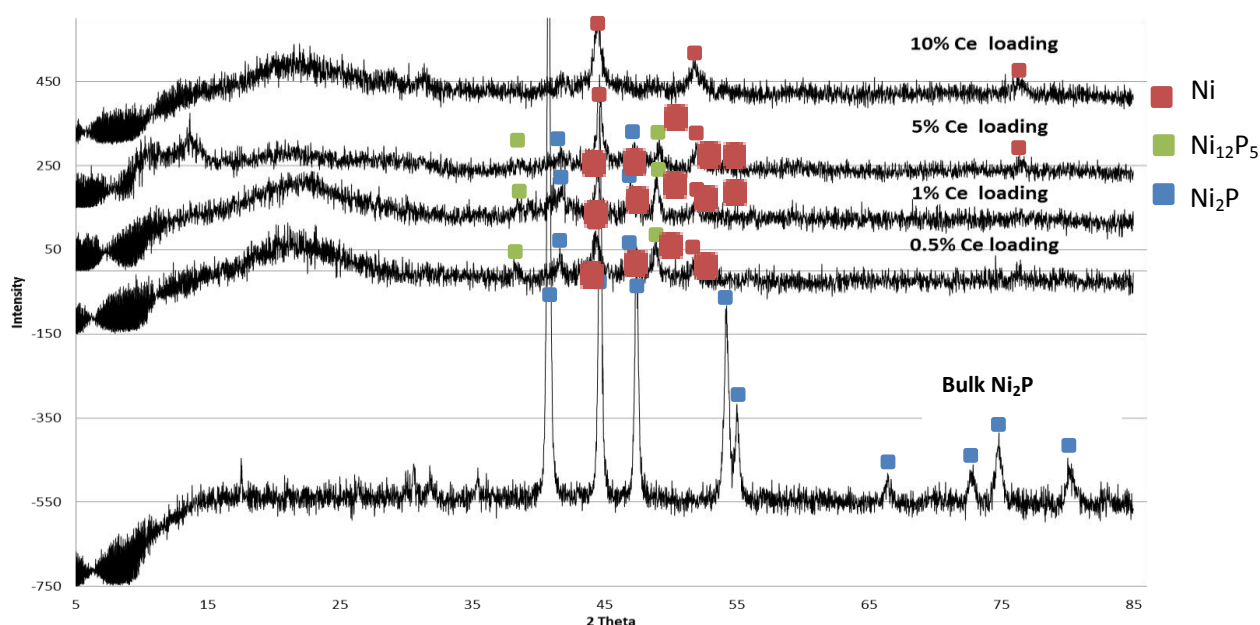


Figure 4-2: XRD patterns for Ce- $\text{Ni}_2\text{P}/\text{SiO}_2$ catalysts with Ce loadings of 0.5%, 1%, 5% and 10%.

Thermogravimetric analyses of the reduction of the phosphate precursors to Ce- $\text{Ni}_2\text{P}/\text{SiO}_2$ catalysts were carried out under flowing H_2/N_2 (5% H_2) up to 800°C with a ramp rate of $10^\circ\text{C}/\text{min}^{-1}$. The TGA reduction profiles for catalysts containing 1% Ce and 10% Ce loadings are shown in Figures 4-3 and 4-4 respectively. The reduction profile for the catalyst with 1% Ce loading (Figure 4-3) shows three distinct peaks, the small peak at 55°C is attributed to loss of water from the material. There is a further small peak at 435°C . This has been attributed to the reduction of nickel oxide to nickel metal. The largest peak shown in the profile at 751°C has been identified as

the reduction of the nickel phosphate to phosphide. This is consistent with TGA reduction profiles displayed in the previous chapter for the reduction of nickel phosphate to nickel phosphide. The derivative weight peak at 751°C is broad, indicating that more than one species of phosphate precursor may be present. The presence of two nickel species is suggested by the occurrence of two reduction peaks, one associated with the formation of nickel metal and the other with nickel phosphide. The assignment of these reduction peaks are based on those identified in the previous chapter. The weight loss for the Ni metal reduction peak is small in comparison to the loss for the Ni₂P reduction peak suggesting more Ni present in the phosphide phase. This is consistent with the diffraction pattern for the catalyst which indicated the catalyst was mostly Ni₂P. The weight percentage was measured 87% of the total weight of sample. The theoretical weight loss for Ni₃(PO₄)₂ to Ni₂P was estimated to be 88% on the basis of 20% loading of Ni on the silica support. This indicates that the reduction is mostly nickel phosphate to nickel phosphide in the 1% Ce loading catalyst.

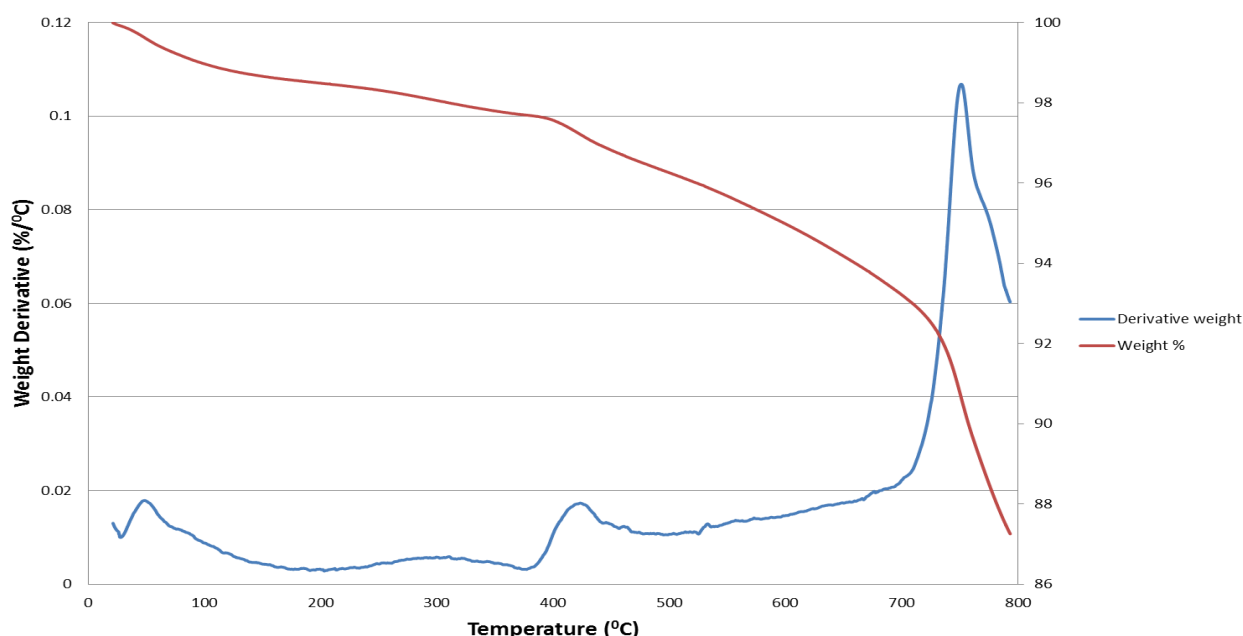


Figure 4-3: TGA reduction profile for Ce-Ni₂P/SiO₂ catalyst with 1% Ce loading

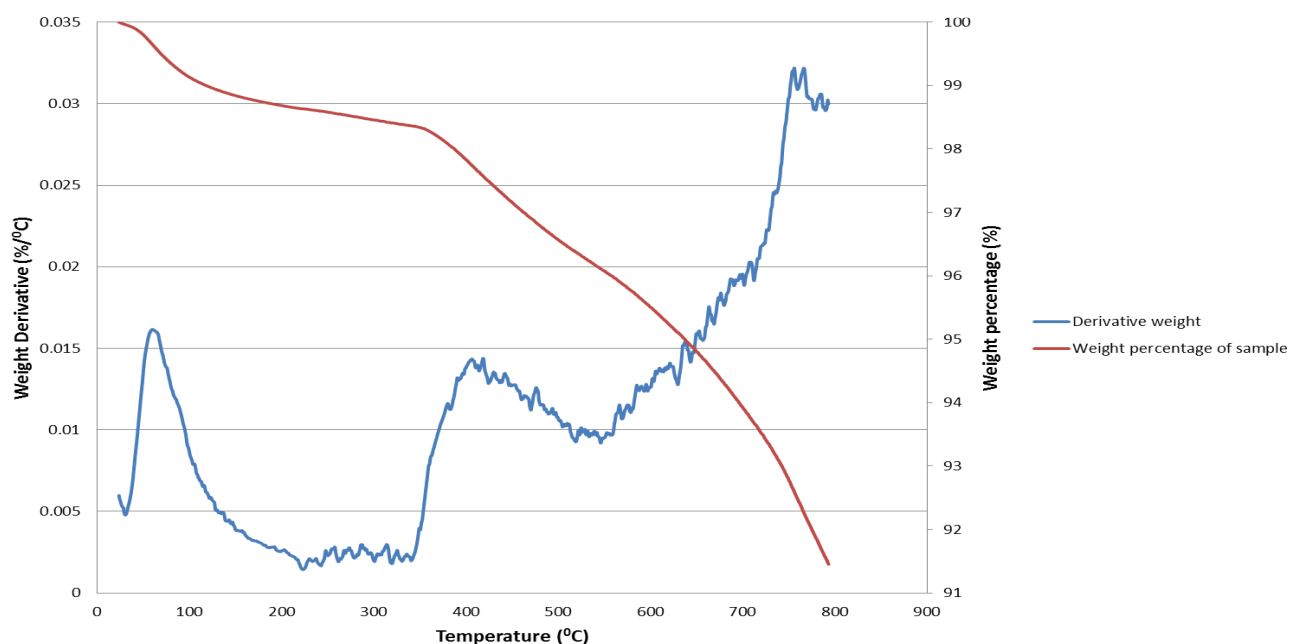


Figure 4-4: TGA reduction profile for Ce-Ni₂P/SiO₂ catalyst with 10% Ce loading.

Figure 4-4 displays the TGA reduction profile for Ce-Ni₂P/SiO₂ with 10% Ce loading. The reduction profile again exhibits 3 distinct peaks; the first at 56°C is attributed to the loss of water from the sample. The peaks at 400°C and 755°C are attributed to the reduction of nickel oxide and nickel phosphate respectively. These reduction temperatures are close to those described in previous studies as well as the catalysts used in this study. [23] The peak in derivative weight at 400°C associated with the reduction of nickel oxide to nickel metal is relatively large, suggesting a significant quantity of nickel is present in the resultant material. This was characterised by a 4% loss in sample weight. The nickel phosphide catalyst with 10% Ce loading shown in Figure 4-4 displays a very different reduction profile in comparison to the 1% Ce loaded material (Figure 4-3). This is due to the increased portion of nickel present in the resultant catalyst in comparison to the 1% Ce loading catalyst. The quantity of nickel phosphide present in the material is lower, as evidenced by the lower sample weight loss exhibited by the material at 755°C.

Ce-Ni₂P/SiO₂ catalysts with 1% and 10% Ce loading were studied using SEM to determine surface morphology of the materials. EDX analysis was carried out a number of points to determine an average weight and atomic percentage for each element within the sample. The micrograph and table of EDX results for the 1% Ce loading Ce-Ni₂P/SiO₂ catalyst are presented in Figure 4-5 and Table 4-1 respectively. The micrograph shows particles, thought to be silica supported nickel phosphide, that are lightly coloured in contrast with the dark carbon support. The particles range in size from 3µm to 25µm. Elemental analysis of these particles (displayed in Table 4-1) is consistent with the presence of Ni₂P in these light coloured particles. EDX analysis of the material was not able to be applied to identify the presence of Ce in the catalyst due to the K-edge of Ce (40.4 keV) being higher than measured range of the instrument.

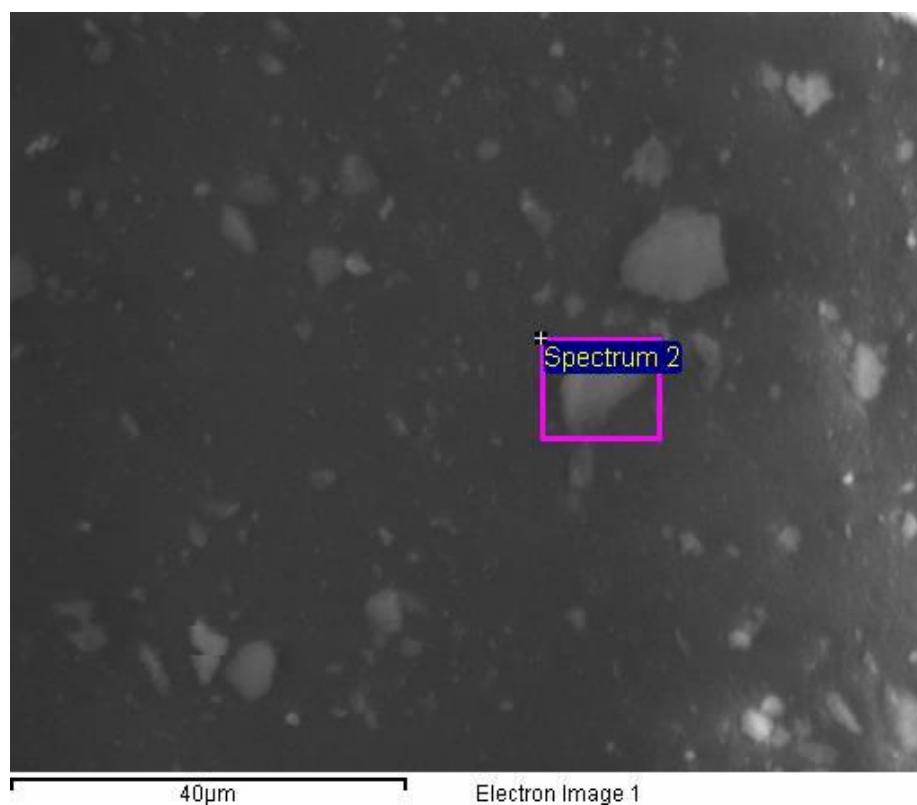


Figure 4-5: SEM micrograph for Ce-Ni₂P/SiO₂ catalyst with 1% Ce loading.

Element (edge)	Weight%	Atomic%	Average At % (deviation)
P (K)	25.20	37	38.2 (± 5)
Ni (K)	74.80	63	63.6 (± 4)
Ce K edge out with range measure by instrument	N/A	N/A	
Total	100.00	100.00	

Table 4-1: Table summarising EDX analysis of target particles.

An SEM micrograph for Ce-Ni₂P/SiO₂ with 10% Ce loading is presented in Figure 4-6. The micrograph for the 10% Ce loading catalyst shows the presence of light particles on a dark surface. These light particles are thought to be the silica supported cerium doped nickel phosphide material. The light appearance of the particles in contrast to the carbon pad is possibly a result of the differing composition of the particles in comparison to the carbon pad. These particles range in size from 1 μ m to 15 μ m. EDX was not carried out on this material as the EDX instrument was not available for use at time of analysis of the material.

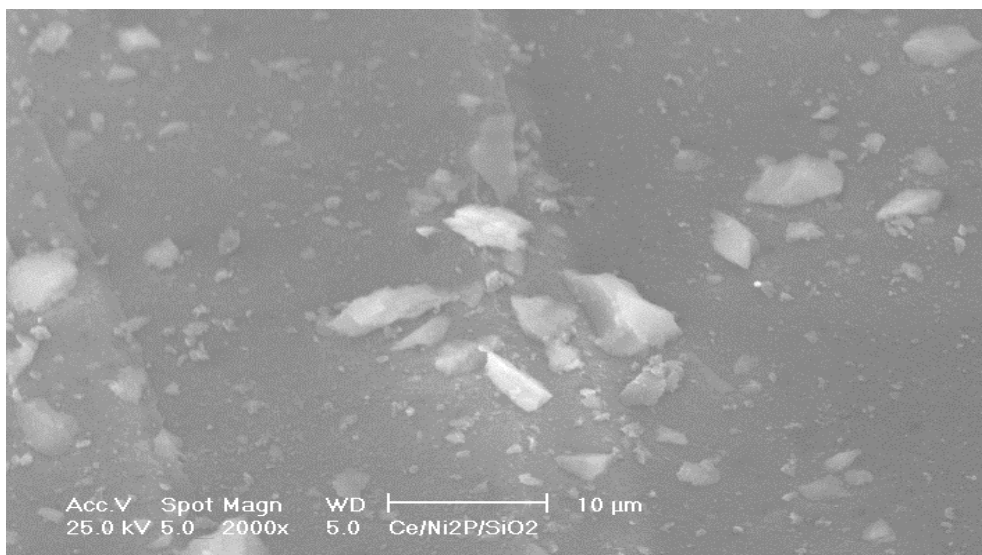


Figure 4-6: SEM micrograph for Ce-Ni₂P/SiO₂ catalyst with 10% Ce loading

The Ce-Ni₂P/SiO₂ (10% Ce loading) catalyst was studied using TEM. The resultant images are presented in Figure 4-7. EDX characterisation was also carried out; Table 4-2 summarises the results of the analysis. The micrographs show uniform particles with sizes between 5-15nm, similar to TEM micrographs presented in the previous chapter for Ni₂P/SiO₂. The micrographs show a mostly uniform dispersion of particles on the support. The TEM micrograph also indicates the ordered crystal phases exhibited by cerium- nickel phosphide on the support, a common feature of transition metal phosphides. The crystal fringes in the TEM image displayed lattice parameters of 1.84 Å and 2.97 Å indicating that there are two crystallographic planes present. The lattice parameter at 1.84 Å corresponds to the reflection at 56.1° 2theta in the XRD pattern for the material. This is consistent with the (2 1 1) crystallographic plane of Ni₂P. The second lattice parameter at 2.97 Å is consistent with the (1 1 1) plane of Ni₂P which corresponds to the reflection at 40.2° 2theta in the XRD pattern for Ni₂P. These reflections are not present in the diffraction pattern for the material. This confirms the presence of Ni₂P on the support, which was not evident in the XRD pattern. The size and shape of the active phase particles appear similar to those seen the micrograph for Ni₂P/SiO₂ presented in the previous chapter. The EDX analysis of the ordered phase highlighted in Figure 4-7 indicates that the material contains both cerium and nickel phosphide. The atomic ratio is estimated to be roughly 1:1:1 with respect to P: Ni:Ce. This was the only point which was analysed

using EDX analysis therefore it cannot be assumed that atomic ratios are the same throughout the material. The elemental analysis does however indicate that the Ce and nickel phosphide appear to co-exist in the same crystal structure in the material.

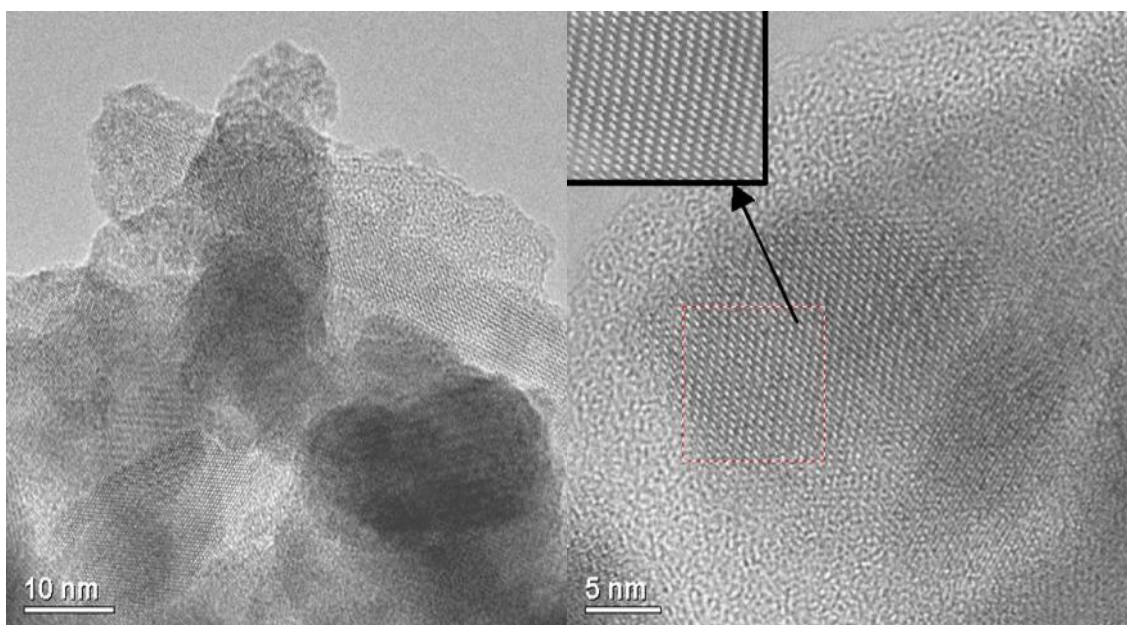


Figure 4-7: TEM micrographs showing Ce-Ni₂P/SiO₂ with 10% Ce loading

Element (edge)	Peak Area	Element %	Sigma %	Atomic %
O (K)	5313	11.56	0.23	37.02
Si (K)	4824	6.81	0.17	12.42
P (K)	5903	8.62	0.20	14.25
Ni (K)	5681	18.96	0.48	16.54
Ce (L)	13011	54.05	0.54	19.76
Total		100.00		100.00

Table 4-2: Summary of EDX analysis results for targeted crystallite structure.

Ce-Ni₂P/SiO₂ with 10% w.t. Ce loading was analysed using Raman spectroscopy. Figure 4-8 displays the resultant Raman spectrum for Ce-Ni₂P/SiO₂. The spectrum is compared alongside the bulk phase Ni₂P and Ni₂P/SiO₂ counterpart spectra. The spectrum shows a sharp peak at 950 cm⁻¹. This peak has been identified as a P=O stretch indicating the presence of oxygen in the nickel phosphide phase of the material. There are further P=O bond stretching modes that have been assigned to the peaks at 811 cm⁻¹ and 898 cm⁻¹ and these peaks indicate the presence of oxyphosphide phases are present in the material. The P=O stretching peaks are also present in both the bulk silica supported nickel phosphide spectra. There is also weak peak at 450 cm⁻¹. This was initially identified the bulk phase material previously as Ni-P bond stretching. The supported nickel phosphide spectra are weaker in comparison to those in the bulk phase material. The Raman spectrum for the supported nickel phosphide catalyst closely resembles that of the bulk phase material, further supporting previous characterisation of the nickel phosphide catalyst suggesting that nickel phosphide is present on the silica support.

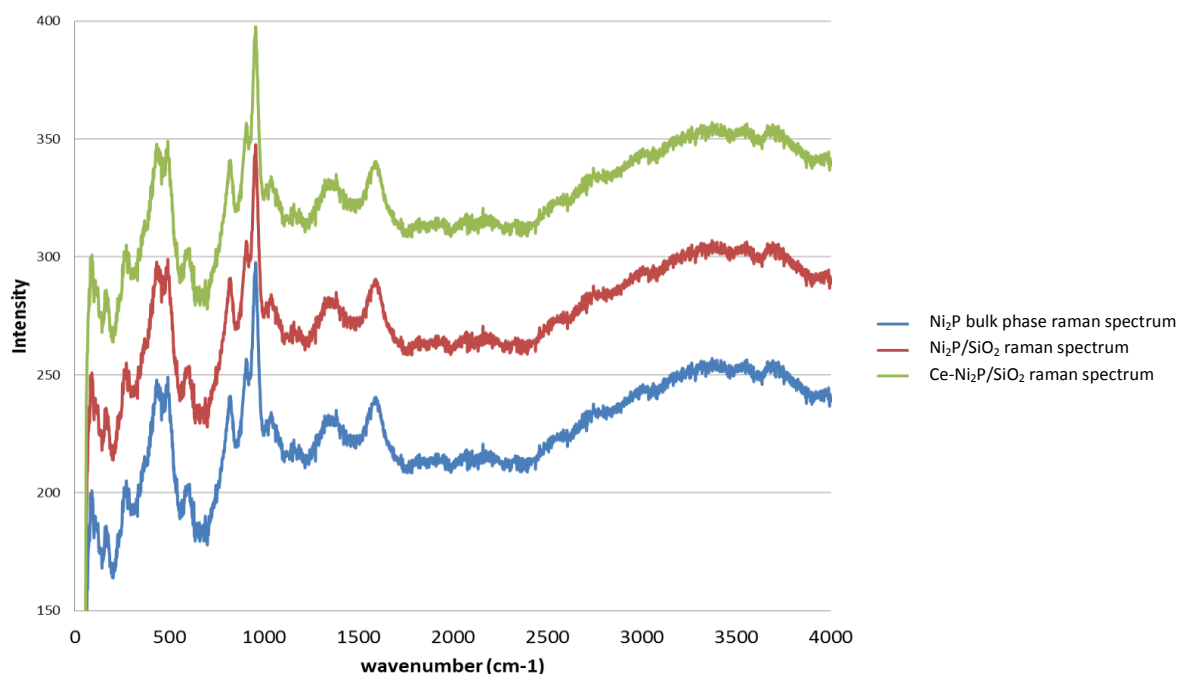


Figure 4-8: Raman spectra for Ce-Ni₂P/SiO₂ (10% Ce loading), Ni₂P/SiO₂ and bulk Ni₂P.

The 10% Ce loading Ce-Ni₂P/SiO₂ catalyst was characterised using XPS, to enable a greater understanding of the chemical state in which nickel and phosphorus exist within the material in the near surface regions. The Ni 2p and phosphorus 2p spectra are shown in Figures 4-9 and 4-10 respectively. Table 4-3 displayed the tabulated binding energies derived from the spectra from Ni₂P/SiO₂ and Ce-Ni₂P/SiO₂.

The nickel 2p spectrum for Ce-Ni₂P/SiO₂ exhibits a number of differences in comparison to Ni₂P/SiO₂. The spectrum for the 10% Ce catalyst shows 3 binding energy peaks associated with nickel species within the material. The binding energy peak at 850.2 eV can be attributed to Ni⁰. This feature was absent in the Ni₂P/SiO₂ nickel 2p spectrum. The XRD pattern and TGA profile for the material presented earlier both suggested the presence of a nickel metal phase fraction. The spectrum shows two further binding energy peaks associated with Ni, a major peak at 853.4 eV and minor peak at 857.1 eV. These were identified in the previous chapter as nickel species related to Ni₂P. The peak at 853.4 eV has been identified as Ni^{δ+}, where 0 < δ+ < 2, which is consistent with it being bonded to phosphorus in Ni₂P. The minor peak in the spectra at 857.1 eV has been assigned to Ni^{II+} species associated with possibly nickel oxide as result of passivation of the nickel species. Another possibility is the formation of oxy-phosphide surfaces that promote the catalytic activity of the material.^[3] The phosphorus 2p spectrum, however for the material does not display any features associated with phosphate or pyrophosphate phases which may be a result of only small amounts of phosphorus being in the state. The Ce 3d binding energy peaks are also visible in the spectrum for Ce-Ni₂P/SiO₂. Two peaks are identified at 880.2 eV and 882.9 eV, the other broad peak at 900.1 eV is identified as a satellite peak. According to previous studied these peaks are associated with Ce^{II+} and Ce^{IV+} respectively, indicating that Ce exists in the material in a mixed phase two different species of Ce.^[13]

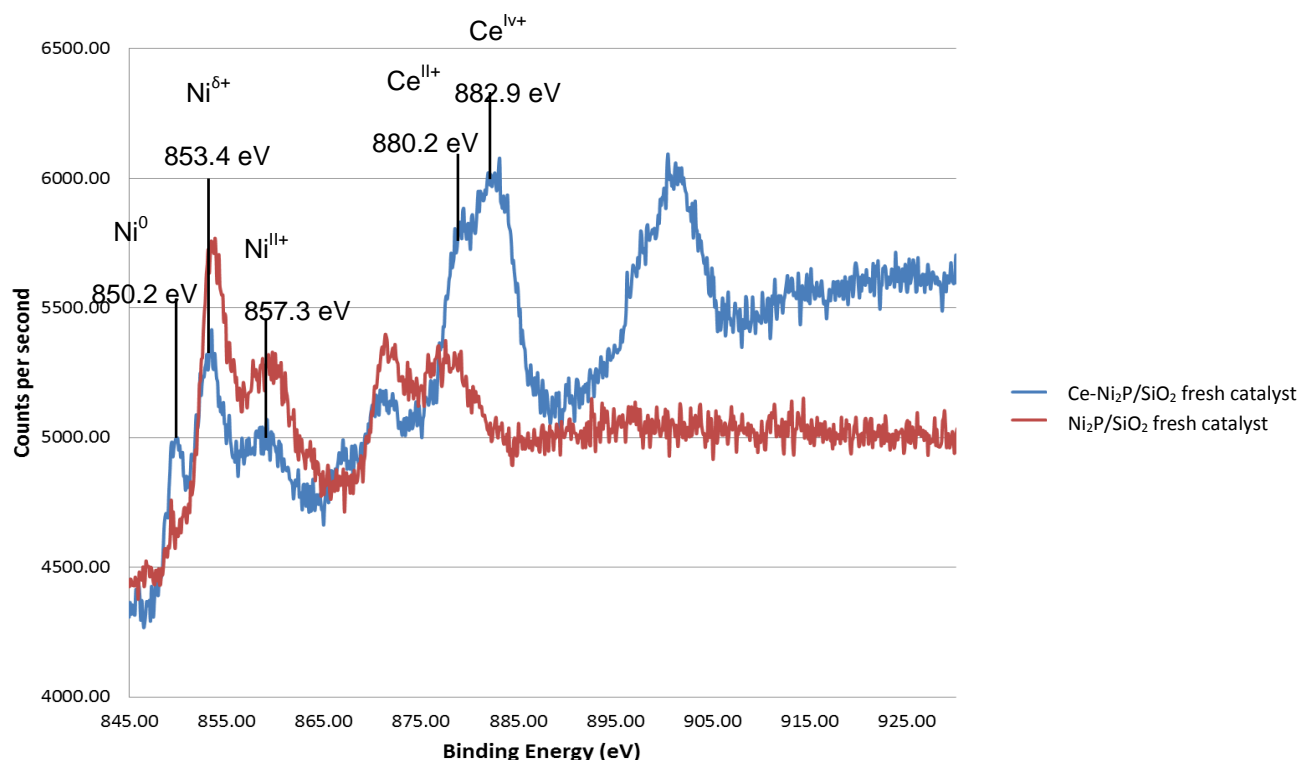


Figure 4-9: XPS Ni 2p and Ce 3d spectrum for Ce-Ni₂P/SiO₂ using 10% Ce w.t loading.

The phosphorus 2p spectrum for 10% Ce loading Ce-Ni₂P/SiO₂ (Figure 4-10) exhibits a single peak at 130.2 eV indicating is a single species of phosphorus present in the catalyst. The peak is centred at 130.2 eV and has been identified as P^{δ-} where 0 < δ- < 1 according to previous studies. The phosphorus peak binding energy peak is slightly lower than P binding energy previously reported for Ni₂P/SiO₂ as can be seen in Figure 4-10 , with the peak centring at 130.6 eV for Ni₂P/SiO₂. The phosphorus species in Ce-Ni₂P/SiO₂ is still within the reported range for Ni₂P. However, the lower binding energy possibly suggests a lower degree of oxygen content within the material in comparison to the Ni₂P/SiO₂. The lower oxygen content is can be attributed to the greater presence of Ni metal sites in material which has resulted in a decrease in Ni₂P sites showing a greater affinity for oxygen than the Ni metal sites. As has been discussed previously, oxy-phosphide phases in the nickel phosphide catalyst are reported to play a crucial role in the catalytic activity of the material there for it can be assumed that the decrease in oxy-phosphide phases in the catalyst may negatively affect the activity of the material as will addressed later in the chapter.

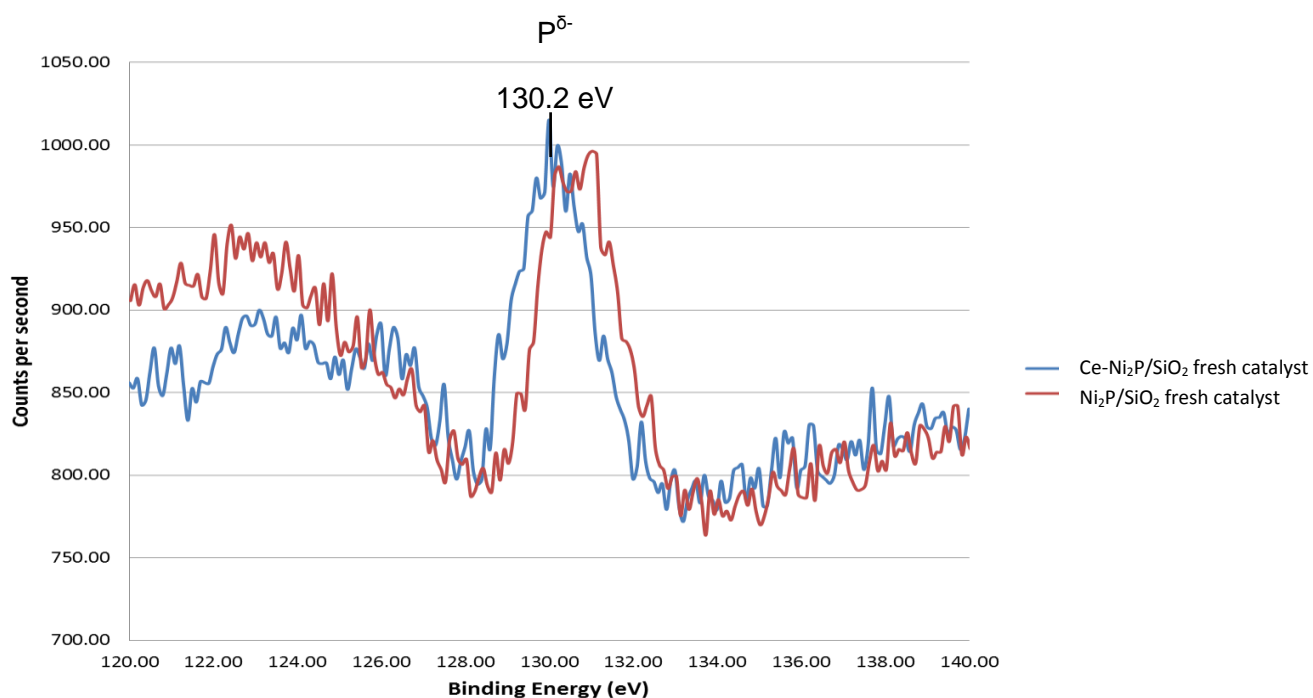


Figure 4-10: XPS P 2p spectrum for Ce-Ni₂P/SiO₂ using 10% Ce w.t. loading

Sample	Ce-Ni ₂ P/SiO ₂	Ni ₂ P/SiO ₂
	Binding energy	Binding energy
Element	(eV)	(eV)
Ni 2p	850.2 (smallest) 853.4 (largest) 857.3	853.5 (largest) 856.8 (smallest)
P 2p	130.2	130.6
O 1s	532.9	532.8
C 1s	285.0	285.0
Ce 3d	880.3(smallest) 882.9(largest)	N/A

Table 4-3: Summary of binding energy peaks shown in spectra for Ni₂P/SiO₂ and Ce-Ni₂P/SiO₂

The cerium doped nickel phosphide catalysts were analysed using X-ray absorption spectroscopy. The study was focused primarily on the extended X-ray absorption fine structure spectrum of the material although the XANES region was briefly explored for the materials as well to gain insight into oxygen affinity for nickel within the catalysts. Figure 4-11 displays the k^3 weighted EXAFS spectrum for Ce-Ni₂P/SiO₂ (10% w.t. Ce) and Figure 4-12 presents the Fourier transformed spectrum for the material. Both spectra have been refined and a theoretical curve has been applied through collaboration with Prof. G. Sankar from University College London. The results of the curve fit for the FT spectra for the material are summarised in Table 4-4.

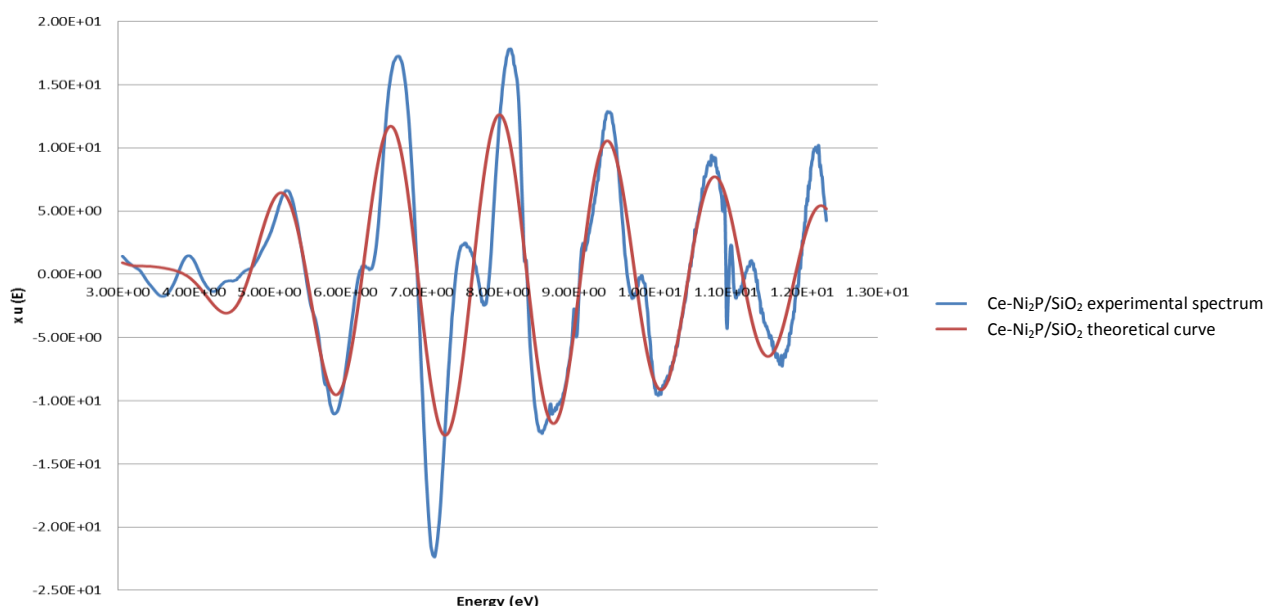


Figure 4-11: k^3 weighted Ni K edge EXAFS spectrum for Ce-Ni₂P/SiO₂ (10% w.t. Ce) catalyst along with theoretical curve fit.

The curve fitting results for the Ce-Ni₂P/SiO₂ (10% w.t. Ce) EXAFS spectrum are presented in Table 4-4. The nickel K edge FT spectrum for the material displays a single broad peak corresponding first shell which has been fitted. There are further peaks associated with 2nd and 3rd shells however these have not be fitted. The 10% Ce loaded catalyst differs from the Ni₂P/SiO₂ which was presented in the previous

chapter. The difference between the two spectra further supports earlier characterisation of the materials which suggested that Ce loading alters the active phase of the material in comparison to $\text{Ni}_2\text{P}/\text{SiO}_2$ without any Ce present. The peak which was fitted with the theoretical curve is centred at 0.243nm this was the only shell from the spectrum fitted. The further shells in the FT spectrum for the material have not been fitted due to unsatisfactory fits being obtained. The theoretical fit has taken into consideration Ni-P, Ni-Ni and Ni-O scattering from the nickel centre to achieve the best curve fit for the spectrum. The Ni-P distance according to the fit is estimated to 0.219nm which is within the reported range (0.218-0.231nm) for Ni-P bond distance reported in the literature.^[4] Comparison of the Ni-P distance for the Ce 10% loading catalysts with $\text{Ni}_2\text{P}/\text{SiO}_2$ shows Ni-P distance has shortened within the Ce containing catalyst from 0.221nm to 0.219nm. The theoretical curve fit for the Ce estimates a decrease in average co-ordination number for Ni-P in comparison to $\text{Ni}_2\text{P}/\text{SiO}_2$ from 4.05 to 3.84. The decrease in the co-ordination number for the Ce doped catalyst suggests that the nickel phosphide particle size has decreased. The decrease in particle size contradicts the estimated particle size calculated from the XRD pattern for the material. This suggests that the particle size increased with the addition of Ce to the system in comparison to monometallic material and highlights the potential limitations of the using the Scherrer equation when estimating particle size. A decrease in the nickel phosphide particle size has been previously documented in the literature as a result of Ce doping influencing the nickel phosphide crystallite formation. The curve fit indicated that a co-ordination number of 4 suggesting that 4 P neighbours are present around the nickel atom. Ni-Ni scattering was identified at a distance of 0.251nm to Ni neighbours, with a co-ordination number of 4.76, suggesting as many as 5 Ni neighbours present. The greater number of Ni-Ni sites in the material in comparison to previously reported values in literature is attributed to the formation of more Ni metal sites in the catalyst due to the influence of Ce. The fitting of the theoretical curve estimates that 40% of nickel in the material exists as Ni metal. Another feature associated with the Ni metal phase in the material is presence of Ni-O. The fit for the $\text{Ni}_2\text{P}/\text{SiO}_2$ did not contain any considerations for oxygen to nickel scattering in the first shell. Comparison of the Ni-Ni scattering for the 10% w.t. Ce catalysts with the $\text{Ni}_2\text{P}/\text{SiO}_2$ shows that Ni-Ni bond distance decreases from 0.258nm to 0.251nm. There was also an increase in co-ordination number which was 4.21 for $\text{Ni}_2\text{P}/\text{SiO}_2$ and 4.76 for the Ce doped nickel

phosphide catalyst. The increase in co-ordination number combined with the decrease in the distance between Ni-Ni scattering of the Ce doped catalyst in comparison to Ni₂P/SiO₂ is consistent with the Ce containing catalyst being richer in Ni metal species than the Ni₂P catalyst.

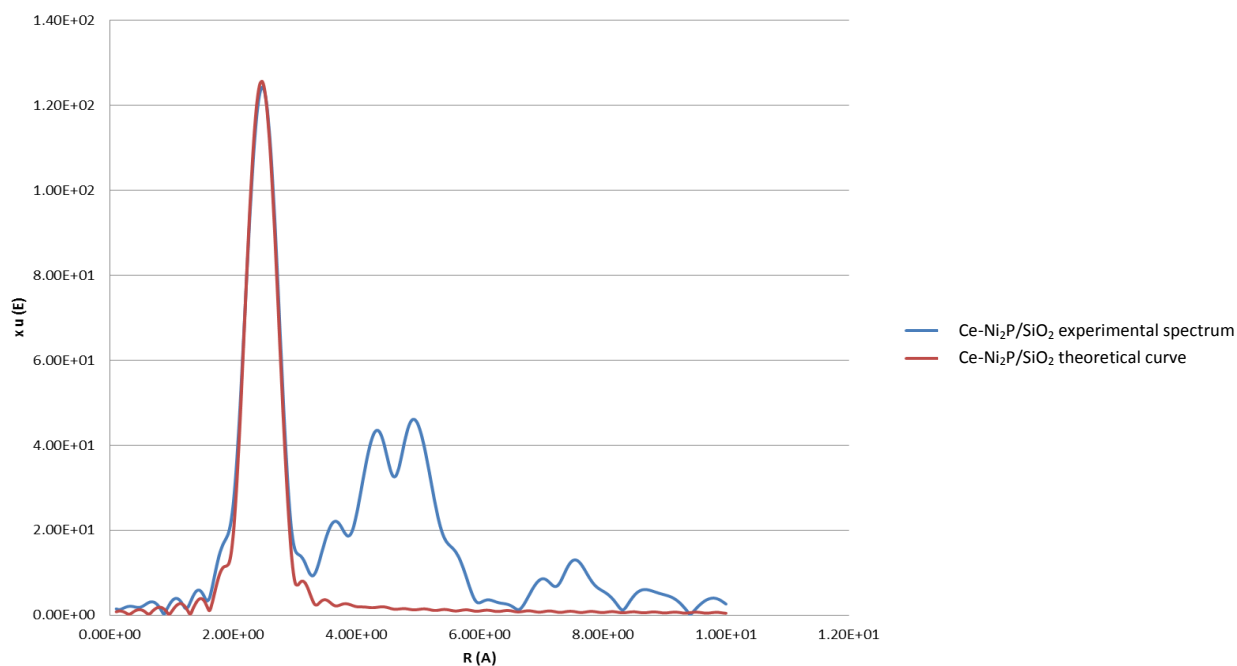


Figure 4-12: Fourier transformed spectrum for Ce-Ni₂P/SiO₂ (10% w.t. Ce) catalyst along with theoretical curve fit.

Shell Factor	Scatterer	Bond distance (Å)	co-ordination No	A	A FAC	ΔE	R-
1	Ni-P	2.19	3.84	0.01303	0.7735	3.9952	45.9107
2	Ni-Ni	2.51	4.76	0.01767	0.7735		
3	Ni-O	2.96	1.27	0.01767	0.7735		

Table 4-4: Summary of curve fit results for Ce-Ni₂P/SiO₂ (10% w.t. Ce) EXAFS spectrum.

4.4 The catalytic testing of cerium doped Ni₂P/SiO₂ catalysts.

The catalytic activity of Ce doped nickel phosphide catalysts with 10%, 5% 1% and 0.5 w.t. % loadings of Ce were tested under high temperature water-gas shift reaction conditions. The catalytic testing was carried out using the same reactor and conditions used previously. The reaction profile for Ce-Ni₂P/SiO₂ (10 w.t. % Ce) is displayed in Figure 4-13. The reaction profile shows the catalyst displays significant activity under the reaction conditions with CO₂, H₂ and CH₄ being produced throughout the run. The run produces significant CO₂ and H₂ indicating that the water-gas shift reaction is taking place. CH₄ is also produced, indicating that a methanation process is also occurring. The carbon balance was calculated to be an average of 95% over the duration of the run. The methanation is most likely due to the presence of the nickel metal phase the in catalyst which was identified in the characterisation of the material. Nickel is known to be a highly active methanation catalyst under these reaction conditions.^[24] The discrepancy between CO₂ and H₂ formation rates in the reaction profile can also be attributed to the methanation activity shown by the catalyst, with H₂ proportionately used to form the CH₄. Formation rates for CO₂ and H₂ reach steady state after roughly 10 hours of running. It is assumed that this process is associated with an induction period within the reactor. This phenomenon is associated with nickel phosphide and has been seen in all catalysts tested. The formation rate for CH₄ reaches steady state more rapidly than CO₂ and H₂ which further suggests that methanation occurs at a different active site to the water-gas shift reaction. The reaction profile shows a drop in CH₄ formation rate combined with an increase in CO after 75 hours of time on stream. This is most likely deactivation of the active sites caused by coking, with the Boudouard reaction being favourable under the reaction conditions. There is no drop in CO₂ or H₂ during this period of time further supporting the suggestion that methanation and the water-gas shift reaction take place at different active sites within the catalyst. The 10% Ce doped catalyst produced more CH₄ and less H₂ in comparison to the Ni₂P/SiO₂ catalyst.

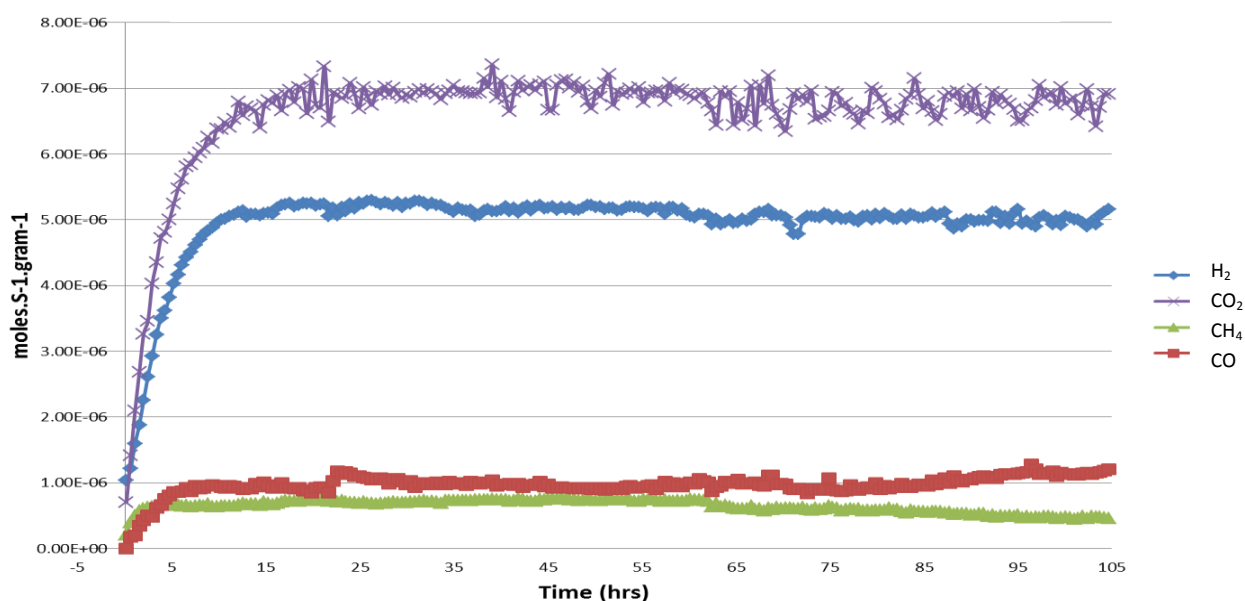


Figure 4-13: Reaction profile for Ce-Ni₂P/SiO₂ (10% w.t. Ce loading) under high temperature water-gas shift conditions

Comparison of hydrogen and carbon dioxide formation rates for Ce-Ni₂P/SiO₂ with 10% Ce loading with the industrial catalyst run under the same reaction conditions per weight of catalyst is shown in Figure 4-14. The formation rates for the 10% Ce doped catalyst for both hydrogen and carbon dioxide are higher than those displayed by the industrial catalyst under the same conditions once the reaction reaches steady state. The carbon dioxide formation rate is roughly 75% greater than that of the industrial catalyst. A similar but less significant trend was seen with the hydrogen formation rate for the 10% Ce doped catalyst. The hydrogen formation rate was approximately 25% greater than was shown by the industrial catalyst. The difference between hydrogen formation rate for the 10% Ce catalyst and the industrial is smaller due to the higher proportionate loss of hydrogen produced caused by methanation.

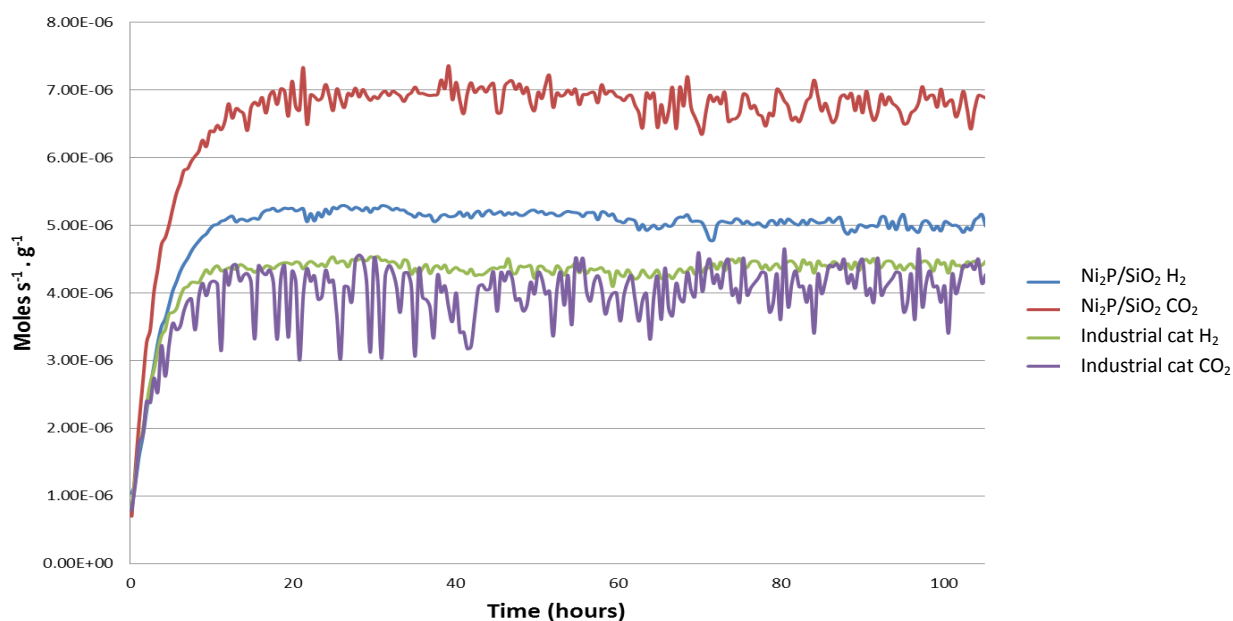


Figure 4-14: Comparison of H₂ and CO₂ formation rates for industrial catalyst and Ce-Ni₂P/SiO₂ (10% w.t. Ce loading) under high temperature water-gas shift conditions.

The reaction profile for the high temperature water-gas shift reaction testing of Ce-Ni₂P/SiO₂ using 5 w.t. % loading of Ce is displayed in Figure 4-15. The reaction profile indicates that the catalyst displays significant activity under the reaction conditions with CO₂, H₂ and CH₄ being produced throughout the run. The run produces significant CO₂ and H₂ indicating that the water-gas shift reaction is taking place. The 5% Ce loaded catalyst also produced a significant amount of CH₄, suggesting methanation is occurring as a result of the nickel metal phase present in the catalyst. The carbon balance was calculated to be an average of 87% over the duration of the run. The reaction does not reach steady state in terms of formation rates of products until after 20 hours on stream and remains steady for the duration of the run. The delay in the catalyst reaching steady state formation rates is thought to be due an activation process occurring within the material during this period of time. This activation period is much longer than was seen with the 10% Ce doped catalyst suggesting a difference in active phase in the two catalysts. The reaction profile shows a large discrepancy between H₂ and CO₂. The difference in H₂ and CO₂ being produced in the reaction highlights the detrimental effect that methanation

has on the quantities of H₂ being produced, with a significant amount of hydrogen being lost as CH₄ is formed. The formation of methane suggests the presence of nickel within the catalyst as was seen with 10% Ce doped catalyst as well, due to the influence of Ce inducing the formation of a nickel phase within the catalyst. The significant formation rate for CH₄ observed in the reaction profile along with large difference between H₂ and CO₂ formation rates suggests the material contains a relatively large proportion of the nickel phase.

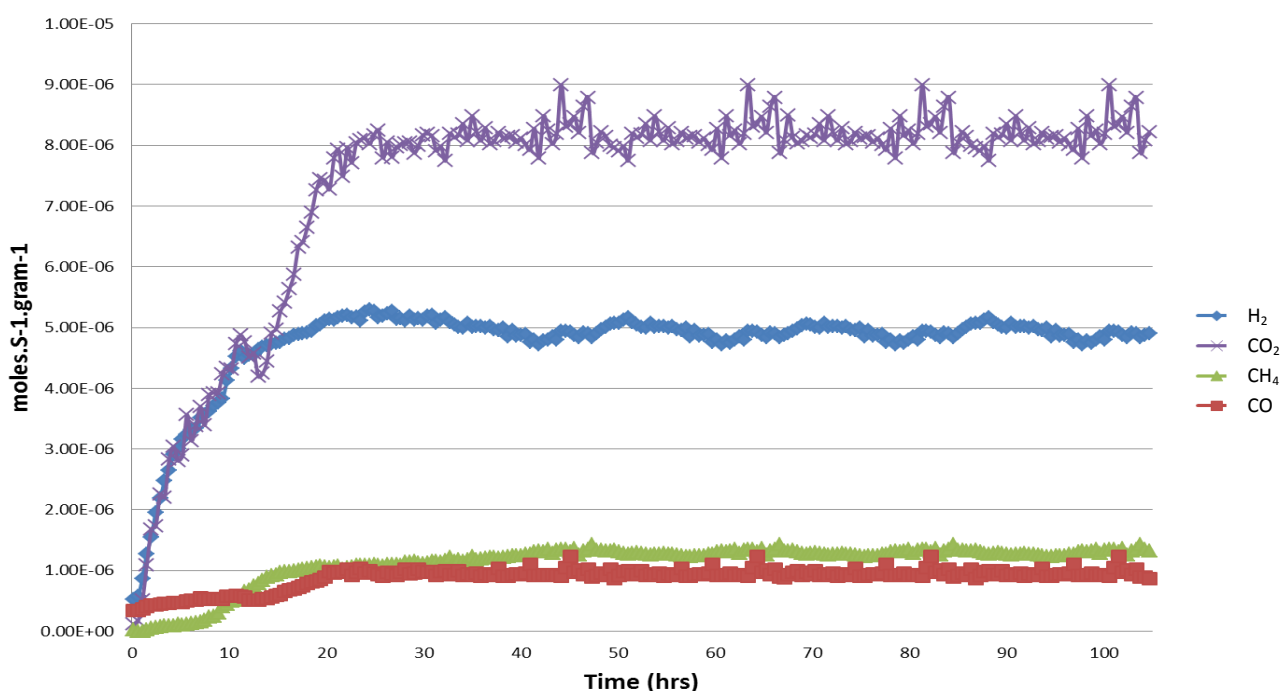


Figure 4-15: Reaction profile for Ce-Ni₂P/SiO₂ (5% w.t. Ce loading) under high temperature water-gas shift conditions

The comparison of hydrogen and carbon dioxide formation rates for Ce-Ni₂P/SiO₂ with 5% w.t. Ce loading with the industrial catalyst run under the same reaction conditions per weight of catalyst is shown in Figure 4-16. The formation rates for the 5% Ce doped catalyst for both hydrogen and carbon dioxide are higher than those displayed by the industrial catalyst under the same conditions once the reaction reaches steady state. The carbon dioxide formation rate is roughly double that of the industrial catalyst. The hydrogen formation rate displayed by the 5% Ce doped

catalyst is only marginally better than that displayed by the industrial catalyst per weight of catalyst. The difference between hydrogen formation rate for the 5% Ce catalyst and the industrial catalyst is lower due to the loss of hydrogen produced caused by significant methanation activity displayed by the catalyst.

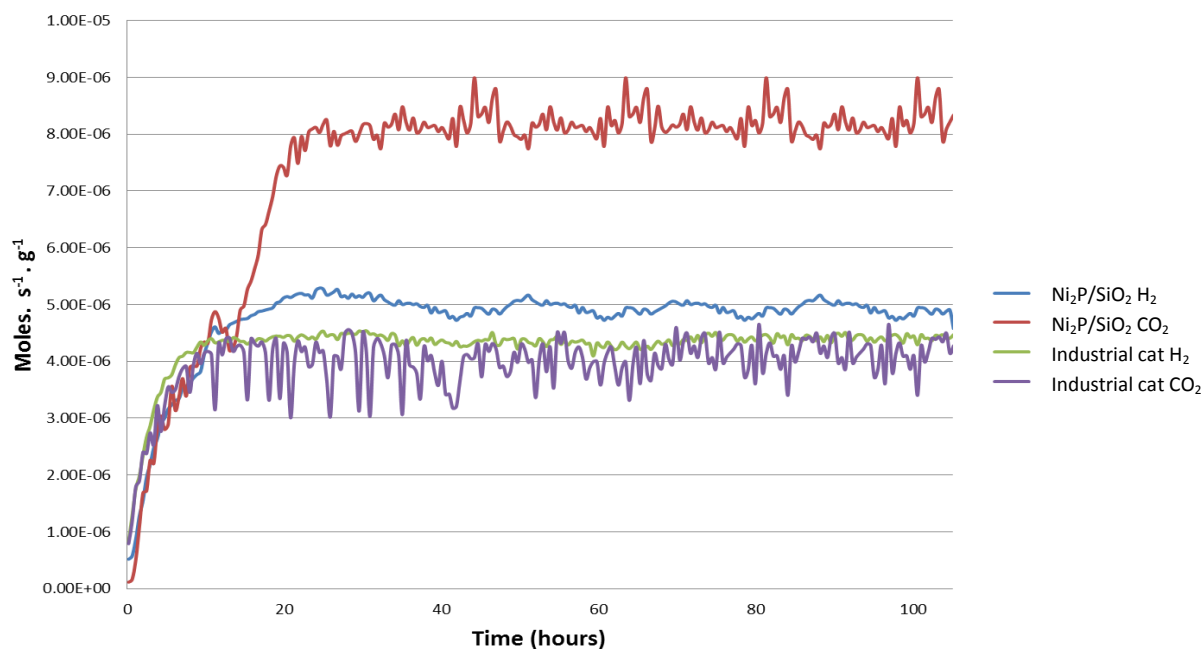


Figure 4-16: Comparison of H₂ and CO₂ formation rates for industrial catalyst and Ce-Ni₂P/SiO₂ (5% w.t. Ce loading) under high temperature water-gas shift conditions.

The reaction profile for Ce-Ni₂P/SiO₂ (1% w.t. Ce) is displayed in Figure 4-17. The catalyst displays significant catalytic activity under the reaction conditions according to the reaction profile CO₂, H₂ and CH₄ display consistent formation rates. The run produces significant CO₂ and H₂ indicating that the water-gas shift reaction is taking place on the catalyst surface. Small amounts of CH₄ are also produced during the reaction due to the nickel in the material. The carbon balance was calculated to be an average of 92% over the duration of the run. The discrepancy between CO₂ and H₂ formation rates in the reaction profile can also be attributed to the methanation activity shown by the catalyst, with H₂ being used to form the CH₄ in secondary reaction. Formation rates for all products reach steady state after roughly 10 hours

on stream. This has previously been identified with other nickel phosphide materials as a catalyst activation period associated with active phase of the catalyst. The difference between the H_2 and CO_2 formation rates is smaller than was seen with the 10% and 5%Ce doped catalyst due to the lower level of methanation displayed by the catalyst. The decreased rate of methanation suggests that few nickel metal sites exists within the active phase of the catalyst. The 1% Ce doped catalyst displayed a CH_4 formation rate which was slightly higher than the Ni_2P/SiO_2 catalyst and roughly the same H_2 formation rate in comparison to the Ni_2P/SiO_2 catalyst.

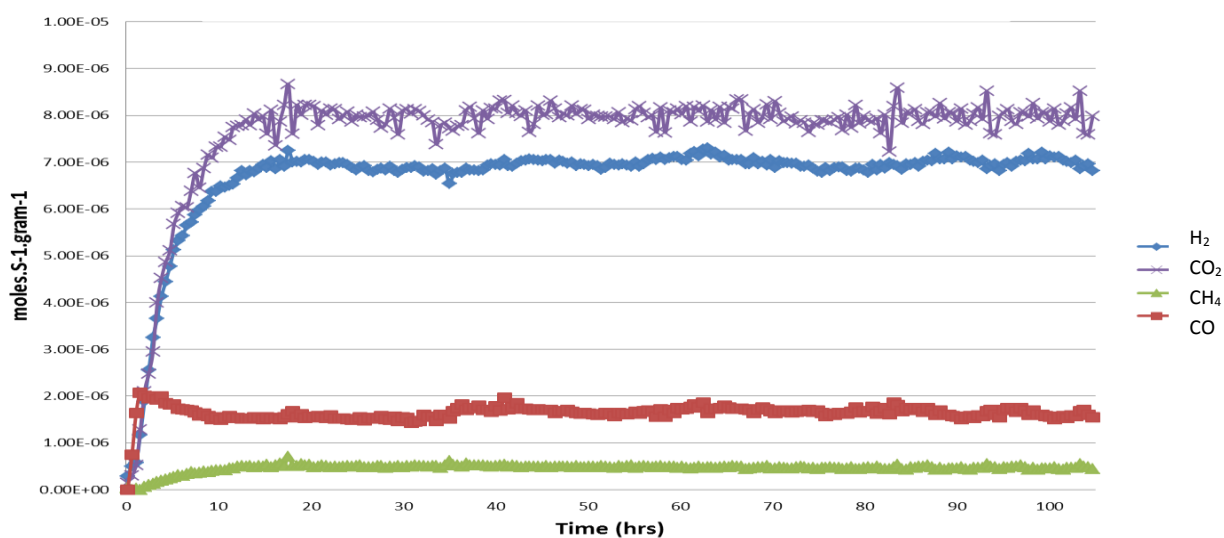


Figure 4-17: Reaction profile for $Ce-Ni_2P/SiO_2$ (1% w.t. Ce loading) under high temperature water-gas shift conditions.

Figure 4-18 displays the performance of the $Ce-Ni_2P/SiO_2$ (1% w.t. Ce loading) with the industrial catalyst in terms of hydrogen and carbon dioxide formation rates for run under the same reaction conditions. The reaction profile reveals that the formation rates for the 1% Ce doped catalyst for both hydrogen and carbon dioxide are significantly higher than those exhibited by the industrial catalyst under the same conditions once the reaction reaches steady state. The carbon dioxide formation rate is roughly double that of the industrial catalyst. The hydrogen formation rate displayed by the 1% Ce doped catalyst is also significantly better than that displayed by the industrial catalyst per weight of catalyst with the 1% Ce doped catalyst

displaying a formation rate approximately 75% greater than the industrial catalyst. The difference between hydrogen formation rate for the 1% Ce catalyst and the industrial is smaller due to the loss of hydrogen produced caused by minor methanation activity displayed by the catalyst. The profile suggests however, that the 1% Ce doped catalyst significantly outperforms the industrial catalyst per weight of catalyst.

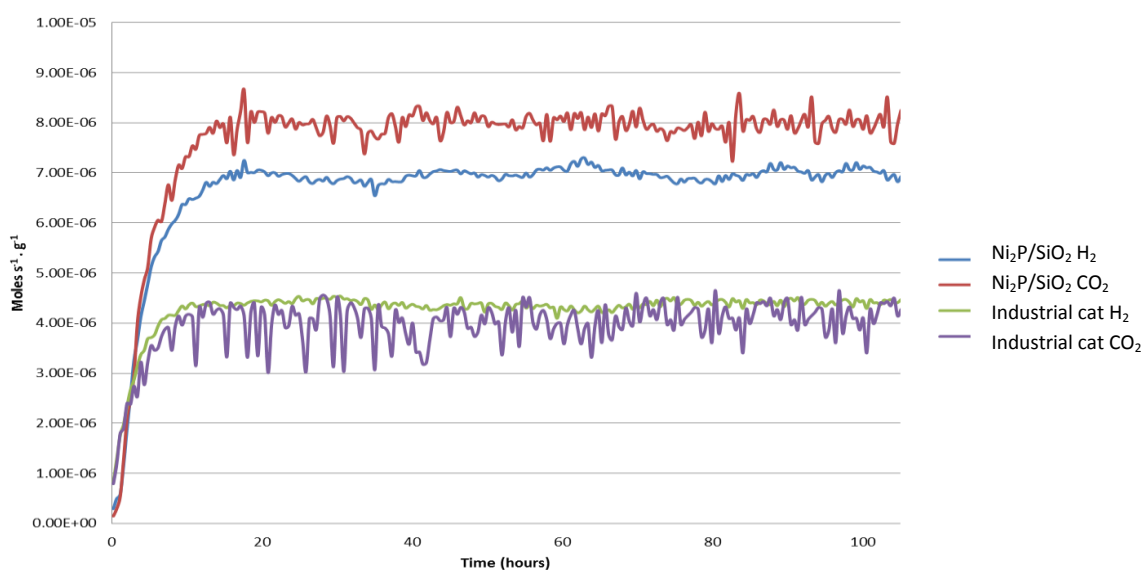


Figure 4-18: Comparison of H₂ and CO₂ formation rates for industrial catalyst and Ce-Ni₂P/SiO₂ (1% w.t. Ce loading) under high temperature water-gas shift conditions.

The reaction profile presented in Figure 4-19 is that of the high temperature water-gas shift reaction testing of Ce-Ni₂P/SiO₂ using 0.5% w.t. loading of Ce. The reaction profile indicates that the catalyst displays significant activity with CO₂, H₂ and CH₄ being produced throughout the run. The good catalytic activity displayed by the materials is consistent with the previously tested Ce doped catalysts in showing good catalytic activity under the reaction conditions. The run produces significant CO₂ and H₂ indicating that the water-gas shift reaction is taking place on the catalyst surface. The formation of CH₄ throughout the reaction run, as was seen in the 10%, 5% and 1% Ce doped catalyst, indicates that methanation is also occurring. The carbon balance was calculated to be an average of 92% over the duration of the run.

indicating only a relatively small loss of carbon, possibly due to liquid phases being produced or the catalyst carbiding which were not analysed. The reaction reaches steady state after approximately 15 hours of running; this has previously been identified with other nickel phosphide materials as a catalyst activation period associated with active phase of the catalyst. The activation period for the 0.5% Ce doped catalyst is longer than is seen with the 10% and 1% Ce doped catalysts but not as long as the 5% Ce doped catalyst suggesting that the activation process for the 0.5% Ce catalyst may differ as a result of the Ce:Ni ratio. Once the reaction reaches steady state the reaction profile showed a small difference between H₂ and CO₂. The difference in H₂ and CO₂ being produced in the reaction can be attributed to the formation of small amounts of methane being produced, as can be seen in the reaction profile. The formation rate of CH₄ is relatively small in comparison to the 5% and 10% Ce doped catalysts suggesting the nickel phase was lower in this catalyst. The formation rate for the 1% Ce doped catalyst was slightly lower than the 0.5% catalyst indicating less nickel present in the 1% Ce catalyst which is unexpected.

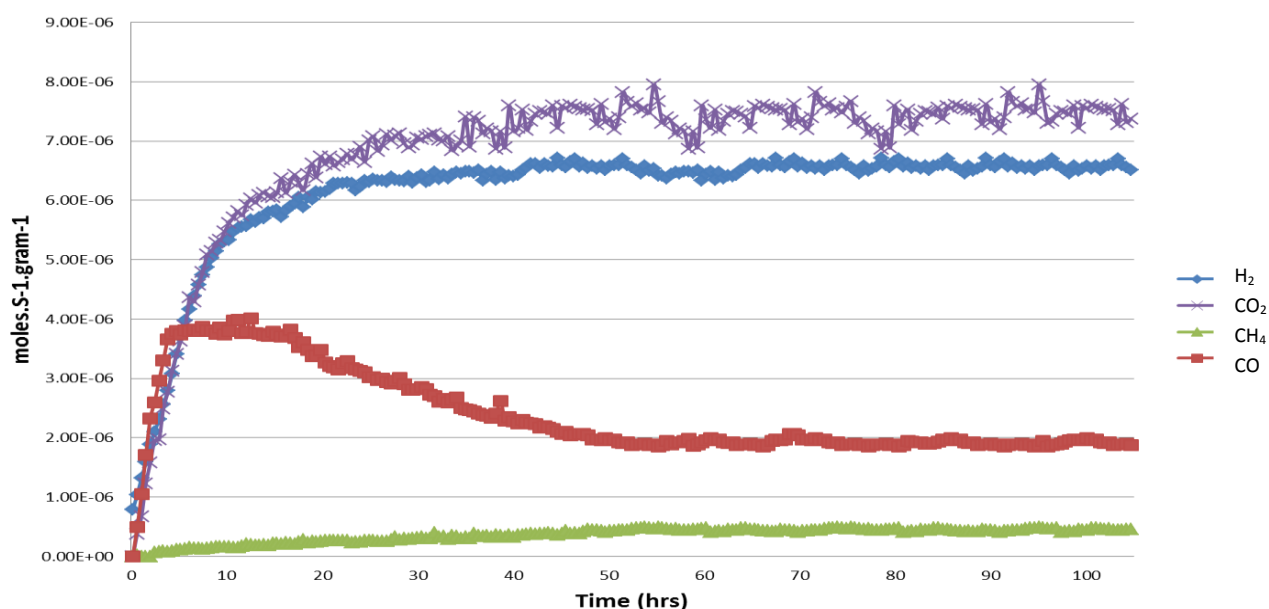


Figure 4-19: Reaction profile for Ce-Ni₂P/SiO₂ (0.5% w.t. Ce loading) under high temperature water-gas shift conditions.

Figure 4-20 displays the performance of the Ce-Ni₂P/SiO₂ (0.5% w.t. Ce loading) with the industrial catalyst in terms of hydrogen and carbon dioxide formation rates for run under the same reaction conditions per weight of catalyst. The reaction profile reveals that the 0.5% Ce catalysts outperformed the industrial catalyst per weight of catalyst. The formation rates for the 0.5% Ce doped catalyst for both hydrogen and carbon dioxide are significantly higher than those exhibited by the industrial catalyst under the same conditions once the reaction reaches steady state. The carbon dioxide formation rate is roughly 75% greater than that of the industrial catalyst. The hydrogen formation rate displayed by the 0.5% Ce doped catalyst is also significantly better than that displayed by the industrial catalyst with the formation rate approximately 50% greater than the industrial catalyst.

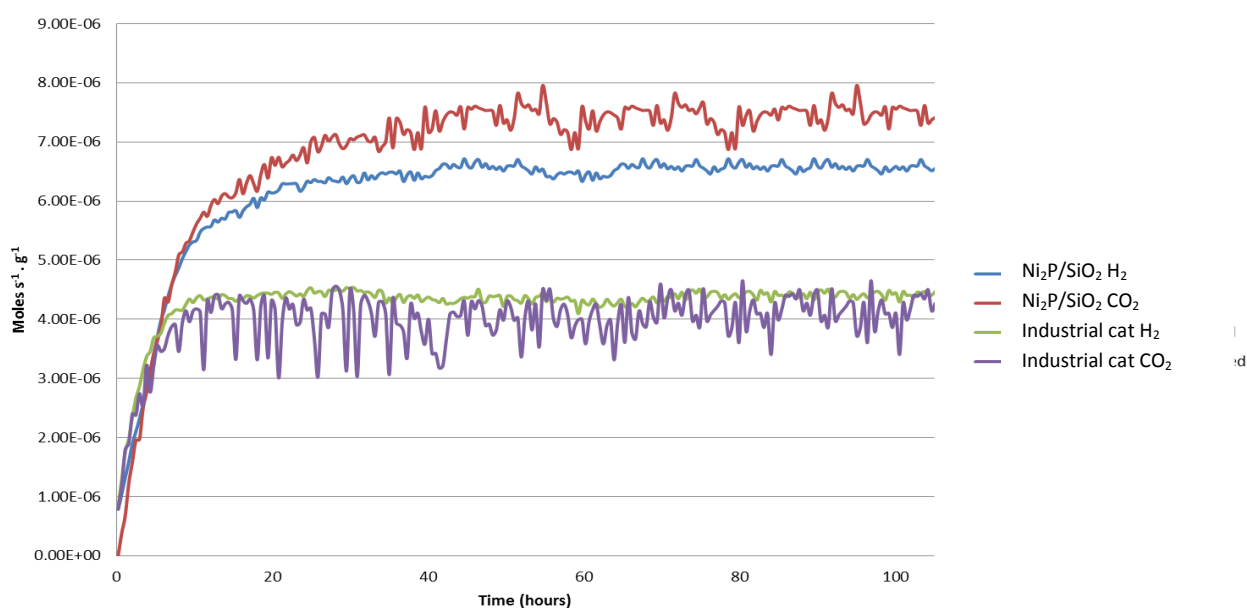


Figure 4-20: Comparison of H₂ and CO₂ formation rates for industrial catalyst and Ce-Ni₂P/SiO₂ (0.5% w.t. Ce loading) under high temperature water-gas shift conditions.

The Ce doped nickel phosphide catalysts are compared and contrasted with one and other along with nickel phosphide with regards to hydrogen formation rates displayed by each catalyst under the high temperature water-gas shift reaction conditions after

24 hours of running time. Figure 4-21 shows the mass normalised formation rates for each of the catalysts. The figure shows 1% Ce possesses the best hydrogen formation rate in comparison to the other Ce doped catalysts. It is still however slightly less than the hydrogen formation rate displayed by $\text{Ni}_2\text{P}/\text{SiO}_2$ after 24 hours of time on stream. Figure 4-21 also indicates a trend between Ce loading and hydrogen formation rates, with lower Ce loading catalysts giving higher formation rates. The 0.5% Ce catalyst displays a slightly lower hydrogen formation rate in comparison to the 1% Ce loading catalyst which was unexpected. The 0.5% Ce catalyst did however significantly outperform the 10% and 5% Ce doped catalysts.

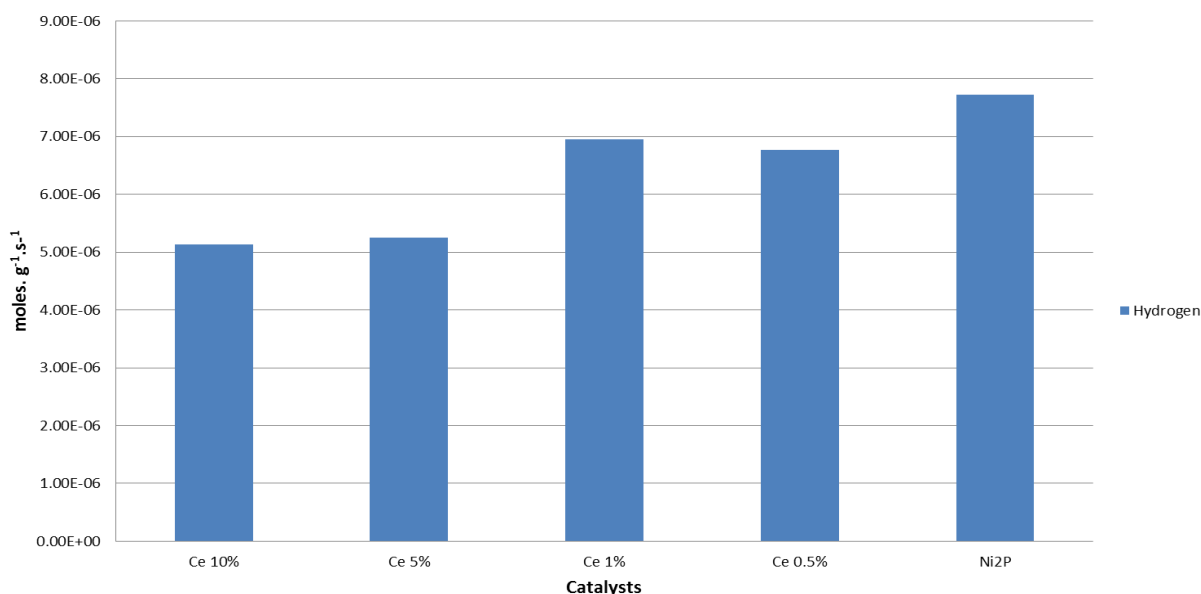


Figure 4-21: Mass normalised hydrogen formation rates after 24hrs of running for all Ce doped catalysts contrasted with $\text{Ni}_2\text{P}/\text{SiO}_2$.

The relationship between Ce loading and hydrogen formation rates displayed by the catalysts can in part be explained by looking at the methane formation rates of each catalyst in comparison to one and other and nickel phosphide. Figure 4-22 shows the mass normalised methane formation rates for 0.5%, 1%, 5% and 10% Ce loadings along with $\text{Ni}_2\text{P}/\text{SiO}_2$. The figure shows a distinct trend with Ce content within the catalyst and methane produced by the catalyst. $\text{Ni}_2\text{P}/\text{SiO}_2$ displays the lowest

formation rate for methane whilst the 0.5% Ce doped catalyst displays the lowest methane formation rate for the Ce doped catalysts. The 0.5% Ce catalyst displays a methane formation rate that is only slightly higher than the $\text{Ni}_2\text{P}/\text{SiO}_2$ catalyst after 24 hours of running. The increase in Ce loading corresponded to an increase in nickel metal sites within the catalysts, which produced methane under the reaction conditions which is thermodynamically favourable. The increased amount of Ni in the Ce doped catalysts has meant that hydrogen produced from the nickel phosphide active sites via the water-gas shift reaction has in part been used to form methane on the nickel metal sites. The 5% Ce loading catalyst displays the highest methane formation rate which is not expected and goes against the trend displayed by the other materials suggesting that the material contains the most nickel metal sites.

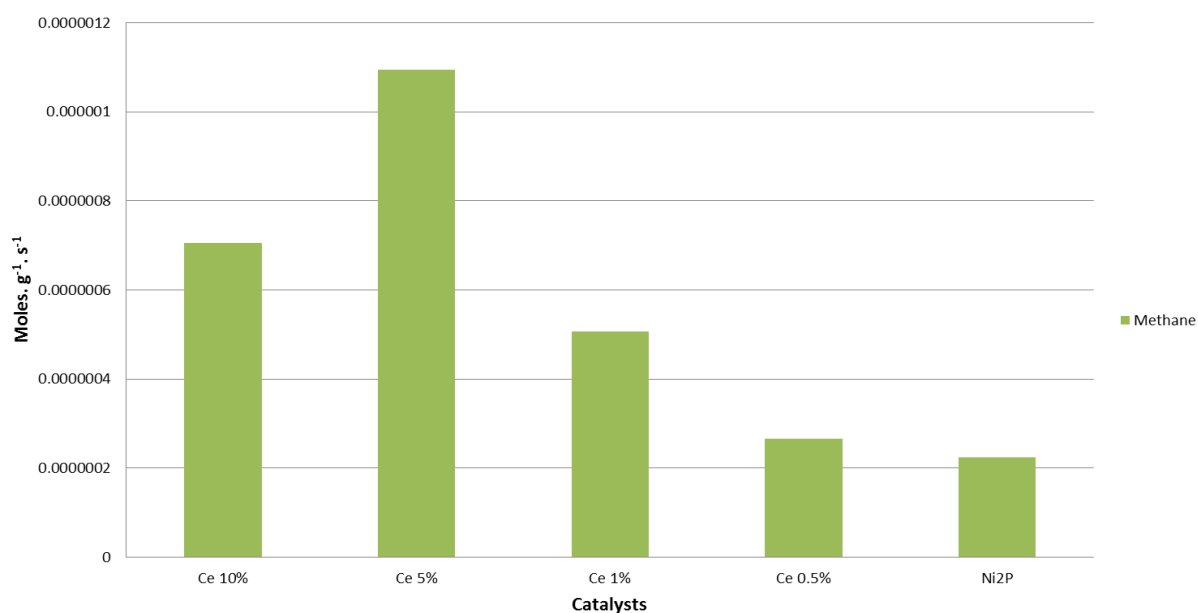


Figure 4-22: Mass normalised methane formation rates after 24hrs of running for all Ce doped catalysts contrasted with $\text{Ni}_2\text{P}/\text{SiO}_2$.

4.5 The characterisation of post-reaction tested cerium doped $\text{Ni}_2\text{P}/\text{SiO}_2$ catalysts.

Post-reaction samples of $\text{Ce-Ni}_2\text{P}/\text{SiO}_2$ with 0.5% and 10% loadings were characterised using XRD as shown in Figures 4-23 and 4-24 respectively. Figure 4-23 displays the XRD patterns for nickel phosphide catalyst containing 0.5% w.t. Ce loading pre- and post- testing. There are no obvious strong differences between the diffraction reflections exhibited by the pre- and post-reaction samples indicating crystalline phases of the material remain stable running under the high temperature water-gas shift conditions applied. The average crystallite size of the nickel phosphide was estimated to be 40.1 nm using the Scherrer equation. The average particle size of the fresh material was 37.1 nm, which indicates that there is not significant aggregation occurring during the reaction testing. This suggests that the catalyst is stable and robust enough to be used over extended periods of time.

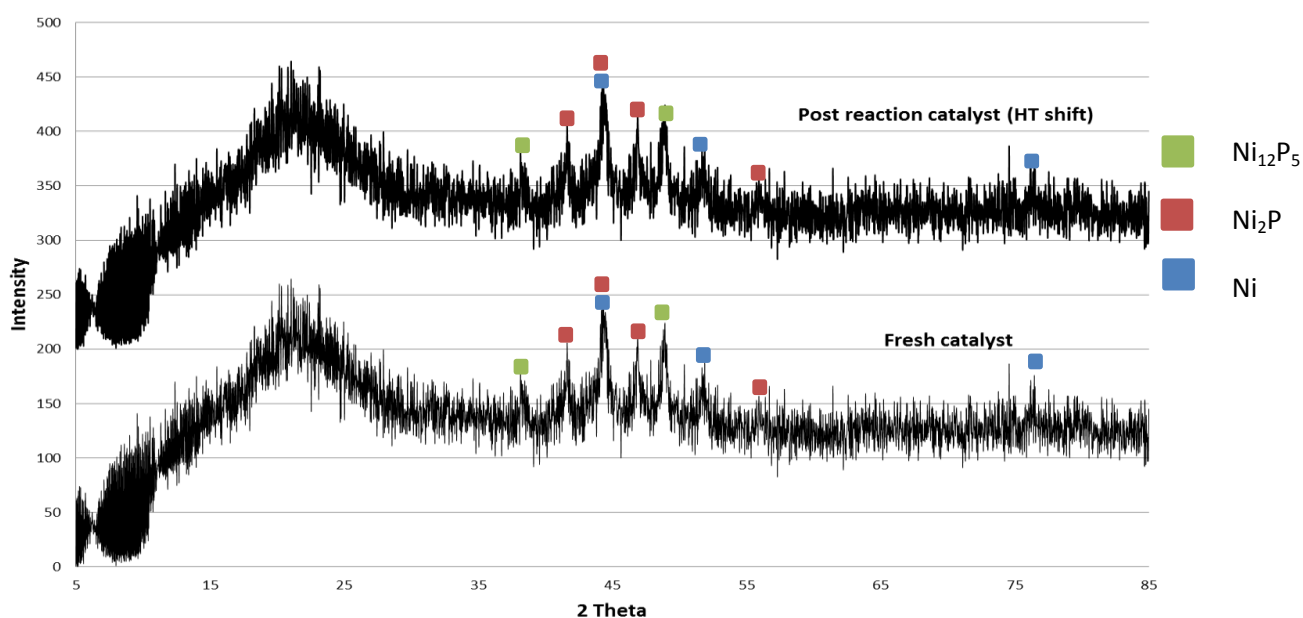


Figure 4-23: XRD patterns for fresh and post-reaction sample of $\text{Ce-Ni}_2\text{P}/\text{SiO}_2$ with 0.5% w.t. Ce loading.

XRD patterns for Ce-Ni₂P/SiO₂ catalyst with 10% Ce loading pre- and post- reaction materials are displayed in Figure 4-24. The diffraction patterns for the pre- and post-reaction samples show very distinctive differences indicating that bulk composition of the material has been significantly altered under the reaction conditions. The fresh catalyst displays two diffraction peaks at 44° and 51° 2theta, these are associated with nickel metal (more specifically the (1 1 1) and (2 0 0) planes) and are associated with nickel phase present in the material. The post-reaction material displays diffraction peaks at 44° and 51° with lower intensity than the pre-reaction sample. The post-reaction sample also displays diffraction peaks associated with Ni₂P at 41°, 44° and 47° as well as one peak associated with Ni₁₂P₅ at 49°. The average crystallite size was estimated to be 35.1 nm using the Scherrer equation. The average particle size of the fresh material was 37.9 nm; a small decrease in particle size is evident. The change in particle size is most likely a result of the conversion of nickel metal to nickel phosphide species. The appearance of diffraction reflections associated with nickel phosphide suggests that the material is becoming more phosphide like during the reaction; this is most like due to unreacted phosphorus containing species present on the support interacting with the nickel metal components, which is supported in further characterisation of the post-reaction catalyst.

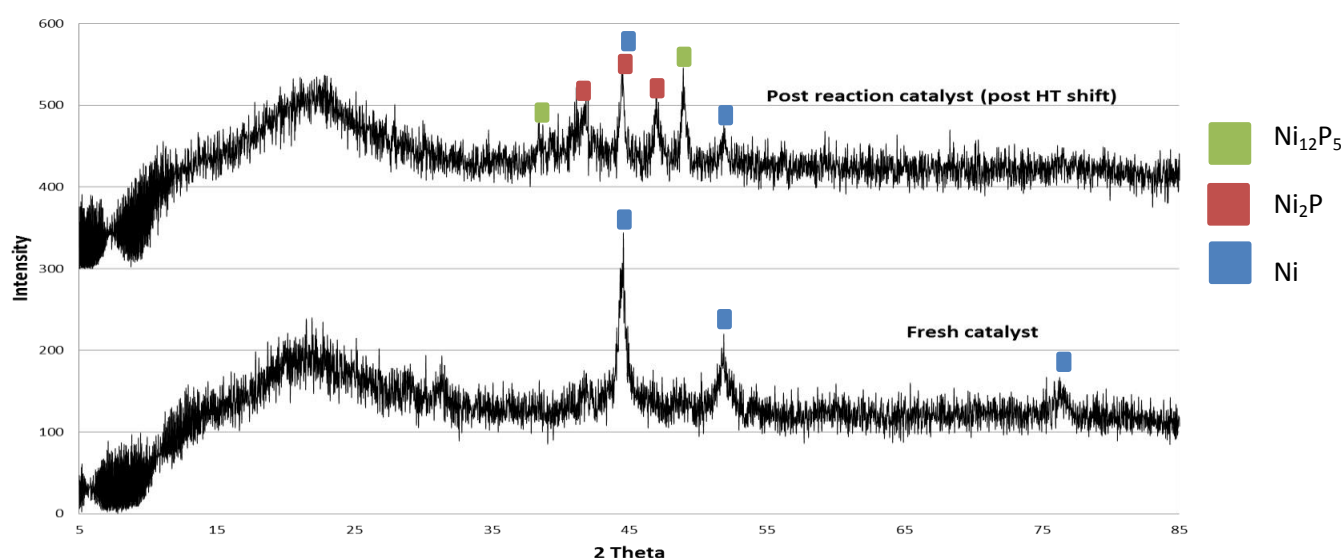


Figure 4-24: XRD patterns for fresh and post-reaction sample of Ce-Ni₂P/SiO₂ with 10% w.t. Ce loading.

The post-reaction sample of the 10% Ce catalyst was further characterised using X-ray photoelectron spectroscopy. The characterisation of catalyst using XPS was conducted to gain an insight to the electronic state of the active phase of the catalyst in the near surface regions. The XP spectra of the Ni 2p, Ce 3d and P 2p regions for the pre- and post-reacted Ce-Ni₂P/SiO₂ are presented in Figures 4-25 and 4-26, accompanied by tabulated binding energies shown in Table 4-4. The Ni 2p and Ce 3d spectrum for the post-reaction catalyst sample shows two peaks, a major peak at 853.7 eV and minor peak at 857.9 eV. The peak at 853.7 eV has been identified as Ni^{δ+} which is consistent with it interacting with phosphorus in Ni₂P as reported in previous studies in the literature. [2] The minor peak in the spectrum at 857.1 eV can be assigned to Ni²⁺ species associated with nickel pyrophosphate, resulting from oxy-phosphide surfaces that promote the catalytic activity of the material. [8] The feature at 871.1 eV in the spectrum is associated with the Ni^{δ+} phase within the 2p_{1/2} Ni spectrum, further peaks would also be expected but these are not visible to the Ce 3d features in the spectrum. Features associated with Ce species are evident in spectrum which shows the Ce 3d region; there is a broad peak associated with two different species of Ce at 880.8 eV and 883.5 eV which can be assigned to Ce³⁺ and Ce⁴⁺ respectively. There is a further satellite peak associated with the Ce divalent species at 901.5 eV.

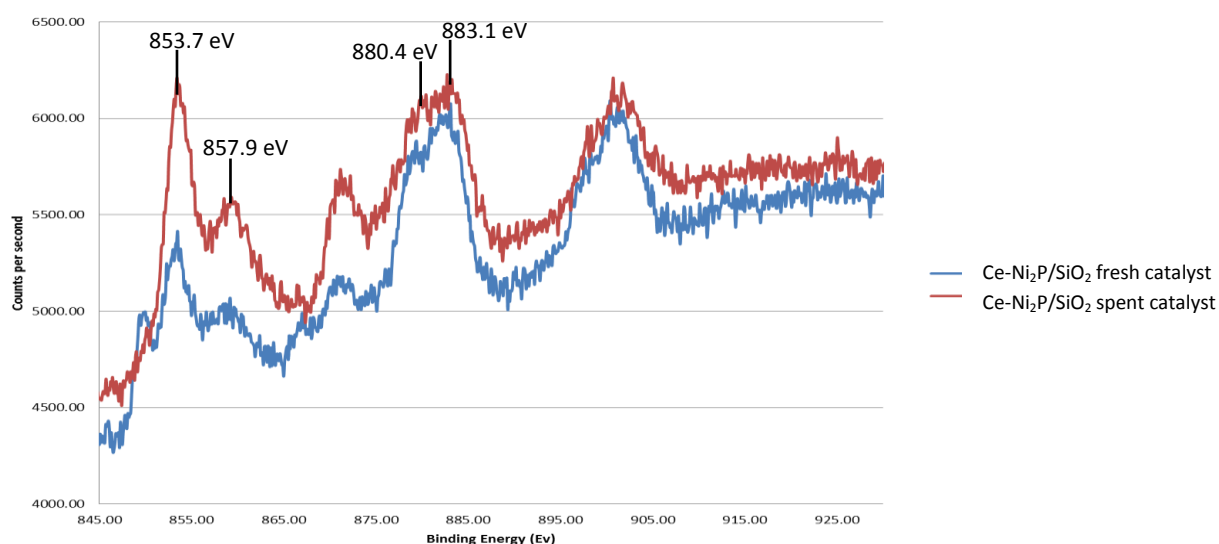


Figure 4-25: Ce-Ni₂P/SiO₂ (10% w.t. Ce) Ni 2p and Ce 3d spectra for pre and post-reaction samples.

The comparison of the pre- and post-reaction spectra for the 10% Ce doped catalyst indicate that the nickel species has changed, as evidenced by the binding energy peak associated with nickel metal at 850.2 eV which is present fresh sample but not seen in the post-reaction sample. The $\text{Ni}^{\delta+}$ has shifted from 853.4 eV to 853.7 eV in post-reaction sample, as well as increasing in intensity suggesting a greater presence of nickel phosphide at the surface of the material. This is consistent with the XRD pattern which also suggests that Ni metal sites are converted into nickel phosphide under the reaction conditions. The binding energy peaks for Ce remain consistent between the pre- and post-reaction samples at 880.4 eV and 883.1 eV for Ce^{3+} and Ce^{4+} respectively indicating that the Ce remains stable throughout the duration of the reaction, this is most probably due to Ce not being directly involved in the active phase of the catalyst.

The Ce- $\text{Ni}_2\text{P}/\text{SiO}_2$ (10 w.t. % Ce) post-reaction spectrum for the P 2p region (Figure 4-26) shows a single peak indicating a single species of phosphorus present in the catalyst. The peak is centred at 131eV and has been identified as $\text{P}^{\delta-}$; the phosphorus peak is slightly higher than previously reported studies, with the peak centring at 129-130.5 eV. ^[25-26] The small difference can be attributed to the presence of oxy-phosphide phases alluded to previously in the previous chapter. Comparison of the pre- and post-reaction samples phosphorus 2p spectra indicate that the phosphorus is more oxygenated after high temperature water-gas shift reaction testing due to the small shift in binding energy displayed by the post-reaction material. The post-reaction phosphorus spectrum has shifted up to 131 eV compared to the 130 eV displayed by the fresh catalyst.

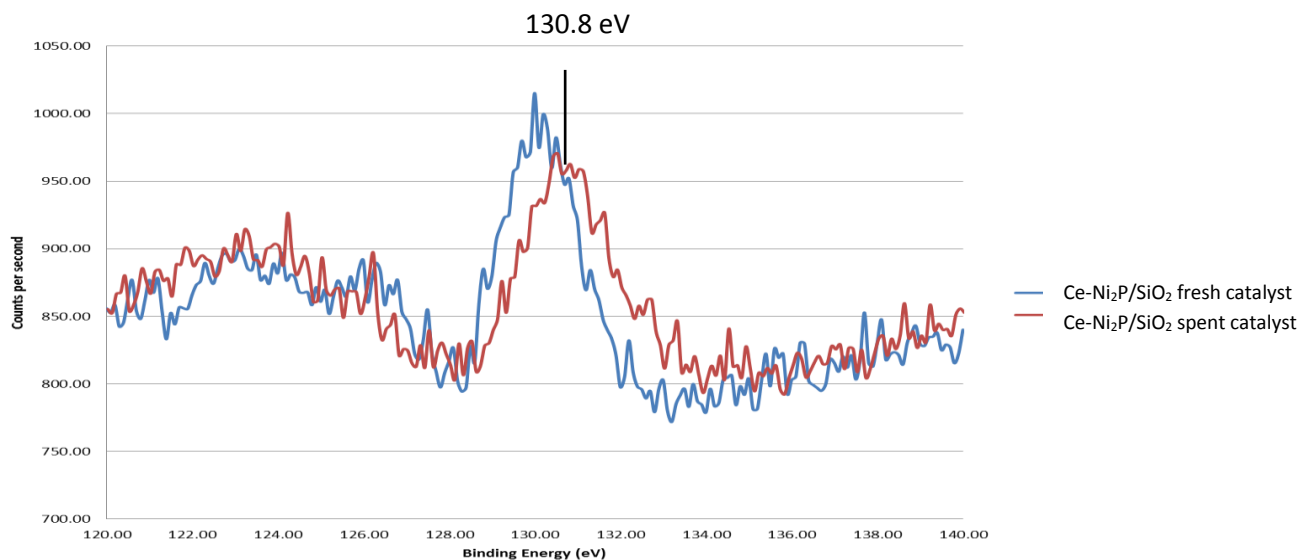


Figure 4-26: Ce-Ni₂P/SiO₂ (10 w.t. % Ce) P 2p spectra for pre- and post-reaction samples

Sample	Ce-Ni ₂ P/SiO ₂ Fresh	Ce-Ni ₂ P/SiO ₂ Post-reaction	Ni ₂ P/SiO ₂
Element	Binding energy (eV)	Binding energy (eV)	Binding energy (eV)
Ni 2p	850.2 (smallest) 853.4 (largest) 857.1	853.7 (largest) 857.9 (smallest)	853.5 (largest) 856.8 (smallest)
P 2p	130.2	130.8	130.6
O 1s	532.9	533	532.8
C 1s	285.0	280 285.0	285.0
Ce 3d	880.3(smallest) 882.9(largest)	880.4(smallest) 883.1(largest)	N/A

Table 4-5: Summary of binding energy peaks shown in spectra for Ni₂P/SiO₂ and Ce-Ni₂P/SiO₂ pre and post HT shift.

The post-reaction Ce-Ni₂P/SiO₂ (10 w.t. % Ce) was further investigated using X-ray absorption spectroscopy. The EXAFS region of the nickel K-edge spectrum for the material was the primary focus of the study. Figure 4-27 displays the k^3 weighted EXAFS spectrum for Ce-Ni₂P/SiO₂ and Figure 4-28 illustrates the Fourier transforms spectrum for the material. Both spectra have been refined and a theoretical curve has been applied through collaboration with Prof. G. Sankar from University College London.

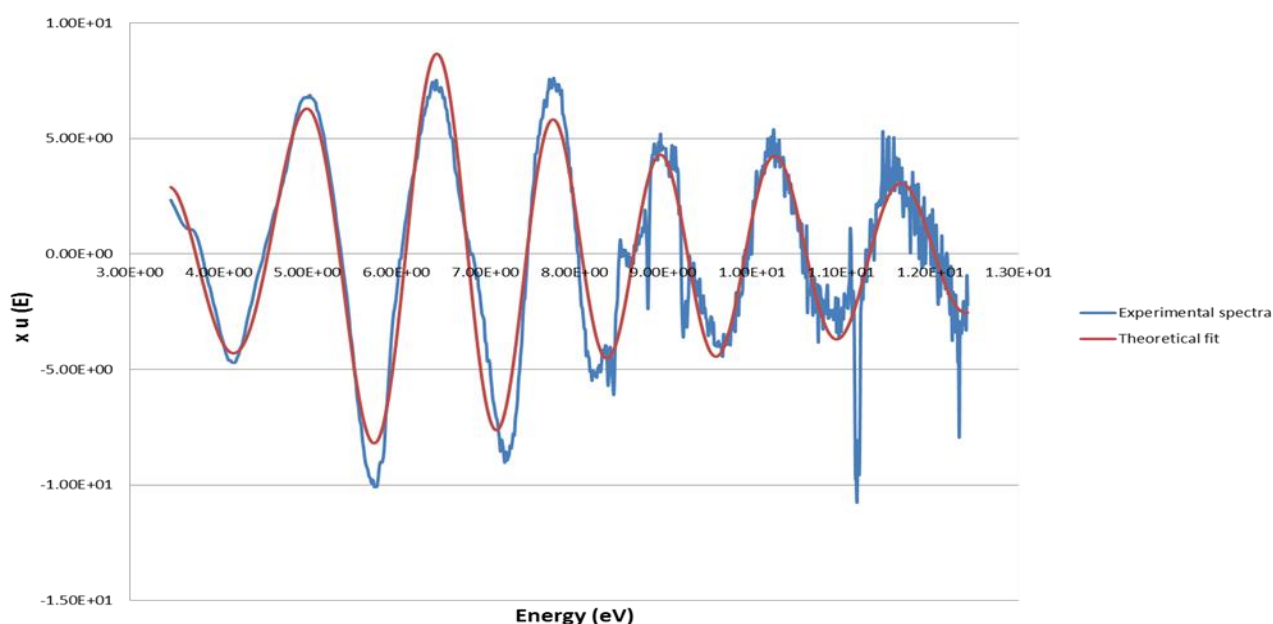


Figure 4-27: Ni K-edge k^3 weighted EXAFS spectrum for post-reaction Ce-Ni₂P/SiO₂ (10% w.t. Ce) along with the theoretical fit.

The curve fitting results for the post-reaction Ce-Ni₂P/SiO₂ EXAFS spectrum is presented in Table 4-6. The nickel K edge FT spectrum for the 10% Ce catalyst displays a number of shells associated with scattering of neighbouring atoms to nickel. The first two shells are the only two used in the theoretical fit to achieve the optimum fit. The first of them is centred 0.222nm and falls within the region of the Ni-P bond which has been reported in range 0.218-0.231nm.^[4] The curve fit indicated that a co-ordination number of 3.95 suggesting that 4 P neighbours are present around the nickel atom. The second peak is centred at 0.258nm and has been

identified as Ni-Ni bonding with a co-ordination number of 4.07, indicating 4 Ni neighbours. These results closely resemble those reported by Lee and Oyama for silica supported nickel phosphide catalysts. As discussed, Lee and Oyama reported the presence of two different nickel sites within nickel phosphide using FT EXAFS data to fit the theoretical curve which took into consideration close proximity of the Ni-Ni and Ni-P peaks. The final scattering element considered for the fit is a further Ni-Ni species with a distance estimated to be 0.297 nm with the co-ordination number as 1.97. This secondary Ni species was not observed in the Oyama and Lee study and it can be attributed to the nickel metal phase seen in the fresh material. It was estimated that 20% of the Ni present in the sample was present as Ni metal. This was based on the theoretical fit of the FT spectrum carried out by Prof. G. Sankar. This suggests that half of the Ni metal present in the fresh sample has been converted to a nickel phosphide phase.

The comparison of the EXAFS curve fit results for the post-reaction sample of Ce-Ni₂P/SiO₂ with the fresh material indicates some significant differences between the two samples. These differences suggest that the reaction testing has altered the composition of the catalyst. The Ni-P characteristics exhibited by fresh and post-reaction samples display a number of differing characteristics. The distance for Ni-P neighbours in fresh 10% Ce doped catalyst was calculated to be 0.219 nm whilst the post-reaction sample Ni-P distance was found to be 0.222nm. The co-ordination number of the Ni-P scatter also increases in the post-reaction sample from 2.29 in the fresh catalyst to 2.97 in the post-reaction catalyst. The post-reaction Ni-Ni scatter also exhibits a number of differences to the fresh sample. The bond distance is shown to increase in the post-reaction sample to 0.258 nm whilst the co-ordination number decreases to 4. The post-reaction Ni-P and Ni-Ni scattering characteristics more closely resemble those shown by the Ni₂P/SiO₂ catalyst. This further supports the notion that the nickel metal sites within the Ce doped catalyst are being converted into nickel phosphide during the reaction most likely due to excess phosphate on the support interacting with the nickel phase. The fresh 10% Ce doped catalyst was estimated to have 40% of the nickel present as nickel metal in comparison to the post-reaction sample which was thought to contain no more than

20% of nickel as nickel metal species showing a significant conversion of nickel metal sites to nickel phosphide.

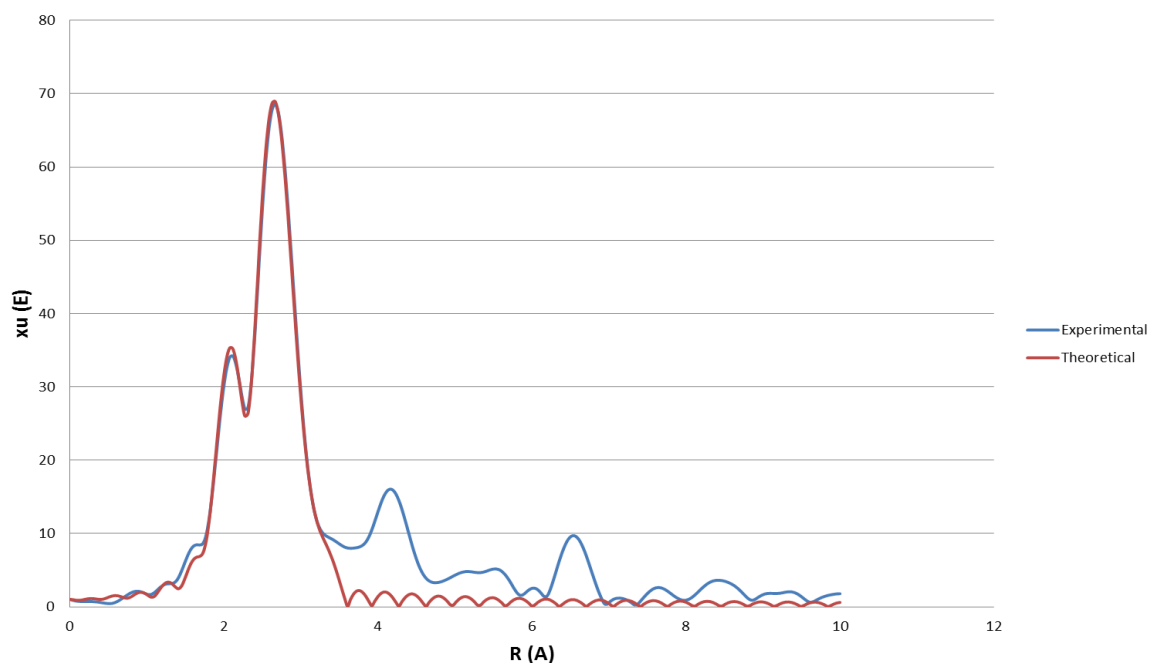


Figure 4-28: Ni K-edge EXAFS Fourier transforms spectrum for post-reaction Ce- $\text{Ni}_2\text{P}/\text{SiO}_2$ (10 w.t. % Ce) along with theoretical fit.

Shell	Scatterer	Bond distance (Å)	co-ordination No	A	AFAC	ΔE	R-Factor
1	Ni-P	2.21955	2.95	0.01434	0.7735	3.1401	31.2796
2	Ni-Ni	2.5817	4.07	0.01343	0.7735		
3	Ni-Ni	2.97756	1.74	0.01655	0.7735		

Table 4-6: Curve fitting results of the Ni K-edge EXAFS spectra for post-reaction Ce- $\text{Ni}_2\text{P}/\text{SiO}_2$ (10 w.t. % Ce)

SEM analysis of the post-reaction Ce-Ni₂P/SiO₂ (10% Ce) and (1% Ce) catalysts are presented in Figures 4-29 and 4-30 respectively. The post-reaction samples were also analysed using EDX. The resulting tables of elemental results are presented in Tables 4-7 and 4-8.

The SEM micrograph for post-reaction catalyst shows the silica supported nickel phosphide particles on the carbon support. The Ni₂P/SiO₂ particles can be distinguished on the micrographs from the carbon support as small light particles that are dispersed on the surface of the carbon pad which is darker in contrast. There is also no evidence of graphitic deposits on the particles. This however may be more evident at higher magnification. EDX elemental analysis of the surface particles was carried out at a number of points in the micrograph to ensure consistency. The micrographs highlight the area that was used to confirm elemental composition of the particle; it is labelled as “spectrum 2” in Figure 4-29 and “spectrum 4” in Figure 4-30. The results of EDX analyses are displayed in Tables 4-7 and 4-8 and show both atomic and weight percentages of particles present. The atomic weight percentages for nickel and phosphorus to be roughly in the ratio 2:1 for both catalysts, consistent with the stoichiometry of Ni₂P. The slightly higher Ni:P ratio shown in the 10% Ce catalyst is consistent with there still being some nickel metal sites still present in the material as alluded to from EXAFS analysis of the material.

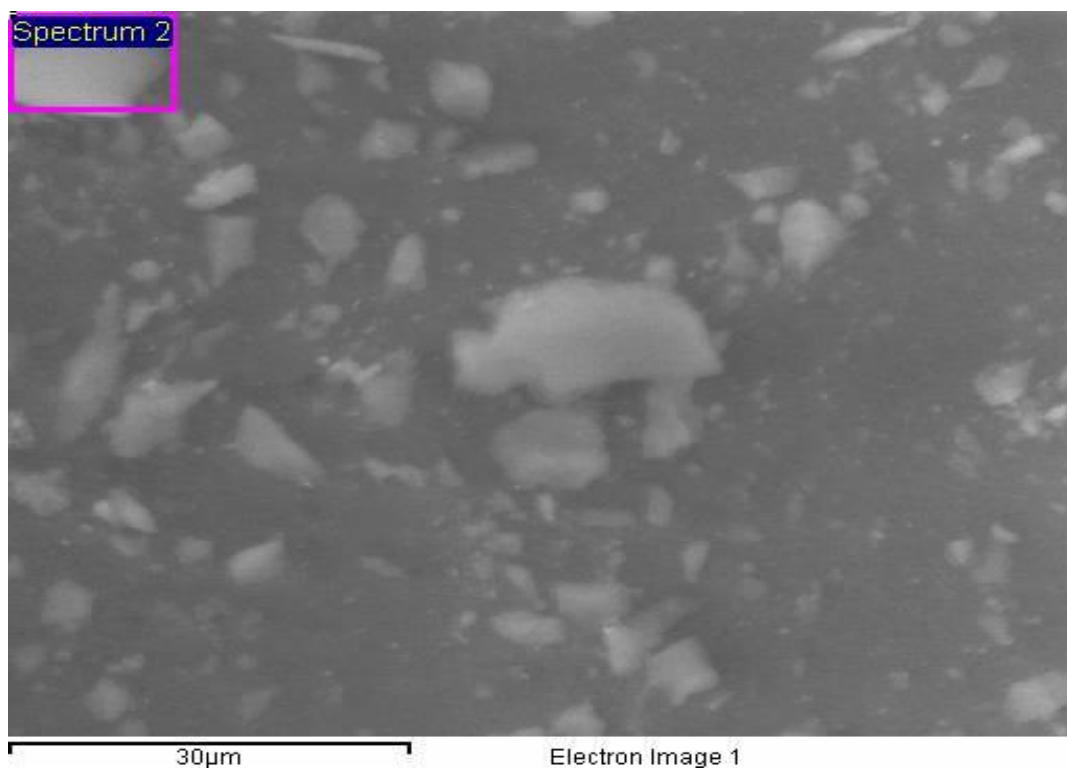


Figure 4-29: SEM micrograph for post HT shift reaction testing $\text{Ce-Ni}_2\text{P/SiO}_2$ catalyst with 10% Ce loading.

Element (edge)	Weight%	Atomic%	Average At % (deviation)
P (K)	28.56	43.11	41.2 (± 3)
Ni (K)	71.44	56.89	58.9 (± 4)
Ce K edge out with range measure by instrument	N/A	N/A	N/A
Total	100.00	100.00	

Table 4-7: Table summarising EDX analysis of target particles.

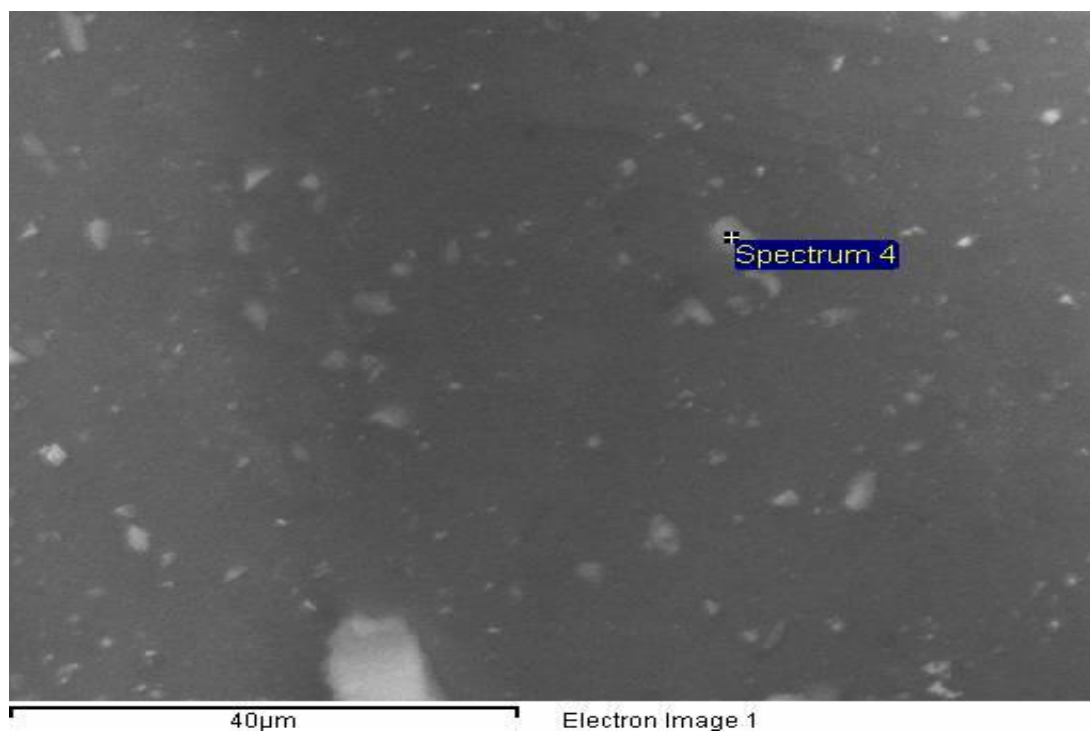


Figure 4-30: SEM micrograph for post HT shift reaction testing Ce-Ni₂P/SiO₂ catalyst with 1% Ce loading.

Element (edge)	Weight%	Atomic%	Average At % (deviation)
P (K)	23.54	36.15	29.5 (±9)
Ni (K)	76.46	63.85	70.5 (±11)
Ce K edge out with range measure by instrument	N/A	N/A	N/A
Total	100.00	100.00	

Table 4-8: Table summarising EDX analysis of target particles

4.6 The development and characterisation of further bimetallic transition metal phosphide catalysts.

The interesting results exhibited by the bimetallic cerium-nickel phosphide catalysts led to the investigation of further bimetallic nickel phosphide systems. As was mentioned earlier, previous studies have shown Ni_2P to be the most active among the transition metal phosphides for a number of hydrotreating and hydrogenation processes.^[1,2,12] The documented synergistic relationship between of Co and Ni with Mo in sulfide catalysts, has led some researchers to investigate mixed metal phosphides like NiMoP and CoMoP.^[10, 15, 16] These compositions were found to be poorly active in a number of hydrotreating and hydrogenation processes. This has been attributed to the alteration of the chemical nature, or interactions with the support, as well as a reduction in number of active nickel phosphide sites due to displacement by secondary metal. Therefore alternative metallic components were considered which may have positive influences on the nickel phosphide catalyst.

The first bimetallic systems to be investigated were transition metals that have historically been shown to display good catalytic activity for the water-gas shift reaction such as iron and copper. The precious metal palladium was used as a dopant to the nickel phosphide system due to its favourable catalytic properties. Final dopant used in the nickel phosphide systems was caesium which has been studied by Rodriguez as dopant for bulk phase nickel phosphide catalyst. In this study it was shown to improve oxygen coverage on the surface of the catalyst which in turn improved catalytic performance of the material.

Silica supported bimetallic iron and copper nickel phosphide catalysts were produced using stoichiometric ratios for Fe:Ni and Cu:Ni ratios based on a 20% w.t. Ni loading on the silica support resulting in an approximate 10% loading of Fe and Cu with regards to the total weight of the material. The bimetallic systems containing caesium and palladium used 1% w.t. of the dopant metal along with the standard

20% w.t. of Ni used for all supported nickel phosphide materials in the project. The bimetallic nickel phosphide catalysts were produced using a similar method to monometallic nickel phosphide catalysts supported on silica described previously in the experimental chapter. The only difference between preparation of bimetallic and monometallic nickel phosphide catalysts was the addition the secondary metal nitrate which was impregnated on to the silica support. The loading of nickel was consistent with the $\text{Ni}_2\text{P}/\text{SiO}_2$ catalyst described previously; this was 20% Ni with respect to the total weight of the catalyst. The impregnation of the support with the second metal solution occurred after the initial impregnation of the silica with the nickel nitrate solution.

The XRD patterns for all four silica supported bimetallic nickel phosphide materials catalysts are presented in Figure 4-31, along with the diffraction pattern for bulk phase Ni_2P . The bimetallic nickel phosphide systems all display a number of differences in comparison to the bulk phase Ni_2P , suggesting the introduction of the additional metals in to the phosphide material alters the crystal phase and composition of the material. The diffraction patterns displayed by the bimetallic phosphide materials all display reflections at 41° , 44° and 45° 2theta; these are synonymous with the Ni_2P phase and are present in all materials suggesting that this phase of nickel phosphide is present on the surface of the support. The patterns for the bimetallic phosphides also indicate the presence of the Ni_{12}P_5 phases of nickel phosphide. These reflections are present at 38.1° and 45.2° and are particularly visible in the palladium and iron bimetallic materials respectively. There is further evidence of cell distortion with a slight shift in the diffraction peak at 41° for Cs- $\text{Ni}_2\text{P}/\text{SiO}_2$ and for Cu- NiP/SiO_2 . The distortion of the nickel phosphide unit cell for these materials may alter the catalytic properties of the material in comparison to nickel phosphide

The addition of a second metal to the nickel phosphide system causes a mixed phase nickel phosphide to be produced. This was evident previously with the addition of various Ce loadings, which all displayed mixed phases of nickel phosphide. This is evident once more in these materials. The lack of fully defined

diffraction peaks associated with Ni_2P crystal phase suggests the bimetallic nickel phosphide systems are much more disordered in terms of the phases of phosphide that are formed in comparison to the mono-metallic materials. Previous studies of bimetallic d-block transition metal phosphides have indicated alloying of the metallic components occurs in these materials with phases that are isostructural to Ni_2P . The diffraction patterns for Fe-NiP/SiO_2 and Cu-NiP/SiO_2 are consistent with this, both materials show peaks associated with Ni_2P phase. The distortion of the peak at 41° 2θ , which corresponds to the (1 1 1) plane, which is evident in the Cu-NiP/SiO_2 material, is likely due to the influence of the Cu on the formation of the crystal phase formed. This is not noticeable in Fe-NiP/SiO_2 possibly due to the isostructural properties of iron and nickel phosphide systems. The differences in the crystal phases displayed by the materials may result in differing catalytic activity.

The average crystallite size was determined for each material using the Scherrer equation based on the diffraction patterns for each material. The average crystallite size for each material was estimated as follows; $\text{Pd-Ni}_2\text{P/SiO}_2$ - 57.2 nm, $\text{Cu-Ni}_2\text{P/SiO}_2$ - 43.8 nm, Fe-NiP/SiO_2 - 31.5 nm and $\text{Cs-Ni}_2\text{P/SiO}_2$ - 34.4 nm. The average crystallite sizes for the bimetallic catalysts were generally much larger than the mono metallic Ni_2P catalyst, which was estimated to have an average crystallite size of 25.2 nm. This was especially true for the Pd and Cu bimetallic phosphide materials. The addition of the secondary metallic component to the nickel phosphide system appears to directly influence crystallite size.

The diffraction patterns for the Cs and Pd doped nickel phosphide catalysts do not display peaks associated with ordered caesium and palladium phases within the $\text{Cs-Ni}_2\text{P/SiO}_2$ and $\text{Pd-Ni}_2\text{P/SiO}_2$ materials. This is most likely due to small quantities of each dopant used (1% w.t. used in both catalysts) meaning that they may be too highly to be apparent in the diffraction patterns of the materials. The diffraction patterns for the bimetallic nickel phosphide materials do not definitively establish a relationship between the secondary metallic component and nickel phosphide. There is however, an indication that the addition of a secondary metal to the system does alter the phase of phosphide formed. This is evident from the cell distortion shown

displayed in the diffraction patterns for the materials when compared with mono metallic Ni₂P.

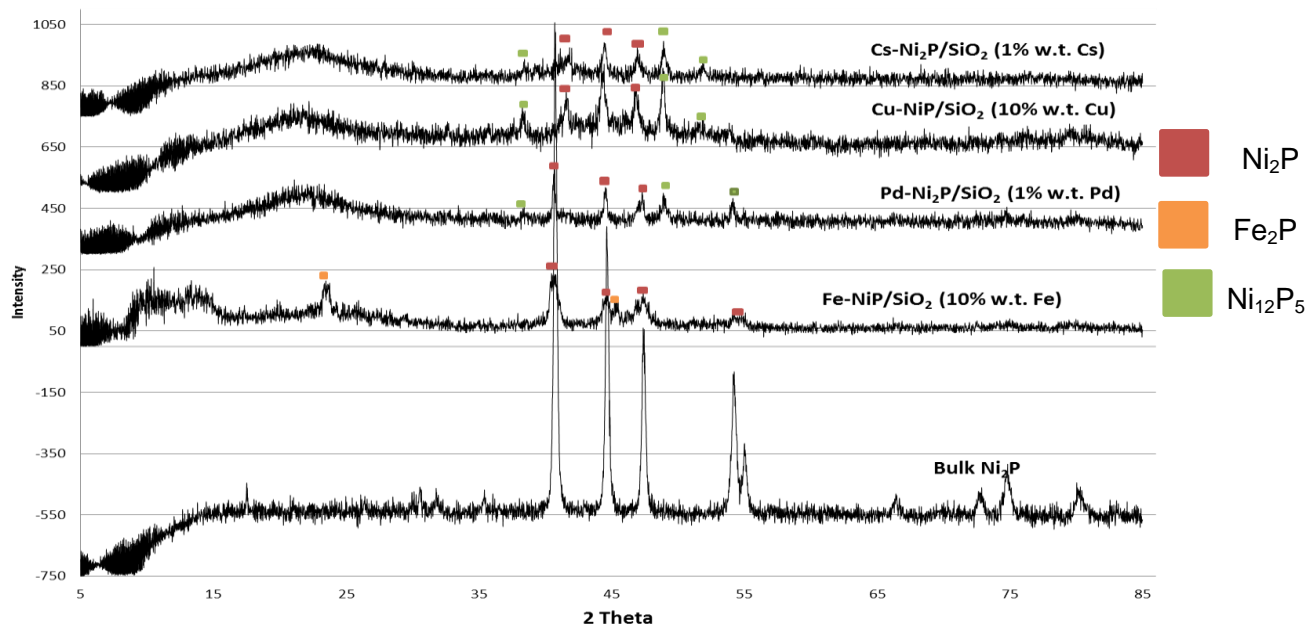


Figure 4-31: XRD patterns for a number of silica supported bimetallic nickel phosphide catalysts.

Thermogravimetric analyses of the reduction of the phosphate precursors to the silica supported bimetallic nickel phosphide catalysts were carried out under flowing H₂/N₂ (5% H₂) up to 800°C with a ramp rate of 10°C/min⁻¹. The TGA reduction profiles for Cu-NiP/SiO₂, Fe-NiP/SiO₂, Cs-Ni₂P/SiO₂ and Pd-Ni₂P/SiO₂ are presented in Figures 4-32 to 4-35.

The reduction profile for the Cu-NiP/SiO₂ catalyst (Figure 4-32) shows a number of distinct peaks. The small peak at 45°C is attributed to loss of water from the material. There is broad and small peak at 300°C which is most likely CuO reduction from a small quantity of copper oxide present in the material. This temperature is consistent with that reported in the literature under similar reduction conditions.^[27] A further small peak at 415°C is also visible. This has been attributed to the reduction of NiO to nickel metal. The largest peak shown in the profile at 749°C has been identified as

the reduction of the nickel phosphate. This is consistent with TGA reduction profiles displayed in the previous chapter for the reduction of nickel phosphate to nickel phosphide. [23] The derivative weight peak at 749°C is relatively narrow possibly indicating a single species of phosphate precursor. The presence of two nickel species is suggested from the presence of the reduction peaks, one associated with nickel metal and the other with copper-nickel phosphide. The weight percentage of the sample after reduction was measured at 87% of the original weight of sample. The theoretical weight loss for $\text{Ni}_3(\text{PO}_4)_2$ to Ni_2P was estimated to be 12% (with 88% of sample weight remaining) on the basis of 20% loading of Ni on the silica support. This indicates that the reduction is mostly phosphate to phosphide in the Cu-NiP/SiO₂ catalyst.

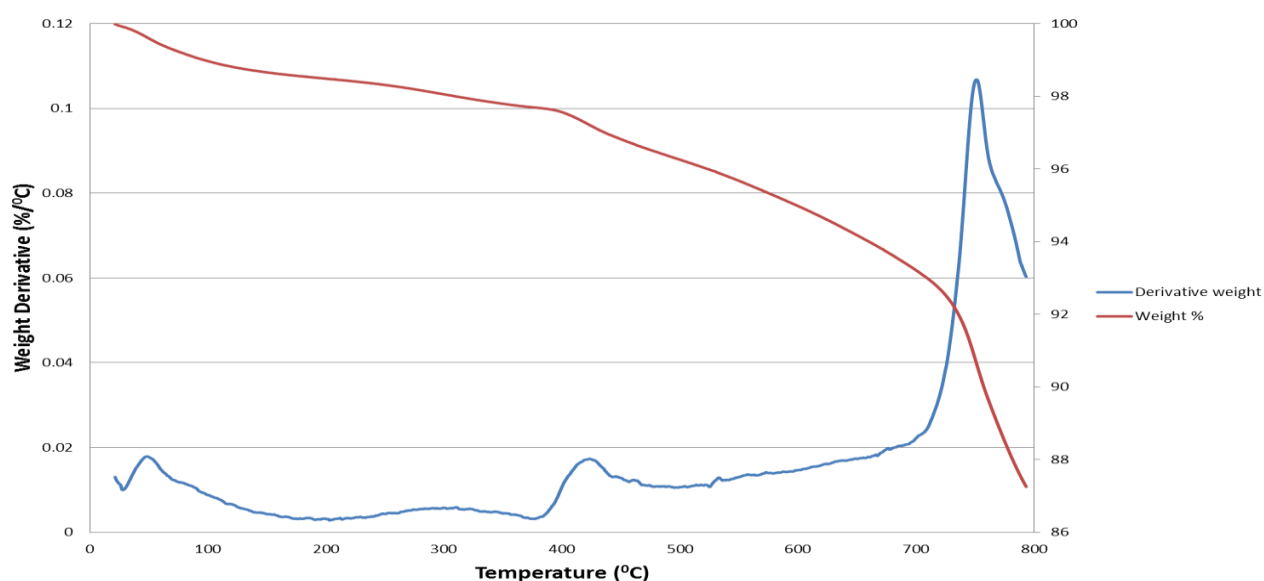


Figure 4-32: TGA reduction profile for the phosphate precursor to Cu-NiP/SiO₂.

Figure 4-33 displays the TGA reduction profile for Fe-NiP/SiO₂. The reduction profile exhibits 3 distinct peaks. The first at 76°C is attributed to the loss of water from the sample. This peak is broad indicating a large amount of moisture present in the precursor. This is further evident from 2% weight loss over this period in the profile. The reduction profile exhibits a very different reduction phase from the Ni₂P/SiO₂ reduction profile shown in the previous chapter. The profile displays a very broad

peak in derivative weight which stretches from 400°C-650°C, indicating a significant amorphous nature in the precursor and a number of reduction processes occurring in the material. This broad peak in derivative weight most likely represents the reduction of iron and nickel oxide phases at the temperatures of 400°C for nickel oxide and 550°C for iron oxide. The further reduction peak at 650°C has been identified as a phosphate-phosphide reduction. This is lower than previously displayed by the other nickel phosphide catalysts developed which were usually found to reduce at 750°C. The profile displays similar features to those of the zeolite supported Fe-NiP catalysts produced by Oyama and co-workers. [29] The weight percentage of the sample after reduction was measured at 90% of the original weight of sample according to the reduction profile. The theoretical weight loss for $\text{Ni}_3(\text{PO}_4)_2$ to Ni_2P was estimated to be 12% (with 88% of sample weight remaining) on the basis of 20% loading of Ni on the silica support. The difference may be attributed to the different composition of alloy present in the Fe-NiP/SiO₂.

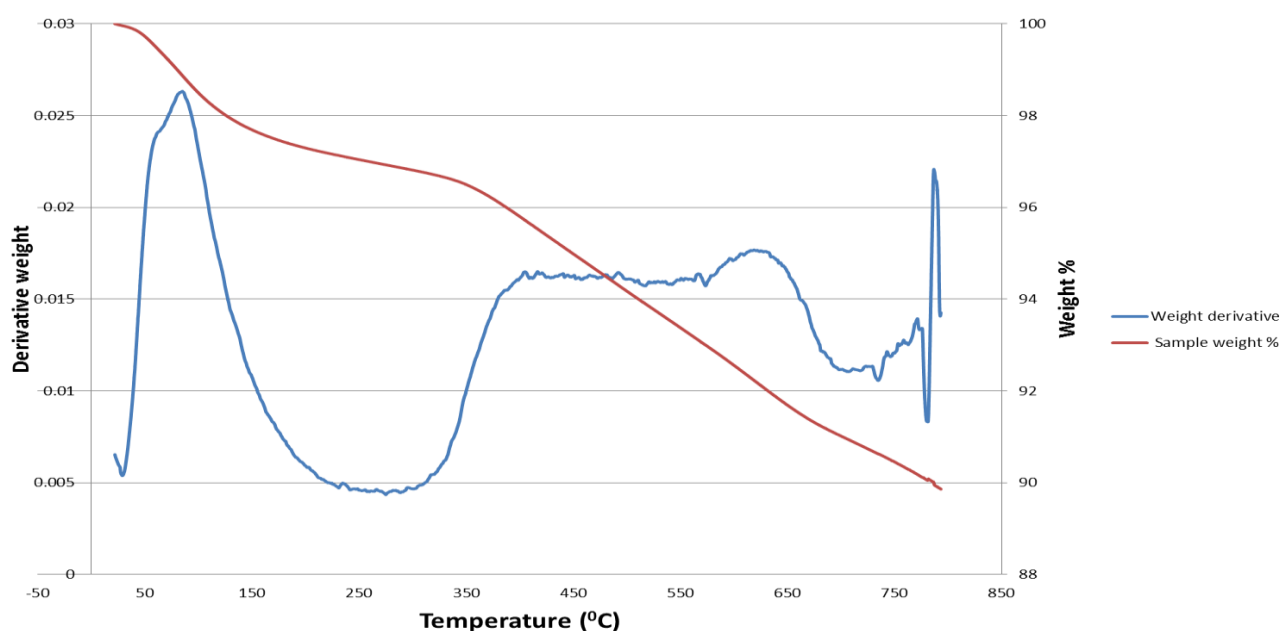


Figure 4-33: TGA reduction profile for the phosphate precursor to Fe-NiP/SiO₂.

The TGA reduction profile for the Cs-Ni₂P/SiO₂ catalyst (Figure 4-34) shows a number of distinct peaks. The small peak at 45°C is attributed to loss of water from

the material. There is broad and small peak at 395°C which has been identified as nickel oxide reduction, a feature visible in the nickel phosphide materials described previously in this chapter. There is a further small peak 660°C and is most likely associated with the reduction of a pyrophosphate species present within the precursor. The largest peak shown in the profile at 752°C has been identified as the reduction of the nickel phosphate. This is consistent with TGA reduction profiles displayed in the previous chapter for the reduction of nickel phosphate to nickel phosphide. The derivative weight peak at 749°C is narrow, indicating a single species of phosphate precursor. The presence two nickel species is suggested from the two reduction peaks, one associated with nickel metal and the other with nickel phosphide. The weight percentage loss for the nickel oxide reduction peak is small in comparison to the weight percentage loss for the phosphate and pyrophosphate reduction peaks, suggesting that nickel phosphide is the phase present in greatest quantity on the support. The weight percentage of the sample after reduction was measured at 91% of the original weight of sample. This is slightly higher than the theoretical weight after reduction for 20% loading of nickel suggesting loading might be slightly higher than anticipated.

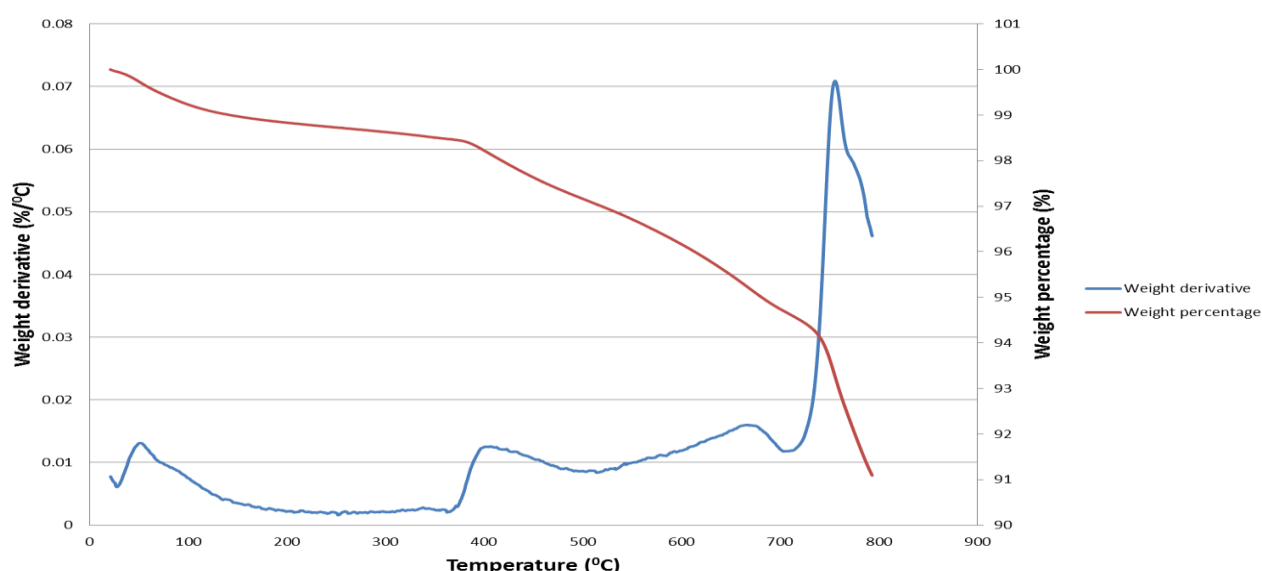


Figure 4-34: TGA reduction profile for the phosphate precursor to Cs-Ni₂P/SiO₂.

Figure 4-35 displays the TGA reduction profile for Pd-Ni₂P/SiO₂. The reduction profile exhibits 3 distinct peaks. The first at 60°C is attributed to the loss of water from the sample. The profile displays two large peaks in derivative weight at 500°C and 680°C. These are attributed to two different phases of nickel phosphate with one most likely being pyrophosphate. The presence of two large and broad peaks highlights the amorphous nature in the precursor, indicating significant weight loss associated with the reduction of different species in the sample across a temperature range. The presence of the two phases of phosphate is most likely due to an uneven dispersion of palladium particles, which influence the formation of the phosphate precursors. The phosphate and pyrophosphate reduction peaks are much lower in temperature than was found with Ni₂P/SiO₂ (phosphate reduction occurs at 750°C). This is consistent with results reported by Da Silva who reported lowering the reduction temperature of Ni₂P/SiO₂ by as much as 200°C by adding small amounts of palladium to the material.^[17] The palladium is thought to activate the hydrogen at a lower temperature for the reduction. The weight percentage of the sample after reduction was measured at 86% of the original weight of sample. This is close to the theoretical estimate for weight of sample remaining after reduction of phosphate to phosphide based on a 20% w.t. of nickel which is known to be 88%.

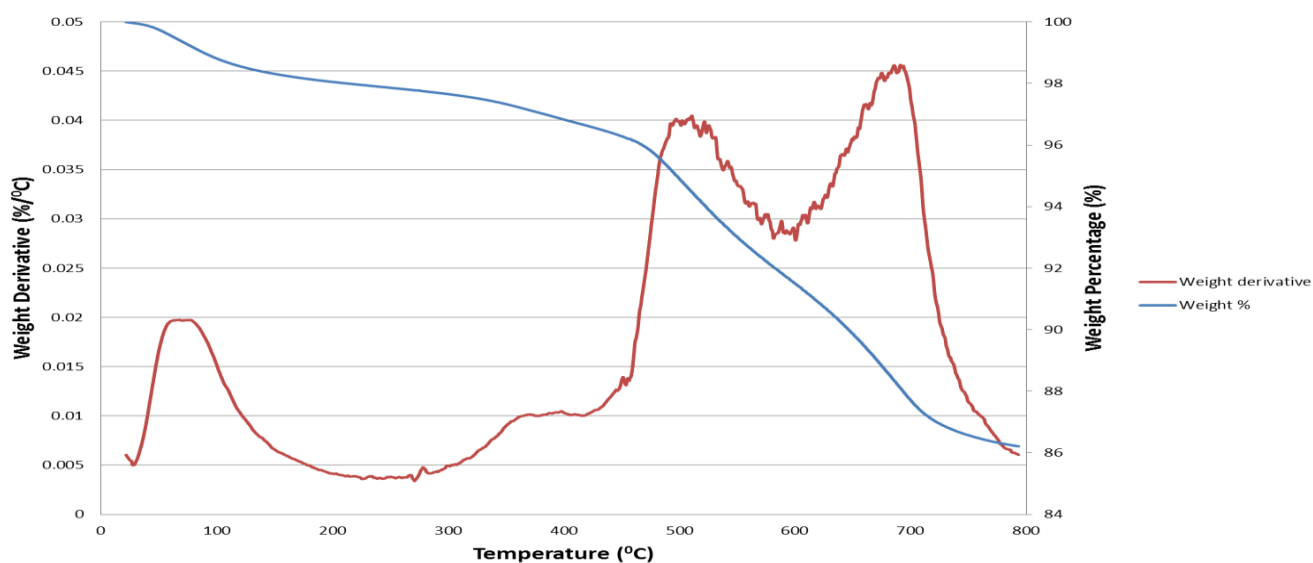


Figure 4-35: TGA reduction profile for the phosphate precursor to Pd-Ni₂P/SiO₂.

The bimetallic nickel phosphide catalysts were characterised qualitatively characterised using SEM characterisation to determine surface morphology of the materials. The materials were studied at several points and EDX analysis was carried out a number of points to determine an average weight and atomic percentage for each element within the sample. The only sample not analysed by EDX was Cu-NiP/SiO₂.

The SEM and EDX results for the Fe-NiP/SiO₂ catalyst are presented in Figure 4-35 and Table 4-9 respectively. SEM and EDX elemental analysis of the material was carried out at a number of points in the micrograph to ensure consistency. The micrograph highlights the area that was used to confirm elemental composition of the particle; it is labelled as “spectrum 2” in Figure 4-36. The micrograph shows light coloured particles on the carbon support, which are thought to be Fe-NiP/SiO₂. The particles are identified as small light coloured phases of material. The particles range in size from 5µm to 25µm. The light particles are confirmed as having nickel, iron and phosphorus present in them by EDX analysis (Table 4-9), which shows nickel, iron and phosphorus in an atomic ratio of roughly 2:1:2. The ratio of elements is consistent with the particles being Fe-Ni₂P. The ratio between the elements varied over the number of sample areas analysed and the average ratio of elements was closer to 1:1:1 which was expected. The target area analysed in this instance was a more nickel and phosphorus rich phase. The variation in elemental composition further highlights the partially amorphous nature of the bimetallic phosphide on the support.

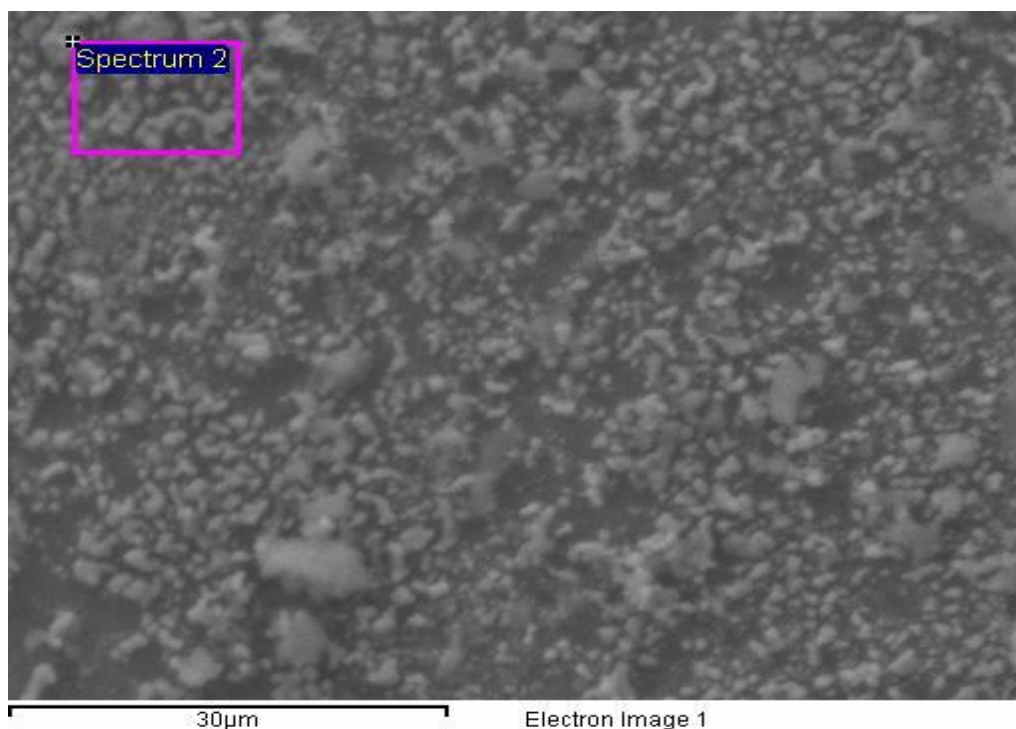


Figure 4-36: SEM micrograph for Fe-NiP/SiO₂

Element (edge)	Weight%	Atomic%	Average At % (deviation)
P (K)	26.72	40.11	37.2 (±13)
Ni (K)	46.19	38.45	37 (±12)
Fe (K)	27.08	21.44	35.3 (±2)
Total	100.00	100.00	

Table 4-9: Summary of EDX results from analysis of target area on the micrograph.

The SEM micrograph for Cu-NiP/SiO₂ is shown in Figure 4-37. The micrograph for the copper-nickel phosphide catalyst shows the presence of light particles on a dark surface. These light particles are thought to contain metallic phases and range in size from 3µm to 10µm. The appearance of these particles suggests that it is likely they contain copper-nickel phosphide species. EDX was not carried out on this material as the EDX instrument was not available for use at time of analysis of the material.

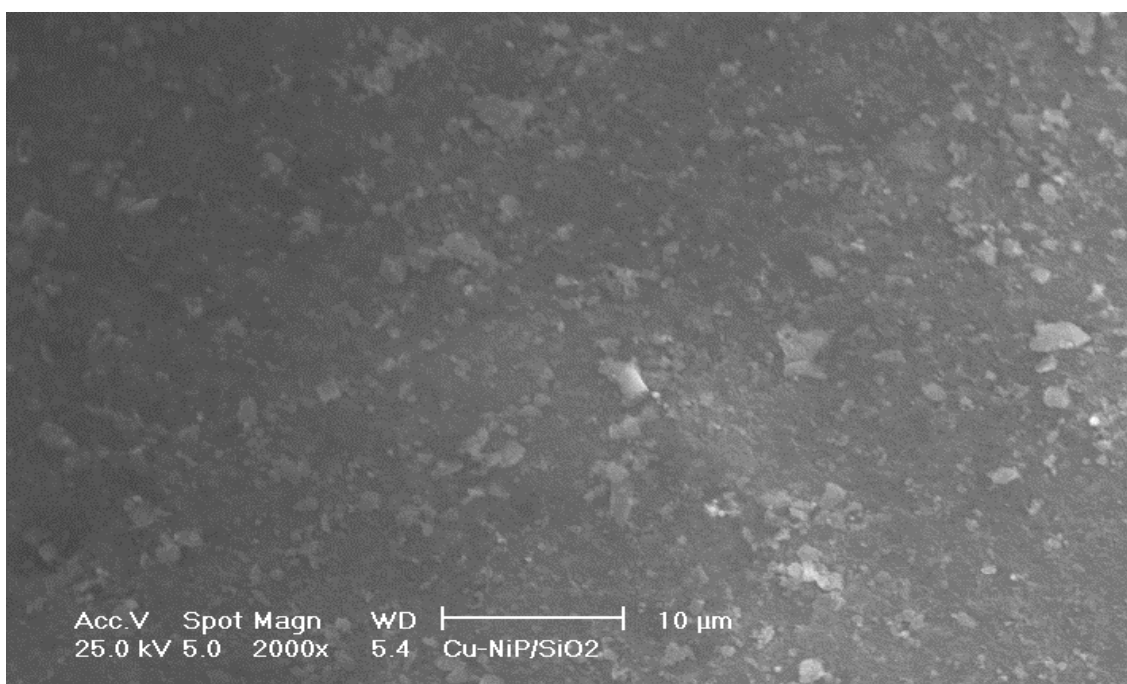


Figure 4-37: SEM micrograph for Cu-NiP/SiO₂

Figure 4-38 shows an SEM micrograph of Cs-Ni₂P/SiO₂. The sample was probed at a number of sites with the microscope with a number of EDX measurements taken for each site. The results of the EDX analysis for the target area highlighted as “Spectrum 2” in the micro graph are given in Table 4-10. The micrograph shows silica supported nickel phosphide dispersed over the carbon support pad. The particles are identified as small light coloured phases of material in contrast to the background. The silica supported nickel phosphide particles range in size from 5µm to 20µm. The presence of nickel and phosphorus within the particles was confirmed by EDX analysis (Table 4-10), which shows nickel and phosphorus in an atomic ratio

in excess of 1:1 with regards to nickel content. The EDX analysis of other points in the sample were estimated to be on average closer to a 2:1 ratio of Ni to P. The average ratio of Ni:P is consistent with the particles being Ni_2P , which has also been confirmed by XRD patterns of the material. The presence of caesium is also confirmed by the EDX analysis in a small quantity consistent with the perceived low doping level in the preparation of the material.



Figure 4-38: SEM micrograph for $\text{Cs-Ni}_2\text{P/SiO}_2$.

Element (edge)	Weight%	Atomic%	Average At % (deviation)
P (K)	29.55	44.73	38.2 (± 6)
Ni (K)	68.23	54.49	62.1 (± 8)
Cs (L)	2.22	0.78	0.7 (± 1)
Total	100.00	100.00	

Table 4-10: Summary of EDX results from analysis of target area on the micrograph.

Figure 4-39 displays the SEM micrograph of Pd-Ni₂P/SiO₂. The sample was probed at a number of sites with the microscope with a number of EDX measurements taken for each site. The results of the EDX analysis for the target area highlighted as “Spectrum 1” in the micro graph are given in Table 4-11. The micrograph shows silica supported nickel phosphide particles dispersed over the surface of the carbon pad. The particles are identified as small light coloured phases in contrast to the background. The particles range in size from 5µm to 25µm. The particles were confirmed as containing nickel and phosphorus by EDX analysis (Table 4-11), which shows nickel and phosphorus in an atomic ratio roughly estimated to be 2:1 with regards to nickel content. EDX analysis of other points in the sample are consistent with the ratio of nickel and phosphorus. The average ratio of Ni:P is consistent with the Ni₂P phase, which has also been confirmed by XRD patterns of the material which displays diffraction peaks associated with Ni₂P and Ni₁₂P₅ which is stoichiometrically similar. The presence of palladium was confirmed by the EDX analysis in a small quantity consistent with the perceived low doping level in the preparation of the material.

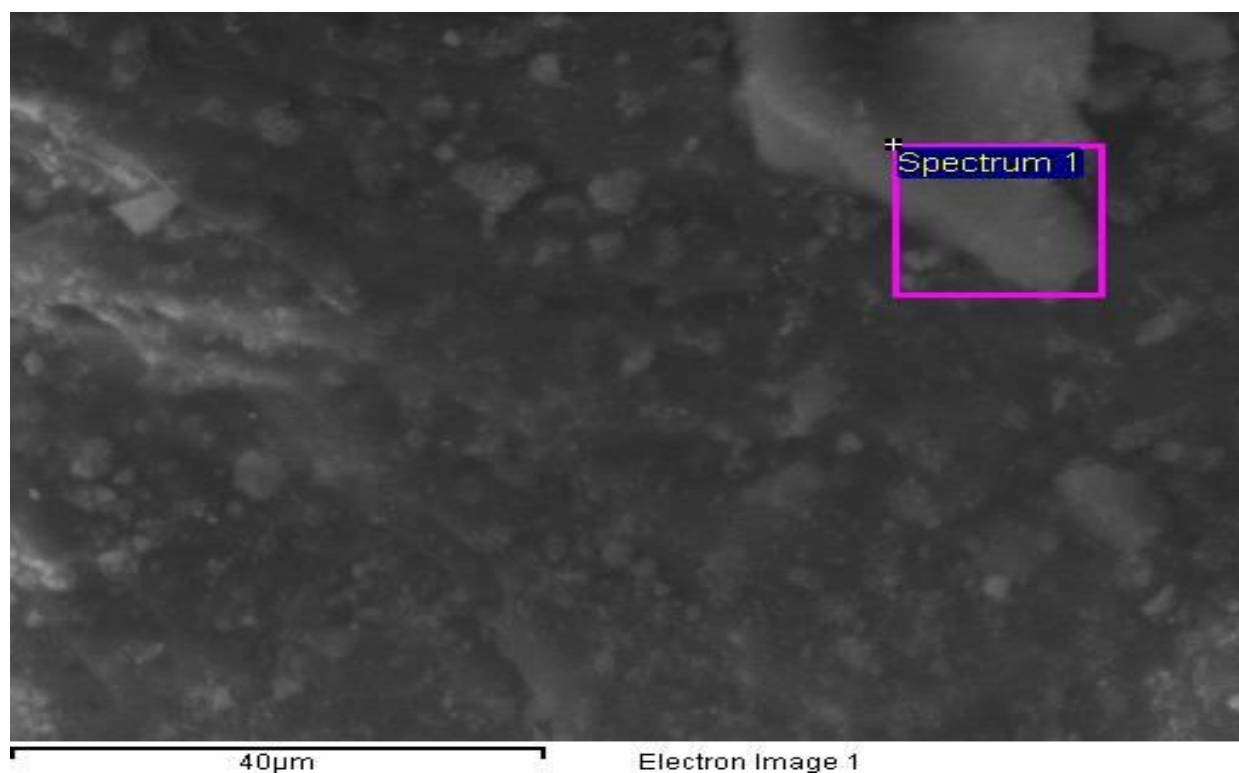


Figure 4-39: SEM micrograph for Pd-Ni₂P/SiO₂

Element (edge)	Weight%	Atomic%	Average At % (deviation)
P (K)	24.60	38.22	33.6 (± 6)
Ni (K)	72.38	60.95	64.5 (± 5)
Pd (L)	3.02	0.83	1.2 (± 0.5)
Total	100.00	100.00	

Table 4-11: Summary of EDX results from analysis of target area on the micrograph.

Transmission electron microscopic analysis of Cu-NiP/SiO₂, Pd-Ni₂P/SiO₂ and Cs-Ni₂P/SiO₂ and associated EDX characterisation was carried out. This was undertaken at the EPSRC TEM access facility in St. Andrews. Fe-NiP/SiO₂ was not analysed using TEM as this study was carried out before the material was produced. The micrographs for Cu-Ni₂P/SiO₂ are shown in Figure 4-40. The EDX analysis of the material is summarised in Table 4-12. The sample was probed at a number of areas and it showed consistence with regards to morphology. EDX was only measured at the site presented the micrograph due to time constraints on the study. There are no visible lattice fringes associated with copper/nickel phosphide crystal phases in the micrographs for the material, similar to SEM micrographs presented in the previously for Cu-NiP/SiO₂ indicating the phosphide has an amorphous nature most likely related to the multiple species of phosphide shown in the XRD pattern for the material. The EDX analysis of the sample highlighted in Figure 4-40 indicates that this particle was copper rich with only small amounts of nickel and phosphorus present. This was the only point which was analysed using EDX analysis. Therefore it cannot be assumed that atomic ratios are the same throughout the material. The elemental analysis does however suggest that copper, nickel and phosphorus do not form phases on the support in the expected stoichiometrically even ratio.

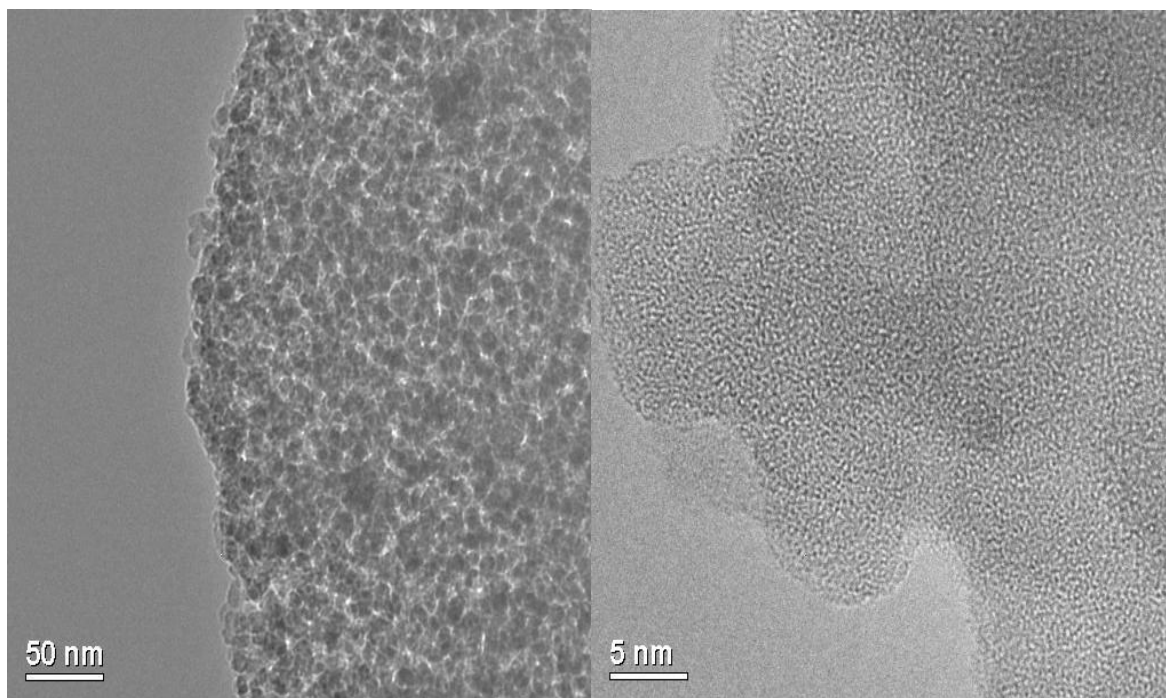


Figure 4-40: TEM micrographs at two magnifications for Cu-NiP/SiO₂

Element (edge)	Peak Area	Element %	Sigma %	Atomic %
O (K)	2232	26.86	0.73	45.61
Si (K)	5352	41.79	0.88	40.43
P (K)	126	1.02	0.25	0.89
Ni (K)	155	2.86	0.59	1.32
Cu (K)	1270	27.46	1.17	11.74
Total		100.00		100.00

Table 4-12 Summary of EDX results from analysis of the micrograph.

Figure 4-41 displays the micrographs for Cs-Ni₂P/SiO₂. The sample was probed at a number of sites. EDX characterisation of the material was carried out. Table 4-13 summaries the results of the EDX analysis. The micrographs show uniform particles with sizes between 10-15nm in size. The crystalline phases on the support are similar in size and shape to those seen in TEM micrographs presented in the previous chapter for Ni₂P/SiO₂. The crystal fringes in the TEM image displayed lattice parameters of 1.91 Å and 2.16 Å indicating that there are two crystallographic planes present. The lattice parameter at 1.91 Å corresponds to the reflection at 54.2° 2theta in the XRD pattern for the material. This is consistent with the (3 0 0) crystallographic plane of Ni₂P. The second lattice parameter at 2.16 Å is consistent with the (2 0 1) plane of Ni₂P which corresponds to the reflection at 45.5° 2theta in the XRD pattern for Ni₂P. These reflections are visible in the diffraction pattern for the material shown previously. The micrographs show a mostly uniform dispersion of species. The EDX analysis of the ordered phase highlighted in Table 4-13 indicates that the material contains both cerium and nickel phosphide. The atomic ratio is estimated to be roughly 2:1 with respect to Ni:P which is consistent with Ni₂P being the species of nickel phosphide formed. The elemental analysis also reveals a large amount of caesium is present in relation to nickel and phosphorus atomic percentages, possibly indicating that caesium is not uniformly dispersed throughout the material. This was the only point which was analysed using EDX analysis therefore it cannot be assumed that atomic ratios are the same throughout the material.

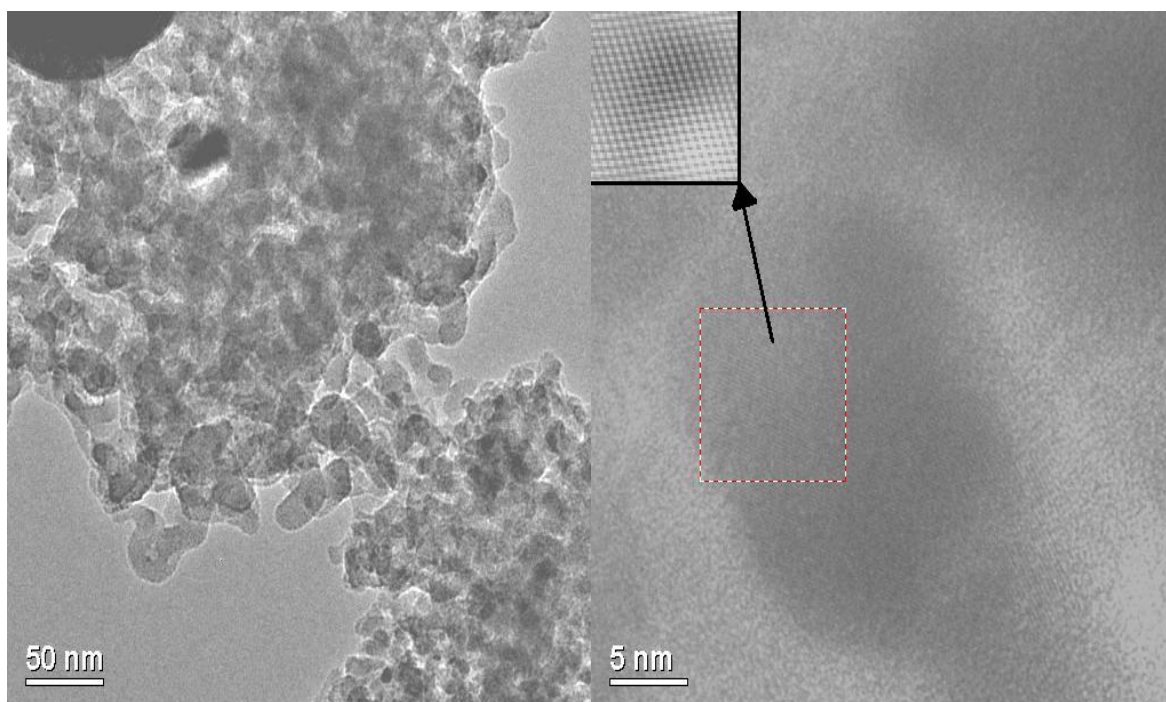


Figure 4-41: TEM micrographs at two magnifications for Cs-Ni₂P/SiO₂

Element (edge)	Peak Area	Element %	Sigma %	Atomic %
O (K)	9630	34.79	0.41	50.91
Si (K)	21879	52.76	0.48	43.98
P (K)	478	1.19	0.16	0.90
Ni (K)	733	4.18	0.41	1.67
Cs (L)	681	4.40	0.41	0.78
Total		100.00		100.00

Table 4-13: Summary of EDX results from analysis of target area on the micrograph.

TEM analysis of Pd-Ni₂P/SiO₂ is presented in Figure 4-42 which displays the micrographs of the material. Table 4-14 contains a summary of results from elemental analysis of the target area within the sample. The sample was probed at a number of sites. The material morphology was consistent at a number of probed

areas within the sample. The micrographs show uniformly shaped ordered phases on the support with sizes between 5-10 nm, similar to TEM micrographs presented in the previous chapter for Ni₂P/SiO₂ and slightly smaller than those seen in Cs-Ni₂P/SiO₂ micrographs. Pd-Ni₂P/SiO₂ displays a uniform dispersion of particles on the support. The crystal fringe in the TEM image displayed a lattice parameter of 2.05 Å, suggesting that a single crystallographic plane was present in this specific crystal fringe. The lattice parameter corresponds to the reflection at 47.6° 2theta in the XRD pattern for the material. This is consistent with the (2 1 0) crystallographic plane of Ni₂P. The corresponding diffraction peak is evident in the diffraction pattern for the material. The elemental analysis of the ordered phase is highlighted in Table 4-14 and indicates that the crystallite contains nickel and phosphorus in the rough atomic ratio of 2:1. The atomic ratio is consistent with EDX analysis of the material shown in SEM analysis further supports that Ni₂P is the phosphide species present on the support. The presence of palladium was confirmed by the elemental analysis in a small quantity, consistent with the perceived low doping level in the preparation of the material. This was the only point which was analysed using EDX analysis therefore it cannot be assumed that atomic ratios are the same throughout the material. The elemental analysis does however indicate that the Ce and nickel phosphide appear to co-exist in the same location within in the material.

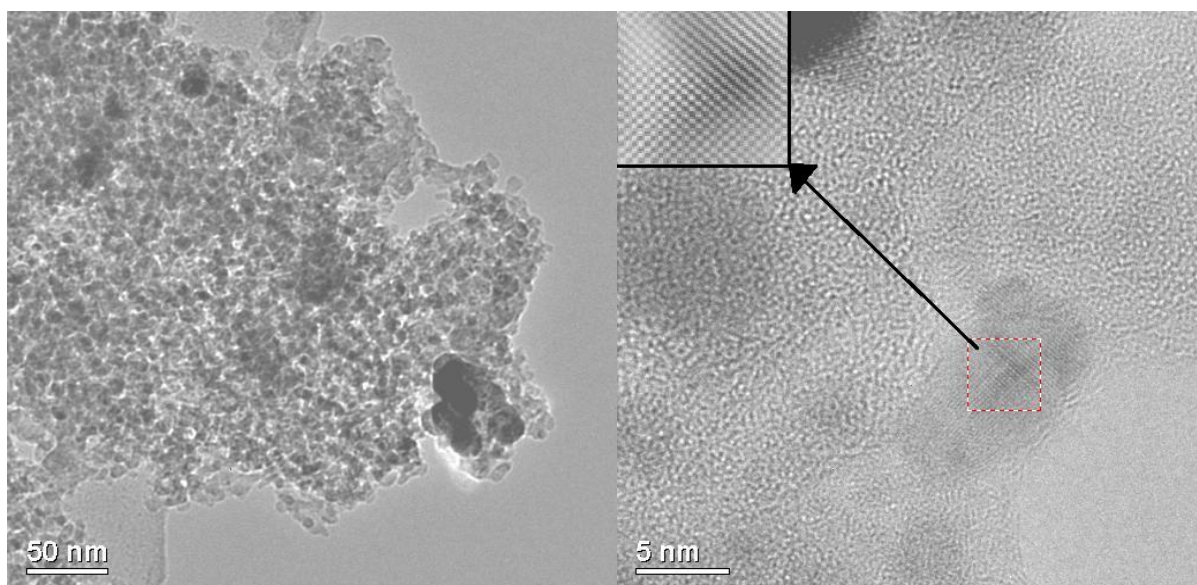


Figure 4-42: TEM micrographs at two magnifications for Pd-Ni₂P/SiO₂

Element (edge)	Peak Area	Element %	Sigma %	Atomic %
O (K)	7334	25.29	0.39	43.80
Si (K)	15930	35.64	0.45	35.16
P (K)	3317	7.67	0.24	6.86
Ni (K)	5375	28.42	0.64	13.41
Pd (L)	657	2.97	0.43	0.77
Total		100.00		100.00

Table 4-14: Summary of EDX results from analysis of target area on the micrograph.

The Cs-Ni₂P/SiO₂ and Fe-NiP/SiO₂ catalysts were characterised using XPS, to enable a greater understanding of the chemical state in which nickel and phosphorus exist within the material at the near surface regions. The other materials were not characterised by XPS due to limited access to the EPSRC XPS service.

The nickel 2p, phosphorus 2p and iron 2p spectra for Fe-NiP/SiO₂ are shown in Figures 4-43 to 4-45. Tabulated binding energies derived from the spectra are presented in Table 4-15, along with those derived from the Ni₂P/SiO₂ XPS spectra presented in the previous chapter. The nickel 2p spectrum for Fe-NiP/SiO₂ shows 3 binding energy peaks associated with nickel species within the material. The binding energy peak at 850.2 eV is recognised as Ni⁰. This is attributed to the presence of Ni metal sites within the material as a result of Fe loading. The presence of nickel metal suggests a nickel-iron alloy phase is present in the material. The binding energy peak associated with Ni metal is not present in the nickel 2p Ni₂P/SiO₂ spectrum, which highlights the effect that the introduction of iron into the phosphide system has with regards to species of nickel formed in the material. The spectrum shows two further binding energy peaks associated with Ni, a major peak at 853.1 eV and minor peak at 857.4 eV. These were identified in the previous chapter as nickel species synonymous with Ni₂P.^[2] The peak at 853.1 eV has been identified as Ni^{δ+}, where 0 < δ+ < 2, which is consistent with it being bonded to phosphorus in Ni₂P.^[2] The minor peak in the spectra at 857.4 eV has been assigned to Ni^{II+} species associated with

nickel pyrophosphate, a result of oxy-phosphide surfaces that promote the catalytic activity of the material. [3] The relative intensity of Ni metal binding energy peak at 850.2 eV is the largest in comparison to the nickel phosphide and phosphate species suggesting a significant presence. The weakest binding energy peak is that of the nickel phosphate species (Ni^{II}). This suggests that this material has fewer oxy-phosphide phases. Lower oxygen content in the material may have a detrimental effect on the catalytic activity; this will be explored later in the chapter.

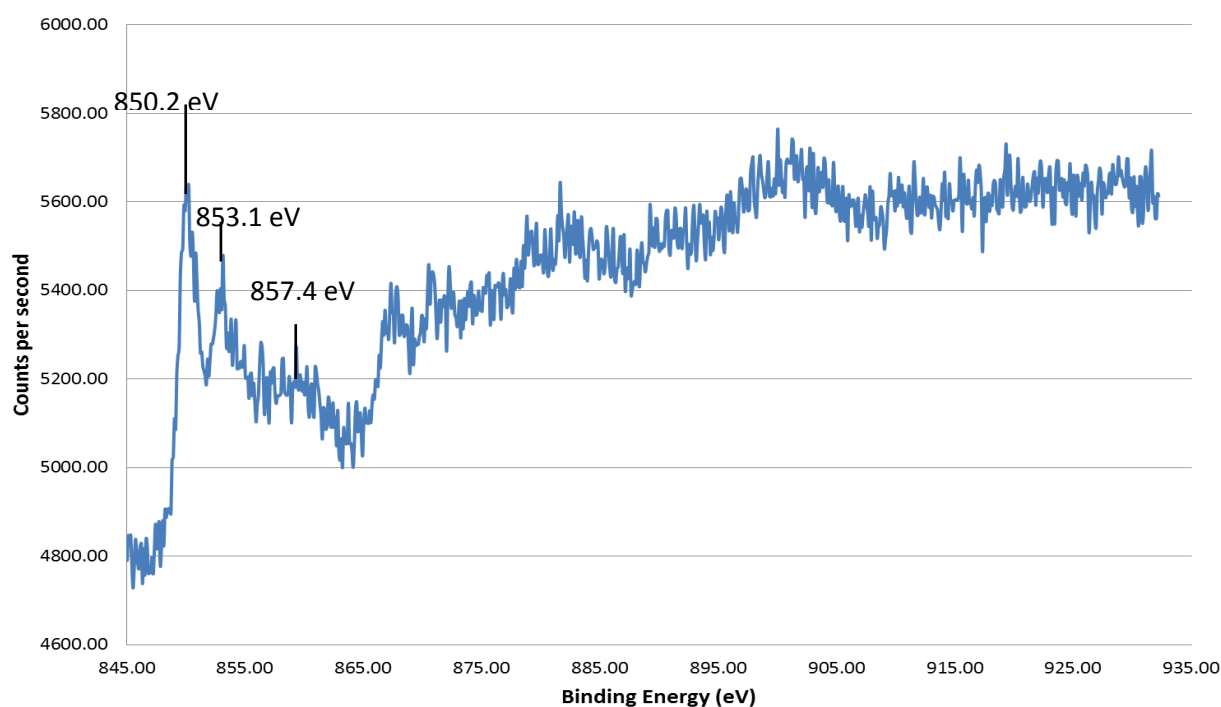


Figure 4-43: XPS nickel 2p spectrum for Fe-NiP/SiO₂.

The Fe-NiP/SiO₂ phosphorus 2p spectrum (Figure 4-44) exhibits two binding energy peaks at 126.1 and 131.1 eV indicating two species of phosphorus are present in the catalyst. The peak centred at 131.1 eV and has been identified as $\text{P}^{\delta-}$ where $0 < \delta < 1$ according to previous studies. This is associated with phosphorus in the form of Ni_2P . [4, 7] The peak at 126.1 eV has been identified as phosphorus in the iron species where $\text{P}^{\delta-}$. The two phosphorus species in Fe-NiP/SiO₂ suggests that multiple species of phosphides exist, further supported by the iron 2p spectrum displayed in Figure 4-45. Table 4-15 displays the tabulated binding energy for iron in

the material. There were two distinct regions in the iron 2p spectrum as a result of spin orbit coupling. The binding energy peak at 703.9 eV has been identified as iron metal. It is likely that this alloyed with the nickel as alluded to in nickel 2p spectrum (Figure 4-43). The XPS analysis of the Fe-NiP/SiO₂ has shown Ni₂P, Fe₂P and an Fe-Ni alloy all exist within the material further highlighting the amorphous nature of the material suggested by the XRD pattern for the material. The XPS spectrum for the Fe-NiP/SiO₂ is also noticeably different from the Ni₂P/SiO₂, as is evident from tabulated binding energies for both materials in Table 4-15 which show Ni₂P/SiO₂ to be more uniform with regards to species present on the support. This amorphous nature of the catalyst may affect its overall catalytic activity due to disordered phases present, as will be addressed later in the chapter.

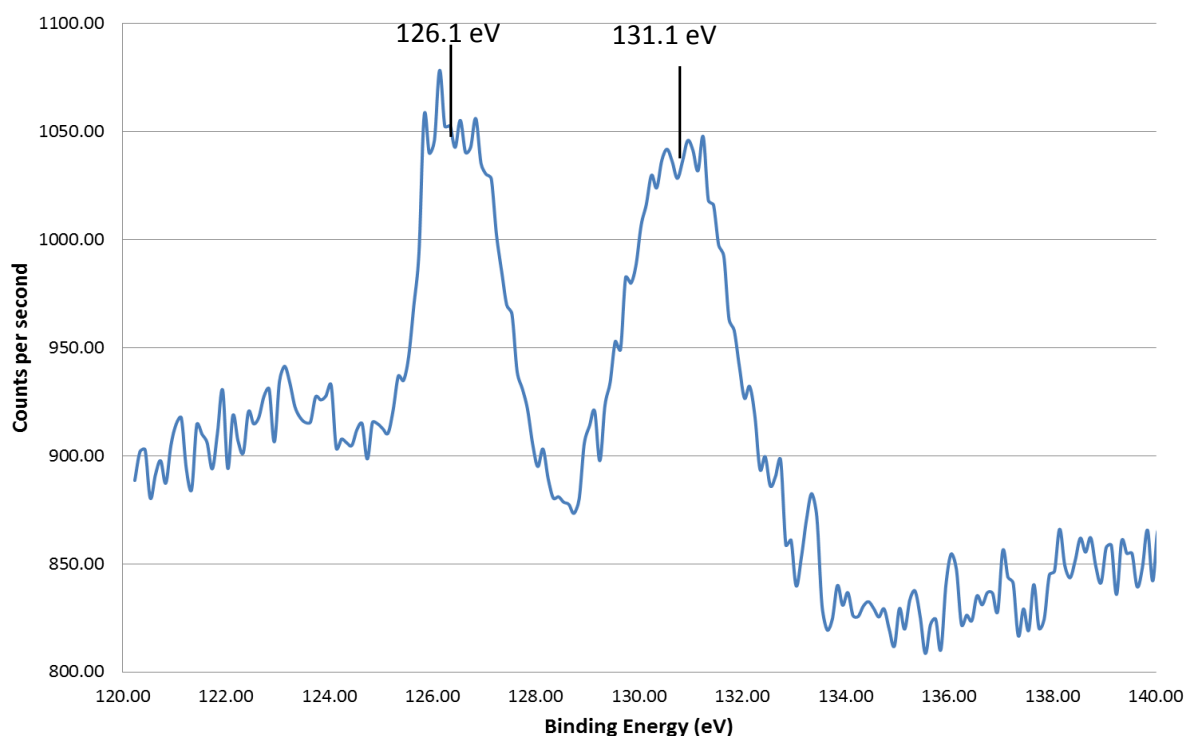


Figure 4-44: XPS phosphorus 2p spectrum for Fe-NiP/SiO₂.

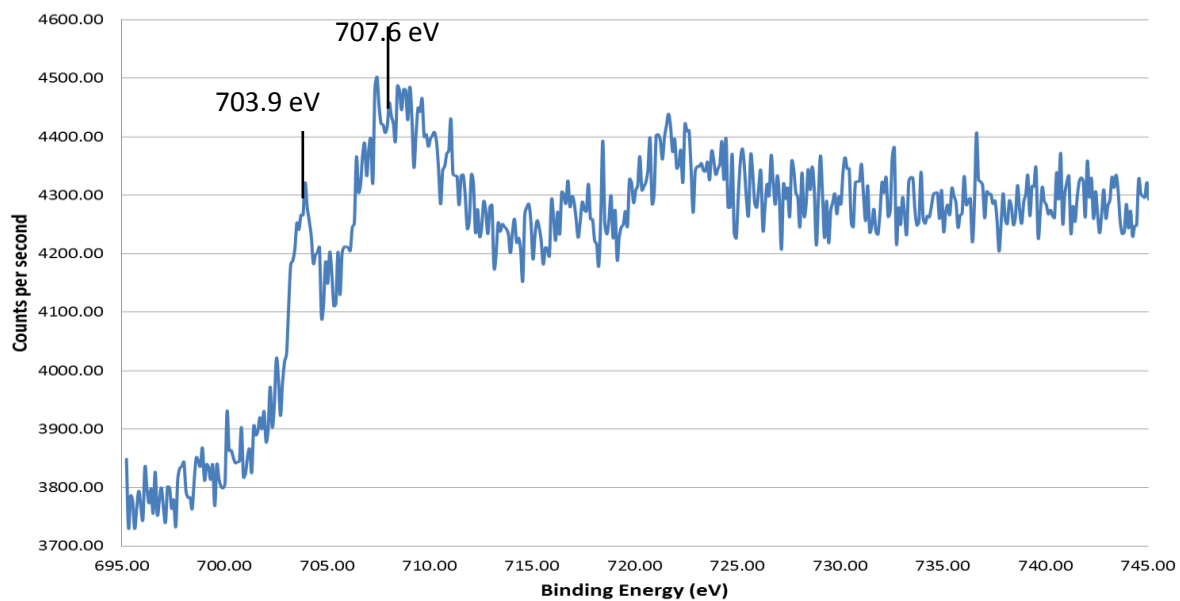


Figure 4-45: Iron 2p spectrum for Fe-NiP/SiO₂.

Sample	Fe-NiP/SiO ₂	Ni ₂ P/SiO ₂
	Binding energy	Binding energy
Element	(eV)	(eV)
Ni 2p	850.2(largest) 853.1 857.4 (smallest)	853.5 (largest) 856.8 (smallest)
P 2p	126.1 131.1	130.6
O 1s	533.1	532.8
C 1s	285.0	285.0
Fe 2p	703.9(smallest) 707.6 (largest)	N/A

Table 4-15: Summary of binding energy peaks shown in the XPS spectra for Ni₂P/SiO₂ and Fe-NiP/SiO₂.

Figures 4-46 and 4-47 show the XPS nickel 2p and phosphorus 2p spectra for Cs-Ni₂P/SiO₂. The binding energies for Cs-Ni₂P/SiO₂ and Ni₂P/SiO₂ are presented in Table 4-16. The nickel 2p spectrum displays a number of binding energy peaks associated with nickel species, indicating a multiple phases present within the material. The binding energy peaks at 852.9 eV and 856.8 eV were identified in the previous chapter as nickel species synonymous with Ni₂P. The peak at 852.9 eV has been identified as Ni^{δ+}, where 0 < δ+ < 2, which is consistent with it being bonded to phosphorus in Ni₂P. The binding energy for the Cs-Ni₂P/SiO₂ is slightly higher than for Ni₂P/SiO₂ as highlighted in Table 4-16 and suggests that caesium may be responsible for this shift. Rodriguez and co-workers suggested that doping bulk phase nickel phosphide with small amounts of caesium increased the material's affinity for oxygen. Therefore the shift seen in binding energy is consistent with an increase in oxidation of the nickel phosphide. The binding energy peak in the spectrum at 856.8 eV has been assigned to Ni^{II+} species associated with nickel pyrophosphate, a result of oxy-phosphide surfaces that promote the catalytic activity of the material. [4] The other peaks at 868.4 eV and 872.2 eV are identified as features of 2p_{1/2} due to spin orbit coupling.

The phosphorus 2p spectrum for Cs-Ni₂P/SiO₂ (Figure 4-47) exhibits two binding energy peaks at 129.4 and 133.3 eV indicating two species of phosphorus are present in the catalyst. The peak centred at 129.4 eV has been identified as P^{δ-} where 0 < δ- < 1 according to previous studies. [4, 7] The binding energy for P^{δ-} is slightly lower than in phosphorus 2p spectra for Ni₂P. It is however still within the reported range for phosphorus in nickel phosphide. The difference is most likely a result of the addition of caesium to the phosphide system. The peak at 133.3 eV has been identified as phosphorus in the nickel phosphate species where phosphorus is in the P^{V-} oxidation state. The presence of the oxygen rich phases is most likely a result of the addition of caesium to the system, this phosphate species is not present in the Ni₂P/SiO₂ phosphorus 2p spectrum. Caesium has a strong affinity for oxygen and has previously been used as a dopant promoting oxygen content in catalysts. As discussed previously, the Rodriguez group reported that the oxy-phosphide phases present in Ni₂P increased after doping with caesium in bulk phase materials. Further to this Rodriguez also suggests that the oxy-phosphide surfaces promote the

catalytic activity of the nickel phosphide. The XPS analysis of the Fe-NiP/SiO₂ has shown that a number of species of nickel phosphate and phosphide are present in the material further highlighting the amorphous nature of the material suggested by the XRD pattern for the material.

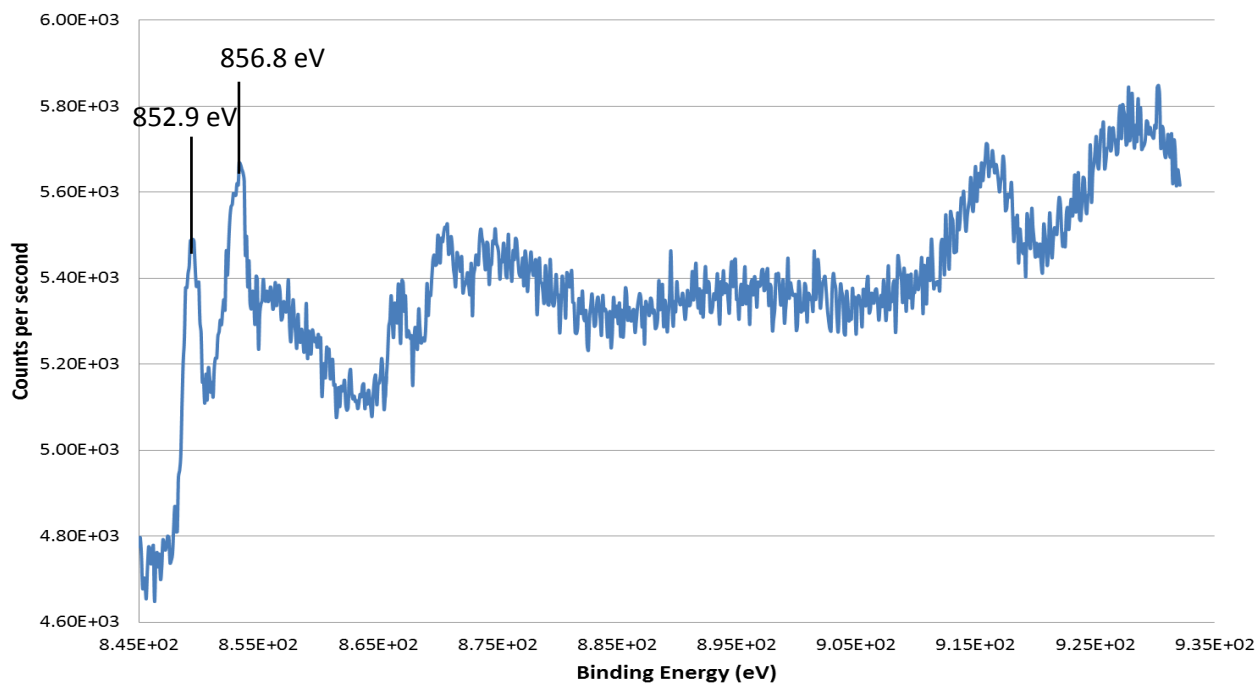


Figure 4-46: XPS nickel 2p spectrum for Cs-Ni₂P/SiO₂.

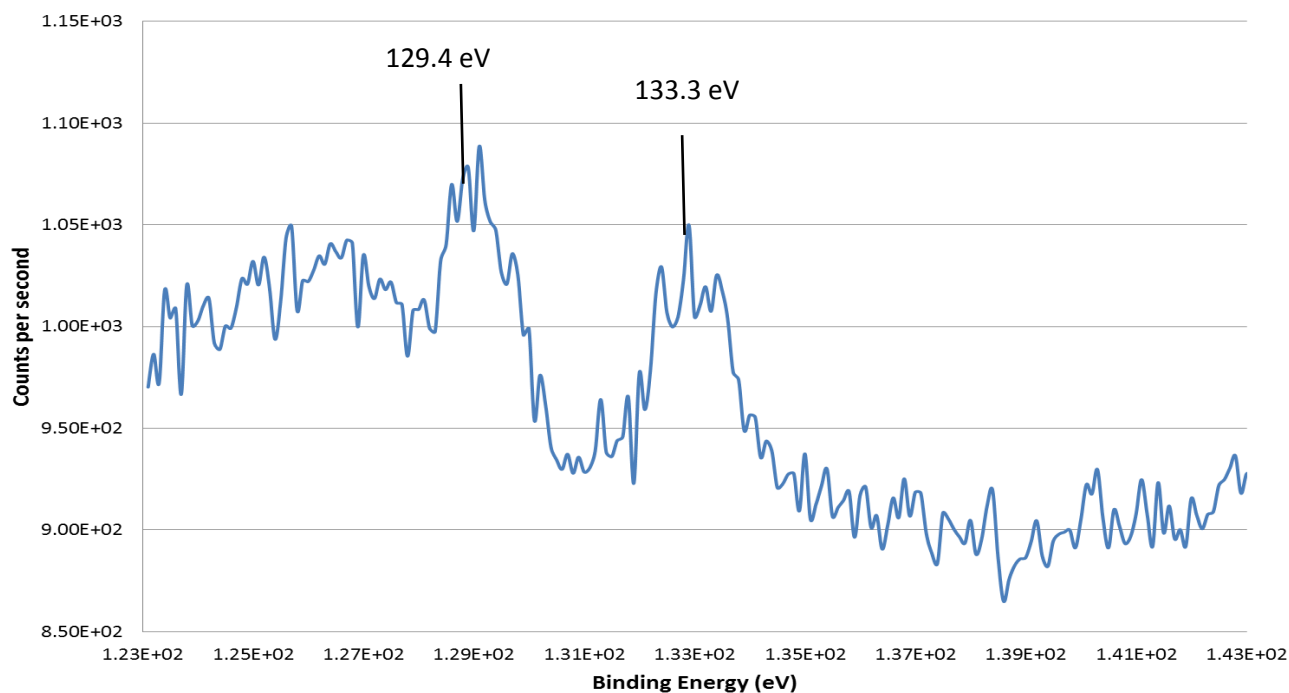


Figure 4-47: XPS phosphorus 2p spectrum for Cs-Ni₂P/SiO₂.

Sample	Cs-Ni ₂ P/SiO ₂	Ni ₂ P/SiO ₂
Element	Binding energy (eV)	Binding energy (eV)
Ni 2p	852.9	853.5 (largest) 856.8 (smallest)
	856.8	
P 2p	129.4	130.6
	133.3	
O 1s	532.9	532.8
C 1s	285.0	285.0

Table 4-16: Summary of binding energy peaks shown in the XPS spectra for Ni₂P/SiO₂ and Cs-Ni₂P/SiO₂

The XPS analysis of the materials has revealed that there are complex relationships between bimetallic components of the phosphide materials which have an overall effect in composition and form of the phosphide catalysts. The Cu-NiP/SiO₂, Fe-NiP/SiO₂ and Pd-Ni₂P/SiO₂ catalysts were analysed using X-ray absorption spectroscopy. This has given a greater insight into the chemical state of the catalyst active phases. The study was focused primarily on the extended X-ray absorption fine structure spectrum of the material although the XANES region was briefly explored for the materials as well to gain insight into oxygen affinity for nickel within the catalysts. Figure 4-48 displays the k^3 weighted EXAFS spectrum for Cu-NiP/SiO₂ and Figure 4-49 illustrates the Fourier transformed spectrum for the material. Both spectra have been refined and a theoretical curve has been applied through collaboration with Prof. G. Sankar from University College London. The results of the curve fit for the FT spectra for the material are summarised in Table 4-17.

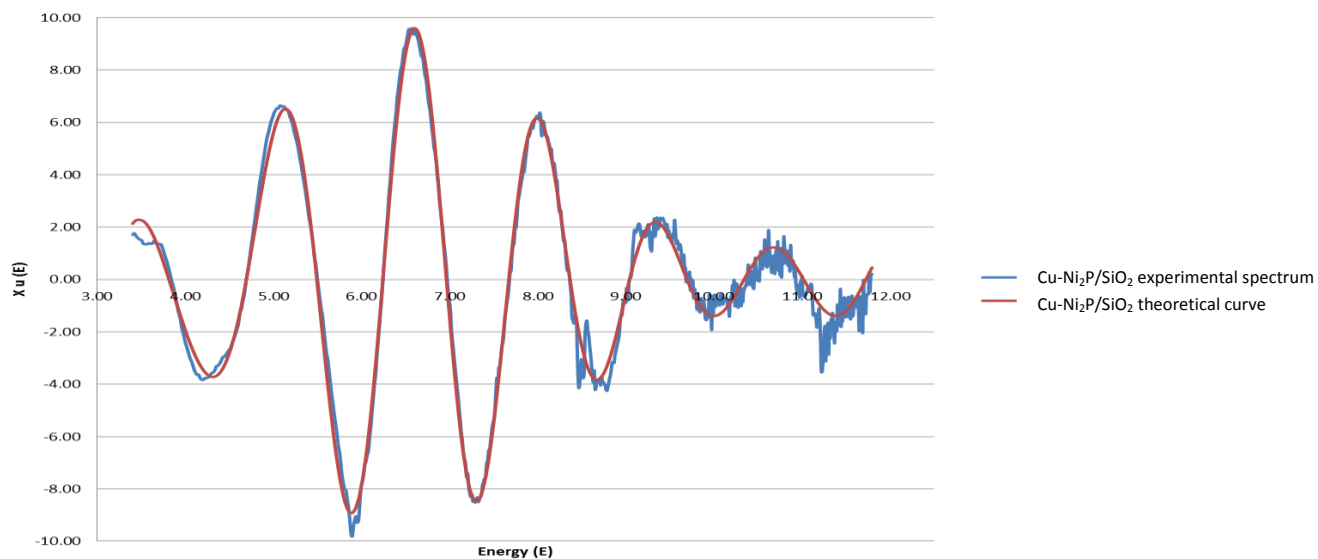


Figure 4-48: The k^3 weighted EXAFS spectrum for Cu-NiP/SiO₂ catalyst along with theoretical curve fit.

The curve fitting results for the Cu-NiP/SiO₂ EXAFS spectrum is presented in Table 4-17. The nickel K edge FT spectrum for the material displays a single broad peak corresponding first shell which has been fitted. There are further peaks associated with 2nd and 3rd shells which have not been fitted. The FT spectrum copper-nickel phosphide catalyst differs from the nickel phosphide presented in the previous chapter. This is consistent with the trend seen with bimetallic nickel phosphide materials differing significantly in composition in comparison to the monometallic nickel phosphide catalyst. The peak which was fitted with the theoretical curve is centred at 0.243nm and the broad nature of this peak suggests multiple features are present. The further shells in the FT spectrum for the material have not been fitted due unsatisfactory fits being obtained. The theoretical fit has taken into consideration Ni-P and Ni-Ni scattering from the nickel centre to achieve the best curve fit for the spectrum. Ni-P distance according to the fit is estimated to 0.219nm which is within the reported range (0.218-0.231nm) for Ni-P distance reported in the literature.^[4] Comparison of Ni-P distance for Cu-NiP/SiO₂ with Ni₂P/SiO₂ shows the Ni-P distance has shortened from 0.221nm to 0.219nm with the addition of copper to the system. The theoretical curve fit for Cu-NiP/SiO₂ estimates a decrease in the co-ordination number for Ni-P in comparison to Ni₂P/SiO₂ from 4.05 to 3.29. The decrease in the

co-ordination number seen in the copper-nickel phosphide catalyst suggests that the nickel phosphide particle size has decreased. This was also seen in Ce-Ni₂P/SiO₂ materials indicating that the introduction of the second metallic component may cause particle size to decrease. Ni-Ni scattering was identified at a distance of 0.250nm to Ni neighbours, with a co-ordination number of 4.76 suggesting as many as 5 Ni neighbours present in relation to the target nickel site. The greater number of Ni-Ni interactions in the material in comparison to previously reported values in the literature is attributed to formation of the nickel-copper alloy phases evident in the XPS spectrum for the material.

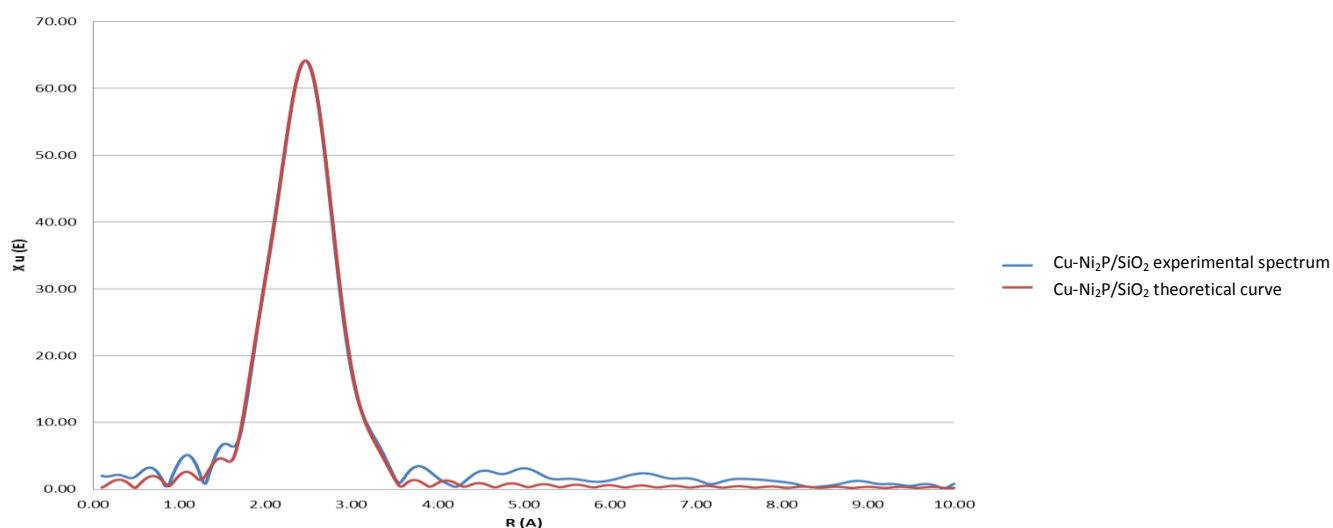


Figure 4-49: Fourier transforms spectrum for Cu-NiP/SiO₂ catalyst along with theoretical curve fit

Shell	Scatterer	Bond distance (Å)	co-ordination No	A	AFAC	ΔE	R-Factor
1	Ni-P	2.1929	3.29	0.01303	0.7735	3.9952	14.4135
2	Ni-Ni	2.50469	4.76	0.01767	0.7735		
3	Ni-Ni	2.95805	1.27	0.01767	0.7735		

Table 4-17: Summary of curve fit results for Cu-NiP/SiO₂ EXAFS spectrum.

The k^3 weighted EXAFS spectrum for Pd-Ni₂P/SiO₂ is displayed in Figure 4-50 whilst Figure 4-51 illustrates the Fourier transformed spectrum for the material. The curve fitting results for the Pd-Ni₂P/SiO₂ EXAFS spectrum is presented in Table 4-18. The nickel K edge FT spectrum for the material displays two distinct peaks corresponding first shell which has been fitted. There are further peaks associated with 2nd and 3rd shells. However, these have not been fitted due to difficulty with effective fitting.

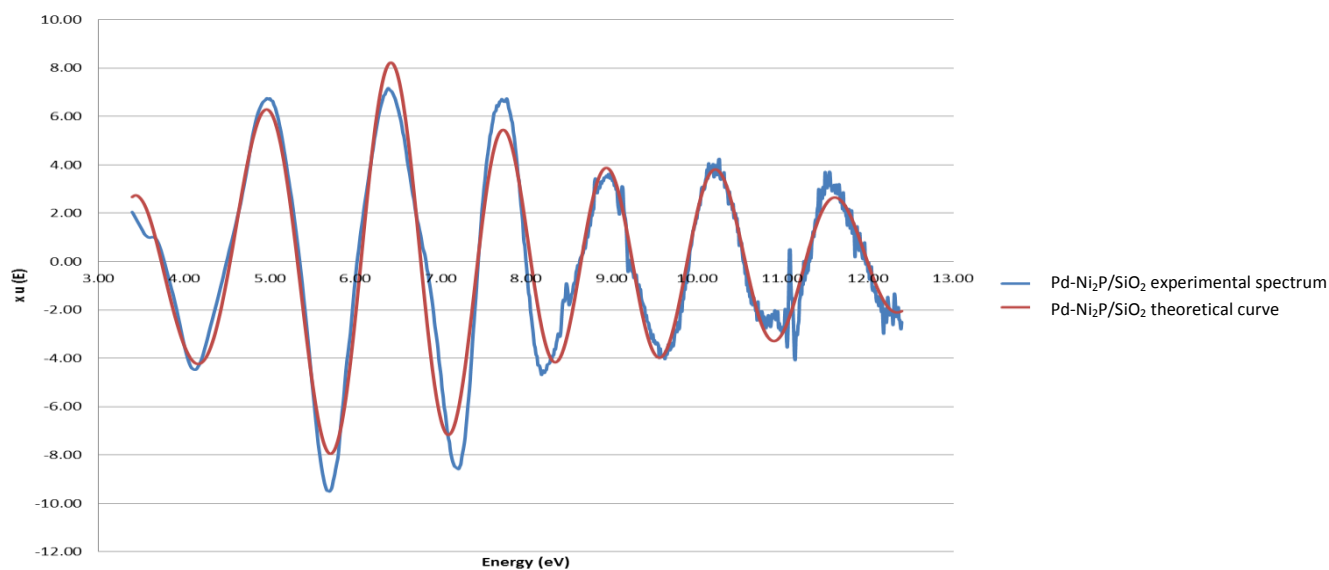


Figure 4-50: The k^3 weighted EXAFS spectrum for Pd-Ni₂P/SiO₂ catalyst along with theoretical curve fit.

The theoretical fit for the spectrum shows Ni-P scattering with a bond distance of 0.223 nm, consistent with Ni-P distances reported which have been found to be in the range of 0.218-0.231 nm.^[4] The curve fit indicated that a co-ordination number of 3.91 suggesting that 4 P neighbours are present around the nickel atom. The second and larger peak is centred at 0.259 nm and has been identified as Ni-Ni interactions with a co-ordination number of 4, indicating 4 neighbouring Ni neighbours. These results closely resemble those reported by Lee and Oyama for silica supported nickel phosphide catalysts, indicating that palladium does not alter the final phase of nickel to the same extent as the other dopants which either formed alloys with the nickel or formed more nickel metal sites. The comparison of the EXAFS curve fit

results for Pd-Ni₂P/SiO₂ with Ni₂P/SiO₂ indicates some differences between the standard material and palladium doped one. The Ni-P bond distance for the palladium doped material is slightly longer and the co-ordination numbers for the Ni-P sites is lower in the material in comparison to monometallic nickel phosphide. The bond distance for Ni-P interactions in the standard nickel phosphide catalyst was calculated to be 0.222 nm whilst the Pd-Ni₂P/SiO₂ Ni-P distance was found to be 0.223 nm. The decrease in distance has been reported previously for supported transition metal phosphides and has been correlated to greater dispersion of the particles on the surface support. [2-4] The co-ordination numbers would also be expected to decrease with bond distance however Oyama has attributed an increase in co-ordination number to an increased presence of phosphorus on particles surfaces indicating that there are some slight differences in the materials due to the influence of the palladium.

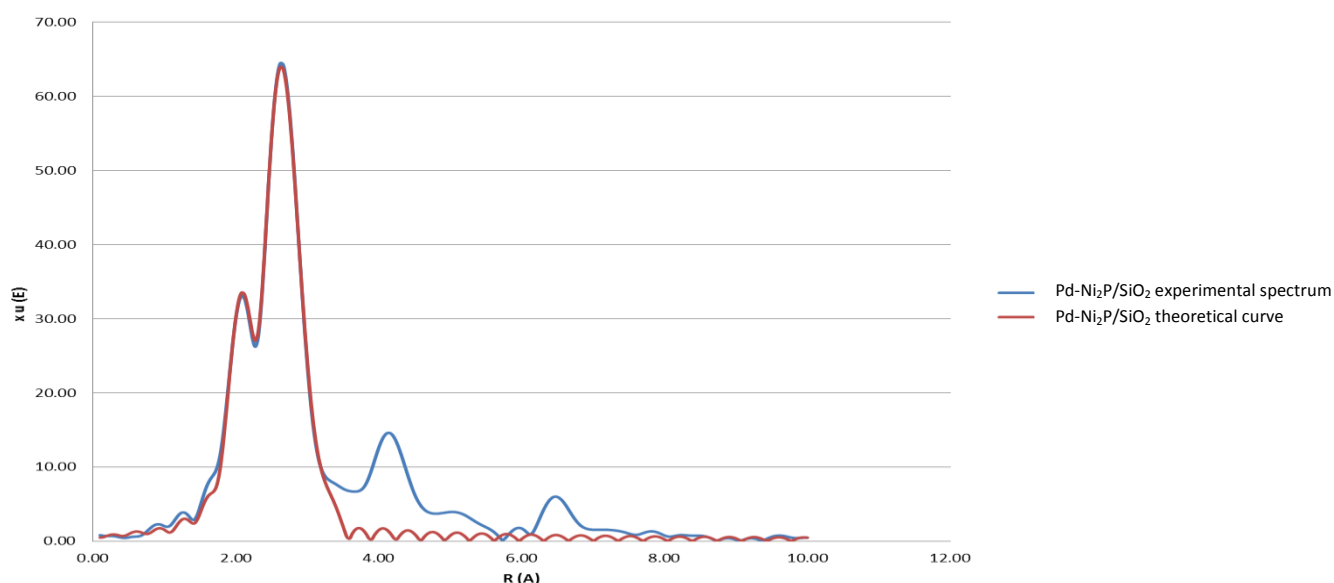


Figure 4-51: Fourier transformed spectrum for Pd-Ni₂P/SiO₂ catalyst along with theoretical curve fit.

Shell	Scatterer	Bond distance (Å)	co-ordination No	A	AFAC	ΔE	R-Factor
1	Ni-P	2.22983	3.91	0.01517	0.7735	0.8645	23.4017
2	Ni-Ni	2.59176	4.45	0.01534	0.7735		
3	Ni-Ni	2.98339	1.25	0.01534	0.7735		

Table 4-18: Summary of curve fit results for Pd-Ni₂P/SiO₂ EXAFS spectrum.

Figure 4-52 displays the k^3 weighted EXAFS spectrum for Pd-Ni₂P/SiO₂ and Figure 4-53 illustrates the Fourier transformed spectrum for the material. Both spectra have been refined and a theoretical curve has been applied through collaboration with Prof. G. Sankar from University College London. The results of the curve fit for the FT spectra for the material are summarised in Table 4-19.

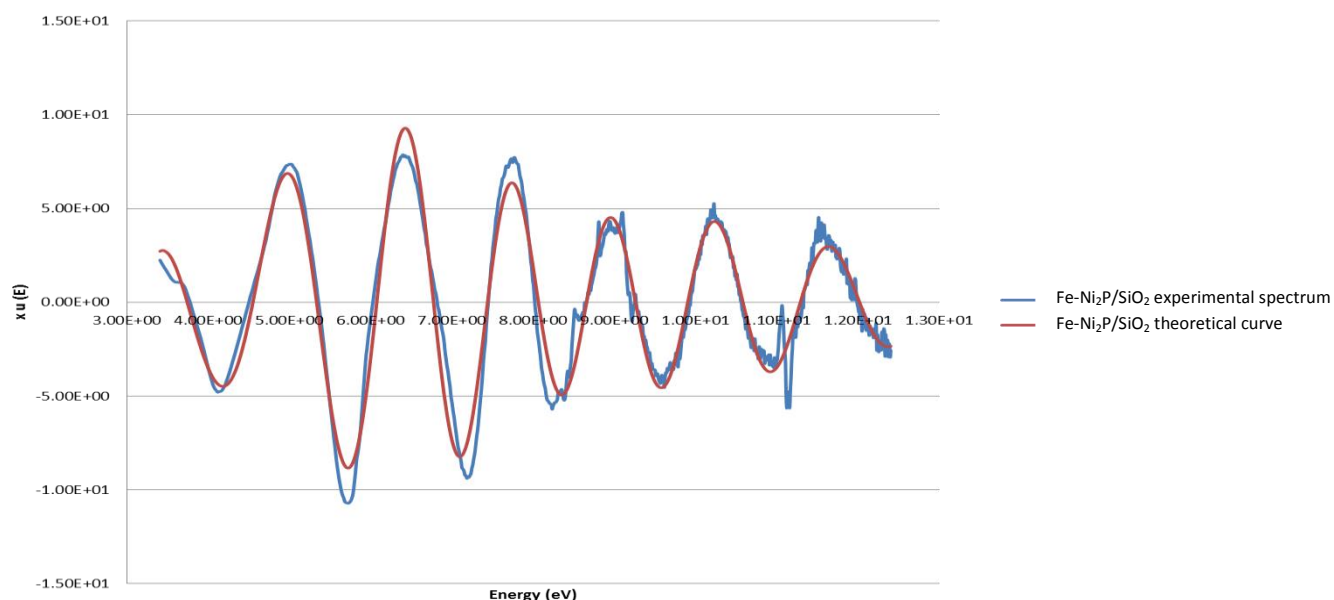


Figure 4-52: EXAFS spectrum for Fe-NiP/SiO₂ catalyst along with theoretical curve fit.

The theoretical fit for the spectrum shows Ni-P scattering with a distance of 0.288 nm; this is much larger than the Ni-P bond values found both in literature and in other nickel phosphide materials studied in this project which are in the range 0.218-0.231 nm.^[4] The difference in the Fe-NiP/SiO₂ Ni-P bond distance may result in the active phase being altered, which could affect the catalytic activity of the material. The curve fit indicated that a co-ordination number of 3.95 suggesting that 4 P neighbours are present around the nickel atom. The theoretical fit also considers two different Ni-Ni interactions. The smaller neighbour was estimated to have a bond distance of 0.154 nm with a co-ordination number of 1.5 suggesting 2 nickel neighbours at this distance. The largest Ni-Ni neighbour has bond distance of 0.528 nm and a co-ordination number of 4. The Ni-Ni distance in the material is larger than those reported by Lee and Oyama for silica supported nickel phosphide catalysts. The lengthened distances for Ni-P and Ni-Ni in the material suggest that the iron nickel phosphide alloy differs significantly to monometallic nickel phosphide. The catalytic activity of Fe-NiP/SiO₂ may differ from Ni₂P/SiO₂ due to the differences in active phase of the materials confirmed by EXAFS and XPS. The XANES region of the nickel K-edge for all the bimetallic nickel phosphide materials was briefly studied as well by Professor Sankar. The XANES region was not fully fitted therefore the resultant spectrum has not been presented. It was suggested however by Professor Sankar that the XANES spectrum for monometallic nickel phosphide when compared with bimetallic nickel phosphide materials suggested a correlation in the decrease in oxygen content in the material with the addition of the second metal in the bimetallic phosphide systems. The synergistic relationship between transition metal phosphide and oxygen as has been discussed previously and is thought play an influential role in catalytic activity of the material. The decrease in oxygen content displayed by the bimetallic nickel phosphide materials could have a negative effect on the catalytic activity of the material.

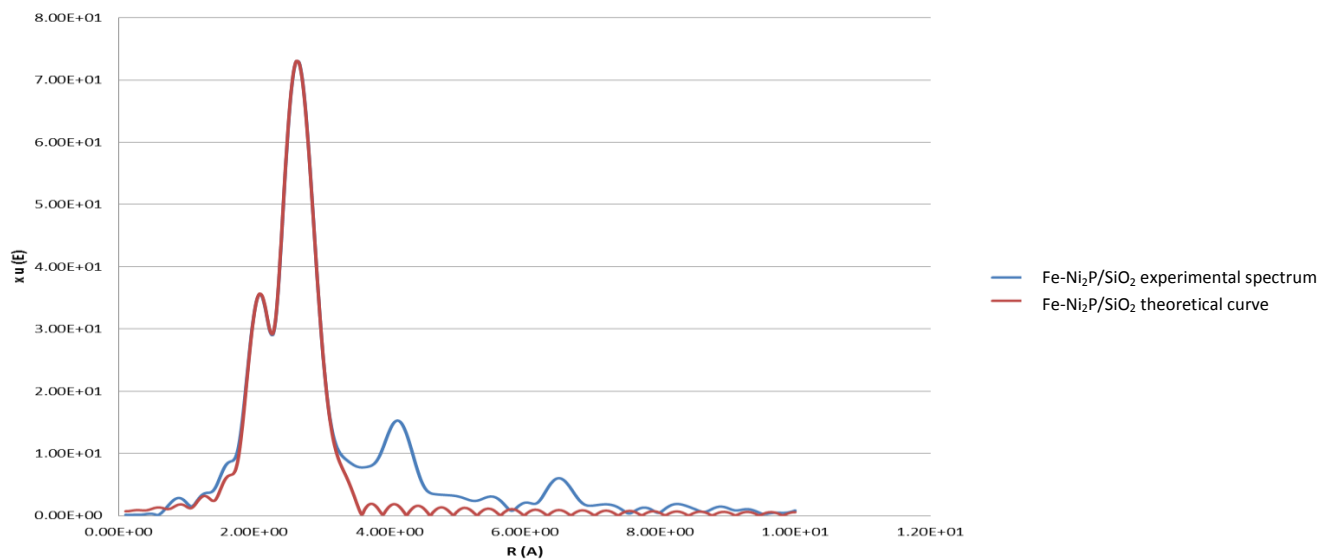


Figure 4-53: Fourier transformed spectrum for Fe-NiP/SiO₂ catalyst along with theoretical curve fit.

Shell	Scatterer	Bond distance (Å)	co-ordination No	A	AFAC	ΔE	R-Factor
1	Ni-P	2.88	3.95	0.01517	0.7735	0.8645	23.4017
2	Ni-Ni	5.28	4.07	0.01534	0.7735		
3	Ni-Ni	1.54	1.54	0.01534	0.7735		

Table 4-19: Summary of curve fit results for Pd-Ni₂P/SiO₂ EXAFS spectrum.

4.7 The catalytic testing of further bimetallic transition metal phosphide catalyst.

The catalytic activity of Cs-Ni₂P/SiO₂, Pd-Ni₂P/SiO₂, Cu-NiP/SiO₂ and Fe-NiP/SiO₂ was tested under high temperature water-gas shift reaction conditions. The catalytic testing was carried out using the same high pressure steam reactor which was used to test previous catalysts under the same reaction conditions.

The reaction profile for Cu-NiP/SiO₂ is displayed in Figure 4-54. The reaction profile shows the catalyst displays some activity under the reaction conditions with CO₂ and H₂ being produced throughout the run. There is no methane produced by the catalyst. The reaction does not reach steady state in terms of formation rates of products until after 20 hours of running and remains steady for the duration of the run. The delay in the catalyst reaching steady state formation rates is thought to be due an activation process occurring within the material during this period of time. This activation period is much longer than was seen with the Ni₂P/SiO₂ catalyst suggesting a difference in active phase in the two catalysts. The carbon balance was calculated to be an average of 97% over the duration of the run. The water-gas shift activity for the catalyst is generally poorer than expected. This is evident from the low formation rates of CO₂ and H₂ combined with high concentrations of unreacted CO present in the exit feed. The reaction profile also indicates deactivation of the catalyst after 60 hours of running. This is characterised by a gradual decrease H₂ and CO₂ formation rates coupled with a gradual increase in CO present in the exit feed. The low catalytic activity of the material is most likely due to addition of copper to the nickel phosphide system which alters the active phase of the material. The composition differences are evident from characterisation of the material. XPS and EXAFS spectra for the material suggest alloying of the copper and nickel which in turn decreases the number of active sites in the catalyst.

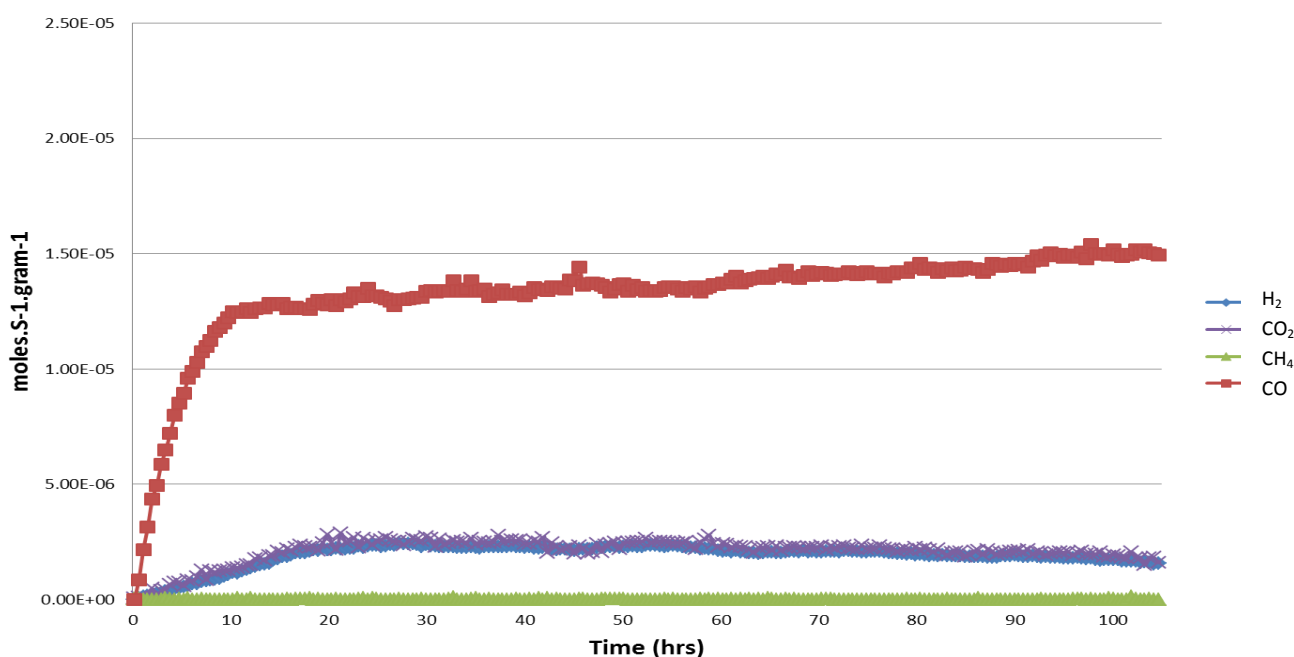


Figure 4-54: Reaction profile for Cu-NiP/SiO₂ under high temperature water-gas shift conditions.

The reaction profile for the high temperature water-gas shift reaction testing of Fe-NiP/SiO₂ is displayed in Figure 4-55. The reaction profile indicates that the catalyst displays activity under the reaction conditions with CO₂, H₂ and CH₄ being produced throughout the run. The run produces CO₂ and H₂ indicating that the water-gas shift reaction is taking place on the catalyst surface. The large concentration of CO present in the exit feed shows a significant quantity of the reactant gas remains unreacted. The carbon balance was calculated to be an average of 98% over the duration of the run. The formation rates for CO₂ and H₂ reach steady state after 10 hours of time on stream. The delay in the catalyst reaching steady state formation rates is thought to be due an activation process occurring within the material during this period of time. The reaction profile shows a small discrepancy between H₂ and CO₂. The difference in H₂ and CO₂ being produced in the reaction this can be attributed to the formation of small amounts of methane being produced, as can be seen in the reaction profile. The formation of methane suggests the presence of a nickel phase within the catalyst. The relatively poor catalytic activity of the Fe-NiP/SiO₂ catalyst is due to very different composition of the material in comparison to

the $\text{Ni}_2\text{P}/\text{SiO}_2$. The differences were alluded to in the characterisation of the catalyst. The XRD, XPS and EXAFS analyses all indicated noticeable differences between the two catalysts. $\text{Fe-NiP}/\text{SiO}_2$ was shown to have a number of different phases of nickel-iron phases and nickel phosphide present, whereas nickel phosphide appears to have a more uniform phase of phosphide present. The amorphous nature of the $\text{Fe-NiP}/\text{SiO}_2$ evidently has a negative effect on the catalytic activity of the material for the water-gas shift reaction under high temperature conditions. The activity of the catalyst with regards to formation rates of hydrogen and carbon dioxide is similar to those exhibited by $\text{Cu-NiP}/\text{SiO}_2$. The poor activities displayed by the bimetallic phosphides are consistent with those reported for non-nickel rich phosphides for other processes. [2, 10-11] This may be a result of the active phase seen in the monometallic material being altered by the addition second metal as was discussed previously.

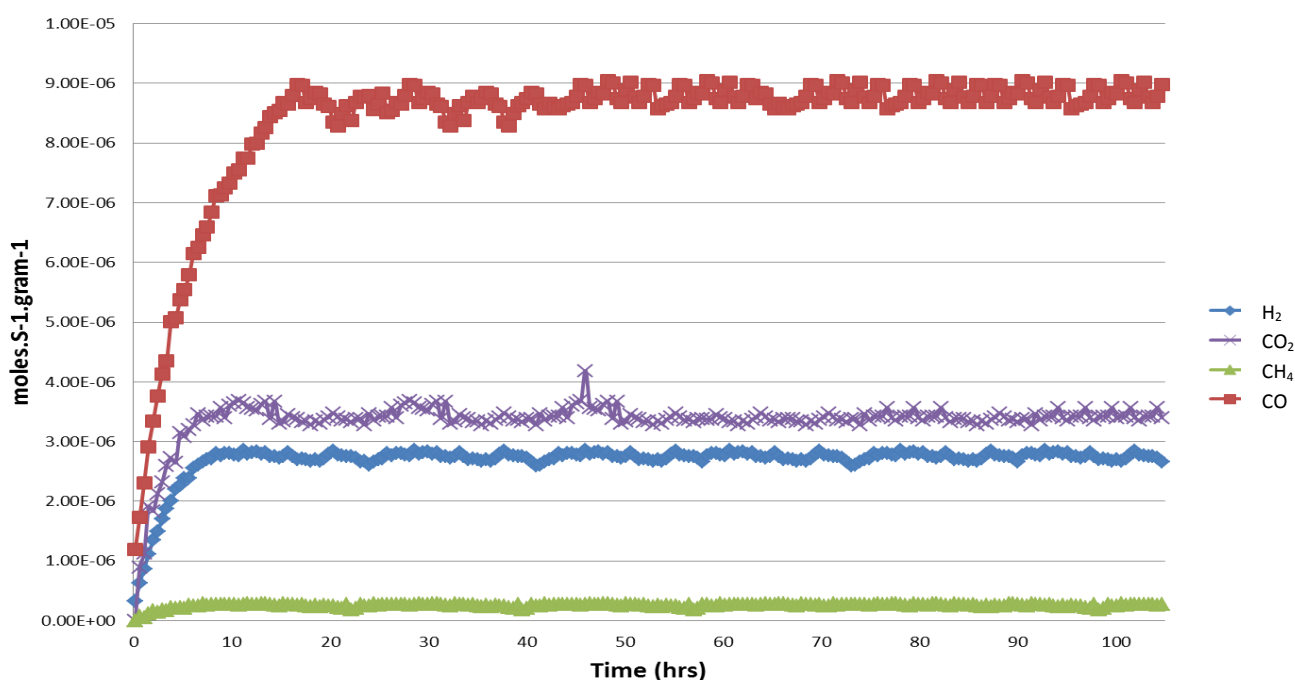


Figure 4-55: Reaction profile for $\text{Fe-NiP}/\text{SiO}_2$ under high temperature water-gas shift conditions.

The high temperature water-gas shift reaction profile for Cs-Ni₂P/SiO₂ is displayed in Figure 4-56. The catalyst displays significant catalytic activity under the reaction conditions. The run produces significant quantities of CO₂ and H₂ indicating that the water-gas shift reaction is taking place. The carbon balance was calculated to be an average of 91% over the duration of the run. Minimal amounts of CH₄ are produced throughout the run, suggesting little of the Ni phase is present. There is no discrepancy between CO₂ and H₂ formation rates in the reaction profile showing no hydrogen is lost to methanation. Formation rates for the products reach do not reach steady state until 30 hours of time of stream. This has previously been identified with other nickel phosphide materials as a catalyst activation period associated with active phase of the catalyst. The activation period is again much longer than that shown by Ni₂P/SiO₂. The activity of Cs-Ni₂P/SiO₂ with regards to formation rates is much higher than exhibited for the Fe-NiP/SiO₂ and Cu-NiP/SiO₂. The TEM and EDX analysis of the material indicated that caesium dispersion was not entirely uniform which may explain the extended period of time taken for it reach steady state. The superior catalytic activity displayed by the material in comparison to the other bimetallic nickel phosphide catalysts is likely a result of the catalyst having only a small amount of the second metal (1% loading in comparison to the 10% used in the Cu and Fe bimetallic phosphide materials) meaning that catalyst is mostly Ni₂P with regards to its composition. EXAFS and XPS analysis of the catalyst suggested the Cs-Ni₂P/SiO₂ catalyst was more similar to Ni₂P/SiO₂ in terms of composition of the active phase. The good activity of the material therefore highlights the importance the Ni₂P species. The characterisation of the other bimetallic phosphides indicate that the Ni₂P phase in these materials is less prevalent.

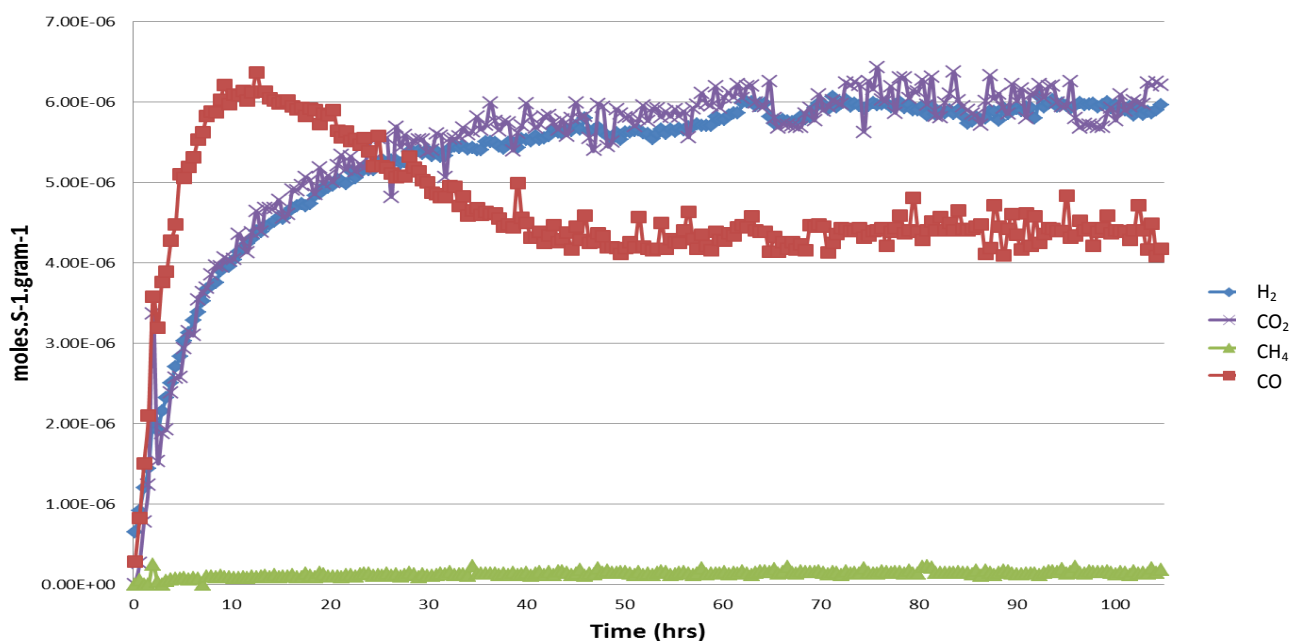


Figure 4-56: Reaction profile for $Cs-Ni_2P/SiO_2$ under high temperature water-gas shift conditions.

The reaction profile for $Pd-Ni_2P/SiO_2$ tested under high temperature water-gas shift conditions shows CO as the predominant component of the exit feed, with very little CO_2 or H_2 apparent. The carbon balance for the reaction was calculated as 96% based on an average for the entire duration of the run. The reaction profile suggests that the catalyst displays poor catalytic activity for the water-gas shift reaction under high temperature conditions. The poor activity displayed by the catalyst may be related to the influence of palladium on the nickel phosphide active phase which is formed. The XRD pattern for the material indicated the formation of mixed phases of nickel phosphide and distortion of the catalytically active Ni_2P crystal phase. Alteration of the active phase by the palladium was further supported by EXAFS analysis of the material which indicates that the Ni-P and Ni-Ni bond distances have lengthened suggesting distortion of the active phase. The alteration of the phosphide due to the influence of the palladium has significantly decreased the activity of the catalyst.

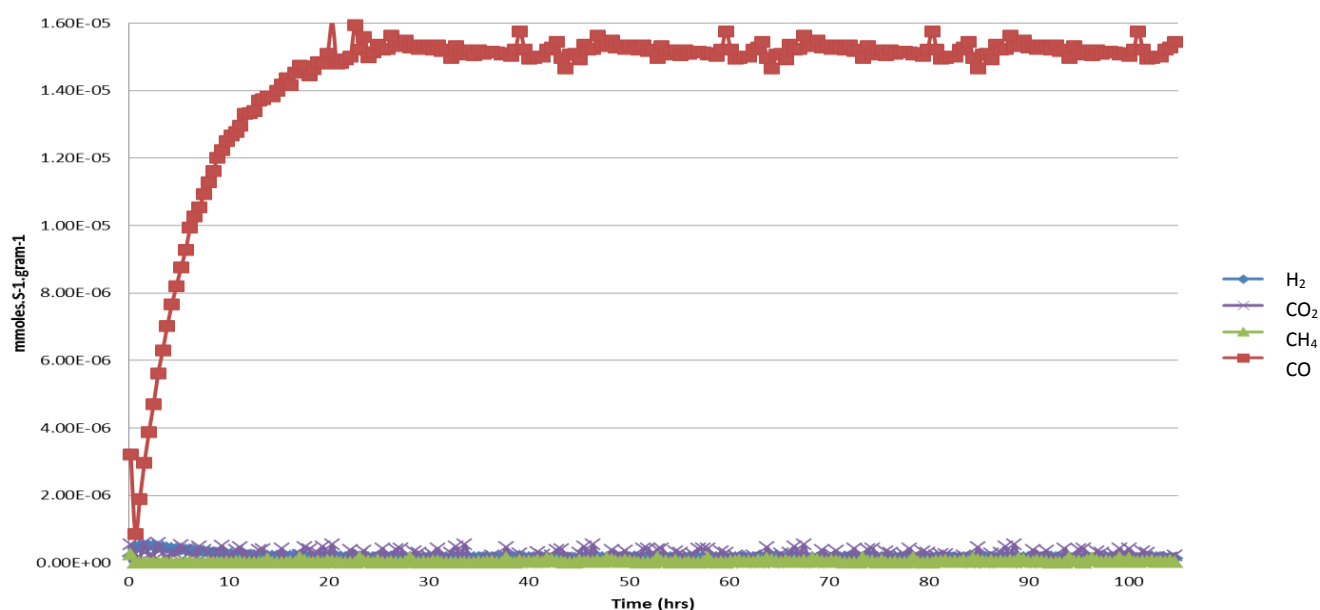


Figure 4-57: Reaction profile for $Cs-Ni_2P/SiO_2$ under high temperature water-gas shift conditions.

The bimetallic nickel phosphide catalysts were compared and contrasted with one and other along with nickel phosphide and the industrial catalyst with regards to mass normalised hydrogen formation rates displayed by each catalyst under the high temperature water-gas shift reaction conditions after 24 hours of running time. Figure 4-58 shows the formation rates for each of the catalysts. Ni_2P/SiO_2 displays the greatest hydrogen formation rate per weight of catalyst followed by the cerium doped nickel phosphide catalysts. The only other bimetallic phosphide catalyst to outperform the industrial catalyst was the caesium doped catalyst. The caesium and cerium doping of nickel phosphide is known to actively promote oxygen rich phases within the nickel phosphide particles. The oxygen rich phases as discussed previously are reported to play an influential role the catalytic activity displayed by the materials.

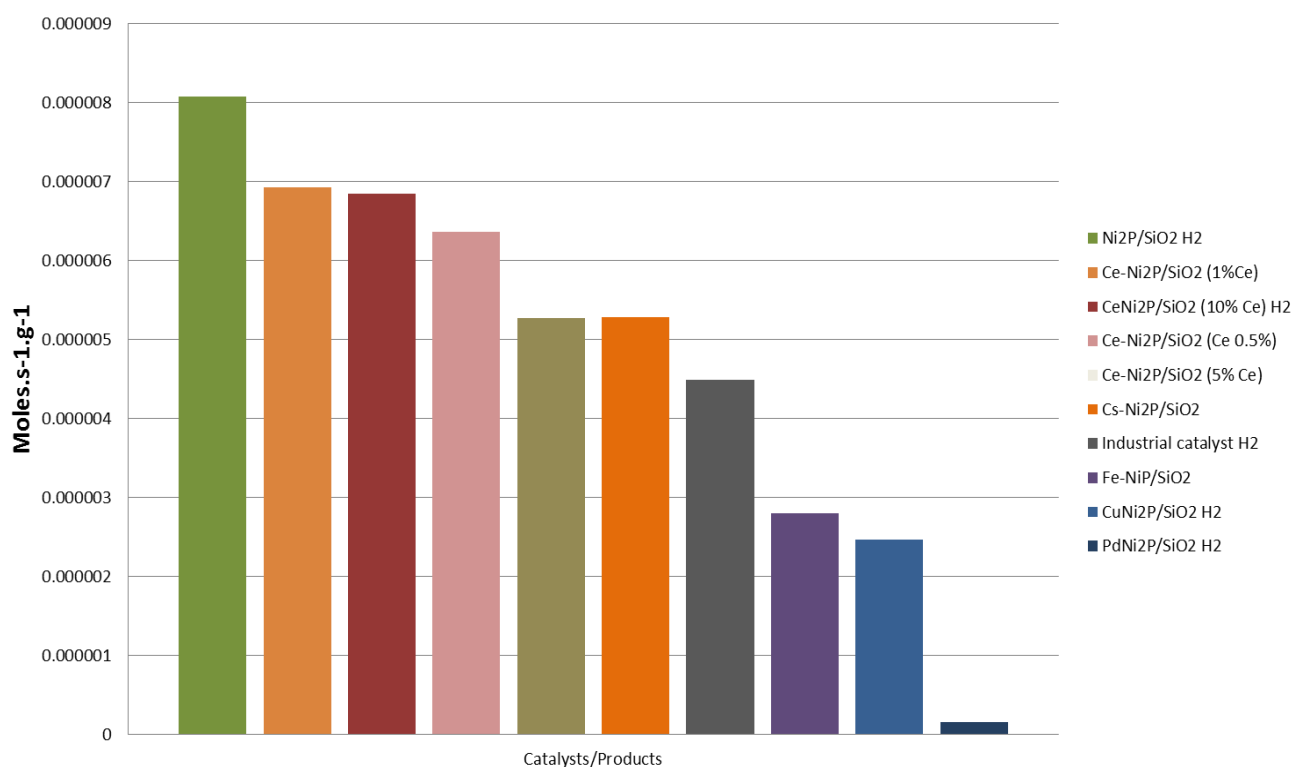


Figure 4-58: Mass normalised hydrogen formation rates after 24hrs of running for all bimetallic nickel phosphide catalysts.

Another important correlation between the catalytic activity displayed by the cerium and caesium doped catalysts in comparison to the other bimetallic phosphides appears to be the larger amount of phosphide in the Ni₂P phase compared to the other materials which display a number of mixed phases of phosphide. Ni₂P is known to be the most catalytically active, this has been widely reported in literature. [1] The characterisation of the materials show a direct link between the addition of secondary metallic elements and a decrease in Ni₂P phases present in the material. This is mostly likely the reason why the Ni₂P/SiO₂ catalyst displays the highest formation rate for hydrogen per weight of catalyst in comparison to all of the bimetallic phosphide catalysts.

Figure 4-59 displays hydrogen formation rates for all the bimetallic nickel phosphide catalysts along with monometallic nickel phosphide and the industrial catalyst after 24 hours of each test run based on the volume of catalyst used. The figure shows that the industrial catalyst displays the highest hydrogen formation rate compared to the mono and bimetallic nickel phosphide catalysts. This is due to a much higher active phase loading in the industrial catalyst, estimated to be roughly 60% iron loading, whereas the catalysts produced in this project only used 20% nickel loading. The cerium doped catalysts and the monometallic nickel phosphide catalysts also displayed relatively high hydrogen formation rates per volume of catalyst. These are not as much as the industrial catalyst. They are however only marginally lower despite have much lower metal loading in the material.

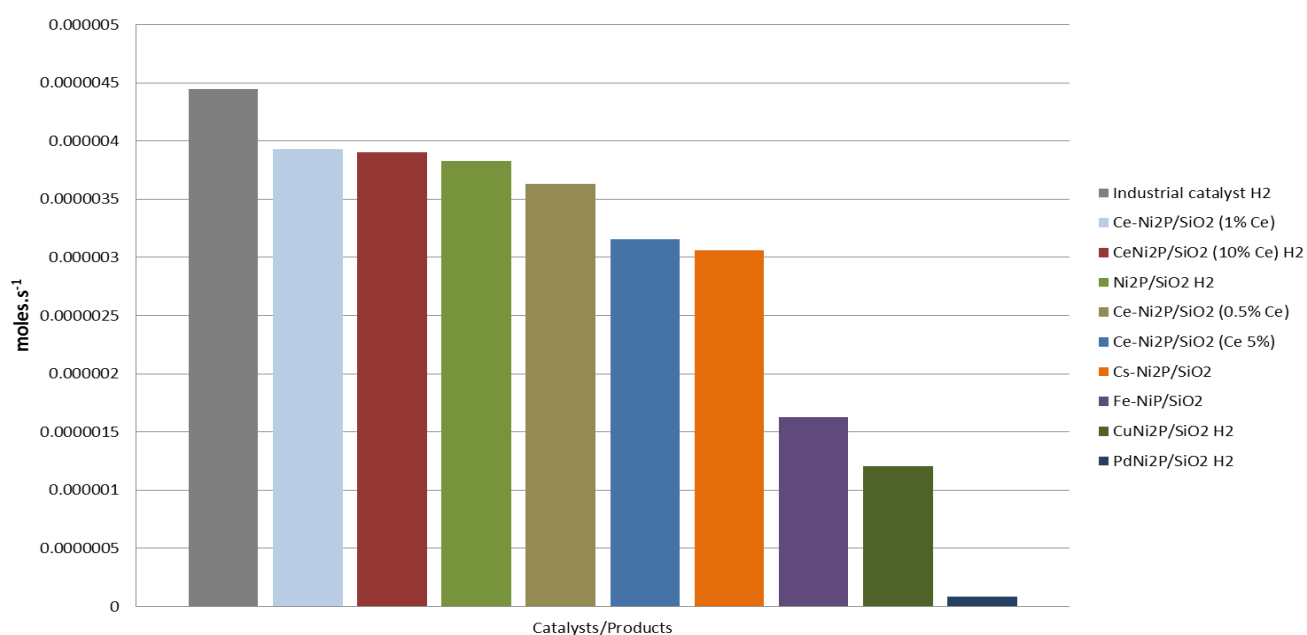


Figure 4-59: Hydrogen formation rates after 24hrs of running for all bimetallic nickel phosphide catalysts per volume of catalyst.

4.8 Conclusions

A range of silica supported bimetallic nickel phosphide catalysts were produced. Ce-Ni₂P/SiO₂ was produced using cerium loadings of 10%, 5%, 1% and 0.5%. Further bimetallic nickel phosphide catalysts were made namely; Fe-NiP/SiO₂, Cu-NiP/SiO₂, Cs-Ni₂P/SiO₂ and Pd-Ni₂P/SiO₂. The materials were characterised using a wide range of techniques including EXAFS, XPS and XRD to gain a greater understanding of the phases and compositions of phosphides present on the support. Characterisation of the materials revealed that the phase of material and chemical state were influenced by the secondary metal when compared with the monometallic nickel phosphide system. The materials were also tested for the catalytic activity in the water-gas shift reaction under high temperature shift conditions. The catalytic activity of the bimetallic nickel phosphide systems varied and was noticeably different to the monometallic nickel phosphide catalyst tested under the same reaction conditions.

The addition of cerium to the nickel phosphide system was shown to alter the nickel phases formed in the catalyst. XRD patterns for the materials indicated that nickel metal was present along with nickel phosphide. The catalysts with lower cerium loadings displayed more diffraction peaks associated with Ni₂P and less associated with nickel metal. This suggested that increasing cerium loading directly influenced the presence of the Ni metal phase. The formation of nickel phases with the addition of cerium to the nickel phosphide system is consistent with previous studies. The addition of cerium to the nickel phosphide catalyst also produced an impure species of nickel phosphide with diffraction peaks for Ni₁₂P₅ and Ni₂P present in all of the cerium doped catalysts. The increasing amorphous nature of the phosphide phase with increasing cerium loading was further highlighted with the TGA reduction profiles for the 1% Ce and 10% Ce doped catalysts which displayed very different reduction profiles. The 10% Ce catalyst displayed large reduction peak for nickel metal with a phosphate reduction peak of a comparable size, suggesting the material contains similar amounts of nickel metal and nickel phosphide. The 1% Ce catalyst displays a much smaller nickel metal reduction peak suggesting much more nickel

phosphide is present in the material than nickel metal. The SEM and TEM analysis of the Ce-Ni₂P/SiO₂ catalyst with 10% Ce loading confirmed the presence of crystallite phases on the silica support. EDX analysis of the SEM micrograph revealed the presence of nickel and phosphorus in the stoichiometric ratio of 2:1 expected for Ni₂P or Ni₁₂P₅. The EXAFS spectrum for the Ce-Ni₂P/SiO₂ catalyst with 10% Ce loading indicated a large number of nickel metal sites present in the material, estimated to be 40%. Further to this both the Ni-P bond distance and coordination was reduced with respect to the monometallic nickel phosphide catalyst, this suggesting that nickel phosphide particle size has decreased due to the addition of cerium. A decrease in nickel phosphide particle size with the addition of cerium was also reported in the literature. The XPS spectrum for the 10% Ce doped catalyst also highlighted the mixed phases present in the material. Binding energy peaks for nickel metal, nickel phosphide and nickel phosphate are all evident in the spectrum along with cerium.

The catalytic activity of the cerium doped catalysts varied. The 10%, 5%, 1% and 0.5% Ce doped catalysts all displayed activity for the water-gas shift reaction. All of the cerium doped catalysts displayed greater hydrogen formation rates per weight of catalyst than the industrial catalyst under the same reaction conditions. None of the cerium doped catalysts performed as well as the monometallic nickel phosphide catalyst per weight of catalyst. The presence of nickel metal phases within the catalysts altered the catalytic activity of the catalysts to varied degrees dependent upon the cerium loading. The presence of nickel metal in the materials caused methanation due to the favourable thermodynamic conditions which the catalytic testing was operated under. The characterisation of the materials revealed that larger loadings of cerium produced more nickel metal phases within the catalyst; this was evident in reaction profiles for the catalysts. Generally the methane formation rates increased with cerium loading from 0.5% to 10% Ce loading. The only exception to this trend was the 5% Ce loading which displayed the highest methane formation rate of all the Ce doped catalysts. The strong methanation activity displayed by the catalysts had a negative effect on the hydrogen formation rates for the catalysts. This is evident in from discrepancy between the carbon dioxide and hydrogen formation rates in the reaction profiles, which should be roughly the same

if these are the only products produced. This was a result of the hydrogen being used up by the methanation process. The 1% Ce doped catalyst displayed the largest hydrogen formation rate per weight of catalyst compared with the other cerium doped catalysts.

The post-reaction 10% Ce loading nickel phosphide catalyst was characterised using a range of techniques. The results indicated that material changed significantly during the reaction testing process. This was evident from the XRD pattern for the post-reaction sample, which differed significantly from the fresh catalyst. The post-reaction sample displayed reflections associated with nickel phosphide (Ni_2P and Ni_{12}P_5). These peaks were not visible in fresh material which only displayed diffraction peaks associated with nickel metal. The appearance of these reflections in the post-reaction sample indicates that the nickel metal sites present in the fresh material are being converted into nickel phosphide phases. This is most likely due to presence of unreacted phosphate on the surface of support which forms the phosphide with nickel under the reaction conditions. This phenomenon was further supported by the post-reaction XPS spectrum which did not display binding energy peaks associated with nickel metal, which was evident in the fresh samples spectrum. The XPS spectrum also showed an upward shift in binding energy of the nickel phosphide species associated with near surface phases becoming more oxygen rich under the reaction conditions. The oxy-phosphide surfaces have been previously identified as being influential in the good catalytic activity displayed by nickel phosphide under water-gas shift conditions. The EXAFS analysis of the post-reaction sample revealed similar trends to the XPS data indicating that the nickel metal sites were being converted to nickel phosphide during the reaction testing. This was evident from the FT spectrum for the post-reaction sample more closely resembling nickel phosphide (Ni_2P). The theoretical curve fit data also was consistent with this; the Ni-P bond distance was longer and resembles that estimated for Ni_2P as was the co-ordination number. The Ni-Ni bond distance also increased to a similar distance to that estimated for Ni_2P . Prof. Sankar was able to estimate from the data that less than 20% of the sample was nickel metal. This is significantly less than fresh sample which was estimated to consist of up to 40% nickel metal sites. The post-reaction characterisation clearly indicates that the nickel species within the

10% Ce catalyst is significantly altered during the reaction testing. The other bimetallic nickel phosphide catalysts produced in this project also showed varied differences from the monometallic nickel phosphide catalyst. This further highlights the influence that the secondary metallic element has on the final phases formed. The XRD patterns for Cu-NiP/SiO₂, Fe-NiP/SiO₂, Pd-Ni₂P/SiO₂ and Cs-Ni₂P/SiO₂ all show diffraction peaks associated with nickel phosphide. However there are a number of phases present suggesting the materials are partially amorphous in nature. The amorphous nature of the materials are further highlighted in the TGA reduction profiles for the materials which each display a number of reduction peaks indicating the reduction of multiple species within the materials.

The SEM and TEM micrographs for Fe-NiP/SiO₂, Cu-NiP/SiO₂, Cs-Ni₂P/SiO₂ and Pd-Ni₂P/SiO₂ all confirmed the formation of crystallite phases of material on the silica support. The dispersion and size of particles on the support differed between catalysts. The Fe-NiP/SiO₂, Cu-NiP/SiO₂ and Cs-Ni₂P/SiO₂ catalysts all displayed a wide dispersion of small particles throughout the samples. The Pd-Ni₂P/SiO₂ catalyst however appeared show the formation of much larger particles of the support. EDX analysis of the micrographs for Cs-Ni₂P/SiO₂, Pd-Ni₂P/SiO₂ and Fe-Ni₂P/SiO₂ revealed the elemental ratio between Ni:P to be roughly 2:1 for all three materials indicating the particles that formed were Ni₂P. The elemental analysis of the materials also identified the secondary metallic elements for each material in ratio that was roughly consistent with the preparation of the catalysts.

The EXAFS and XPS spectra for the Fe-NiP/SiO₂ catalyst revealed that an iron-nickel phosphide alloy is formed along with Ni₂P. This was characterised in the XPS spectrum by the appearance of nickel and iron metal binding energy peaks as well as nickel and iron phosphide binding energy peaks indicating an extensive mixed phase phosphide alloy existed within the material. This was further confirmed by EXAFS data for the material which showed lengthening of Ni-P and Ni-Ni in comparison to monometallic nickel phosphide. This difference was attributed to the presence of iron and formation of the alloy within the material. The distortion of the phosphide phase had a negative effect on the catalytic activity of Fe-NiP/SiO₂, which

was evident from the lower hydrogen formation rates displayed by the catalyst in the reaction profile for the high temperature water-gas shift reaction test.

The EXAFS data for Cu-NiP/SiO₂ suggested distortion of the phosphide phase in comparison to the monometallic system. The EXAFS fit data for the material indicated that Ni-P bond distance and co-ordination both decrease indicating a decrease in particle size. The number of nickel metal sites associated with nickel-copper alloying also increased. As was seen with the Fe-NiP/SiO₂, the addition of the second metallic component to the nickel phosphide system had a negative effect on the catalytic activity of the material. This was evident from the low hydrogen formation rates displayed by the catalyst throughout the high temperature water-gas shift reaction testing of the material. The addition of the second metal alters the phase of phosphide formed within the material and this limits the number of catalytically active sites in the material which results in the lower activity of the Fe-NiP/SiO₂ and Cu-NiP/SiO₂ catalysts in comparison to the Ni₂P/SiO₂ catalyst which has more active sites present. The greater catalytic performance of the monometallic nickel phosphide catalyst was highlighted by comparison of hydrogen formation rates, the industrial catalyst also performed better than both the iron and copper bimetallic phosphide catalysts.

The Cs-Ni₂P/SiO₂ catalyst performed better than the industrial catalyst under the high temperature water-gas shift reaction conditions with regards to hydrogen formation rates displayed by the two catalysts. The caesium doped catalyst did not perform as well as the monometallic nickel phosphide catalyst. The XPS spectrum for the catalyst showed binding energy peaks associated with nickel phosphide and nickel phosphate suggesting oxygen rich near surface phases were present in the material and that no nickel metal or alloy was present. Oxygen rich phases are known to be responsible for promoting the catalytic activity of the nickel phosphide species however the presence of two different phosphate species suggests that the material may be partially over oxidized resulting in poor catalytic activity compared with monometallic nickel phosphide catalyst. The catalyst still outperforms the industrial catalyst and a number of the other bimetallic phosphide catalysts per

weight of catalyst. This is a result of the significant number of active nickel phosphide species present which is evident from the moderate water-gas shift activity that the catalyst displays.

Pd-Ni₂P/SiO₂ displayed the poorest catalytic activity of all the bimetallic nickel phosphide catalysts tested under high temperature water-gas shift reaction conditions. The poor catalytic activity was attributed to the influence palladium had on the phosphide active phase. Distortion of the phosphide phase was evident in the EXAFS spectra for the material which showed a significant increase in Ni-P and Ni-Ni bond distance in the phosphide in comparison to the monometallic nickel phosphide catalyst.

Generally the addition of a second metallic element to the nickel phosphide materials has been shown to distort the phosphide phase formed on the support. It is thought that this modification has a negative effect on the formation of active catalytic sites in the phosphide. This has ultimately led to poorer catalytic activity in the bimetallic nickel phosphide catalysts in comparison to the monometallic nickel phosphide catalyst for the high temperature water-gas shift reaction.

4.9 References

- 1) S.T. Oyama , J. Catal; 216; (2003) pg 343–352
- 2) M. Bussell, R. Prins; Catal. Lett; 142; (2012); pg 1413–1436
- 3) P. Liu, J. A. Rodriguez, Y. Takahashi, K. Nakamura; J. Catal; 262; (2009) pg 294–303
- 4) S.T. Oyama, Y.K. Lee; J. Catal; 258; (2008) pg 393–400
- 5) S. Carenco, A. Leyva-Pérez, P. Concepción, C. Boissière, N. Mézailles, C. Sanchez, A. Corma; Nano Today; (2012); 7; pg 21-28
- 6) A. F. Gaudette, A. W. Burns, M. C. Smith, R. H. Bowker, T. Seda, M. E. Bussell; J. Catal; 272 ; (2010) pg18–27
- 7) A.W. Burns, A. F. Gaudette, M. E. Bussell; J. Catal; 260; (2008) pg 262–269
- 8) J. Rodriguez, J.-Y. Kim, J. Hanson, S. Sawhill, M. Bussell; J. Phys. Chem. B, 107, (2003), p. 627-636
- 9) I.I. Abu, K.J. Smith; Ap. Catal. A: Gen; 328; (2007) pg 58–67
- 10) I.I. Abu, K.J. Smith J. Catal; 241; (2006), p. 356-363
- 11) K. Smith, R. Wang; Ap. Catal. A: Gen; 361; (2009) 18–25
- 12) D.R Mullins, S.H Overbury, D.R Huntley; Surface Science; 409; (1998), pg. 307–319
- 13) Q. Li , P. Wu, L. Lan, N. Wei; J. Appl. Petrochem; Res, 2013, DOI 10.1007/s13203-013-0039-5
- 14) Q. Guan, W. Li; J. Catal; 271; (2010) pg 413–415
- 15) C. Stinner, R. Prins, T. Weber, J. Catal; 202; (2001) pg 187.
- 16) J.A. Rodriguez, J.-Y. Kim, J.C. Hanson, S.J. Sawhill, M.E. Bussell, J. Phys. Chem. B (2003) pg 6276.

- 17) V.T. da Silva; J. Catal; 279, (2011), pg 88–102
- 18) Z. Liu, X. Huang, Z. Zhu, J. Dai; Cer.Int; 36; (2010) pg 1155–1158
- 19) S. Yang, C. Liang, R. Prins; J. Catal; 237; (2006) pg 118.
- 20) S.L. Brock, K. Senevirathne; J. Solid State Chem; 181; (2008) pg 1552–1559
- 21) C. Zerva, C. Philippopoulos; Ap. Catal B; 67, (2006), pg 105–112
- 22) S. Hilaire, X. Wang, T. Luo, R. Gorte, J. Wagner ; Ap. Catal A; 258, (2004), pg 271–276
- 23) P.A. Clark, S.T. Oyama, X. Wang; J. Catal.; 208, (2002), pg 321-331
- 24) M. V. Twigg; ICI Catalyst Handbook 2nd Ed.; Wolfe Publishing; pg 283-338
- 25) S. Sawhill, K. Layman, D. Van Wyk, M. Engelhard, C. Wang, M. Bussell; J. Catal; 231 (2005) pg 300–313
- 26) H. Song, M.Dai, X.Wan, X. Xu, C. Zhang, H. Wang; Catal Comm; 43 (2014) pg.151–154
- 27) J.A. Rodriguez, J. Y. Kim, J. C. Hanson, M. Perez, A. I. Frenkel; Catal Letters; 85, (2003), pg 247-254
- 28) L. Liu, L. Hong; Fuel; 96, (2012), pg 348–354
- 29) A. Cho, J. Shin, A. Takagaki, S. T. Oyama; Top. Catal. (2012) pg

Chapter 5 : The catalytic performance of silica supported nickel phosphide catalysts under high-temperature water-gas shift conditions in the presence of sulfur

5.1 Introduction

The water-gas shift reaction is an important industrial process which plays a vital role in the production of ammonia and the steam reforming of syn-gas. The finite supply of natural gas means that poorer quality feedstocks containing impurities such as sulfur containing compounds will be used more frequently in the future. The activity of industrial catalysts used at both high temperature and low temperature water-gas shift reactions conditions are both negatively affected by sulfur poisoning. The poisoning of the copper based catalyst used under low temperature conditions is permanent and rapidly decreases activity meaning that the catalyst will have to be replaced if exposed to sulfur; the FeCr catalyst used under high temperature water-gas shift reaction conditions on the other hand will change into the sulfide form, which is active for the WGS but not as active as the oxide form.^[1]

An alternative to the industrial catalysts, if there are high concentrations of sulfur in the gas, is to use sulfide-based catalysts which are normally Mo or Co-based or mixtures of the two whilst they do not perform as well as the aforementioned industrial catalysts they do remain active when sulfur is present.^[2] Many of these alternative sulfide catalysts require either pre-treatment with sulfur or high levels of sulfur in the feed. These methods impractical and inefficient for application in the water-gas shift reaction.^[3]

There has been significant interest over the years in the development of sulfur resistant catalysts for the water-gas shift reaction. One such catalyst is the sulfur-tolerant high-temperature shift catalyst. Based on cobalt chromium oxide it has

displayed good catalytic activity even under high concentrations of sulfur. ^[4] The relatively high activity and low methanation of the catalyst as well as the stability catalyst was shown to relate to the ratio of cobalt to chromium with a ratio of 3-to-1 giving optimum activity. Catalyst deactivation did not occur even with sulfur present in the stream over an extended period of time. ^[4] Another recent development of interest is the use of lanthanide oxy-sulphide catalysts for the high temperature water-gas shift reaction. ^[5] While these materials showed little, if any, deactivation under sulfur containing conditions, the catalytic performance of the materials are far lower than the FeCr-based industrial catalyst.

The application of noble metals in water-gas shift catalysis has also attracted interest in recent years. ^[6] There have been numerous publications on supported precious metals (such as Pt, Rh, Ru, Au, and Pd) supported on easily and partially reducible supports (such as cerium, zirconia, titania, iron oxides, and mixed oxides of cerium, like cerium- zirconia) which show the materials performed as well, if not better, than the industrial catalysts under both high and low temperature water-gas shift reaction regimes. ^[3, 6] However, the addition of sulfur to the feedstock at low concentrations caused the mixed phase these noble metal catalysts to become irreversibly deactivated at rapid rate. ^[9, 10] The catalytic activity of noble metal phosphides was shown to be proportionately affected by increasing concentrations of sulfur being introduced to the feed.

The major flaw with catalysts which display resistance to sulfur for the water-gas shift reaction is the poorer catalytic displayed by the materials in comparison to the more easily poisoned current industrial catalysts currently used. It is therefore essential that alternative materials are investigated which display novel characteristics such as high catalytic activity under conditions which more closely resemble industrial conditions over long periods of time, whilst maintaining a resistance to sulfur.

Transition metal phosphides have been investigated over a number of years as hydrotreating catalysts, removing unwanted elements from feedstocks and could be utilised as catalysts showing a greater resistance to poisoning. The catalytic potential of nickel phosphide has been extensively studied due to its reputation as the most catalytically active of the transition metal phosphides, with focus on its application as alternative hydrotreating catalyst. [12, 15] A synergistic relationship between the HDS performance of the nickel phosphide active phase and sulfur has been alluded to in a number of studies by the Oyama group. [15] Recent publications by the group have focus more on the structure of the phosphides themselves to give help understand them and the activity they displayed more fully. [20-21] The first study focused on the structure of nickel phosphide under hydrotreatment of thiophene. [21] To characterise the materials they used infrared spectroscopy and X-ray absorption spectroscopy both in situ. The results of this work show that whilst the bulk phase of the material remain in the Ni₂P phase the surface of the nickel phosphide formed a thiophosphate phase (NiPS) which promoted the activity of the surface sites for the reaction. Once the NiPS phase is generated and covers the Ni₂P particle, it facilitates activation of hydrogen molecules and promotes HDS, which prevents the corrosive attack of sulfur. It was found that nearly half of the nickel present in a particle form these thiophosphate phases. Oyama suggests that it is likely that the Ni atoms surrounding the NiPS phases are subjected to some influence from them, the effect of the NiPS phase spreads all over the Ni₂P surface. As a result, the NiPS surface phase works not only as an active site for the hydrodesulfurisation reaction but also as a protecting layer on Ni₂P. This synergistic relationship between the nickel phosphide and sulfur identified by Oyama may also be true for nickel phosphides application in water-gas shift process under sulfur containing conditions.

The potential of supported nickel phosphide as catalysts for syn-gas related reactions has been relatively unexplored, with Rodriguez and colleagues the only other group to apply the materials in this area. Therefore the chemical and physical effects of sulfur on supported nickel phosphide catalysts remain relatively unknown for the water-gas shift reaction. The previous chapters have shown nickel phosphide to be a highly active water-gas shift catalyst under high temperature water-gas shift conditions. The promising catalytic activity of nickel phosphide is combined with the

physical properties of ceramics, such as hardness and strength and the transport properties of metals, such as high thermal and electrical conductivity making nickel phosphide an ideal potential catalyst for the water-gas shift reaction. [12]

The addition of secondary metallic elements to the nickel phosphide system may also yield positive results with regards to the catalysts resistance to deactivation by sulfur poisoning. A study published by Hong and Li described the beneficial effects due to the presence cerium oxide being used as a support for nickel phosphide. [20] Cerium ions were shown to greatly increase water-gas shift activity on the active sites. It is suggested that the presence of Ce^{3+} ions promote Ni active sites not only in activity but also in terms of resistance to coking and sulfur poisoning. Therefore the presence of cerium in bimetallic nickel phosphide catalysts may have beneficial effects on the catalyst resistance to sulfur poisoning.

5.2 The catalytic testing of silica supported nickel phosphide under sulfur poisoning conditions.

Diffuse Reflectance Infrared Fourier Transforms Spectroscopy (DRIFTS) studies were carried out *in situ* on $\text{Ni}_2\text{P}/\text{SiO}_2$ and Ni/SiO_2 catalysts which were pre-treated with a sulfur containing compound, thiophene. The pre-treatment of the catalysts with thiophene was carried out using a glass bubbler containing thiophene using a carrier gas through the micro reactor containing the catalyst at 400°C . The experimental procedure for this is detailed in the experimental chapter. Chemisorption of CO onto the catalyst surface was carried out in an *in situ* DRIFTS microreactor at a range of temperatures between room temperature and 400°C . This has enabled an insight into the interaction between CO with the catalyst surface after the material has been exposed to significant amounts of sulfur. CO is a good probe molecule for surface interactions as well as being an integral part of the water-gas shift reaction. As was the case with the other materials studied using DRIFTS, the purging of unbound CO was undertaken using argon to purge the cell. This was

carried out to allow for CO bound directly to the surface of the catalyst to be detected. This however resulted in the removal of both the bound and unbound CO.

As a result peaks associated with both forms of CO were not present after purging the system. DRIFTS studies of absorption of CO onto Ni metal sites have been extensively reported in literature. From the literature alternative modes of CO bonding onto the Ni site have described as follows; CO bridge bonding occurring at 1800-2000 cm^{-1} and terminal CO bonding occurring at 2045-2145 cm^{-1} .^{[10][11]} Fresh $\text{Ni}_2\text{P}/\text{SiO}_2$ was also studied using FT-IR and was presented in Chapter 3. In the fresh material CO adsorption was clear visible via two modes of bridge bonding was evident at wavelengths of 1850-1950 cm^{-1} at all set temperature conditions between room temperature and 400°C. Terminal bonding was also evident at temperatures in excess of 300°C, it was concluded that terminal bonding mode was the catalytically active mode due to catalytic activity only being significant at temperatures under which terminal bonding occurs.

The results of the DRIFTS studies carried out on the thiophene treated catalysts $\text{Ni}_2\text{P}/\text{SiO}_2$ and Ni/SiO_2 are presented in Figures 5-1 and 5-2 respectively. The DRIFTS spectra for CO chemisorption onto the thiophene treated $\text{Ni}_2\text{P}/\text{SiO}_2$ displayed in Figure 5-1 show a broad peak 1940 cm^{-1} . This peak is present in each temperature profile above 200°C. This peak at 1940 cm^{-1} has been identified as CO bridging bond on the Ni sites as it falls within the range. The presence of this peak at elevated temperatures indicates strong interaction between CO and the Ni site of the material as well as indicating an increase in available active sites for adsorption. The DRIFTS study of the fresh material showed bridge bonding at lower temperature which are not present in the thiophene treated material suggesting the active nickel sites are inhibited by the presence of sulfur below 200°C. The influence of sulfur in the bridge bonding mode of the CO molecules was further evident upon comparison with the fresh $\text{Ni}_2\text{P}/\text{SiO}_2$ exhibited bridge bonding at a lower wavelength (1850 cm^{-1}) suggesting that the presence of sulfur has modified the system.

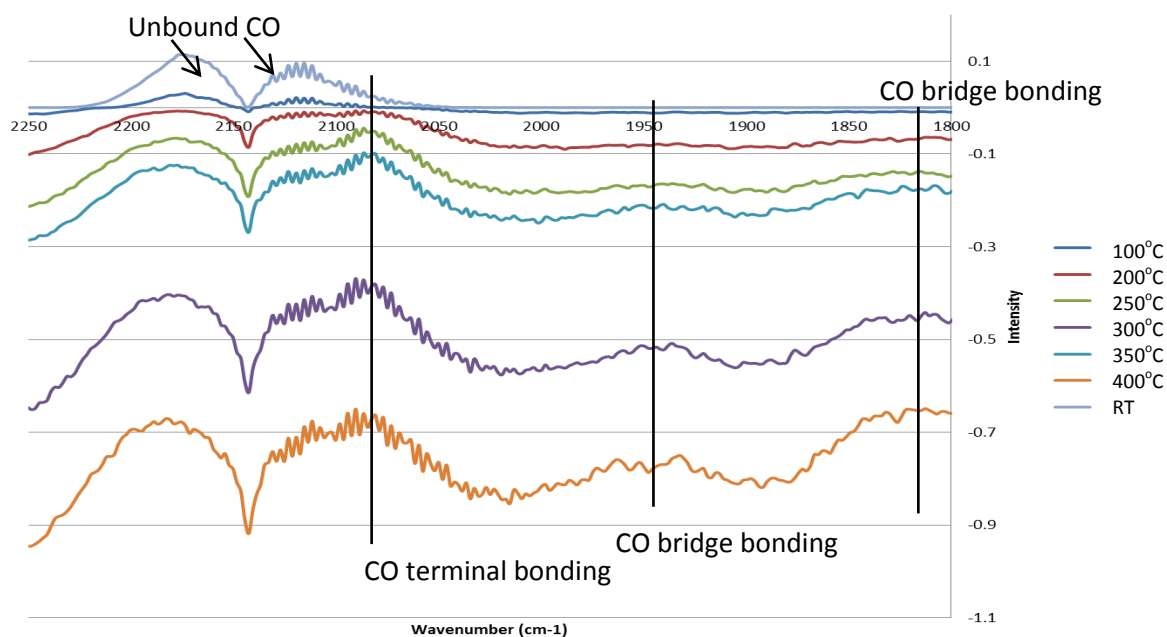


Figure 5-1: CO DRIFTS profile for $\text{Ni}_2\text{P}/\text{SiO}_2$ treated with thiophene.

The DRIFTS spectra display the distinctive broad double peaks associated with free unbound CO in the cell at 2115 and 2170 cm^{-1} . These peaks are present at each temperature the material is tested. This is to be expected with CO flowing through the microreactor. The terminal bonding mode is visible at 2079 cm^{-1} . This peak is most pronounced above 250°C . This is consistent with temperature at which the fresh $\text{Ni}_2\text{P}/\text{SiO}_2$ also exhibited terminal bonding of CO on the nickel active site. As was seen with the bridge bonding, there is an upward shift in the wavelength at which the bonding occurs in comparison to the fresh material. The fresh material exhibits terminal bonding at 2075 cm^{-1} . This is slightly lower than thiophene treated $\text{Ni}_2\text{P}/\text{SiO}_2$ this is a result of the influence of sulfur on the nickel active site. The terminal bonding site has previously been identified as the catalytically active adsorption site therefore indicating that sulfur may have an effect on the catalytic activity of $\text{Ni}_2\text{P}/\text{SiO}_2$.

Figures 5-2 and 5-3 display the CO adsorption DRIFT spectra for Ni/SiO₂ pre-treated with thiophene and fresh Ni/SiO₂ material respectively. The profiles display the FT-IR spectrum for the material at temperatures between room temperature and 400°C at 50°C intervals. The DRIFT spectra for the thiophene pre-treated catalyst shown in Figure 5-2 do not show any clear CO adsorption peaks at any temperature profile for either bridge or terminal bonding modes. The fresh material displayed in Figure 5-3 clearly displays terminal CO bonding between 2055 cm⁻¹ and 2080 cm⁻¹ for IR spectra at 100°C and above. The fresh material also exhibits terminal CO adsorption peaks at 1940 cm⁻¹ at temperatures in excess of 300°C. The presence of the CO adsorption peaks in the fresh Ni/SiO₂, along with the lack of the corresponding adsorption peaks, in the thiophene pre-treated material highlights the effect which the sulfur containing material has on the nickel active sites ability to effectively adsorb CO at temperatures similar to the operating conditions of the water-gas shift reaction. Comparison of the DRIFTS profiles for the thiophene pre-treated Ni₂P/SiO₂ and Ni/SiO₂ catalysts (Figures 5-1 and 5-2) indicate that the nickel phosphide material displayed greater resistance to deactivation by sulfur poisoning of nickel sites in comparison to the nickel catalyst. This was evident from the appearance of the adsorption peaks at temperatures in excess of 200°C for the pre-treated nickel phosphide but not in the pre-treated nickel catalyst. These results suggest that nickel phosphide may exhibit a greater degree of sulfur resistance in terms of catalytic performance of the two materials under high temperature water-gas shift reaction conditions.

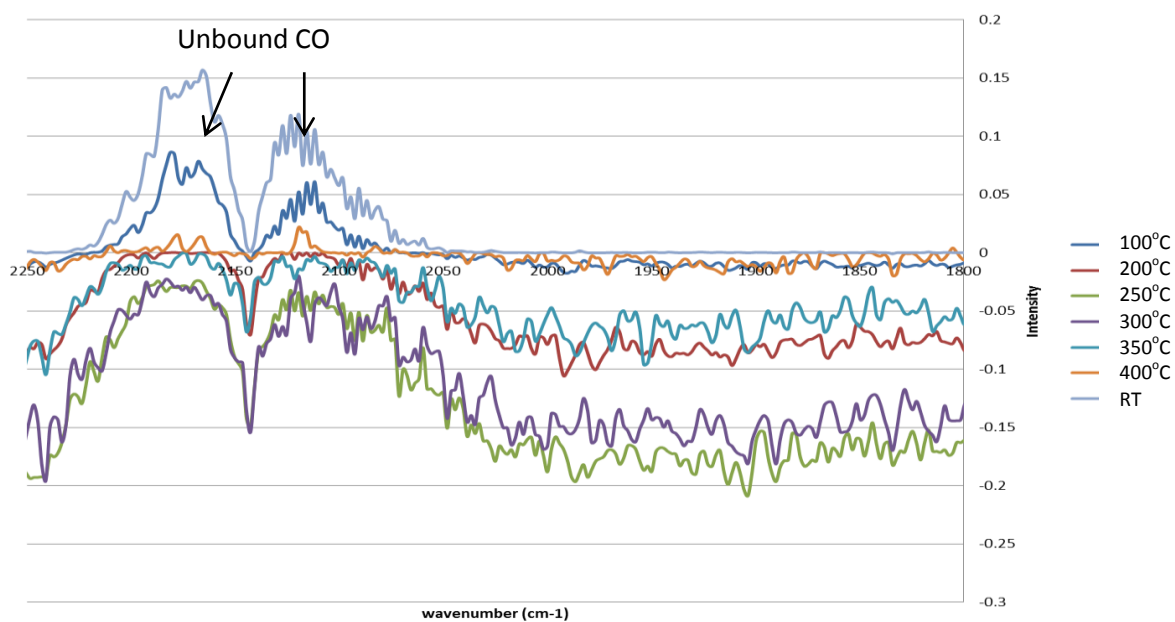


Figure 5-2: CO adsorption DRIFTS profile for Ni/SiO₂ treated with thiophene.

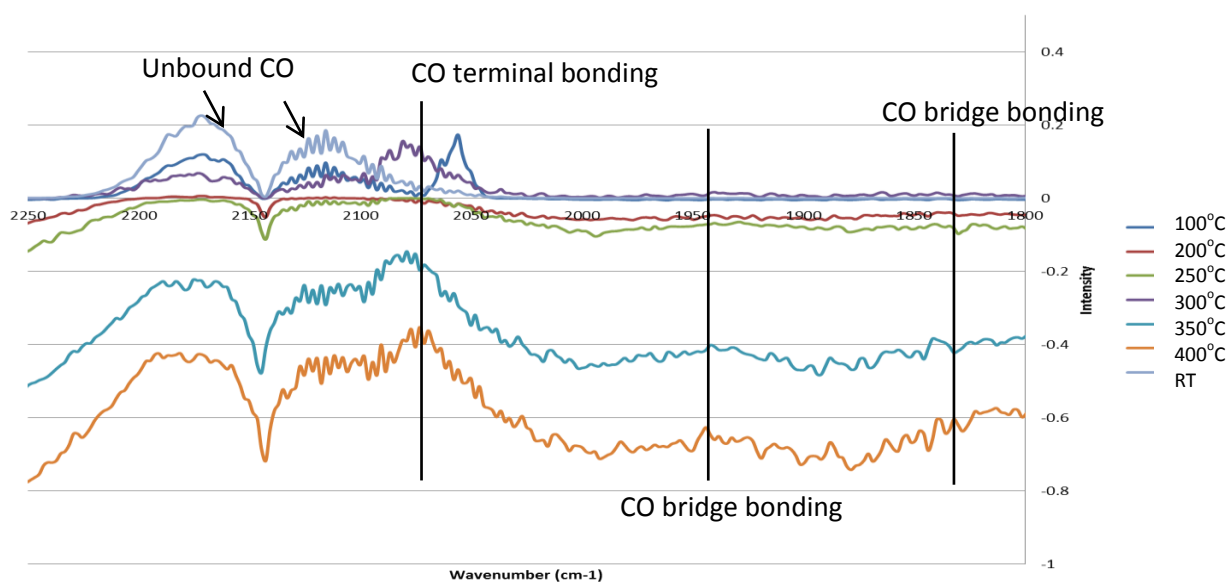


Figure 5-3: CO adsorption DRIFTS profile for Ni/SiO₂

The catalytic activity of Ni₂P/SiO₂ under high temperature water-gas shift reaction conditions was tested in the presence of sulfur. The catalyst was run under normal high temperature water-gas shift reaction conditions for 48 hours to ensure catalyst activity reached steady state. The sulfur was introduced to feed in the form of H₂S which was dissolved in water. The concentration of sulfur was approximately 10 ppm with regards to the total feed of H₂O and CO used. The reaction was run under the sulfur containing conditions until the hydrogen formation rate began to drop; this was after a period of 24 hours on stream. The H₂O feed to the reactor was then switched back to the non-sulfur containing feed to establish if the catalytic activity of nickel phosphide returned to a similar level as was displayed before the introduction of sulfur. The 1% Ce doped Ce-Ni₂P/SiO₂ catalyst was also tested under the same conditions as the nickel phosphide catalyst in order to establish if the addition of cerium (which has been documented as being a sulfur resistant water-gas shift catalyst) had any beneficial effects with regards to sulfur resistance displayed by the material. The industrial iron based catalyst and a Ni/SiO₂ catalyst were also tested under sulfur poisoning reaction condition for means of comparison. The reaction profiles for all four catalysts along with CO conversion rates and sulfur deactivation profiles are presented in the following section.

The reaction profile for the iron based industrial catalyst tested under high temperature water-gas shift conditions in the presence of 10 ppm H₂S is presented in Figure 5-4. The H₂ and CO₂ formation rates reach steady state after 5 hours of time on stream and remain steady until the catalyst is poisoned by sulfur. The average carbon balance during the steady state running was estimated to be approximately 87%. The introduction of sulfur to the feedstock is highlighted in the reaction profile shown in Figure 12 after 48 hours of running. The H₂S containing H₂O feed was run for a period of roughly 24 hours of time on stream after which GC data showed a drop in H₂ and CO₂ concentrations, indicating a drop in activity. After this point the sulfur feed was removed and the normal feed was reintroduced to establish if catalytic activity could be restored to any degree. The delay in deactivation after introduction of H₂S to the feed has been attributed to the saturation of the reactor with sulfur; this is mostly likely a result of the alumina boiling chips used to pack the catalyst in the reactor tube. This phenomenon is evident in the

reaction profiles for materials that will be presented later. To limit any variation between the catalysts tested the same volume of boiling chips were used each time to ensure consistency. CO_2 and H_2 formation rates begin to rapidly decrease after 58 hours on stream; this is accompanied by the rapid increase of CO concentration in the exit feed from the reactor. This is roughly 10 hours after the introduction of H_2S to the feed. After the removal of the H_2S feed the H_2 and CO_2 formation rates continue to fall towards zero whilst inversely the CO concentration increases. The continuing deactivation of the catalyst is due to the build-up of mobile sulfur particles which have saturated the reactor which continues to poison the catalyst after the clean feed is reintroduced. After the feed is switched back to the sulfur free feed catalytic activity does not return. This is characterised by the minimal concentrations of H_2 and CO_2 detected in the exit feed of the reactor by GC analysis. This indicates that the material is permanently deactivated upon interaction with sulfur under the reaction conditions.

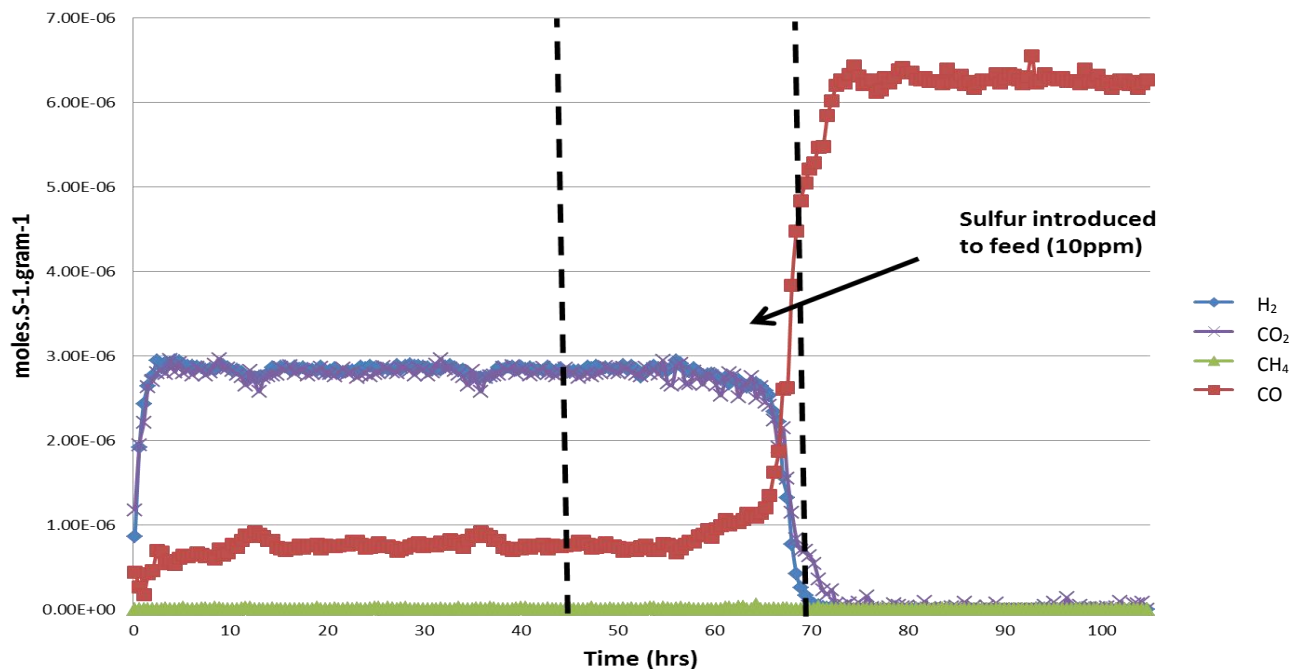


Figure 5-4: Reaction profile for sulfur testing of the HT industrial catalyst.

Figure 5-5 displays the corresponding fractional CO conversion profile for the industrial catalyst. The equation used to calculate CO conversion is presented in the experimental chapter. The fractional conversion of CO is shown to be roughly 0.90 at steady state; this begins to rapidly decrease after 58 hours of time on stream. At the end of the test run, the fractional CO conversion was estimated to be below 0.05 which constitutes a significant and irreversible drop in CO conversion. The drop in CO conversion after sulfur poisoning is much larger in comparison to the $\text{Ni}_2\text{P}/\text{SiO}_2$ and the $\text{Ce-Ni}_2\text{P}/\text{SiO}_2$ catalysts; which will be shown later in this section. This sharp drop in CO conversion was also seen with a Ni/SiO_2 catalyst.

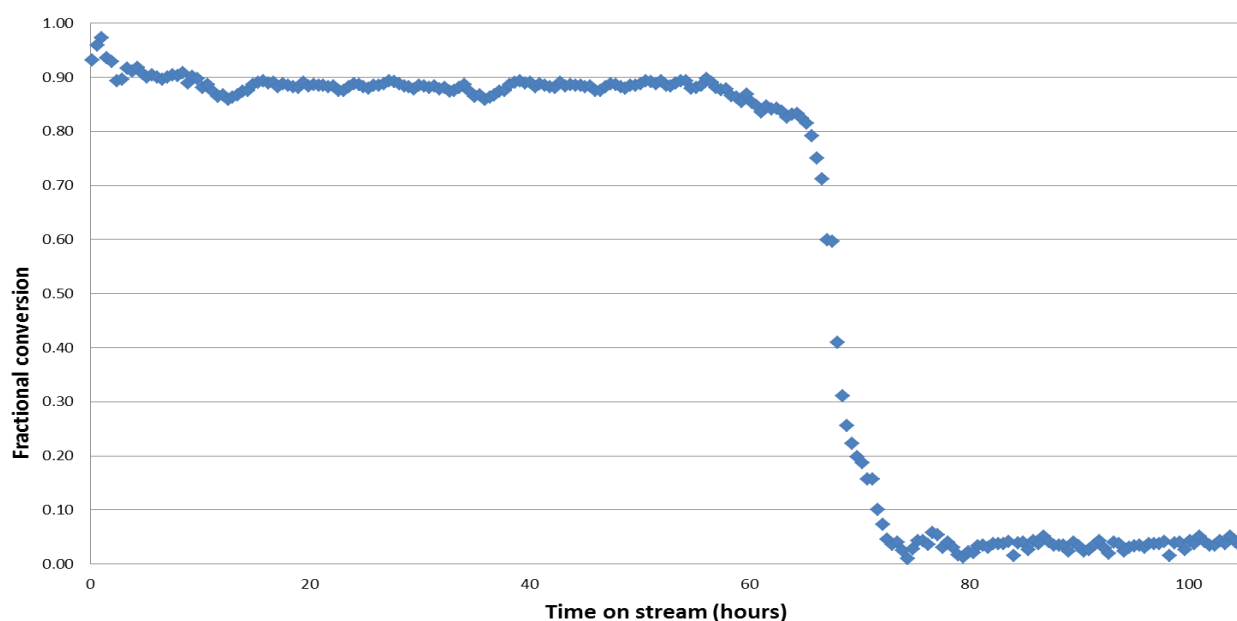


Figure 5-5: CO conversion profile for sulfur testing of the HT industrial catalyst.

Figure 5-6 displays the deactivation plot for the industrial catalyst based on the CO conversion profile for the reaction. The deactivation rate for the industrial catalyst via sulfur poisoning under high temperature water-gas shift reaction conditions was derived assuming first order kinetics for deactivation using a plot of $\ln(\text{CO}_{\text{conv}}/1-\text{CO}_{\text{conv}})$ versus time on stream which gave a straight line plot. The straight line equation (i.e $y=m.x+c$) $\ln(\text{CO}_{\text{conv}}/1-\text{CO}_{\text{conv}}) = k_{\text{deactivation}} \cdot T$ was used to calculate the

deactivation constant for the reaction. The deactivation rate constant was obtained from the data plotted after the initial deactivation of the catalyst ensuring that the establishment of reactants did not influence the deactivation constant. The plot displays a single rapid deactivation stage with deactivation rate constant calculated from the slope of the plot to be 0.2759 h^{-1} . As will be shown in follow section, the deactivation displayed by the industrial catalyst is much greater than that displayed by both silica supported phosphide catalysts.

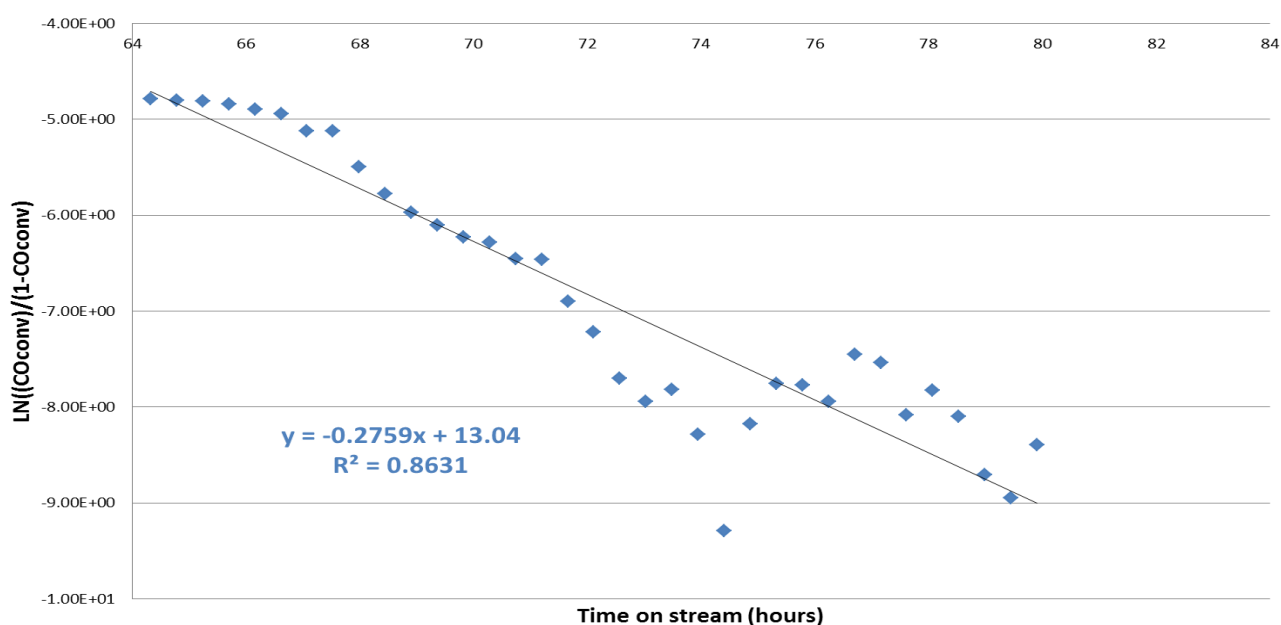


Figure 5-6: Sulfur deactivation plot for the HT industrial catalyst.

Figure 5-7 displays the reaction profile for $\text{Ni}_2\text{P}/\text{SiO}_2$. The material was tested under high temperature shift conditions and exposed sulfur. The reaction profile indicated that the reaction reached steady state after 10 hours of running and remains steady for the duration of the run until the introduction of sulfur. The carbon balance for the reaction was calculated as an average of 89% when the reaction was at steady state. The delay in the catalyst reaching steady state formation rates is thought to be due an activation process occurring within the material during this period of time. The reaction profile shows a slight discrepancy between H_2 and CO_2 . The difference in

H₂ and CO₂ being produced in the reaction can be attributed to formation of small amounts of methane being produced. The introduction of sulfur to the feedstock is highlighted in the reaction profile shown in Figure 5-4, as mentioned previously; this was introduced after 48 hours of time on stream. The reaction profile shows that after exposure to sulfur the catalyst begins to deactivate after 20 hours of exposure to the “sour feed”. After this point, the sulfur feed was removed and the normal feed was reintroduced. The reaction profile shows CO concentration begins to increase 8 hours after the introduction of H₂S time on stream; this also corresponds to a drop in the rate of CH₄ formation displayed by Ni₂P/SiO₂. The CO₂ and H₂ formation rates do not decrease until after more than 20 hours of exposure to H₂S. This suggests that methanation and water-gas shift active sites are two different sites which deactivate at differently. The delay in deactivation after introduction of H₂S to the feed has been attributed to the saturation reactor with sulfur; this is mostly likely the alumina boiling chips used to pack the catalyst in the reactor tube. After the removal of the H₂S feed the H₂ and CO₂ formation rates continue to fall whilst inversely the CO concentration increases. The continuing deactivation of the catalyst is due to the build-up of mobile sulfur particles which have saturated the reactor which continues to poison the catalyst after the clean feed is reintroduced. The H₂ and CO₂ formation rates eventually plateau after 95 hours on stream and remain steady. The H₂ formation rate has drop by 80% in comparison to the formation rate displayed by the catalyst before sulfur poisoning. The catalytic activity does not improve after the removal of the sulfur feed. This suggests that the deactivation of Ni₂P/SiO₂ is permanent rather than temporary which would have shown an increase in H₂ and CO₂ formation rates once sulfur was removed from the feedstock. The catalyst is only run for a short period of time at steady state, therefore it may require longer running post-sulfur exposure to fully determine if the catalyst is permanently deactivated.

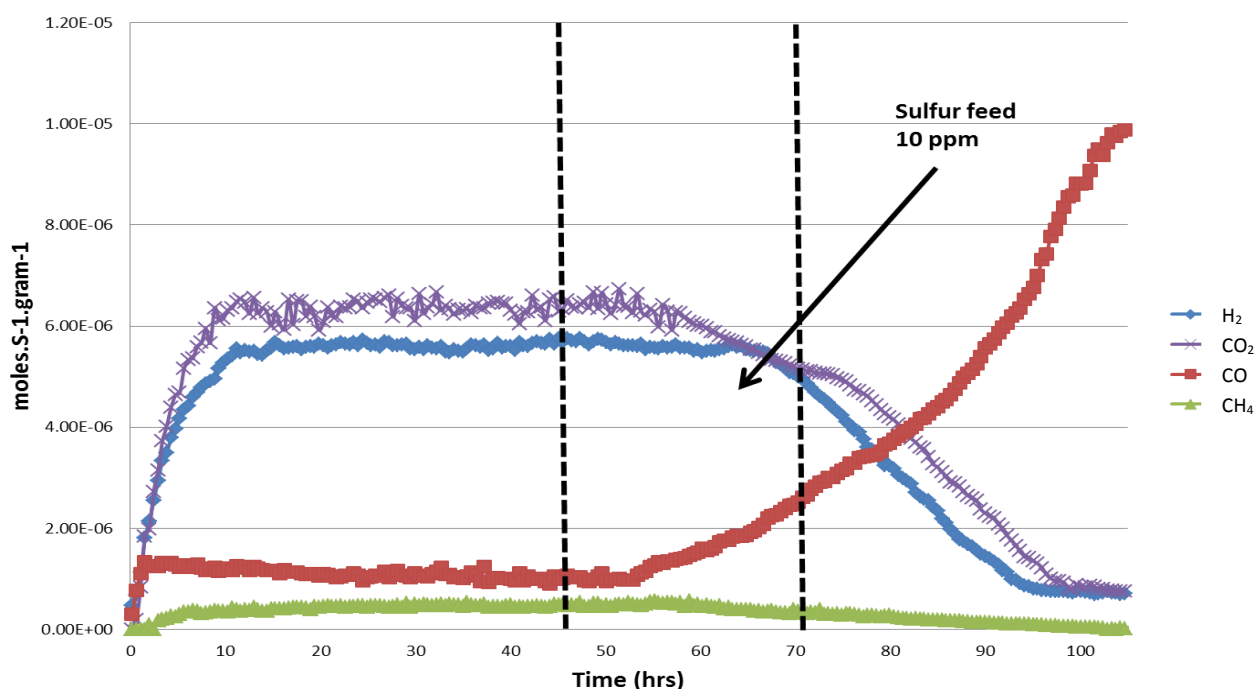


Figure 5-7: Reaction profile sulfur testing of $\text{Ni}_2\text{P}/\text{SiO}_2$ catalyst tested under HT water gas shift conditions.

The CO conversion rate for the sulfur testing of $\text{Ni}_2\text{P}/\text{SiO}_2$ is presented in Figure 5-8. The equation used to calculate CO conversion is presented in the experimental chapter. The profile indicates that the fractional CO conversion rate is approximately 0.9 under steady state reaction conditions; this begins to decrease after 55 hours of time on stream. This is attributed to the deactivation of the catalyst by sulfur poisoning. At the end of the test run, the fractional CO conversion rate was estimated to be just 0.2 which is a significant drop by 0.7 in the rate of conversion.

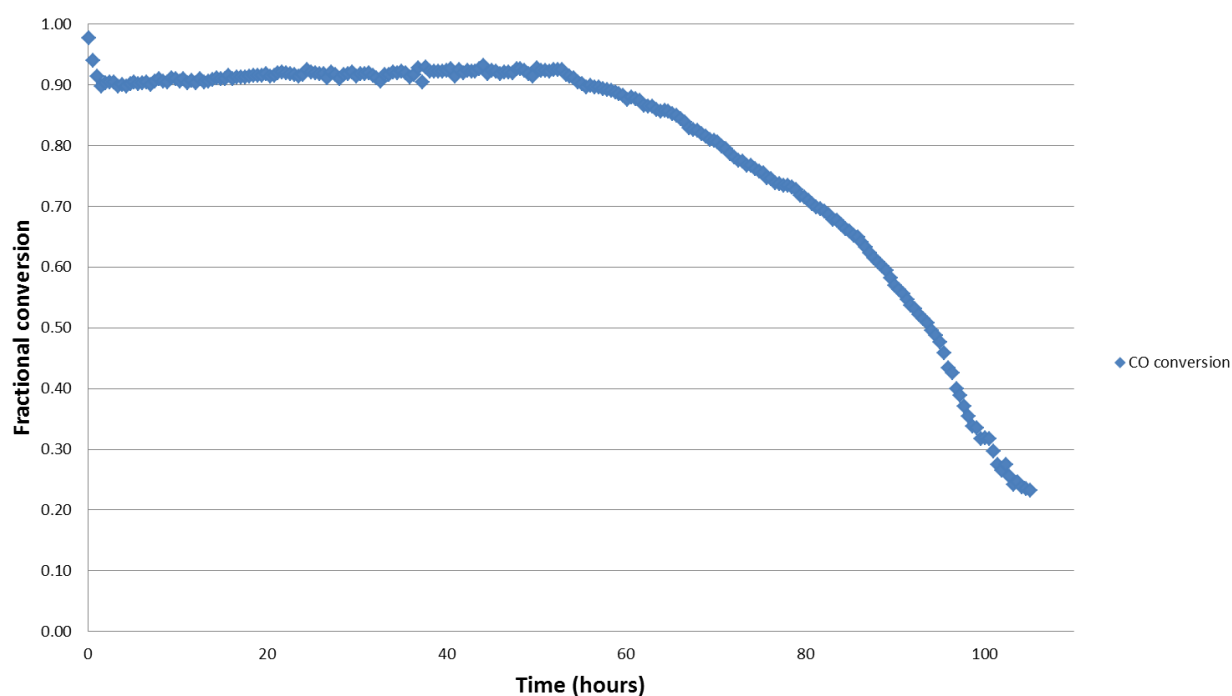


Figure 5-8: CO conversion profile for sulfur testing of $\text{Ni}_2\text{P}/\text{SiO}_2$ catalyst tested under HT water gas shift conditions.

The deactivation rate for the $\text{Ni}_2\text{P}/\text{SiO}_2$ catalyst via sulfur poisoning under high temperature water-gas shift reaction conditions was derived assuming first order kinetics for deactivation using a plot of $\ln(\text{CO}_{\text{conv}}/1-\text{CO}_{\text{conv}})$ versus time on stream which gave a straight line plot. The straight line equation (i.e $y=m.x+c$) $\ln(\text{CO}_{\text{conv}}/1-\text{CO}_{\text{conv}}) = k_{\text{deactivation}} \cdot \text{Time}$ was used to calculate the deactivation constant for the reaction. The deactivation rate constant was obtained from the data plotted after the initial deactivation of the catalyst ensuring that the deactivation constant was accurately calculated. Figure 5-9 shows the deactivation plot for $\text{Ni}_2\text{P}/\text{SiO}_2$, plot and shows that the deactivation proceeded via two different stages. The two are thought to be related to the different phases present in the material. Due to the different compositions of these phases, they are thought to be deactivated at differing rates by the sulfur. The mixed phases present in the catalyst were discussed previously in Chapter 3; these phases were responsible for the methanation (Ni metal phase) and water-gas shift (Ni_2P phase) activity displayed by the catalyst. The first deactivation slope attributed to the deactivation of the methane active Ni phase has a given

constant of 0.0153 h^{-1} . The second deactivation slope, associated with the water-gas shift reaction active Ni_2P phase in the material displays a much greater deactivation constant (0.0709 h^{-1}) than the Ni metal phase. The two different deactivation stages displayed by the two phases of nickel may be a result of an ensemble size effect on the active sites. For example, methanation could require 6 active sites for complete dissociation of the reactants. This process could be disrupted if one of these sites becomes poisoned. The superior sulfur resistance displayed by the nickel phosphide catalyst in comparison to the industrial catalyst evident from inspection of the reaction profiles are clearer upon comparison of the deactivation rate constants displayed by the materials. The industrial catalyst displays a deactivation constant almost four times greater than $\text{Ni}_2\text{P}/\text{SiO}_2$, suggesting the catalyst is much more susceptible to poisoning.

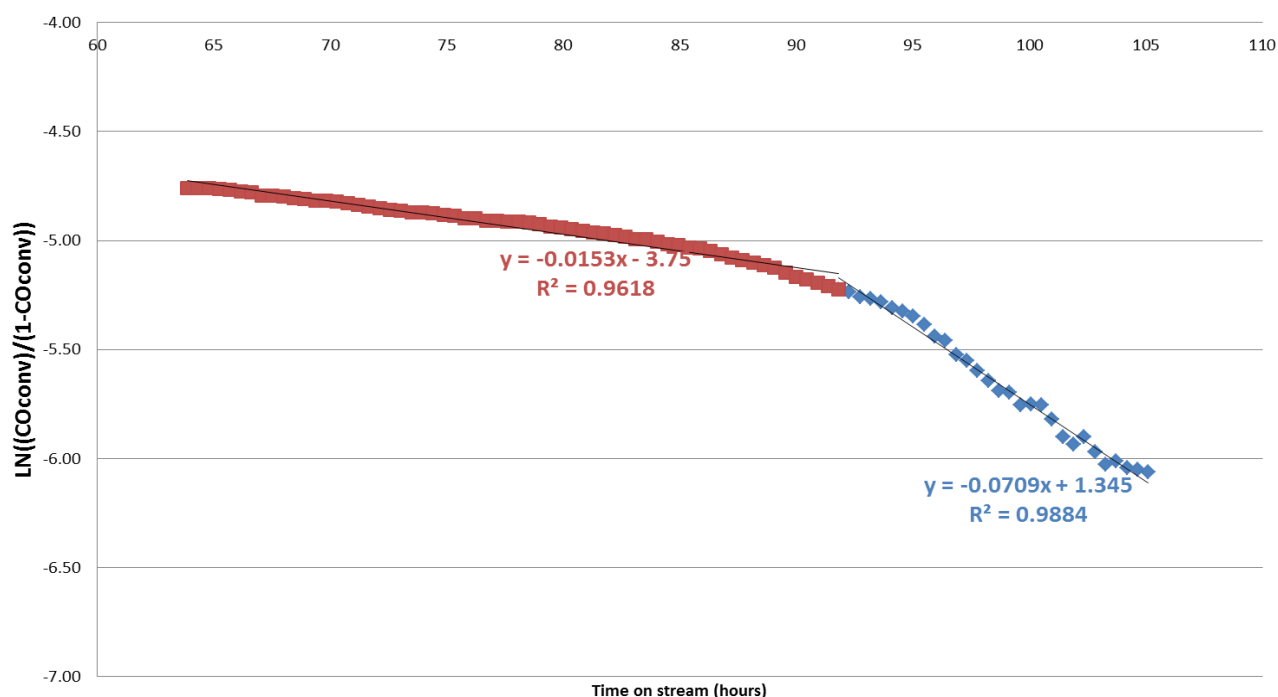


Figure 5-9: Sulfur deactivation plot for $\text{Ni}_2\text{P}/\text{SiO}_2$ catalyst

The reaction profile for sulfur testing of the Ce-Ni₂P/SiO₂ (1% w.t. Ce) catalyst is displayed in Figure 5-10. The catalyst displays significant catalytic activity under the reaction conditions. According to the reaction profile CO₂, H₂ and CH₄ display steady formation rates before the introduction of the H₂S containing feed. The run produces significant CO₂ and H₂ indicating that the water-gas shift reaction is taking place on the catalyst surface. Small amounts of CH₄ are also produced during the reaction due to the nickel metal sites in the material. The carbon balance was calculated to be an average of 93% whilst the reaction is run under steady state conditions. The discrepancy between CO₂ and H₂ formation rates in the reaction profile can also be attributed to the methanation activity shown by the catalyst. Formation rates for all products reach steady state after roughly 20 hours on stream, as has previously been observed with other nickel phosphide materials. After 48 hours of time on stream, the H₂O feed into the reactor was switched to an H₂O feed containing H₂S of an estimated concentration of 10ppm with regards to total amount of reactants. The reaction profile indicated that CO concentration does not begin to increase until roughly 60 hours on stream; this is approximately 12 hours after the H₂S feed is introduced into the reactor. This is 4 hours longer than was seen in the Ni₂P/SiO₂ reaction profile shown in Figure 5-4. CO₂ and H₂ formation rates begin to decrease after approximately 66 hours on stream, 18 hours after H₂S is initially introduced into the reactor. As was seen with the Ni₂P/SiO₂, the 1% Ce doped catalyst displayed H₂ and CO₂ formation rates after sulfur poisoning at a much lower rate than initially displayed by the catalyst before poisoning. After poisoning, the H₂ formation rate approximately 10% of that before catalyst poisoning. Methane formation was completely deactivated by sulfur poisoning as was seen in the Ni₂P/SiO₂ presented previously. The catalytic activity of the material does not return to pre-sulfur feed indicating that poisoning is permanent. The catalyst is only run for a short period of time at steady state, therefore it may require longer running post-sulfur exposure to fully determine if the catalyst is permanently deactivated.

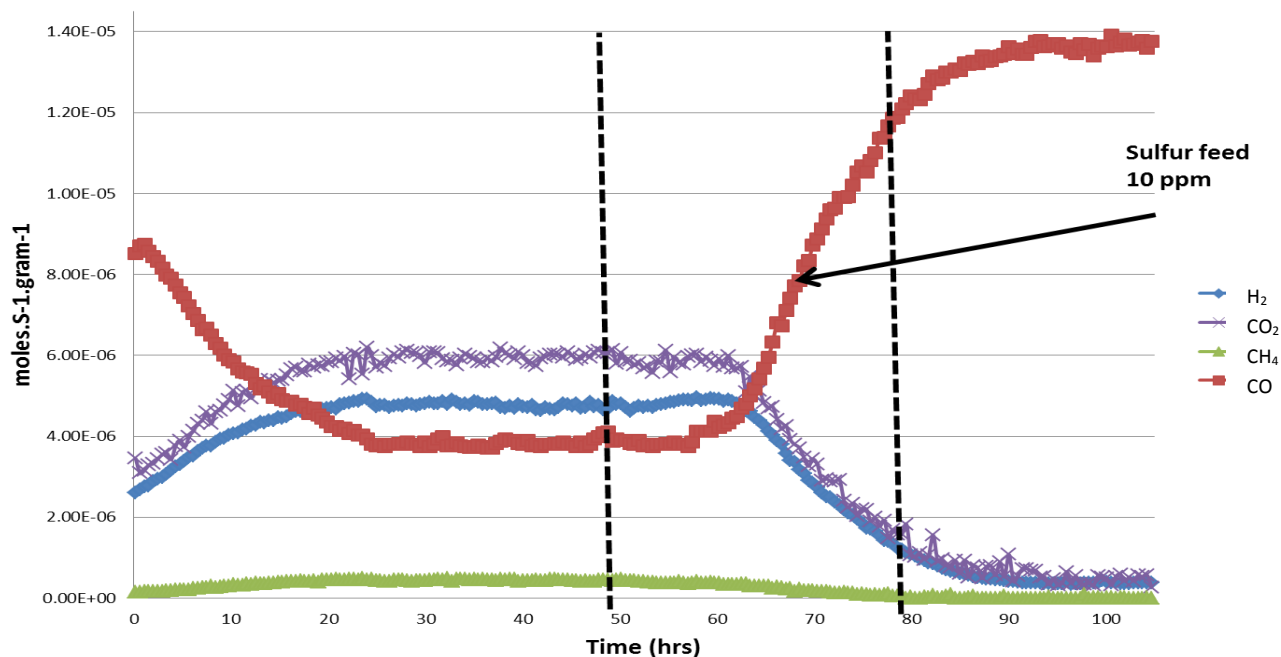


Figure 5-10: Reaction profile for then sulfur testing of $\text{Ce-Ni}_2\text{P/SiO}_2$ (1%Ce loading) catalyst tested under HT water-gas shift conditions.

The CO conversion rate for the sulfur testing run using the $\text{Ce-Ni}_2\text{P/SiO}_2$ (1% Ce loading) catalyst is presented in Figure 5-11. The CO conversion profile is based on the figures displayed in the reaction profile for the test run. The fractional CO conversion rate is shown to be roughly 0.75 at steady state; this begins to decrease after 60 hours of time on stream. This is attributed to the deactivation of the catalyst by sulfur poisoning. At the end of the test run the fractional CO conversion was estimated to be just 0.1 which is a significant drop by 0.65 in conversion in comparison to the initial conversion rate displayed by the catalyst.

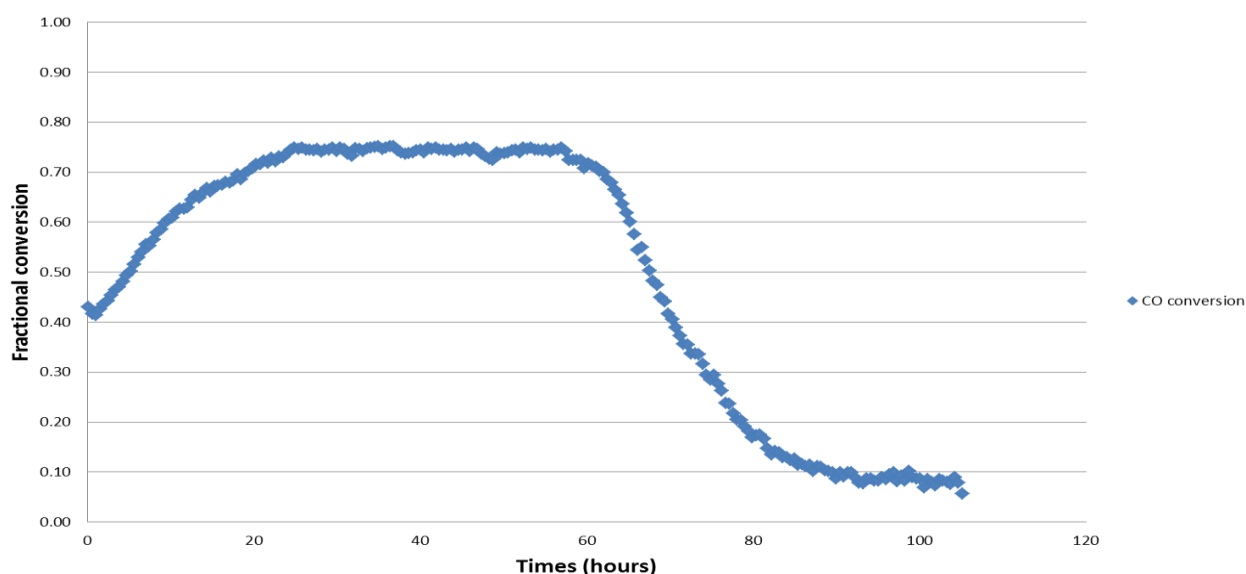


Figure 5-11: CO conversion profile for sulfur testing of Ce-Ni₂P/SiO₂ (1% Ce loading) catalyst tested under HT water gas-shift conditions.

The deactivation rate for the Ce-Ni₂P/SiO₂ (1% Ce loading) catalyst via sulfur poisoning was estimated using the same method as before with Ni₂P/SiO₂ catalyst. It was derived assuming first order kinetics for deactivation using a plot of $\ln(\text{CO}_{\text{conv}}/1-\text{CO}_{\text{conv}})$ versus time on stream which gave a straight line plot. The straight line equation (i.e $y=m.x+c$) $\ln(\text{CO}_{\text{conv}}/1-\text{CO}_{\text{conv}}) = k_{\text{deactivation}} \cdot \text{Time}$ was used to calculate the deactivation constant for the reaction. The deactivation rate constant was obtained from the data plotted after the initial deactivation of the catalyst ensuring that the establishment of reactants did not influence the deactivation constant. The deactivation plot for the catalyst is present in Figure 5-12. A single deactivation rate was derived from the plot and was calculated to be 0.0744 h^{-1} , indicating that the catalyst displays only one phase of deactivation. The Ce doped catalyst displays only one deactivation phase in comparison to the Ni₂P/SiO₂ catalyst. This suggests that the active sites in the Ce catalyst are more uniform in nature and do not deactivate at different rates as was seen with the monometallic catalyst. The difference between the two catalysts may be a result of the presence of cerium which was shown in the previous chapter to influence the final phase of nickel formed on the catalyst support. The addition of cerium to the phosphide system resulted in the formation of more nickel metal sites in the catalyst, resulting in a

material with greater mixed phase in comparison to the monometallic phosphide. The deactivation rate for the Ce doped catalyst is close to that displayed by the $\text{Ni}_2\text{P}/\text{SiO}_2$ catalyst in the second stage of deactivation displayed which was calculated to be 0.0709 h^{-1} indicating both materials deactivate at a similar rate. Cerium has also previously been investigated for its sulfur resistance in water-gas shift application; the addition of cerium to the nickel phosphide shows no significant difference with regards to lowering the deactivation rate of the catalyst. The cerium doped catalyst displays a marginally larger deactivation constant than the monometallic nickel phosphide catalyst.

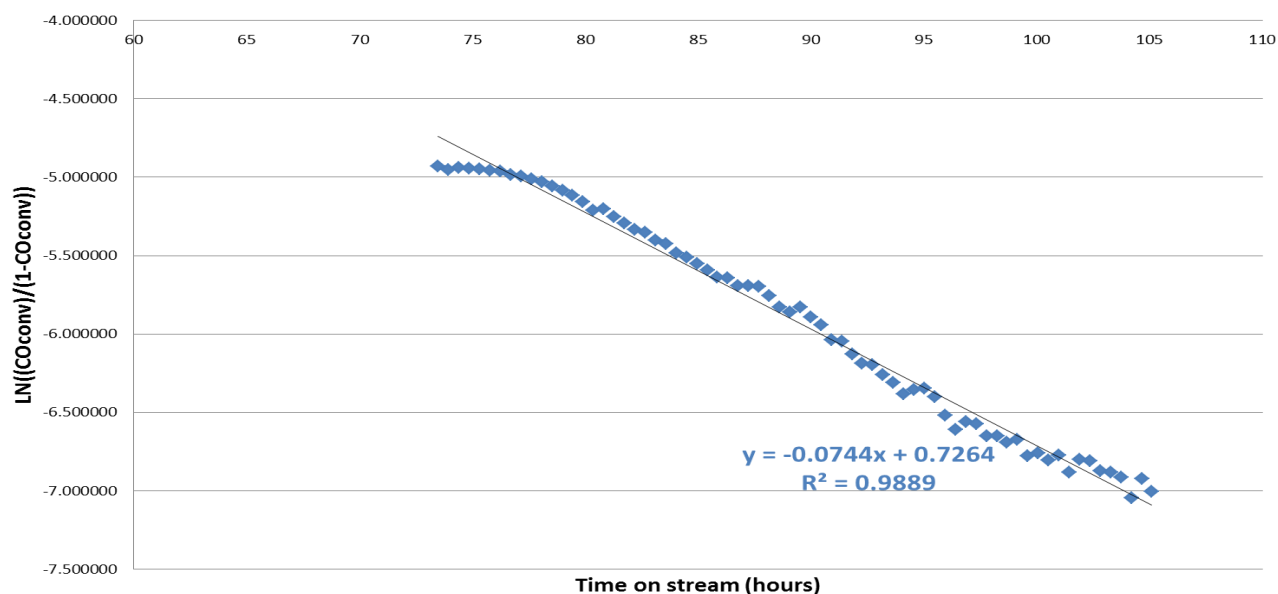


Figure 5-12: Sulfur deactivation plot for $\text{Ce-Ni}_2\text{P}/\text{SiO}_2$ (1% Ce loading) catalyst.

The reaction profile for the Ni/SiO_2 catalyst is shown in Figure 5-13. The reaction profile for the nickel catalyst shows the reaction reached steady state after 10 hours of running and the carbon balance was calculated as 91%. The nickel catalyst produces a significant amount of methane in comparison to the nickel phosphide catalyst. Nickel is a highly effective methanation catalyst under high temperature water-gas shift reaction conditions so high methane formation rates are to be expected. The introduction of sulfur to the feedstock is highlighted in the reaction profile shown in Figure 5-10 after 48 hours on stream. The H_2S containing H_2O feed

was run for a period of roughly 24 hours on stream after which GC data showed a drop in H_2 and CO_2 concentrations, corresponding to a drop in activity. After this point the sulfur feed was removed and the normal feed was reintroduced. The delay in the deactivation of the catalyst after introduction of H_2S to the feed has been attributed to the saturation of the reactor with sulfur; this is mostly likely the alumina boiling chips used to pack the catalyst in the reactor tube. This phenomenon was viewed previously tested materials presented earlier as well. CO_2 , CH_4 and H_2 formation rates begin to rapidly fall after 65 hours on stream, this is accompanied by the rapid increase of CO concentration in the exit feed from the reactor. This is roughly 17 hours after the introduction of H_2S to the feed. After the removal of the H_2S feed the H_2 , CH_4 and CO_2 formation rates continue to fall whilst inversely the CO concentration increases. The continuing deactivation of the catalyst is due to the build-up of mobile sulfur species which have saturated the reactor which continues to poison the catalyst after the clean feed is reintroduced. After the feed is switched back to the sulfur free feed catalytic activity does not return. This is characterised by the minimal concentrations of H_2 , CH_4 and CO_2 detected in the exit feed of the reactor by GC analysis.

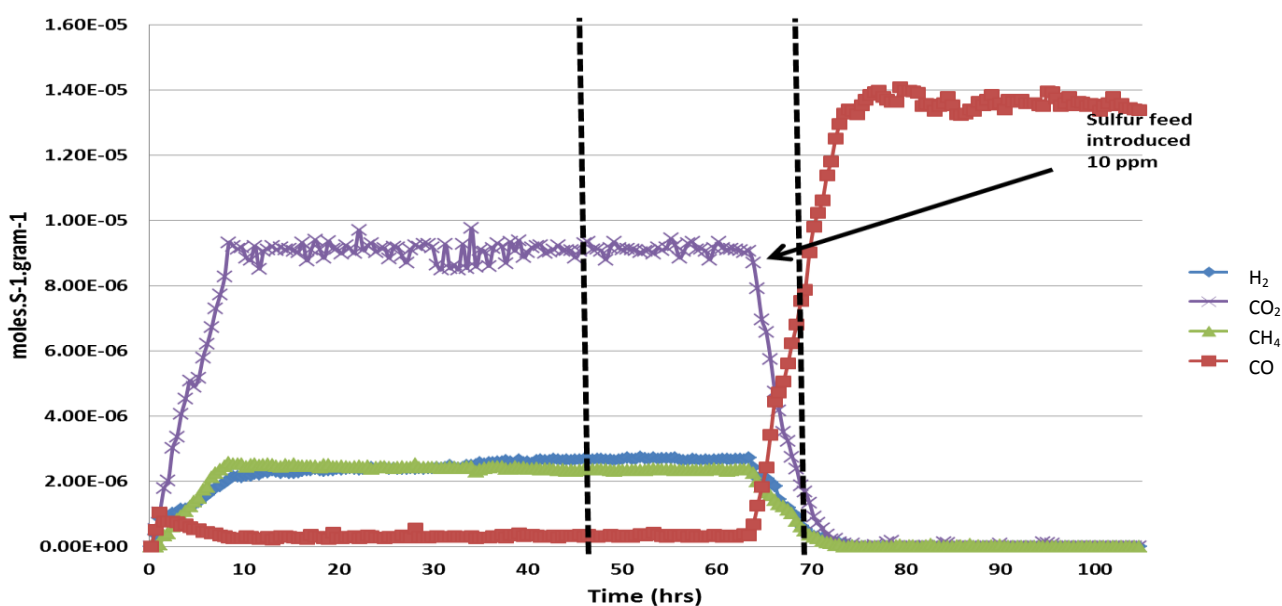


Figure 5-13: Reaction profile for sulfur testing of Ni/SiO_2 catalyst tested under HT water-gas shift conditions.

The CO conversion rate for the sulfur testing run using the Ni/SiO₂ catalyst is presented in Figure 5-14. The CO conversion profile is based on the figures displayed in the reaction profile for the test run. The CO conversion is shown to be roughly 0.98 at steady state; this begins to rapidly decrease after 65 hours of time on stream. This is attributed to the deactivation of the catalyst by sulfur poisoning. At the end of the test run the CO conversion was estimated to be just 0.05 this constitutes a loss of 0.93 in conversion of CO. The drop in CO conversion after sulfur poisoning is much larger in comparison to the Ni₂P/SiO₂ and the Ce-Ni₂P/SiO₂ catalysts. Both of the phosphide materials still exhibit some CO conversion after poisoning whilst the Ni/SiO₂ catalyst displays effectively no CO conversion after poisoning, highlighting the improved performance of nickel phosphide catalysts under sulfur containing reaction conditions in comparison to nickel catalyst.

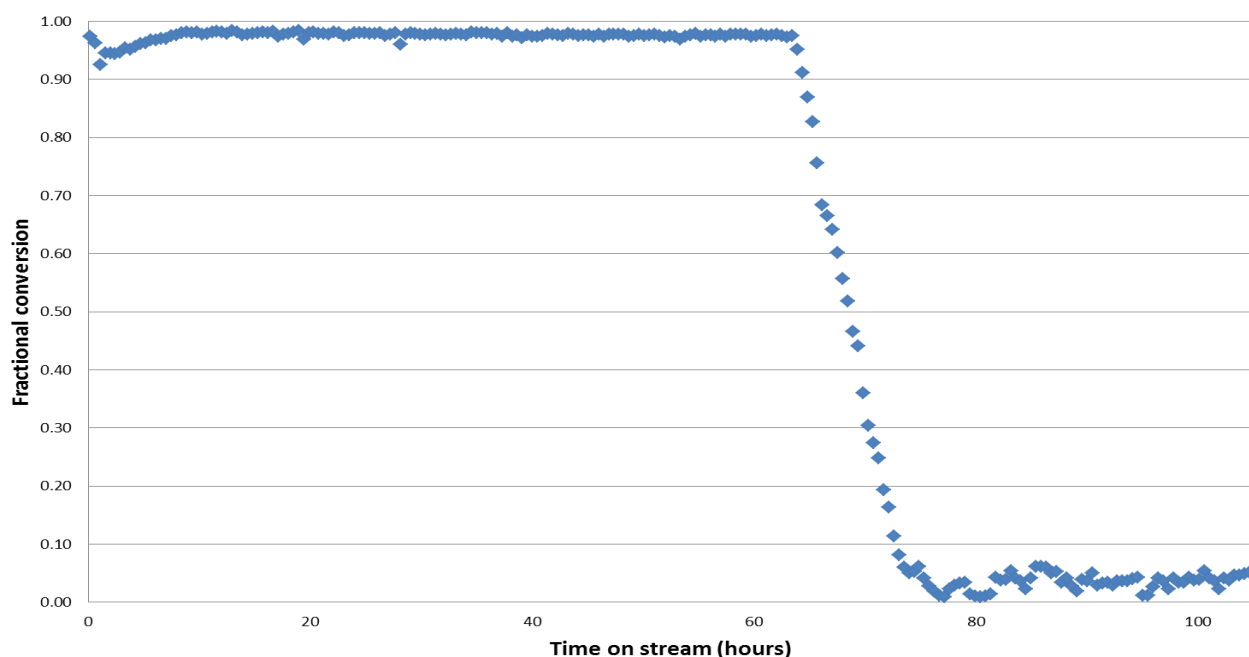


Figure 5-14: CO conversion profile for sulfur testing of Ni/SiO₂ catalyst tested under HT water gas-shift conditions.

Figure 5-15 shows the deactivation plot derived from the sulfur testing run for the Ni/SiO₂ catalyst. The deactivation plot highlights the superior catalytic performance of the Ni₂P/SiO₂ and Ce-Ni₂P/SiO₂ under sulfur containing conditions in comparison to the Ni/SiO₂ catalyst. The deactivation rate was derived from the plot of $\ln(\text{CO}_{\text{conv}}/(1-\text{CO}_{\text{conv}}))$ versus time on stream which gave a straight line plot. The plot displays two different stages of deactivation. The first slower with a deactivation rate constant of 0.1365 h⁻¹ and is preceded by a much more rapid second deactivation stage with a rate constant calculated as 0.4128 h⁻¹. The two deactivation stages exhibited indicate an amorphous nature in the active sites within the material with regards to the rate at which they are deactivated by the presence of sulfur. The deactivation rate for the Ni/SiO₂ catalyst is much larger in both stages than those displayed by the Ni₂P/SiO₂ and Ce-Ni₂P/SiO₂ catalysts. The second deactivation rate constant displayed by Ni/SiO₂ is approximately 6 times larger than the largest deactivation rate constants displayed by the two phosphide catalysts. This shows that the phosphide catalysts are far more effective and resistant to deactivation by sulfur poisoning in contrast to the nickel catalyst under the conditions of testing.

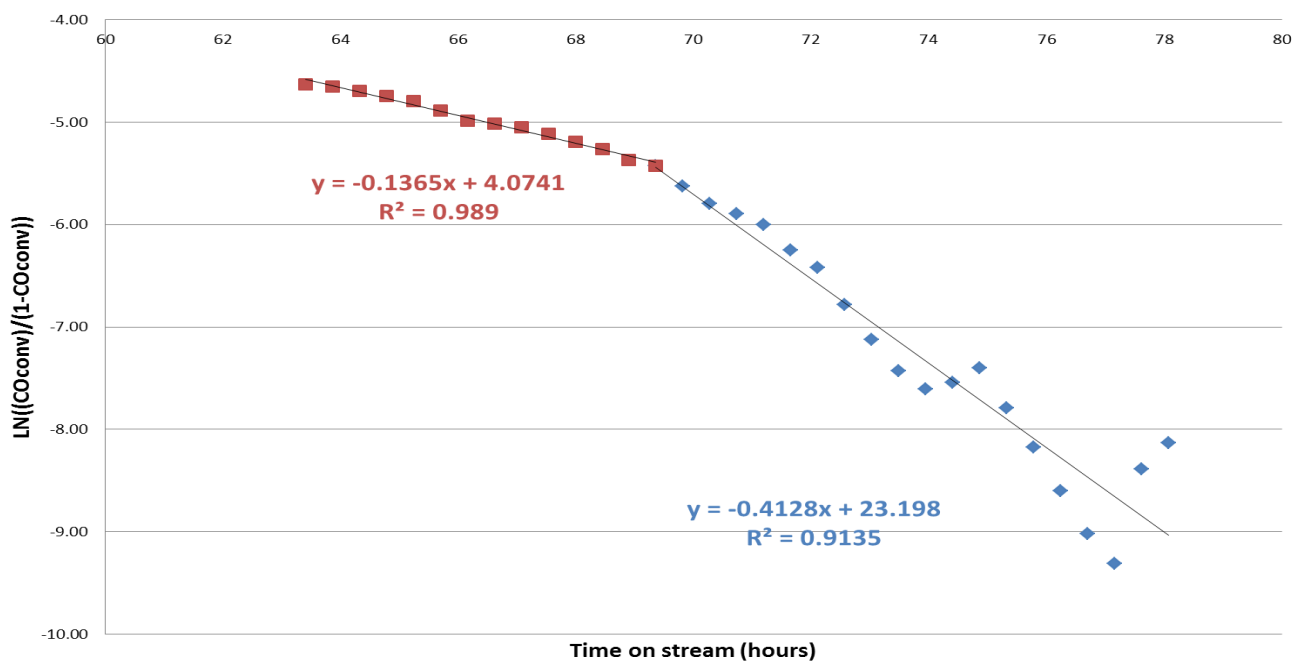


Figure 5-15: Sulfur deactivation plot for Ni/SiO₂ catalyst.

$\text{Ni}_2\text{P}/\text{SiO}_2$, $\text{Ce-Ni}_2\text{P}/\text{SiO}_2$ and Ni/SiO_2 were all compared with regards to the amount of sulfur taken to reduce the initial conversion displayed by the catalyst by 50%. Figure 5-16 shows the estimated sulfur to nickel ratio for the three catalysts based on the number of moles of nickel present with the equivalent number of moles of sulfur taken to cause the initial CO conversion to drop to by 50% based on the reaction profile data. Figure 5-16 shows $\text{Ni}_2\text{P}/\text{SiO}_2$ catalyst exhibits the highest sulfur content (0.87) in comparison to the cerium doped catalyst (0.295) and the nickel catalyst (0.14). The higher sulfur content displayed by $\text{Ni}_2\text{P}/\text{SiO}_2$ indicates approximately eight times the amount sulfur is required to deactivate the catalyst in comparison to the Ni/SiO_2 catalyst. The lower sulfur coverage displayed by $\text{Ce-Ni}_2\text{P}/\text{SiO}_2$ suggests that the cerium doped catalyst requires less sulfur to be deactivated in comparison to $\text{Ni}_2\text{P}/\text{SiO}_2$. This suggests that cerium does not improve the sulfur resistant properties of nickel phosphide as was initially thought it may do. Cerium doping of the nickel phosphide catalyst was shown to increase the number of nickel metal phases present in the material so this is most likely the reason for the poorer performance of the catalyst in comparison to the monometallic nickel phosphide catalyst due to increase in methanation displayed by the material. The greater susceptibility of the nickel metal sites to poisoning may be a result of a higher degree of ensemble size effect occurring in comparison to the nickel phosphide therefore deactivating the nickel metal phase more rapidly.

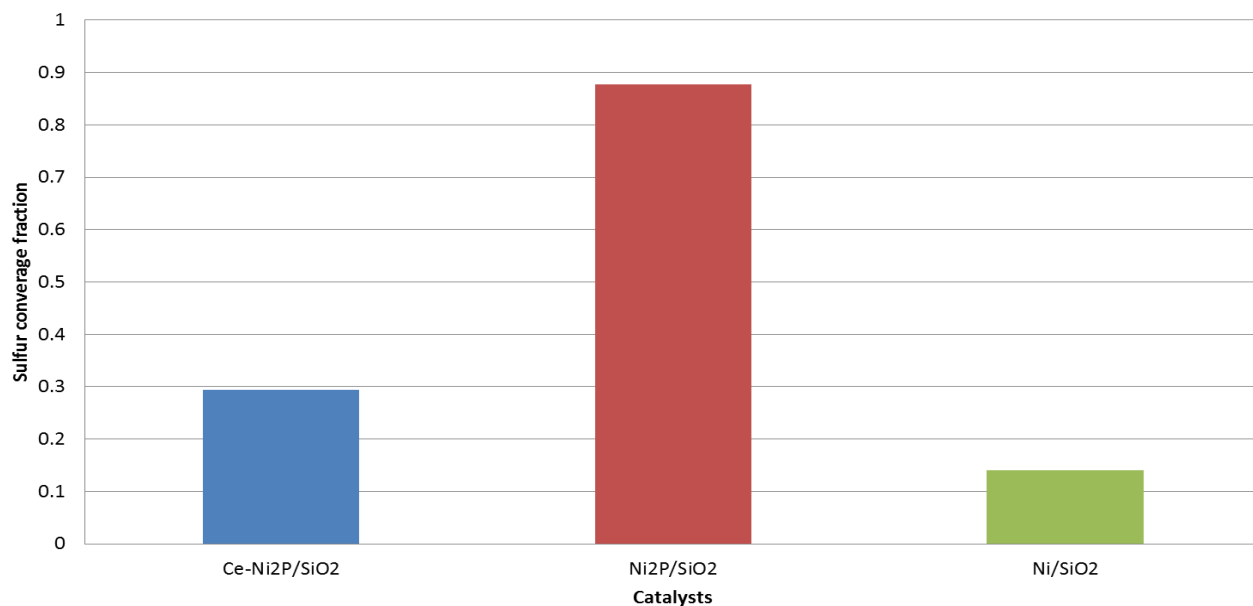


Figure 5-16: Estimated S:Ni ratio of nickel based catalysts at which the initial CO conversion drops by 50%.

The comparison of catalysts using sulfur saturation highlights the greater sulfur resisting properties of nickel phosphide in comparison to nickel with regards to the catalytic activity of the two materials. The large fraction of sulfur coverage in Ni₂P/SiO₂ may also indicate that nickel thiophosphate (NiPS₃) phases are being formed in the material. Studies by Oyama and Burns have previously reported the formation of nickel thiophosphate phases on nickel phosphide catalysts used in HDS reactions. It was suggested that the formation of the thiophosphate phase had beneficial effects on the hydrotreating ability of the catalysts. If a thiophosphate phase has formed during the sulfur testing it has not had a beneficial effect on the catalytic activity of the material for the water-gas shift reaction. There is the possibility however that the catalyst may be regenerated with the reduction of the thiophosphate to phosphide and potentially regain some if not all of the activity displayed by the material originally. The properties of nickel thiophosphate were explored in Chapter 3 where it was shown that it will readily reduce under flowing hydrogen at 400-500°C.

5.3 Post-sulfur testing characterisation of materials

The post-reaction $\text{Ni}_2\text{P}/\text{SiO}_2$, $\text{Ce-Ni}_2\text{P}/\text{SiO}_2$ and Ni/SiO_2 catalysts were studied by XRD to establish if the crystal phases displayed by the catalysts were altered after interaction with sulfur. The XRD patterns for the pre and post-reaction samples of $\text{Ni}_2\text{P}/\text{SiO}_2$ are presented in Figure 5-17. The diffraction pattern for the post-reaction catalyst shows the material is largely amorphous in comparison to the fresh material. This may be due to formation of thiophosphate phases within the catalyst. Comparison with fresh material shows the fresh material to be much more crystalline in nature. The post-reaction sample does show small diffraction peaks in the range 44° to 47° which line up with those seen in the fresh material suggesting that some of the crystalline Ni_2P phase still remains in the material. This is consistent with what was seen in the reaction profile for the material which shows some catalytic activity still remains after interaction with H_2S .

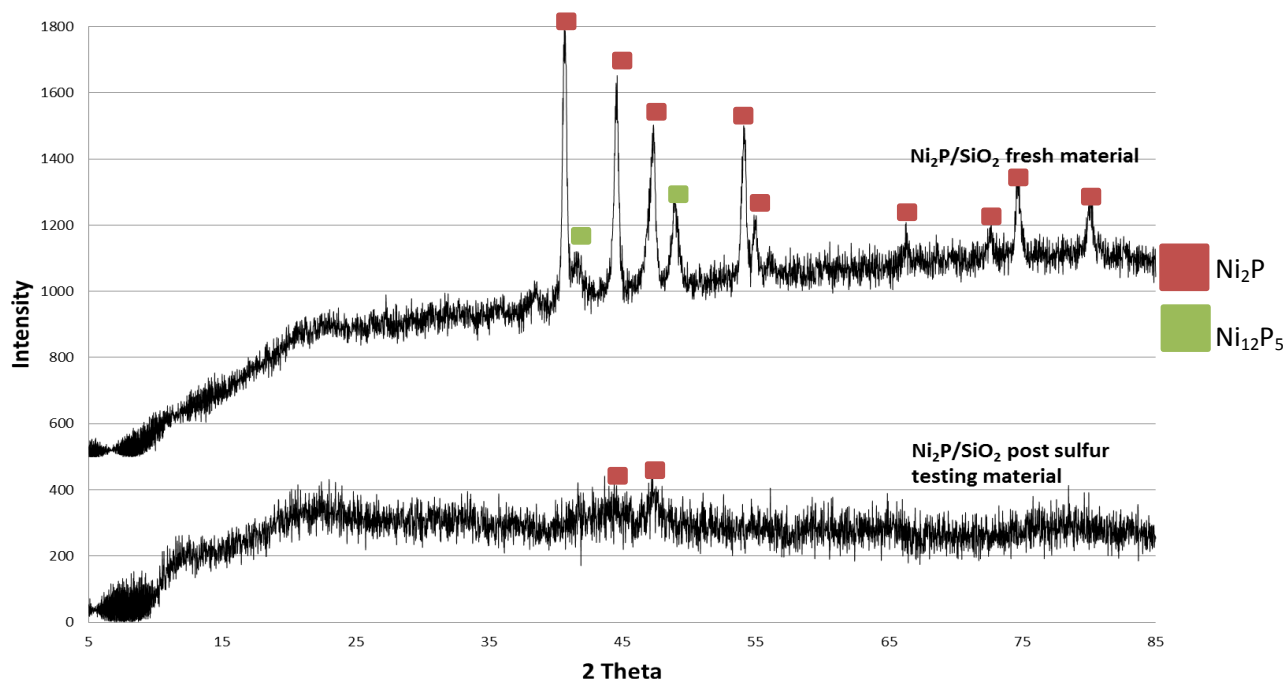


Figure 5-17: XRD patterns for pre- and post-sulfur testing $\text{Ni}_2\text{P}/\text{SiO}_2$.

The pre- and post-sulfur testing diffraction patterns for $\text{Ce-Ni}_2\text{P}/\text{SiO}_2$ are shown in Figure 5-18. As was seen with the $\text{Ni}_2\text{P}/\text{SiO}_2$ catalyst, the $\text{Ce-Ni}_2\text{P}/\text{SiO}_2$ post-sulfur

diffraction pattern shows the material is largely amorphous. This is due to the mixed phases of nickel thiophosphate and nickel phosphide present in material after interaction with H_2S during the sulfur testing reaction. Some small diffraction peaks are visible in the post sulfur testing material and these peaks approximately matching with those displayed by much more crystalline fresh material. The partial crystallinity displayed by the post-reaction material indicates that Ni_2P phases are still present in material; this explains the remaining catalytic activity seen in the reaction profile for the catalyst after sulfur testing.

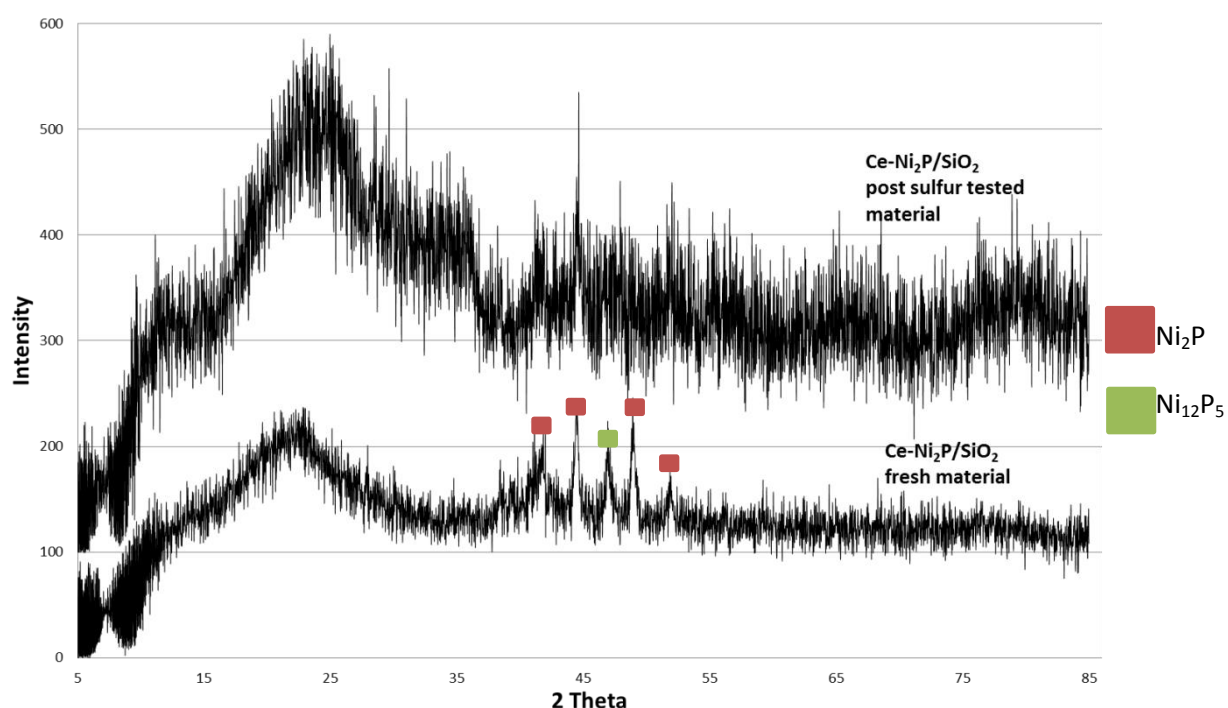


Figure 5-18: XRD patterns for pre- and post-sulfur testing $\text{Ce-Ni}_2\text{P/SiO}_2$.

Figure 5-19 displays the pre and post-reaction XRD patterns for Ni/SiO_2 . The post-reaction material displays a number of diffraction peaks suggesting the bulk phase on nickel is mostly crystalline in nature, unlike the post-reaction nickel phosphide catalyst which are both largely amorphous. The diffraction peaks for the post-reaction material differ to those seen in the fresh material. The additional diffraction peaks in the post-reaction material have been identified as nickel sulfide (NiS) which occur at 37° , 43° and 63° . The appearance of these peaks suggests that bulk nickel

phase has been sulfided after interaction with H₂S during the reaction testing. The conversion of the bulk phase of nickel to sulfide also suggest why the catalytic activity of the catalyst completely drops after sulfur testing.

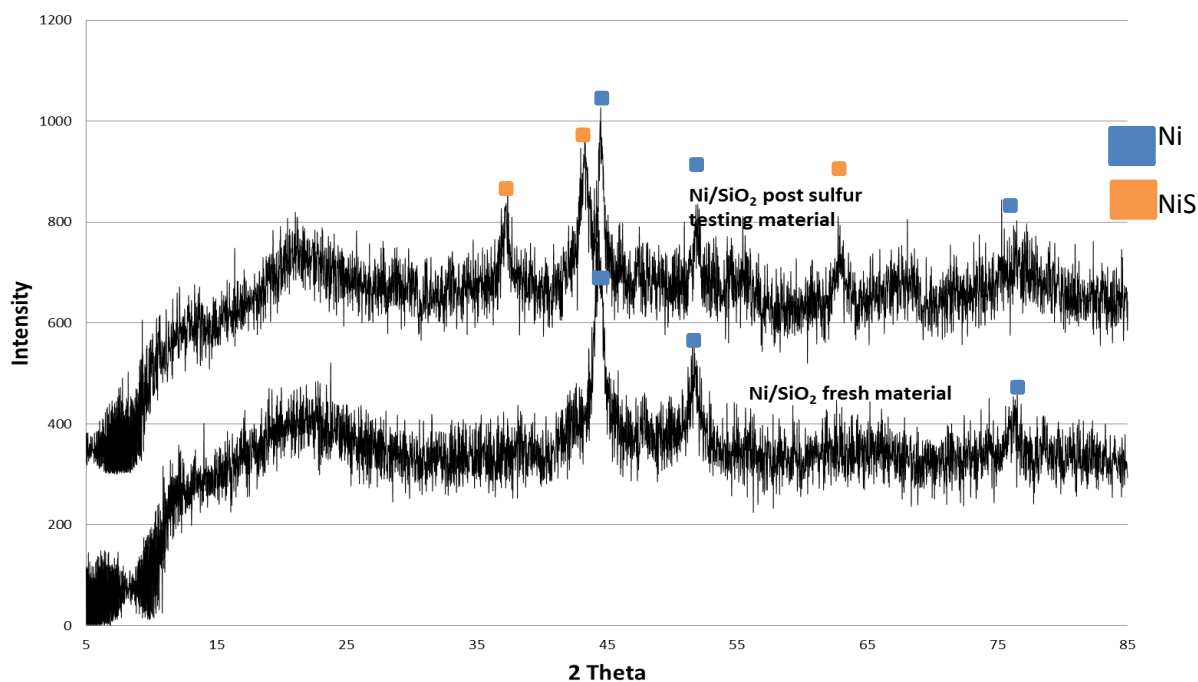


Figure 5-19: XRD patterns for pre and post sulfur testing Ni/SiO₂.

The post-reaction samples of Ce-Ni₂P/SiO₂, Ni₂P/SiO₂ and Ni/SiO₂ were further characterised using X-ray photoelectron spectroscopy. The characterisation of catalysts using XPS was carried out to gain an insight to the electronic state and composition of the active phase of the near surface regions of the catalysts. This was carried out after XRD patterns of pre- and post-reaction samples revealed differences in the catalyst composition and evidence of mixed phases of phosphides and thiophosphates present in the materials after the sulfur testing reactions. The XPS spectra depicting Ni 2p and P 2p regions for pre- and post-reacted Ni₂P/SiO₂ are presented in Figures 5-20 and 5-21 respectively accompanied by tabulated binding energies shown in Table 5-1. The Ni 2p spectrum for the post sulfur testing catalyst presented in Figure 5-20 shows two peaks, a major peak at 853.8eV and minor peak at 858.4 eV. The peak at 853.8 eV has been identified as Ni^{δ+} which is

consistent with it being bonded to phosphorus in Ni_2P as reported previously in Chapter 3 which explored the XPS characterisation of fresh $\text{Ni}_2\text{P}/\text{SiO}_2$ as well as in literature. [7, 12, 13] The minor peak in the spectra at 858.4 eV has been assigned to Ni^{2+} species associated with nickel pyrophosphate, a result of oxy-phosphide surfaces that promote the catalytic activity of the material. [3] There are two further peaks in spectra at 871.1 eV and 878.0 eV have been identified as features associated with $2p_{1/2}$. The comparison of the pre- and post-reaction spectra for nickel indicates that the nickel oxidation state is consistent. This is evident from binding energy peaks associated with the both species of nickel present in the catalyst remaining similar with the fresh material being slightly lower at 853.5 eV. The similarity of the Ni 2p spectra for the fresh and post sulfur tested $\text{Ni}_2\text{P}/\text{SiO}_2$ samples suggests that near surface nickel sites have not been significantly electronically altered after interaction with sulfur. Therefore deactivation of the catalyst is not due to sulfur directly influencing the Ni, suggesting that sulfur possibly indirectly affects the Ni through phosphorus, resulting in only a small change in binding energy between the pre- and post-sulfur materials.

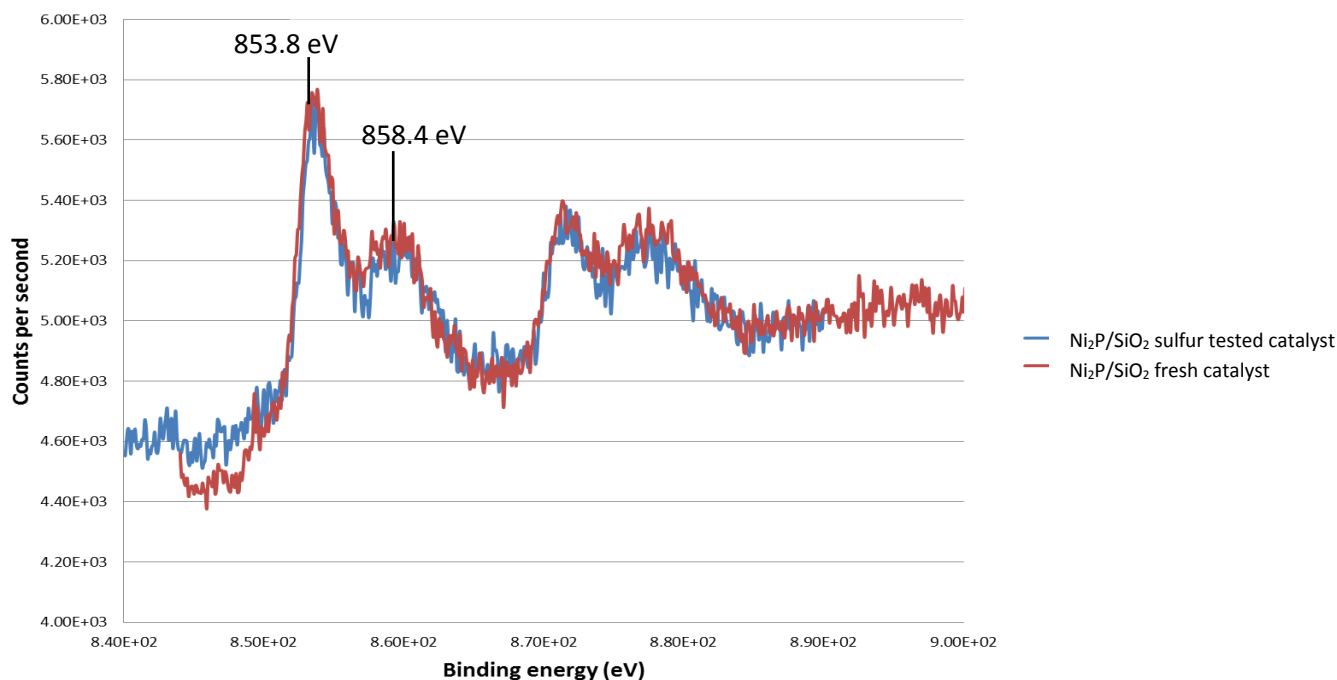


Figure 5-20: $\text{Ni}_2\text{P}/\text{SiO}_2$ Ni 2p spectra for pre- and post-sulfur testing reaction samples.

The post sulfur testing reaction P 2p spectrum for Ni₂P/SiO₂ (Figure 5-21) shows a single peak indicating a single species of phosphorus present in the catalyst. The peak is centred at 131.1 eV and has been identified as P^{δ-}; the phosphorus peak is slightly higher than previously reported studies, with the peak centring at 129.0-131.0 eV. [7, 12, 13] The small difference can be attributed to the presence of thiophosphide phases that were suggested previously when discussing the Ni 2p spectrum for the post sulfur tested catalyst. The fresh Ni₂P/SiO₂ P 2p spectrum in comparison to the post-reaction material is shifted slightly lower at 130.6 eV. The increase in binding energy displayed by the post-reaction sample in comparison to the fresh material may be a result of influence of sulfur rather than oxidation of the catalyst during the reaction due to the phosphate binding energy shift being higher. From the literature, the phosphate species binding energy is approximately 134.0-135.0 eV whilst the thiophosphate species has been reported to have a binding energy of 132.5 eV. [17] The small increase in binding energy indicates that small amounts of sulfur are present in the material. In Chapter 3, the pre- and post-reaction X-ray photoelectric spectra for Ni₂P/SiO₂ are compared and do not display this magnitude of binding energy shift. The formation of thiophosphate phases under sulfur containing conditions have previously been reported for nickel phosphide catalysts. Oyama and Bussell have both alluded to the formation of nickel thiophosphate phases during hydrotreating reactions. These were found to have a beneficial effect in small amounts on the catalytic activity of the material. [6, 14] This was not the case with catalyst activity for the water-gas shift reaction. The negative effect of the sulfur on nickel phosphides water-gas shift activity was evident from the reaction profile which showed that the hydrogen formation rate declined after exposure to sulfur. The activity did not return after clean feed was reintroduced suggesting that poisoning was permanent. There is however the possibility that the catalyst may be regenerated relatively easily due to the sulfur appearing to favour formation of P-S over Ni-S. In Chapter 3 the reduction profile for nickel thiophosphate species revealed the formation of Ni₂P at 400-500⁰C, meaning that under the high temperature water-gas shift regime the catalyst could be regenerated simply by introducing hydrogen for a small period of time to remove the sulfur.

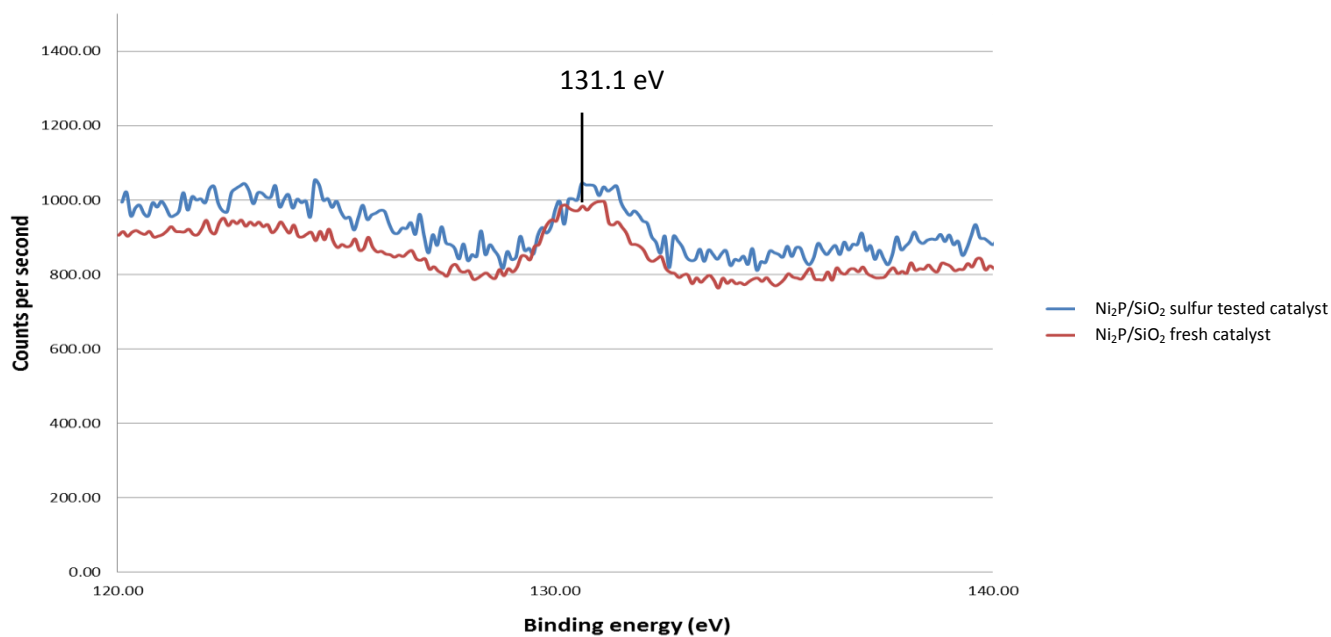


Figure 5-21: Ni₂P/SiO₂ P 2p spectra for pre and post sulfur testing reaction samples.

Sample	Ni ₂ P/SiO ₂	Ni ₂ P/SiO ₂ post sulfur testing
Element	Binding energy (eV)	Binding energy (eV)
Ni 2p	853.5 (largest)	853.8 (largest)
	856.8 (smallest)	858.4 (smallest)
P 2p	130.6	131.1
O 1s	532.8	533.1
C 1s	285.0	285.0

Table 5-1: Summary of binding energy peaks shown in spectra for Ni₂P/SiO₂ pre and post HT shift sulfur testing.

Figures 5-22 and 5-23 display the Ni and P 2p spectra for Ce-Ni₂P/SiO₂ (1% Ce loading) both pre- and post-sulfur tested samples are presented. Table 2 contains the summary of binding energies derived from the spectra. The Ni 2p and Ce 3d spectra for the post-reaction catalyst sample shows three peaks, a major peak at 853.7 eV and minor peak at 858.5 eV and a final peak at 872.7 eV is identified as features of 2p_{1/2}. The peak at 853.7 eV has been identified as Ni^{δ+} which is consistent with it being bonded to phosphorus in Ni₂P as described earlier. The minor peak in the spectra at 858.5 eV has been assigned to Ni²⁺ species associated with nickel pyrophosphate, a result of oxy-phosphide surfaces that promote the catalytic activity of the material. There is no evidence in the spectrum of nickel metal sites associated with Ce-Ni₂P/SiO₂ described in Chapter 4. This most likely due to the all nickel metal sites being converted to nickel thiophosphate or nickel phosphide as was seen in post-reaction materials under non-sulfur containing reaction conditions. The presence of the dominant binding energy peak at 853.7 eV is similar to that of the fresh Ni₂P catalysts. It is therefore safe to assume that the nickel electronic state was not significantly affected by the influence of sulfur after exposure. This was consistent when compared with XPS spectra for the mono metallic nickel phosphide catalyst after sulfur testing. The Ce 3d binding peaks are not visible in the spectrum. This is most likely due to the low loading content combined with high dispersion of the particles. The lack of Ce binding energy peaks makes it difficult at this stage to determine the effect that sulfur has on the cerium or indeed if cerium influences the relationship between the nickel active phase and the sulfur.

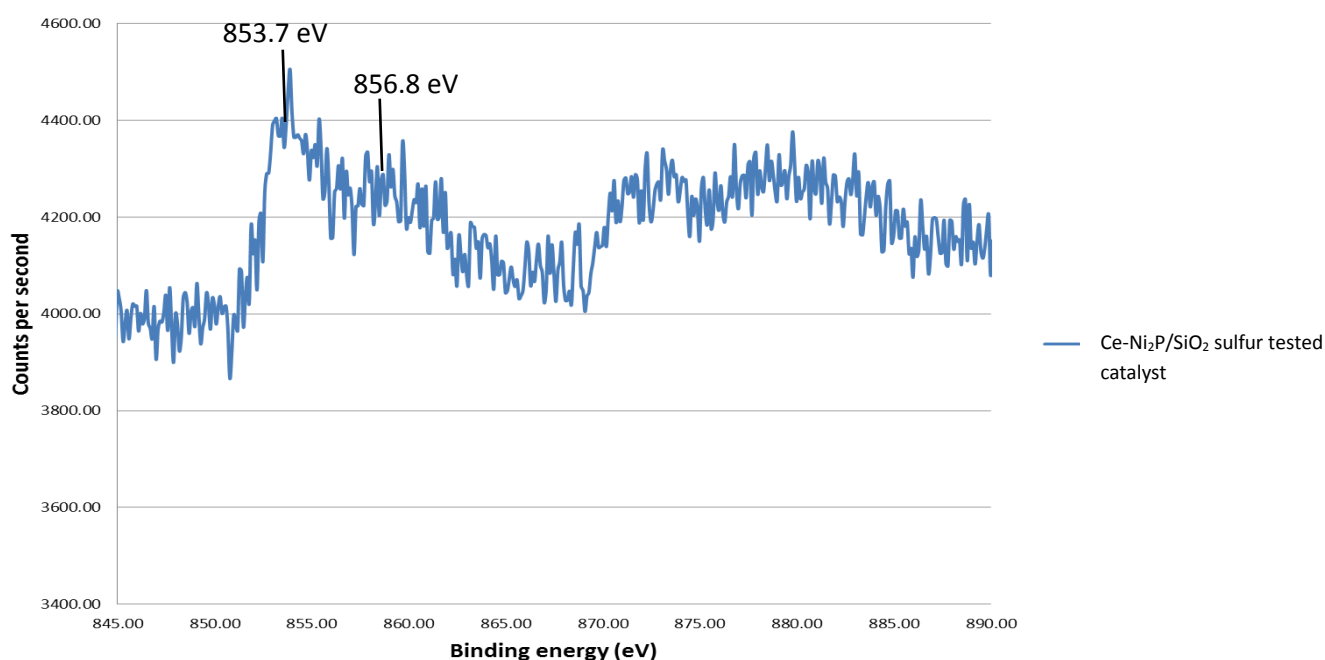


Figure 5-22: Ce-Ni₂P/SiO₂ Ni 2p spectrum for the post sulfur testing reaction sample.

The post-reaction P 2p spectrum for Ce-Ni₂P/SiO₂ (10% w.t. Ce) (Figure 5-23) shows a single peak indicating a single species of phosphorus present in the catalyst. The peak is centred at 130.9 eV and has been identified as P^{δ-}. The phosphorus peak is slightly higher than previously reported studies, which has an estimated binding energy at 129.0-131.0 eV. The small difference can be attributed to the presence of thiophosphate phases at or near the surface of the phosphide particles as was also seen in the mono metallic nickel phosphide X-ray photoelectric spectrum. Comparison of the post-reaction sample with the fresh mono metallic nickel phosphide catalyst phosphorus 2p spectrum indicate that the phosphorus binding energy is marginally higher in the post sulfur testing material (from 130.6 to 130.9 eV). The shift in binding energy displayed in the phosphorus spectrum is consistent with presence of sulfur in small amounts as was seen in the mono metallic material.

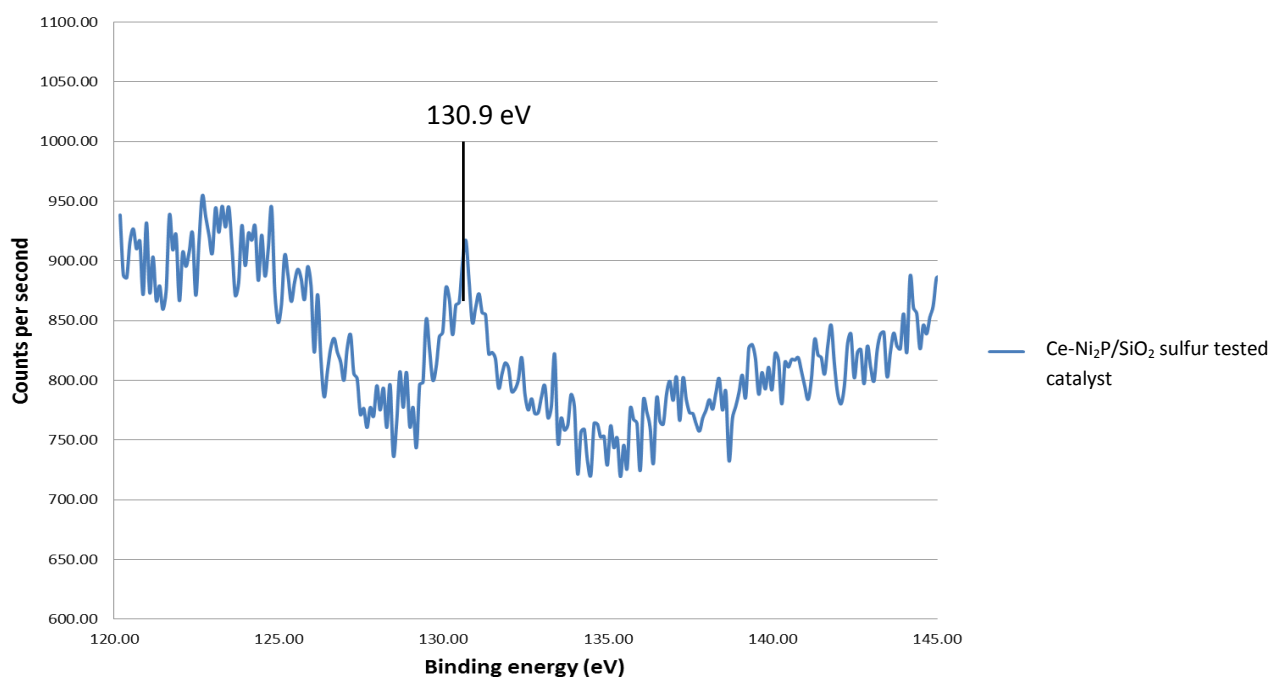


Figure 5-23: Ce-Ni₂P/SiO₂ P 2p spectrum for the post sulfur testing reaction sample.

Sample	Ni₂P/SiO₂	Ce-Ni₂P/SiO₂ post sulfur testing
Element	Binding energy (eV)	Binding energy (eV)
Ni 2p	853.5	853.7 (largest)
	856.8	858.5 (smallest)
P 2p	130.6	130.9
O 1s	532.8	533.3
C 1s	285.0	285.0

Table 5-2: Summary of binding energy peaks shown in spectra for Ni₂P/SiO₂ with Ce-Ni₂P/SiO₂ post HT shift sulfur testing.

Figure 5-24 shows the nickel 2p X-ray photoelectric spectrum for the post-sulfur tested Ni/SiO₂ catalyst. The tabulated binding energies for the material along with binding energies reported in literature are presented in Table 5-3 for comparison of the materials. The nickel 2p spectrum for the catalyst displays a number of binding energy peaks associated with nickel species, indicating a multiple phases present within the material. The binding energy peak at 856.8 eV is much higher than expected for Ni⁰, which has a binding energy usually in the range 852.0-853.0 eV. The peak is associated with nickel in the NiSO₄ species where Ni has an oxidation state of (+II), which is consistent with the binding energy values for NiSO₄ in the literature.^[16] The binding energy peak at 862.7 eV has been assigned as a satellite peak associated with the formation of oxy-sulfide phases of material due to the potentially oxidising conditions within the reactor due to larger concentrations of steam in the reactor. The other peaks in the spectrum at 872.2 eV and 880.1 eV are peaks associated with the 2p_{1/2} features of the Ni spectrum. The XPS data also supports the XRD pattern for the post-reaction sample which indicated the formation of nickel sulfide after exposure to sulfur during reaction conditions. This suggests that the active phase of nickel is fully sulfided in the presence of sulfur containing water-gas shift reaction conditions. The XPS data for the Ni/SiO₂ catalyst highlights the significant influence that sulfur has on the electronic state of the Ni/SiO₂ catalyst. The difference between the nickel and nickel phosphide catalysts are also evident from XPS Ni 2p spectra of the catalysts, with only minor shifts seen in the nickel phosphide catalysts. This is consistent with the reaction profile data for the catalysts which showed nickel phosphide to be more resist to deactivation via sulfur poisoning in comparison to the nickel catalyst.

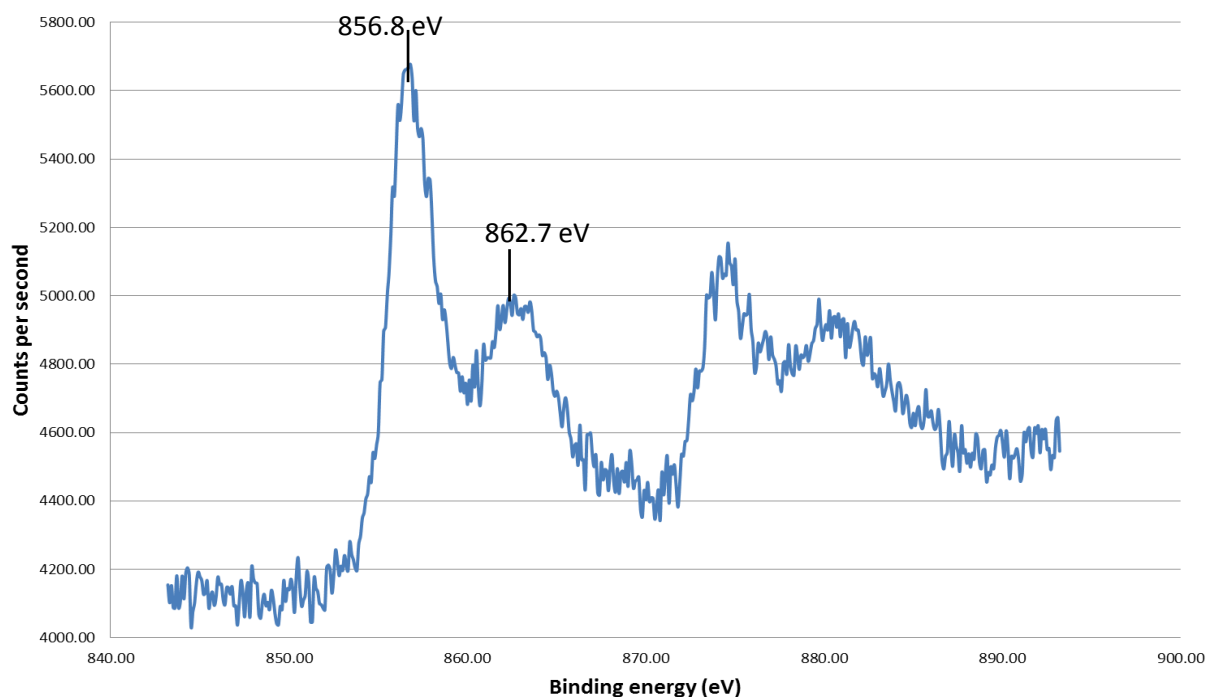


Figure 5-24: Ni/SiO₂ P 2p spectrum for the post sulfur testing reaction sample.

Sample	Ni/SiO ₂ post sulfur testing	Ni metal
Element	Binding energy (eV)	Binding energy (eV)
Ni 2p	856.8 862.7	852.3(largest) 860.1 (smallest)
O 1s	533.1	533.2
C 1s	285.0	285.0

Table 5-3: Summary of binding energy peaks shown in literature for Ni metal with Ni/SiO₂ post HT shift sulfur testing.

5.4 Conclusions

A range of catalysts used previously in the project were studied with regards to their catalytic performance as well as physical and chemical properties after interaction with sulfur containing compounds. These compounds were namely hydrogen sulfide (H_2S) and thiophene ($\text{C}_4\text{H}_4\text{S}$). The catalysts tested were $\text{Ni}_2\text{P}/\text{SiO}_2$ and $\text{Ce-Ni}_2\text{P}/\text{SiO}_2$ (1% Ce loading); these were found to be the two most catalytically active catalysts under standard high temperature water-gas shift reaction conditions along with two standard catalysts: an industrial iron based catalyst and Ni/SiO_2 .

An *in-situ* DRIFTS study was used to investigate the surface interactions of $\text{Ni}_2\text{P}/\text{SiO}_2$ and Ni/SiO_2 catalysts which were pre-treated with thiophene. Flowing CO was run through the microreactor from room temperature to 400°C at increments of 50°C . The $\text{Ni}_2\text{P}/\text{SiO}_2$ catalyst displayed both bridge and terminal CO bonding modes indicating strong interactions between CO molecules and the nickel active sites at a range of temperatures up to 400°C . This indicated that the material may still be catalytically active after interaction with thiophene. The Ni/SiO_2 catalyst under the same conditions did not exhibit any significant CO bonding modes at any temperature indicating the nickel active sites had become deactivated due to pre-treatment with thiophene. The DRIFTS study indicated that there were differences between the nickel and nickel phosphide catalysts with regards to the sulfur resistance displayed by both materials with regards to CO adsorption onto the catalyst surface.

The catalytic testing $\text{Ni}_2\text{P}/\text{SiO}_2$ under high temperature water-gas shift conditions showed that after the introduction of H_2S to the feedstock that formation rates for H_2 and CO_2 began to drop after 20 hours of exposure to H_2S . After feedstock was switched back to the sulfur free feed both H_2 and CO_2 formation rates stabilised. However, the product formation rates did not return to pre-sulfur levels. The formation rates displayed by the catalyst dropped by approximately 80% after sulfur poisoning. The drop in catalyst activity was further highlighted by the CO conversion

profile, which showed a drop in conversion from 0.7 down to 0.2 after poisoning. The deactivation rate constant was calculated from the CO conversion data for the reaction testing and revealed two different stages of deactivation were present during deactivation. The first stage of deactivation produced a deactivation rate constant of 0.0153 h^{-1} which was slower in comparison to the second stage which produced a constant of 0.0709 h^{-1} . The two stages are thought to be due to different species of nickel sites present in the catalyst which deactivate differently via sulfur poisoning.

The reaction profile for Ce-Ni₂P/SiO₂ under sulfur containing conditions showed catalyst activity began to drop after 12 hours of exposure to the H₂S containing feed. The earlier deactivation displayed by the catalyst was attributed to the greater number of nickel metal sites present in the catalyst in comparison to the mono metallic counterpart due to the influence of the cerium dopant on the nickel phases formed. Like the monometallic catalyst, Ce-Ni₂P/SiO₂ product formation rates continued to drop until the sulfur free feed was reintroduced. The H₂ and CO₂ formation rates stabilised but did not return to the rates displayed by the catalyst before in the introduction of the sulfur containing feedstock. The deactivation of the catalyst after exposure to H₂S was further highlighted by the CO conversion profile for the reaction which displayed a drop in conversion from 0.65 before poisoning down to 0.1 after exposure. The CO conversion was used to calculate the deactivation rate constant for the reaction and was revealed to be a single stage deactivation with a deactivation constant of 0.0744 h^{-1} . The deactivation constant for Ce-Ni₂P/SiO₂ was larger than that of Ni₂P/SiO₂ indicating that the catalyst deactivated more quickly. This was due to increased number of nickel metal sites present in catalyst which deactivated more rapidly than the nickel phosphide sites. The difference between the two highlighted the sulfur resistant potential that nickel phosphide catalysts display over nickel itself.

The industrial iron based catalyst and a Ni/SiO₂ catalyst were also tested under the same conditions as the Ni₂P/SiO₂ and Ce-Ni₂P/SiO₂ catalyst to allow for comparison of results. Both the standard catalyst rapidly deactivated after exposure to the H₂S

containing feedstock. The reaction profile for the iron based industrial catalyst showed H_2 and CO_2 formation rates steeply declined to zero. This was highlighted by the CO conversion profile for the reaction which showed CO conversion to initially be 0.90 which dropped to 0.05 after exposure to the sulfur feed. The industrial catalyst did not recover any activity after the sulfur free feed was re-introduced. The deactivation rate constant for the catalyst was calculated to be 0.2759 h^{-1} which was almost four times greater than both the nickel phosphide and cerium doped catalysts. The much larger deactivation rate constant displayed by the industrial catalyst in comparison to both phosphide catalyst highlights the much more rapid deactivation displayed by the iron based catalyst.

The reaction profile for Ni/SiO_2 showed the catalyst also rapidly deactivated after the introduction of the H_2S feed with H_2 and CO_2 formation rates beginning to drop after 17 hours of exposure to sulfur. The product formation rates sharply decline with total deactivation of the catalyst occurring after 27 hours of exposure to H_2S . The catalyst activity does not return after the feed is switched back to the sulfur free feed. The drop in catalytic activity displayed by Ni/SiO_2 is highlighted in the CO conversion profile for the reaction which shows CO conversion is initially 0.93 before the introduction of H_2S and drops down below 0.05 afterwards; representing a massive loss in activity which was greater than was seen with Ni_2P/SiO_2 and $Ce-Ni_2P/SiO_2$. The deactivation rate constant was derived from the CO conversion plot for the reaction and was revealed to deactivate in two stages, similar to the mono metallic nickel phosphide catalyst. The first deactivation phase was slower with a deactivation constant given as 0.1365 h^{-1} which was then followed by a much more rapid stage of deactivation with a constant of 0.4128 h^{-1} . The two stages of deactivation displayed by the catalyst indicated that nickel sites in the catalyst were not fully uniform. The deactivation constant for the main stage of deactivation was the second phase and this was almost six times greater than both the Ni_2P/SiO_2 and $Ce-Ni_2P/SiO_2$ catalysts. The much larger deactivation constant displayed by Ni/SiO_2 in comparison to the two phosphide catalysts signifies a much quicker deactivation of the catalyst due to sulfur poisoning.

The sulfur resistant properties of the $\text{Ni}_2\text{P}/\text{SiO}_2$ catalyst in comparison to the $\text{Ce-Ni}_2\text{P}/\text{SiO}_2$ and Ni/SiO_2 were further supported upon comparison of sulfur saturation of bulk nickel within each of the catalysts. $\text{Ni}_2\text{P}/\text{SiO}_2$ was almost fully saturated by sulfur (0.95) in comparison to $\text{Ce-Ni}_2\text{P}/\text{SiO}_2$ (0.65) and Ni/SiO_2 (0.54). The sulfur saturation data for the catalysts indicated that $\text{Ni}_2\text{P}/\text{SiO}_2$ required the largest sulfur saturation of the nickel present in the catalyst to elicit the deactivation of the active sites. The $\text{Ni}_2\text{P}/\text{SiO}_2$ catalysts greater sulfur resistance is supported upon comparison of the previously discussed deactivation constants displayed by each catalyst which show $\text{Ni}_2\text{P}/\text{SiO}_2$ exhibiting the lowest constant.

Post-reaction testing characterisation of the catalysts was carried out using XRD. The post- reaction diffraction patterns for $\text{Ni}_2\text{P}/\text{SiO}_2$ and $\text{Ce-Ni}_2\text{P}/\text{SiO}_2$ revealed that both catalysts exhibited amorphous phases resulting in no discernable diffraction peaks. The diffraction patterns for both fresh phosphide catalysts displayed a number of diffraction peaks associated with nickel phosphide crystal phases. The disappearance of these peaks in post-reaction materials were concluded to be due to the presence of sulfur which influence the formation of amorphous phases. The XRD pattern for the post-reaction Ni/SiO_2 catalyst revealed that the bulk phase of nickel had become sulfided under the reaction conditions. This was evident from the diffraction peaks associated with the crystal phase of NiS present in post-reaction diffraction pattern. These peaks were not seen in fresh material. The post-reaction samples were also studied using XPS analysis. The Ni 2p spectra for both phosphide catalysts post-reaction testing showed that near surface nickel sites remained electronically stable after sulfur testing. This was evident upon comparison of the pre and post-reaction Ni 2p spectra for both catalysts, which showed no significant shifts in binding energy of nickel. The lack of change in the nickel species between the pre and post-reaction materials suggest that sulfur poisoning is not directly on the nickel sites. The P 2p spectra for both materials displayed a slight shift upward in binding energy suggesting that sulfur poisoning of the catalyst takes place via bonding to phosphorus to form thiophosphate phases which have been previously reported in literature to form in sulfur containing conditions.

5.5 References

- 1) S.T. Oyama , J. Catal; 216; (2003) pg 343–352
- 2) M. Bussell, R. Prins; Catal. Lett; 142; (2012); pg 1413–1436
- 3) P. Liu, J. A. Rodriguez, Y. Takahashi, K. Nakamura; J. Catal; 262; (2009) pg 294–303
- 4) S.T. Oyama, Y.K. Lee; J. Catal; 258; (2008) pg 393–400
- 5) S. Carencó, A. Leyva-Pérez, P. Concepción, C. Boissière, N. Mézailles, C. Sanchez, A. Corma; Nano Today; (2012); 7; pg 21-28
- 6) A. F. Gaudette, A. W. Burns, J. R. Hayes, M. C. Smith, R. H. Bowker, T. Seda, M. E. Bussell; J. Catal; 272 ; (2010) pg18–27
- 7) A.W. Burns, A. F. Gaudette, M. E. Bussell; J. Catal; 260; (2008) pg 262–269
- 8) J. Rodriguez, J.Y. Kim, J. Hanson, S. Sawhill, M. Bussell; J. Phys. Chem. B; 107, (2003), pg 300-313
- 9) I.I. Abu, K.J. Smith; Ap. Catal. A: Gen; 328; (2007) pg 58–67
- 10) S.S.C. Chuang, S.I. Pien; Catal. Lett; 3 (1989), pg. 323–330
- 11) L. Qian, Z. Ma, Y. Ren, H. Shi; Fuel; 122 (2014) pg.47–53
- 12) H. Song, M. Dai, X. Wan, X. Xu, C. Zhang, H. Wang; Catal. Comm; 43 (2014) pg.151–154
- 13) A. Iino , A. Cho, A. Takagaki, R. Kikuchi , S. T. Oyama ; J. Catal; 311 (2014) pg.17–27
- 14) S.T. Oyama, X. Wang, Y.K. Lee, W.J. Chun; J. Catal; 221 (2004) pg.263–273

- 15) S.T. Oyama, *Catal. Today*; 143; (2009) pg 94–107
- 16) H.W. Nesbitt, D. Legrand, G.M. Bancroft; *Phys. Chem. Minerals*; 27, (2000) pg 357-366
- 17) M. Piacentini, F.S. Khumalo, C.G. Olson, J.W. Anderegg, D.W. Lynch; *Chem. Physics*; 65, (1982), Pg 289–304
- 18) I.I. Abu, K.J. Smith *J. Catal*; 241 (2006), pg. 356-364
- 19) K. Smith, R. Wang; *Ap. Catal. A: Gen*; 361 (2009) pg. 18–25

Chapter 6 : Conclusions and future work

6.1 General conclusions

Bulk phase nickel phosphide in a number of stoichiometries was produced using a number of synthetic approaches. The XRD patterns confirmed the phases of nickel phosphide formed and showed nickel phosphide could be produced using a number of routes. Using *in-situ* XRD during reduction of the phosphate precursor it was revealed that Ni₂P was the predominant phase produced under the conditions, however nickel phosphide in a number of additional stoichiometries were produced by tuning the Ni:P ratio in the precursors. Ni₂P was characterised using a number of techniques including SEM, DRIFTS, XPS, and EXAFS to better understand the materials chemical and physical properties. The characterisation of Ni₂P revealed that the material's produced were similar to those reported previously in the literature. The high reduction temperature applied in the reduction of nickel phosphate resulted in low surface area materials. The DRIFTS study indicated that CO adsorption was not visible for bulk nickel phosphide under any of the temperature regimes investigated. The low CO adsorption was attributed to the low surface area exhibited by the material and suggested the materials to be possibly ineffective for application in the water-gas shift reaction. The poor catalytic activity of bulk phase Ni₂P was confirmed upon testing. The resultant reaction profile showed no catalytic activity under both high and low temperature water gas shift conditions. The low catalytic activity of bulk phase nickel phosphide led to the decision to produce supported nickel phosphide, to improve dispersion of particles as well as mechanical properties to the catalyst to allow for application under greater operating conditions. Nickel phosphate was impregnated onto a silica support which was then reduced under hydrogen to give the supported nickel phosphide catalyst (Ni₂P/SiO₂). TGA, TEM, XRD, Raman spectroscopy, SEM and EDX spectroscopy confirmed the presence of nickel phosphide. However, due to the amorphous nature of the support, XRD patterns were not fully conclusive. The qualitative nature of SEM and EDX spectroscopy led to the use of XPS and EXAFS to better characterise the catalyst

and such studies further supported the presence of nickel phosphide on the silica support through the conformation of the chemical and physical states exhibited by the nickel and phosphorus present on the support.

Improved catalytic activity of the supported nickel phosphide was apparent in the DRIFT spectra for the material which showed strong CO adsorption on the nickel phase at temperatures in excess of 250⁰C indicating that the material to be potentially active under high temperature water-gas shift conditions. Catalytic testing of Ni₂P/SiO₂ under low temperature water-gas shift temperature regimes confirmed this, with poor catalytic activity shown at 210⁰C, a poor comparison to a copper based low temperature water-gas shift industrial catalyst. However, the catalyst exhibited good activity for the high temperature water-gas shift reaction. The promising catalytic activity of Ni₂P/SiO₂ under high temperature shift conditions was confirmed upon comparison with an industrial iron based high temperature water-gas shift catalyst with Ni₂P/SiO₂ performing better than an iron based catalyst per unit weight of catalyst. The nickel phosphide catalyst displayed hydrogen formation rates almost double that of the commercial iron catalyst. Post-reaction characterisation of the catalyst revealed that material remained generally unchanged highlighting the catalyst's robust and stable nature. XRD analysis revealed no peak broadening; suggesting that the particle size did not greatly increase under reaction. EDX spectroscopy also showed the Ni:P ratio in particles to be constant between fresh and spent samples, confirming no significant loss of phosphorus upon reaction. The XPS for the post-reaction catalyst indicated both the nickel and phosphorus oxidation states were comparable between fresh and spent samples. There was however a noticeable increase in peak intensity in the post-reaction materials in the phosphorus spectrum indicating the surface was enriched with phosphorus; this was attributed to relationship between phosphorus and oxygen which has been identified previously as a major factor in the catalytic activity of the material.

A range of silica supported bimetallic nickel phosphide catalysts were produced. Ce-Ni₂P/SiO₂ was produced using cerium loadings of 10%, 5%, 1% and 0.5% by mass. These materials were characterised using XPS, XRD, TEM, SEM and EXAFS. The

characterisation of the materials revealed that the addition of cerium influenced the species of nickel formed in the catalyst with nickel metal and nickel phosphide phases being formed. Increasing amounts of cerium led to an increased nickel metal phase fraction in the catalyst. The bimetallic cerium doped nickel phosphides displayed good catalytic activity for high temperature water-gas shift. All of the cerium doped catalysts displayed greater hydrogen formation rates per weight of catalyst than the industrial iron containing catalyst under the same reaction conditions; however none of the cerium doped catalysts performed as well as the monometallic nickel phosphide counterpart. The presence of nickel metal within the catalysts altered the catalytic activity of the catalysts to varied degrees dependent on the cerium loading. The presence of nickel metal in the materials led to methanation as a side reaction. The 1% Ce doped catalyst displayed the highest hydrogen formation rates of all the cerium doped catalysts as a result of a lower fraction of nickel metal being present which meant less hydrogen was lost due to methanation. The post-reaction tested 10% Ce loading nickel phosphide catalyst was characterised using XRD, XPS, EXAFS and SEM. The results indicated that material changed significantly during the reaction testing process. The XRD pattern for the post-reaction sample was compared with the fresh sample and noticeably differed. The post-reaction sample displayed reflections associated with nickel phosphide (Ni_2P and Ni_{12}P_5); these peaks were not visible in fresh material which only displayed diffraction peaks associated with nickel. This suggests that the nickel metal phase was converted into nickel phosphide upon reaction. This phenomenon was further supported by post-reaction XPS which did not display binding energy peaks associated with nickel metal, as was evident in the fresh sample's spectrum. The X-ray photoelectron spectrum also showed an increase in binding energy of the nickel phosphide species associated with near surface phases becoming more oxygen rich under the reaction conditions. Oxy-phosphide surfaces have been previously identified as being influential in the good catalytic activity displayed by nickel phosphide under water-gas shift conditions. EXAFS analysis of the post-reaction sample revealed similar trends to the XPS data indicating that the nickel metal phase was converted to nickel phosphide during the reaction. The theoretical curve fit data also was consistent with this; the Ni-P bond distance was longer and resembles that estimated for Ni_2P as did the co-ordination number. The Ni-Ni bond distance also increased to be a similar distance to that expected for Ni_2P

Further bimetallic nickel phosphide catalysts were made namely; Fe-NiP/SiO₂, Cu-NiP/SiO₂, Cs-Ni₂P/SiO₂ and Pd-Ni₂P/SiO₂. The materials were characterised using a wide range of techniques including EXAFS, XPS and XRD to gain a greater understanding of the phases and compositions of phosphides present on the support. Characterisation of the materials revealed that the phase of material and chemical state were influenced by the second metal when compared with the monometallic nickel phosphide system. The materials were also tested for their catalytic activity in the high temperature water-gas shift reaction. The activity of the bimetallic nickel phosphide systems varied and was noticeably different to the monometallic nickel phosphide counterpart. The most catalytically active of the other bimetallic transition metal phosphides was nickel phosphide doped with 1% caesium, which performed better than the industrial catalysts normalised to mass with regards to hydrogen formation rates, although it was less active than the monometallic nickel phosphide catalyst. The other bimetallic nickel phosphide catalysts did not perform as well as the industrial catalyst. Characterisation of the bimetallic phosphides using XRD, SEM and TEM combined with EDX spectroscopy confirmed the presence of crystalline Ni₂P phases within the materials. However there was also a great deal of amorphous content in the materials due to a number of mixed phases of phosphides being formed. XPS and EXAFS were also used to investigate the materials and indicated a number of differences in comparison to the monometallic catalyst suggesting that the addition of the secondary metallic element modified the nickel phosphide species. The distortion of the Ni₂P phase by the second metallic element ultimately led to poorer activity for the bimetallic nickel phosphide catalysts in the high temperature water-gas shift reaction in comparison to the monometallic catalyst.

The Ni₂P/SiO₂ and Ce-Ni₂P/SiO₂ (1% Ce loading) catalysts were shown to display the best activity for the water-gas shift reaction based on the hydrogen formation rates. In previous studies of HDS nickel phosphide catalysts have been shown to display significant potential with regards to sulfur tolerance. These two catalysts were tested under high temperature water-gas shift conditions with the introduction of H₂S at a concentration of 10ppm. Two standard catalysts were also tested under the same conditions, these were the iron based high temperature water-gas shift industrial catalyst and Ni/SiO₂. As expected, the Ni₂P/SiO₂ and Ce-Ni₂P/SiO₂

catalysts both showed good catalytic activity before the introduction of sulfur to the system, as was characterised by high CO conversion and hydrogen formation rates. After the introduction of sulfur to the feedstock both phosphide catalysts began to show signs of deactivation. This was evident from a drop in both hydrogen formation rates and CO conversion displayed by the materials. After the feed was switched back to the sulfur free feed, both catalysts still displayed some water-gas shift activity. The activity exhibited by the materials after poisoning was significantly lower in both catalysts with CO conversion dropping from 70% to 20% in Ni₂P/SiO₂ and from 65% to 10% in the Ce-Ni₂P/SiO₂ after exposure to H₂S.

The iron and nickel standard catalysts were both rapidly deactivated after the introduction of H₂S to the feedstock. The hydrogen formation and CO conversion rates quickly dropped to zero in both catalysts. After the H₂S feed was removed the catalytic activity of either catalyst did not return indicating that both catalysts were completely deactivated by exposure to sulfur. Comparison of the deactivation rate constant of the standard catalysts with phosphide catalysts revealed that the iron based industrial catalyst deactivated four times more quickly than the phosphide catalysts, whilst the nickel catalyst deactivated almost six times more quickly than both phosphide catalysts. The more rapid rate of deactivation displayed by both the iron and nickel catalysts in comparison the nickel phosphide and cerium-nickel phosphide catalysts highlights the improved sulfur resistant properties of the phosphides in comparison to commercially used catalysts for the high temperature water-gas shift reaction.

The post- reaction diffraction patterns for sulfur exposed Ni₂P/SiO₂ and Ce-Ni₂P/SiO₂ revealed that both catalysts exhibited amorphous phases resulting in no discernable diffraction peaks. The diffraction patterns for both fresh phosphide catalysts displayed a number of diffraction peaks associated with nickel phosphide phases. The loss of these peaks in post-reaction materials was attributed to result from the presence of sulfur leading to the formation of amorphous phases. The XRD pattern for the post-reaction Ni/SiO₂ catalyst revealed that the bulk phase of nickel had become sulfided under the reaction conditions. This was evident from the diffraction

peaks associated with the crystal phase of NiS present in post-reaction diffraction pattern. The post-reaction samples were also studied using XPS analysis. The Ni 2p spectra for both phosphide catalysts post-reaction testing showed that near surface nickel sites remained electronically stable after sulfur testing. This was evident upon comparison of the pre- and post-reaction Ni 2p spectra for both catalysts, which showed no significant shifts in binding energy of nickel. There was a small upward shift in the binding energy of nickel species of the post sulfur tested materials. However, the lack of significant change in the nickel species between the pre- and post-reaction materials suggests that sulfur poisoning is not directly on the nickel sites. The P 2p spectra for both materials displayed a more apparent shift upward in binding energy suggesting that sulfur poisoning of the catalyst takes place via bonding to phosphorus to form thiophosphate phases which have been previously reported in literature to form in sulfur containing conditions

6.2 Future work

This project has highlighted the potential displayed by nickel phosphide as a high temperature water-gas shift catalyst. However, there remains a great deal left unexplored with regards to metal phosphide catalysts and their application in the water-gas shift reaction. The bimetallic phosphides tested in this project yielded disappointing catalytic activity in comparison to the monometallic nickel phosphide catalyst. Characterisation of the catalysts revealed that introduction of a second metallic element caused distortion of the Ni₂P active phase which ultimately led to poor activity. This was also reported in the literature with regards to bimetallic phosphide application in hydrotreating processes. Literature has suggested that nickel rich phosphides have yielded positive catalytic results; therefore it would be of great interest to the continuation of this project to further explore alternative phosphide composition using a varied stoichiometric ratio of components. Another interesting area to explore would be the catalytic application of Nobel metal phosphides, using noble metals such as palladium, platinum and rhodium which have previous been investigated for their application in a number of hydrogenation reactions. The noble metal phosphide catalysts were shown to perform as well or

better than commercially used catalysts. Noble metal catalysts have been well documented as highly active water-gas shift catalyst however they are susceptible to poisoning and sintering under the reaction conditions, therefore the use of noble metal phosphides may improve upon these drawbacks. The sulfur resistant potential of Ni_2P catalysts was highlighted in the sulfur poisoning chapter. The results of the sulfur testing of the nickel phosphide catalysts suggested the possible formation of nickel thiophosphate phases. Nickel thiophosphate is easily reduced to nickel phosphide at the temperature which the high temperature water-gas shift reaction is run therefore it may be possible to regenerate the catalyst to the pure Ni_2P phase which is the essential active phase. It would also be useful to further explore the relationship between nickel phosphide and sulfur by using EXAFS to characterise the post-reaction samples, this would allow for a more rounded understanding of how the active phase of the catalyst is affected by sulfur. A better understanding of the relationship between the sulfur and nickel phosphide may lead to the development of more sulfur tolerant catalysts in future.

Chapter 7 Appendix

Bulk phase nickel phosphide Ni_3P and Ni_5P_2 phases were also investigated using XPS. The fresh materials were analysed along with steam treated materials. The spectra and tables of binding energies for these materials are presented in the following section.

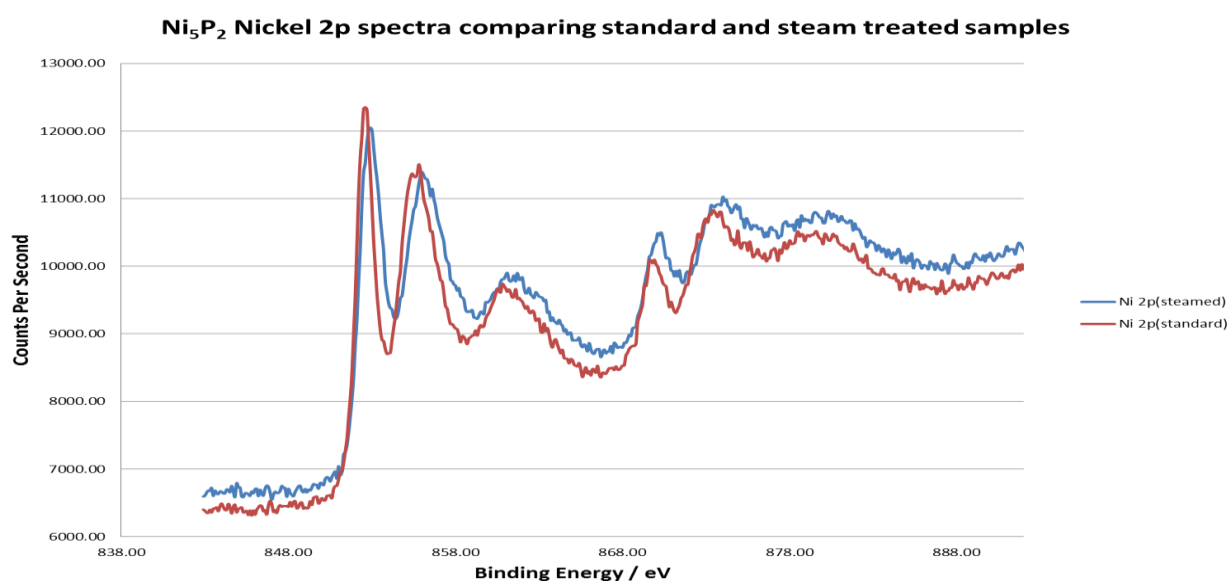


Figure 7-1 Nickel 2p spectra for pre- and post-steam treated bulk phase Ni_5P_2

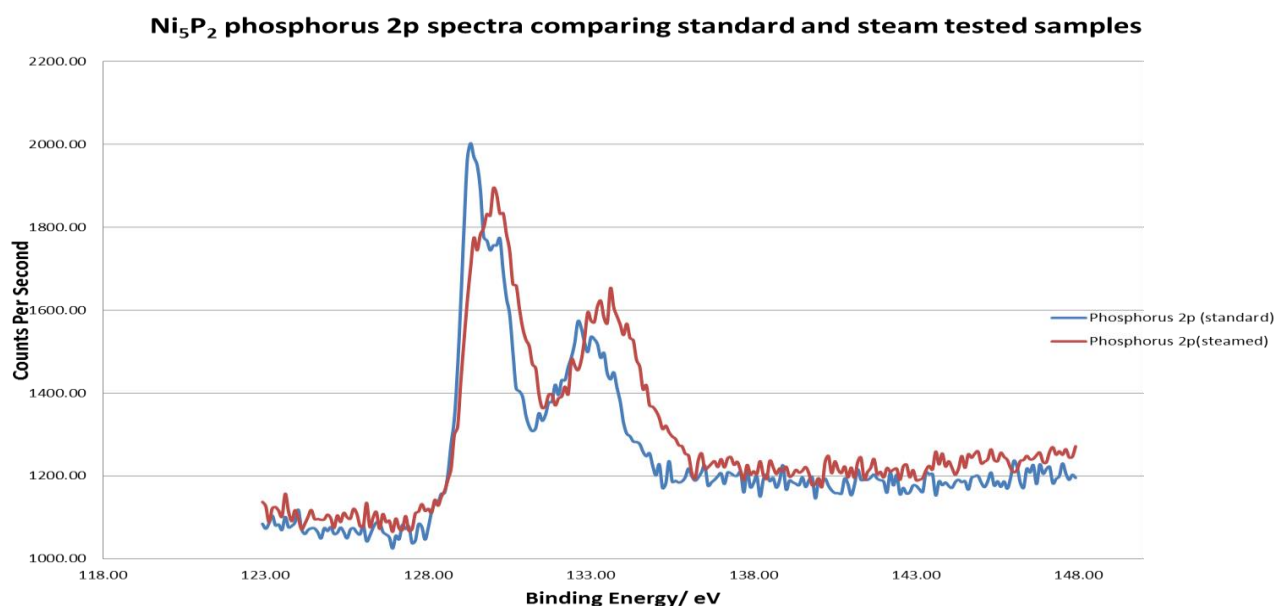


Figure 7-2: Phosphorus 2p spectra for pre- and post-steam treated bulk phase Ni_5P_2

Sample	Ni ₂ P	Ni ₅ P ₄ fresh material	Ni ₅ P ₄ post-steam treated
Element	Binding energy (eV)	Binding energy (eV)	Binding energy (eV)
Ni 2p	853.9 (Ni ^{δ+})	852.7 (Ni ^{δ+})	853.0 (Ni ^{δ+})
	857.4 (Ni ⁱⁱ⁺)	855.9 (Ni ⁱⁱ⁺)	856.2 (Ni ⁱⁱ⁺)
		861.6 (satellite)	862.0 (satellite)
P 2p	130.2 (P ^{δ-})	129.3 (P ^{δ-})	130.1 (P ^{δ-})
	134.1 (P ^{v-})	132.8 (P ^{v-})	133.6 (P ^{v-})
O 1s	533.2	531.1	531.4
C 1s	285.0	285.0	285.0

Table 7-1: Binding energies associated with given spectra for pre- and post-steam treated bulk phase Ni₅P₂

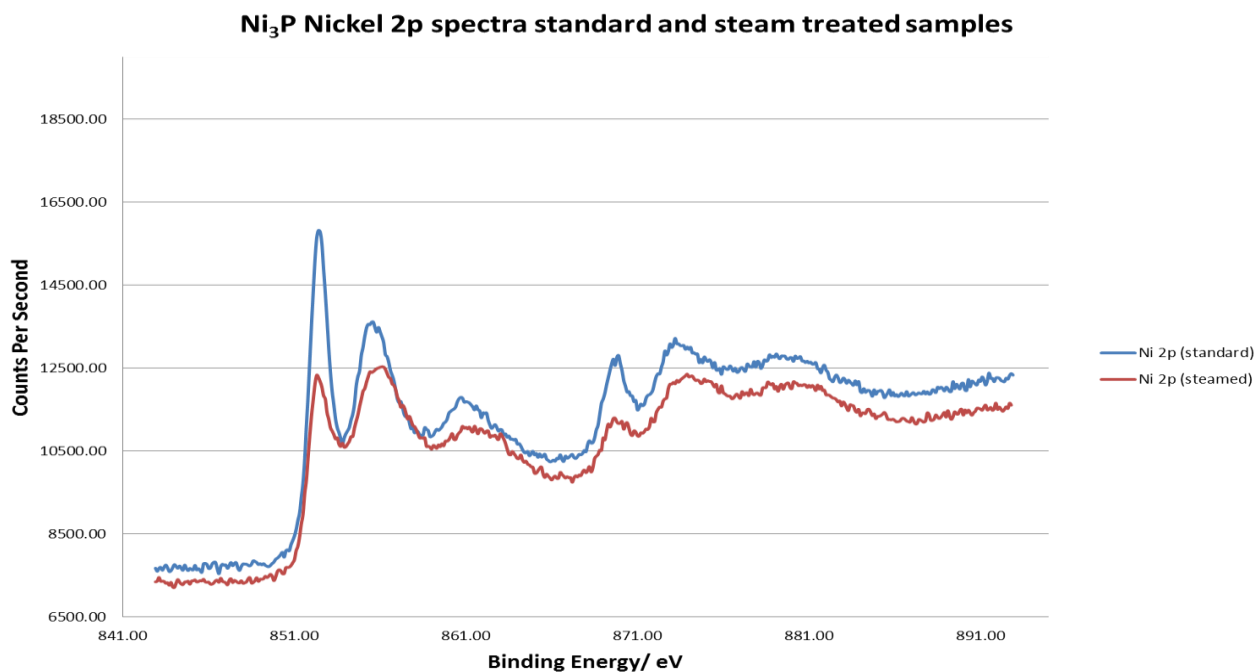


Figure 7-3: Nickel 2p spectra for pre- and post-steam treated bulk phase Ni₃P

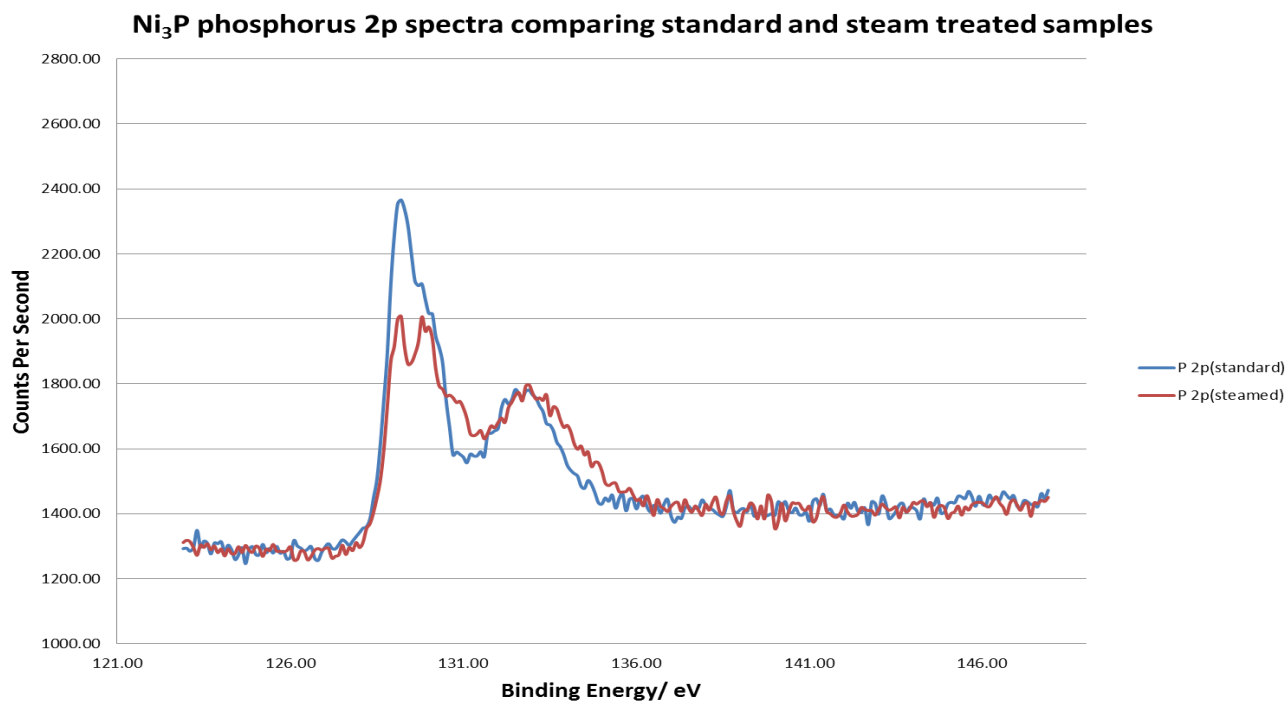


Figure 7-4: Phosphorus 2p spectra for pre- and post-steam treated bulk phase Ni₃P

Sample	Ni ₂ P	Ni ₃ P fresh material	Ni ₃ P post-steam treated
Element	Binding energy (eV)	Binding energy (eV)	Binding energy (eV)
Ni 2p	853.9 (Ni ^{δ+})	852.5 (Ni ^{δ+})	852.6 (Ni ^{δ+})
	857.4 (Ni ⁱⁱ⁺)	855.9 (Ni ⁱⁱ⁺)	856.3 (Ni ⁱⁱ⁺)
		861.3 (satellite)	861.9 (satellite)
P 2p	130.2 (P ^{δ-})	129.3 (P ^{δ-})	129.9 (P ^{δ-})
	134.1 (P ^{v-})	132.8 (P ^{v-})	133.2 (P ^{v-})
O 1s	533.2	531.1	531.2
C 1s	285.0	285.0	285.0

Table 7-2: Binding energies associated with given spectra for pre- and post-steam treated bulk phase Ni₃P